Towards ferromagnetic 2D MXenes: Thermal activation of $Ti_3C_2T_x$ and Fe intercalation in ultra high vacuum

Zum Erwerb des akademischen Grades
Doktor der Naturwissenschaften
Dr. rer. nat.
der Fakultät für Physik der Universität Duisburg-Essen vorgelegte

Dissertation

von

Tim V. Salzmann

aus Essen

Erstgutachter: Prof. Dr. Ulf Wiedwald
Zweitgutachter: Prof. Dr. Thierry Ouisse

Tag der Disputation: 27.06.2024

Prologue

The process of writing a dissertation has many ups and downs. The main challenge is to achieve maximum depth of content with short but precise formulations. This naturally makes it easier for the reader to absorb the information and to hold his/her attention. In order to make a small contribution in this direction in advance, the reader is familiarized here with the terms frequently used in this work in connection with the investigated $Ti_3C_2T_x$ MXenes. In this way, the description of the actual sample state can be kept as short as possible, which greatly improves readability.
The term 'MXene'/'MXenes' is used in the following for a large number of individual 2D MXene sheets that interact with one another via van der Waals bonds. Depending on the context, the term 'MXenes' can refer to a variety of these materials as well as to a specific one. The singular form 'MXene' generally refers to a specific representative of these materials. Individual 'MXene sheets' are always labelled as such. In addition, the term 'stack' is used for multiple layered MXene sheets of similar size.
An additional index '*th*' used with the investigated $Ti_3C_2T_x$ MXenes, as expressed in $Ti_3C_2T_{x,th}$, means that the MXenes underwent thermal activation. Moreover, '$Ti_3C_2T_{x,th,800K}$' indicates that in this case the MXenes were thermally activated at 800 K. Furthermore, '$Ti_3C_2T_{x,th} + Fe$' describes a MXene on which an Fe film has been deposited after thermal activation. Alternatively, '$Ti_3C_2T_{x,th} + Fe$' can also refer to a MXene into which Fe was intercalated after thermal activation. And finally, '$Ti_3C_2T_{x,th} + Fe_{700K}$' denotes that the intercalation of Fe has taken place, here for instance at a temperature of 700 K.

Note that figures taken from external sources are used in this work with the permission of the rightsholder and are identified as such. Permissions are conveyed through the Copyright Clearence Center, Inc.

"Just when you think you know something, you have to look at in another way. Even though it may seem silly or wrong, you must try."

Robin Williams as Professor Keating
in *Dead Poets Society*

Abstract

Achieving intrinsically ferromagnetic behavior of 2D materials at room temperature (RT) is $>$ the challenge $<$ of the 2D community. Success here promises a variety of applications, for example as novel spintronic devices or magnetic sensors. MXenes, a new family of 2D van der Waals (vdW) materials, are promising candidates in this respect. However, MAX phases from which MXenes are synthesized by selective etching of the A element are not compatible with Fe, Co or Ni. Therefore, Fe is intercalated into MXenes in ultra high vacuum (UHV) within the scope of this work to master ferromagnetic properties.

First, $Ti_3C_2T_x$ MXenes, functionalized by surface groups $T_x := O$, $-OH$, $-F$ and $-Cl$ from the wet-chemical etching, are deposited on $Si(100)/SiO_2$ substrates and annealed under UHV conditions up to 1000 K (thermal activation). This leads to a removal of $T_x : -OH$, $-F$ and $-Cl$ as well as H_2O intercalated in between MXene sheets to various degrees as confirmed by *in situ* mass spectrometry and Auger electron spectroscopy (AES). As a result, the interplanar spacing between MXene sheets is decreased from initially $d = 1.44 \pm 0.06$ nm to $d = 1.21 \pm 0.09$ nm and $d = 1.03 \pm 0.07$ nm, respectively, as shown by wide-angle X-ray scattering (WAXS).

A 6 nm Fe film deposited on MXene samples is intercalated *in situ* by thermally driven diffusion at temperatures between 400 K and 1000 K. The diffusivity of Fe perpendicular to layered MXene sheets ($D_\perp \sim 10^{-21}\,m^2\,s^{-1}$ to $\sim 10^{-20}\,m^2\,s^{-1}$) and the activation energy of Fe diffusion ($E_A = 0.10 \pm 0.01$ eV) are remarkably low, as extracted from AES measurements, X-ray photoelectron spectroscopy (XPS) depth profiles and scanning transmission electron microscopy together with energy-dispersive X-ray spectroscopy (STEM-EDS) cross section analysis. Despite intercalated water in MXenes, Fe remains metallic under vacuum conditions and is stable in air after intercalation. In MXenes thermally activated at 1000 K, Fe penetrates up to 25 nm, whereby the interplanar spacing does not change, as WAXS measurements have shown. Here, near-surface Fe clusters are formed in voids of MXene samples showing a bcc structure as demonstrated by X-ray absorption near-edge structure (XANES) spectroscopy and the X-ray linear dichroism (XLD) at the Fe K-edge. For lower thermal activation temperatures $T_{th} < 675$ K, 35 times higher diffusivities of Fe into stacked MXenes as well as a higher penetration depth are observed. Furthermore, XANES and XLD spectra at the K-edge of Fe indicate a formation of Fe_3C and/or Fe in a local environment similar to that of Fe_3C, e.g. upon binding to MXene sheets as a termination species. Diffusion of Fe in between MXene sheets is supported here by a systematic upward deviation of the interplanar spacing ($d = 1.39 \pm 0.11$ nm) after Fe intercalation, based on X-ray diffraction (XRD) measurements.

For MXenes, thermally activated at $T_{th} < 675$ K with intercalated Fe, vibrating sample magnetometry (VSM) measurements at 300 K in in-plane geometry show hysteresis loops with a saturation magnetization of 740 ± 130 kA/m and a coercive field of 58 ± 1 mT. At $T < 100$ K there is a significant increase of the coercive field, which amounts to 239 ± 1 mT at 5 K. The Curie temperature equals $T_C = 544 \pm 8$ K and is 60 K higher than the one of Fe_3C ($T_C = 485$ K). Moreover, X-ray magnetic circular dichroism (XMCD) spectra at the Fe K-edge at 300 K show spectroscopic features of Fe_3C, but also additional features pointing to diverse atomic configurations of intercalated Fe in MXenes thermally activated at temperatures $T_{th} < 675$ K.

Zusammenfassung

Intrinsisch ferromagnetisches Verhalten von 2D Materialien bei Raumtemperatur (RT) zu erzielen ist > Die Herausforderung < der Forschung an 2D Werkstoffen. Ein Erfolg verspricht hier eine Vielzahl von Anwendungen, beispielsweise als neuartige Spintronic Bauelemente oder magnetische Sensoren. MXenes, eine neue Familie von 2D van der Waals (vdW) Materialien, sind in dieser Hinsicht vielversprechende Kandidaten. Allerdings sind MAX Phasen, aus denen MXenes durch selektives Ätzen des A Elements synthetisiert werden, nicht kompatibel mit Fe, Co oder Ni. Daher wird im Rahmen dieser Arbeit Fe im Ultrahochvakuum (UHV) in die MXenes interkaliert, um die angestrebten ferromagnetischen Eigenschaften zu erzielen.
$Ti_3C_2T_x$ MXenes, terminiert durch Oberflächengruppen $T_x := O$, $-OH$, $-F$ und $-Cl$ vom nasschemischen Ätzen, werden zunächst auf $Si(100)/SiO_2$ Substraten deponiert und unter UHV Bedingungen bis zu 1000 K getempert (thermische Aktivierung). Dabei werden $T_x : -OH$, $-F$ und $-Cl$ sowie interkaliertes H_2O zu verschiedenen Graden entfernt, wie durch *in situ* Massenspektrometrie und Auger-Elektronenspektroskopie (AES) verifiziert. Infolgedessen verringert sich der interplanare Abstand zwischen MXene Schichten gemäß Weitwinkel-Röntgenstreuung (WAXS) von anfänglich $d = 1.44 \pm 0.06$ nm auf $d = 1.21 \pm 0.09$ nm bzw. $d = 1.03 \pm 0.07$ nm.
Ein auf den MXene Proben deponierter 6 nm Fe Film wird *in situ* durch thermisch getriebene Diffusion bei 400 K bis 1000 K interkaliert. AES Messungen, Röntgen-Photoelektronenspektroskopie (XPS) Tiefenprofile, und eine Probenquerschnittsanalyse durch Rastertransmissionselektronenmikroskopie in Verbindung mit energiedispersiver Röntgen-Spektroskopie (STEM-EDS) zeigen dabei auffallend geringe Diffusivitäten ($D_\perp \sim 10^{-21}\,m^2\,s^{-1}$ bis $\sim 10^{-20}\,m^2\,s^{-1}$) des Fe senkrecht zu den MXene Lagen, und eine geringe Aktivierungsenergie von Diffusion ($E_A = 0.10 \pm 0.01$ eV). Trotz des in MXenes interkalierten Wassers bleibt Fe unter Vakuumbedingungen metallisch und ist nach der Interkalation an Luft stabil. In thermisch aktivierte MXenes (1000 K) dringt Fe bis zu 25 nm ein, wobei sich der interplanare Abstand nicht ändert, wie durch WAXS Messungen gezeigt. Hier bilden sich oberflächennahe Fe Cluster in Hohlräumen der MXene Proben die eine bcc Struktur aufweisen, wie durch Röntgen-Nahkantenspektroskopie (XANES) und den Röntgen-Lineardichroismus (XLD) an der Fe K-Kante gezeigt. Bei thermischen Aktivierungstemperaturen $T_{th} < 675$ K werden 35-mal höhere Diffusivitäten, sowie höhere Eindringtiefen von Fe in die MXenes beobachtet. Darüber hinaus deuten XANES und XLD Spektren an der Fe K-Kante auf die Bildung von Fe_3C und/oder Fe in einer lokalen Umgebung ähnlich der von Fe_3C hin, z.B. bei Bindung an die MXene Lagen als Terminierung. Eine Fe Diffusion zwischen die MXene Lagen wird hier durch eine systematische Erhöhung des interplanaren Abstands ($d = 1.39 \pm 0.11$ nm) nach der Fe Interkalation, basierend auf Röntgen-Beugungsmessungen (XRD), bestärkt.
Für bei $T_{th} < 675$ K thermisch aktivierte MXenes mit interkaliertem Fe, zeigt Vibrationsmagnetometrie (VSM) bei 300 K und Messung in der Probenebene Hystereseschleifen mit einer Sättigungsmagnetisierung von 740 ± 130 kA/m und einem Koerzitivfeld von 58 ± 1 mT. Bei $T < 100$ K wächst das Koerzitivfeld stark an und beträgt 239 ± 1 mT bei 5 K. Die Curie Temperatur ist $T_C = 544 \pm 8$ K und um 60 K höher als jene von Fe_3C ($T_C = 485$ K). Spektren des zirkularmagnetischen Röntgen-Dichroismus (XMCD) bei 300 K an der Fe K-Kante zeigen spektroskopische Eigenschaften von Fe_3C, sowie zusätzliche Merkmale. Dies weist auf verschiedene atomare Konfigurationen von interkaliertem Fe in den bei $T_{th} < 675$ K thermisch aktivierten MXenes hin.

Contents

List of abbreviations

AES	Auger electron spectroscopy
AFM	Atomic force microscopy
CMA	Cylindrical mirror analyzer
DFT	Density functional theory
DOS	Density of states
E-beam	Electron beam
EDS	Energy-dispersive X-ray spectroscopy
EXAFS	Extended X-ray absorption fine structure
FFT	Fast Fourier transform
FM	Ferromagnet/ferromagnetic
FMR	Ferromagnetic resonance
FWHM	Full width at half maximum
HAADF	High-angle annular dark-field
HR	High resolution
HRTEM	High resolution transmission electron microscopy
HV	High vacuum
ICSD	Inorganic Crystal Structure Database
IGP	Ion getter pump
IMFP	Inelastic mean free path
LAMS	Lewis acidic molten salt
MFP	Mean free path
MFT	Monolayer formation time
MILD	Minimally intensive layer delamination
ML	Monolayer
M(T) curve	Magnetization vs. temperature curve
MV	Medium vacuum
NP	Nanoparticle
OM	Optical microscope
PVD	Physical vapor deposition
QCM	Quartz crystal monitor
RMS	Root mean square
RT	Room temperature

RV	Rough vacuum
SEM	Scanning electron microscopy
STEM	Scanning transmission electron microscopy
TEM	Transmission electron microscopy
TMP	Turbo molecular pump
TSP	Titanium sublimation pump
UHV	Ultra high vacuum
UPS	Ultraviolet photoelectron spectroscopy
vdW	van der Waals
VSM	Vibrating sample magnetometry
WAXS	Wide angle X-ray scattering
XANES	X-ray absorption near-edge structure
XAS	X-ray absorption spectroscopy
XLD	X-ray linear dicroism
XMCD	X-ray magnetic circular dicroism
XPS	X-ray photoelectron spectroscopy
XRD	X-ray diffraction

1. Introduction

In the past decade, 2D van der Waals (vdW) materials have attracted increasing attention from researchers, particularly in the areas of physics and chemistry. In addition, there is also a growing interest from companies in the use, development and commercialization of these materials. Examples here are the start-up *Nanoplexus* from Manchester or the multinational *Taiwan Semiconductor Manufacturing Company Limited* [1]. This can be attributed in particular to the unique combination of reduced dimensionality and the associated exceptional optical, electronic, mechanical and thermal properties of this class of materials [2].
Due to their mechanical and electronic properties as well as their surface chemistry, 2D materials are used in the fields of nanoelectronics, energy storage, as surface coatings for corrosion protection, sensors, and as filtration materials and catalysts in the environmental and chemical sector, to name just a few examples [3].
The aforementioned properties and areas of application can be further enriched by ferromagnetic properties. This includes, in particular, applications in the fields of spintronics, magnonics, quantum computing and magnetic sensing [4]. However, the search for 2D materials with ferromagnetic behavior proves to be difficult. Narrowing this down, the search for a 2D vdW material that is ferromagnetic above room temperature (RT) can literally be compared to the search for the holy grail of the 2D community. This can be justified by the Hohenberg-Mermin-Wagner theorem, which rules out the occurrence of magnetic long-range order in 2D systems with continuous symmetry above 0 K due to infrared fluctuations [4]. Experimentally however, this effect can be mitigated by finite sample sizes, breaking the symmetry and interlayer coupling, the latter being particularly important in layered 2D vdW materials and heterostructures [4, 5]. The result is 2D ferromagnetism with $T_C > 0$. Examples here are the 2D ferromagnets CrI_3 and Fe_3GeTe_2 which have Curie temperatures ranging from 20 K to 130 K [6, 7]. Although this is significantly higher than T = 0 K, they are still far below RT and the observed values in bulk ferromagnets. An example of a ferromagnetic 2D material with a Curie temperature above RT is freestanding CrTe which shows intrinsic ferromagnetism up to a Curie temperature of 367 K [8]. The limitation here, however, is that CrTe is a non-vdW material.
The examples described above nevertheless raise hopes that ferromagnetism in 2D vdW materials with Curie temperatures above RT is reachable. However, there is still a long way to go. This includes in particular the search for potential ferromagnetic 2D materials with maximum Curie temperatures, the understanding of their ferromagnetic properties and, last but not least, the development of synthesis and manufacturing methods that enable production with repeatable

properties on a large scale [9].
2D MXenes are a potential game changer in the search for layered 2D vdW materials with ferromagnetic behavior above RT. This is due to their extraordinary surface chemistry and intrinsic metallic or semiconducting behavior allowing for the engineering of the density of states (DOS). MXenes, first discovered in 2011, are a relatively new family of 2D vdW materials whose members are composed of $n + 1$ layers of an early transition metal (M) separated by $n = 1$-3 layers of carbon or nitrogen (X), which is described by the general formula $M_{n+1}X_n$ [10]. Thereby, numerous MXene compounds appear to be chemically stable such as Ti_3C_2, so far the most investigated MXene [11]. On the other hand, stable MXenes with late 3d M elements like Fe, Co or Ni are only expected from calculations so far [12].
Compared to other 2D vdW materials, MXenes are characterized in particular by their highly functionalized surface. This leads to the binding of so-called surface terminations T_x, typically $= O$, $-OH$, $-F$ and $-Cl$, to the surface M atoms of the 2D MXene sheets during synthesis. Here, the surface terminations have a considerable influence on the MXene properties such as electrical conductivity or magnetic behavior [10]. However, ongoing research promises targeted compositions of T_x through specific synthesis processes and subsequent treatments in the near future, making MXenes with tailored properties feasible [13].
At this point, the connection between MXenes and the search for ferromagnetic 2D materials with high Curie temperatures $T_C > RT$ is to be taken up. Although MXenes with M elements consisting of the ferromagnetic elements Fe, Co or Ni have not yet been synthesized, the surface terminations offer a possibility to achieve ferromagnetic properties of these materials. Here, a suitable change of T_x can lead to an enhancement of the DOS at the Fermi level for MXenes [14]. Analogous to the 3d metals Fe, Co and Ni, this may result in ferromagnetic behavior according to the Stoner criterion as predicted by Kumar et al. (2017) [15] and Frey et al. (2018) [16] for various MXenes. Here, high magnetic moments of $2.5\,\mu_B$ per unit cell for $Ti_{n+1}C_n$ MXenes, and Curie temperatures above RT for Mn_2NT_2 MXenes are results of their calculations [14, 15].
This leads to the aim of this work which is to partially remove the initial surface terminations $T_x := O$, $-OH$, $-F$ and $-Cl$ of $Ti_3C_2T_x$ MXenes by thermal annealing and to intercalate Fe in between the stacked MXene layers in a second step. The starting hypothesis here is that the intercalated Fe binds to the termination-free M atoms as a new termination species, resulting in a hybridization of the electronic states of Fe and the Ti atoms of the MXenes. Since Fe has a high DOS at the Fermi level [17], this is expected to increase the DOS of the MXenes and thus satisfy the Stoner criterion, leading to ferromagnetic behavior of the 2D MXenes with Curie temperatures $T_{C,bulkFe} > T_{C,MXene} > RT$. The central questions arising here are:

1. To what extent can the surface terminations $T_x := O$, $-OH$, $-F$ and $-Cl$ of $Ti_3C_2T_x$ MXenes be removed by annealing in ultra high vacuum (UHV)? What temperatures are necessary to remove which T_x species and how does the interplanar spacing between the stacked MXene sheets change?

2. Is it possible to intercalate a film of Fe deposited on a MXene sample in between the MXene sheets in UHV, and how does the diffusion process take place? What is the chemical state of the intercalated Fe? Is there an interaction between the intercalated Fe and the MXene layers? How does the intercalation of Fe change the interplanar spacing?

3. Do the $Ti_3C_2T_x$ MXenes show ferromagnetic behavior after the removal of the surface terminations and Fe intercalation? What is the Curie temperature and what is the saturation magnetization? And to what extent does the intercalated Fe contribute to the magnetism of the MXene samples?

The steps to answer these questions are taken in this experimental PhD thesis. First, in Chapter 2 the essential knowledge regarding the properties of MXenes in Chapter 2.1 as well as in Chapter 2.2, 2.3 and 2.4 the underlying physics of magnetism, diffusion and the UHV are conveyed.
The removal of the surface terminations and subsequent Fe intercalation under UHV conditions offers several advantages over a high vacuum (HV) or rough vacuum (RV) as described in Chapter 2.4. Therefore, a UHV chamber ($p < 10^{-10}$ mbar) is refurbished for these experiments as outlined in Chapter 3. Furthermore, the synthesis of $Ti_3C_2T_x$ MXenes and the preparation of MXene samples consisting of stacked $Ti_3C_2T_x$ MXene sheets is described in Chapter 4.
To remove the surface terminations $T_x := O$, $-OH$, $-F$ and $-Cl$ the $Ti_3C_2T_x$ MXenes are subjected to an annealing procedure in UHV. This is referred to in the following as thermal activation. The hypothesis here is that the thermal energy generates sufficient vibrations to break the covalent bonds of the terminations to the surface Ti atoms of MXene sheets and enable desorption/diffusion from multilayer sheets. This has already been observed in the HV by Hart et al. (2019) [18] for the removal of $T_x : -OH$ and $-F$ from $Ti_3C_2T_x$ MXenes. However, complete removal of the terminations leads to a collapse of the MXene sheets [13], which hinders the intercalation of Fe. Therefore, the desired goal is to maintain a small amount of the initial termination species and thus ensure a sufficiently large interplanar spacing and vdW structure between MXene sheets for the diffusion of Fe. As a result of the small amount of residual gas atoms in UHV conditions, the temperatures at which the respective terminations T_x and adsorbed H_2O sitting in between the MXene sheets diffuse out of the samples can be precisely determined using mass spectrometry as shown in Chapter 5.1. This allows very accurate control of the removal of the surface terminations according to the aims described above. In addition, diffusion of residual gas atoms and H_2O into the MXenes during thermal activation can be avoided in UHV. This ensures that the exposed, termination-free M atoms on the surface of MXene sheets remain unoccupied by residual gas atoms and are available for the subsequently intercalated Fe.
Also, the atomic composition within the top few nm of the MXene samples is measured before and after thermal activation using *in situ* Auger electron spectroscopy (AES). In this way, the amount of terminations remaining after thermal activation can be quantitatively verified, as shown in Chapter 5.1. For the reasons mentioned above, it is also important to investigate how

the interplanar spacing between MXene sheets changes upon removal of the surface terminations. This is why the structural state of the MXenes before and after thermal activation is checked by *ex situ* X-ray diffraction (XRD) and wide angle X-ray scattering (WAXS) in Chapter 5.2.
Following thermal activation, an Fe film is evaporated on the MXene samples in UHV and subsequently intercalated by annealing. The hypothesis in this context is that the thermal energy supplied during the heating process enables a diffusion of Fe in between the stacked MXene sheets allowing it to bind to termination-free surface M atoms. In this context, it will also be experimentally shown that no oxidation of Fe occurs due to the small amount of residual gas in the UHV chamber. The diffusion of Fe in MXenes and its intercalation states are investigated in Chapter 6. First, in Chapter 6.1 the intercalation of Fe is examined using *in situ* AES as well as *ex situ* X-ray photoelectron spectroscopy (XPS) depth profiling, and scanning transmission electron microscopy together with energy dispersive X-ray spectroscopy (STEM-EDS) cross section analysis to quantitatively determine the diffusion parameters and activation energy of diffusion. Based on these quantitative observations, a qualitative model to describe the distribution of intercalated Fe in the MXene samples is drafted and discussed in Chapter 6.2. In order to also live monitor the intercalation process of Fe *in situ*, electrical transport measurements are performed on the samples during Fe intercalation as described in Chapter 6.3.
The diffusion study only provides a qualitative model to trace the local distribution of Fe in the MXenes. Therefore, X-ray absorption spectroscopy (XAS) measurements are conducted on the samples. This enables the investigation of the X-ray linear dichroism (XLD) at the K-edge of Fe and Ti, and thus gives insights into the local environment and structural coordination of the intercalated Fe. Consequently, it can be deduced whether Fe merely forms clusters in voids between stacks of MXene sheets or actually diffuses between the hexagonal MXene layers. Furthermore, the XAS measurements provide information on the chemical state of the intercalated Fe and $Ti_3C_2T_x$ MXenes. Potential binding of Fe to the termination-free Ti atoms of the MXenes can thus be recognized. The results of the XAS measurements on the samples are discussed in Chapter 7.1. Beyond that, *ex situ* WAXS and XRD measurements are used to monitor the structure and interplanar spacing of the MXene sheets after Fe intercalation as part of Chapter 7.2. This provides further information on whether diffusion of Fe atoms occurs between the MXene sheets.
In Chapter 8 the magnetic properties of the $Ti_3C_2T_{x,th}$ + Fe MXenes are investigated. In this context, first in Chapter 8.1 *ex situ* magnetometry measurements are carried out. Here, magnetization vs. temperature curves (M(T) curves) and magnetic hysteresis loops are recorded to determine the Curie temperature as well as the saturation magnetization and coercive field for different thermal activation and Fe intercalation temperatures. In addition, the local electronic structure of the intercalated Fe is investigated element specifically in external magnetic fields via X-ray magnetic circular dichroism (XMCD) measurements at the Fe K-edge. These measurements promise to provide a "magnetic fingerprint" of the intercalated Fe in the MXenes. The results of the XMCD study are analyzed in Chapter 8.2.

2. Fundamentals

The aim of this work is the realization and subsequent study of $Ti_3C_2T_{x,th}$ + Fe MXenes with ferromagnetic properties. Accordingly, a general overview of the current knowledge on 2D MXenes is given first in Chapter 2.1, while fundamental aspects of magnetism are discussed in Chapter 2.2. To achieve ferromagnetic MXenes, a treatment under UHV conditions is performed. A key issue in this process is the intercalation of Fe into the MXenes, which is based on diffusion. Concerning this, the fundamentals of diffusion are presented in Chapter 2.3. The small amounts of residual gases in the UHV are necessary to prevent the diffusion of foreign atoms into the MXenes and thus their binding to the termination-free M atoms formed after thermal activation. In addition, the oxidation of the intercalated Fe can be effectively avoided under UHV conditions. Consequently, Chapter 2.4 discusses the special features and generation of a UHV.

2.1. 2D transition metal carbides and nitrides - the MXenes

MXenes are classified in the category of so-called 2D vdW materials [19]. Generally speaking, 2D materials have properties that are fundamentally different from the 3D bulk behavior due to the limitation of dimensionality, bringing them more and more into the focus of scientists [20]. Here, the first discovered 2D material was graphene in 2004 [21]. In the following time period increased research in this field led to the finding of whole new families of 2D materials like MXenes, transition metal borides (MBenes) or metal-organic frameworks (MOFs) [22].
The categorization as a 2D material is thereby based on two factors. First the thickness, which if one follows the name given must be only 1 monolayer. However, 2D materials do not necessarily require a single monolayer thickness. Also, materials consisting of up to 10 monolayers can be classified as 2D [23]. This is where the second factor becomes relevant, the easy delaminability of 2D materials. MXene sheets, for example, have a thickness of at least 3 monolayers showing strong covalent bonds within the layers and weak vdW interactions between layers [13]. The latter enables easy delamination of the sheets and thus preserves the 2D character [24].
MXenes are a relatively new family of 2D materials. They were first discovered in 2011 and represent early transition metal carbides and nitrides whereby they are synthesized by removing the A element of an associated MAX phase [25], which is discussed in Chapter 2.1.1. In more detail, MXenes consist of $n + 1$ layers of an early transition metal (M) interspersed with $n = 1$-3 layers of carbon or nitrogen (X). This leads to the general formula given by $M_{n+1}X_n$. Note that also one MXene with $n = 4$ was reported, namely Mo_4VC_4 [26]. In addition, during the synthesis,

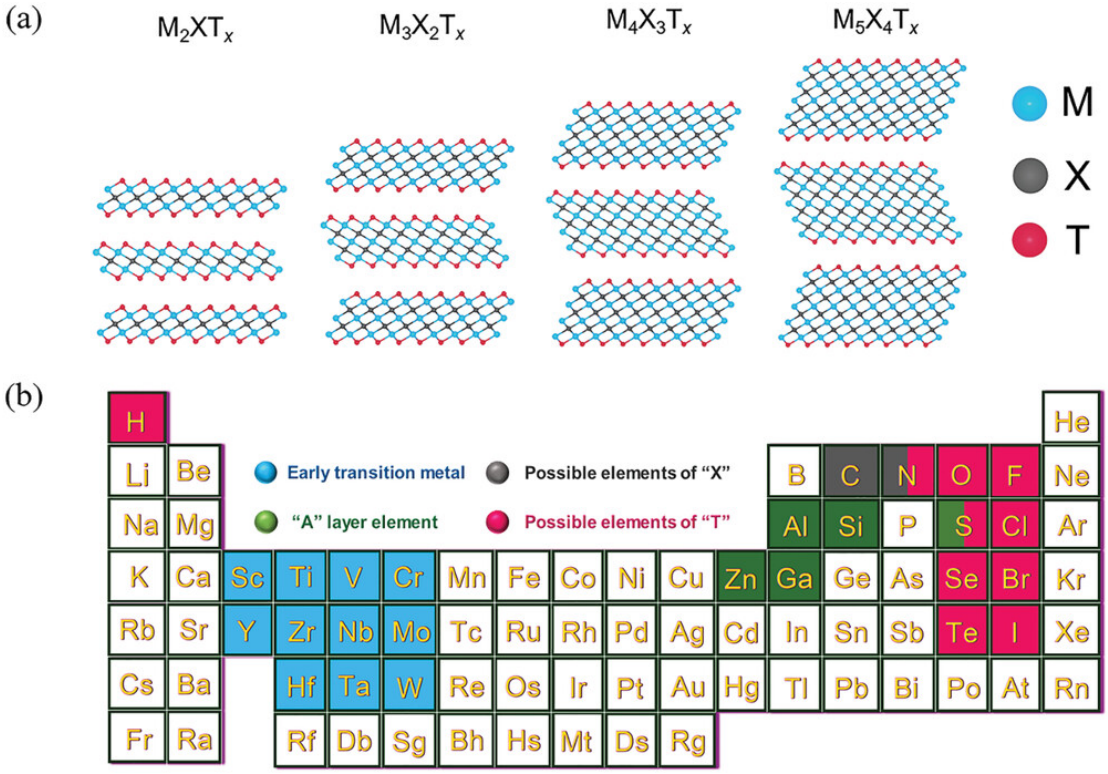

Figure 2.1.: Four structures observed for MXenes according to the general formula $M_{n+1}X_nT_x$, where n + 1 layers of the M element in blue are separated by n = 1-3(4) layers of the X element in gray. In addition, the surface terminations T_x on the top and bottom of the MXene sheets are shown in red. Furthermore common elements of M (blue), X (grey) and T (red) are depicted here as well as typical A elements of MAX phases in green. Used with permission of John Wiley and Sons - Books, from [27].

surface terminations $T_x := O, -OH, -F, -Cl$, bind to the surfaces of the MXene layers. With the surface terminations, the general formula for MXenes becomes $M_{n+1}X_nT_x$ [28]. Here, as an example, the thickness of a $M_3X_2T_x$ MXene sheet amounts to 7 monolayers as can be seen from Figure 2.1. Furthermore, Figure 2.1 sketches all four structures observed for MXenes and shows typical elements for M, X, and T. The surface terminations T_x significantly affect the physical properties of MXenes [29], as described in Chapter 2.1.2 for several examples. The tuning of surface terminations will be discussed in Chapter 2.1.3.

The first MXene $Ti_3C_2T_x$ was discovered at Drexel University in 2011 and is the most studied MXene so far [11]. Following this discovery, more than 40+ MXenes compounds have been synthesized as of 2023 while over 100 possible compositions are predicted but not synthesized so far [30]. $Ti_3C_2T_x$ is selected as the MXene for the experiments conducted in this work as its properties have already been extensively studied, allowing the focus to be on obtaining and studying its magnetic properties after Fe intercalation. Also, the synthesis of $Ti_3C_2T_x$ is well established and reproducible and this compound is chemically stable [31], which facilitates its handling during the experiments performed.

Despite the extensive research in the field of MXenes, knowledge about the ferromagnetic properties of these materials has so far been limited to findings from simulations. In Chapter 2.1.4 an overview of these insights is given.

2.1.1. From 3D MAX phases to 2D MXenes

MXenes are the 2D counterparts to the 3D MAX phases. MAX phases are hexagonal, layered transition metal carbides and nitrides. They consist of a transition metal (M), an A group element (A) and carbon or nitrogen (X). Structurally, MAX phases alternate octahedral $M_{n+1}X_n$ sites (n = 1-4) with layers of the A element, resulting in the general formula $M_{n+1}AX_n$ [27]. Here, the covalent binding of the M-X elements is stronger than the metallic M-A bonds [13, 33]. Typical A elements of MAX phases can be viewed in Figure 2.1.

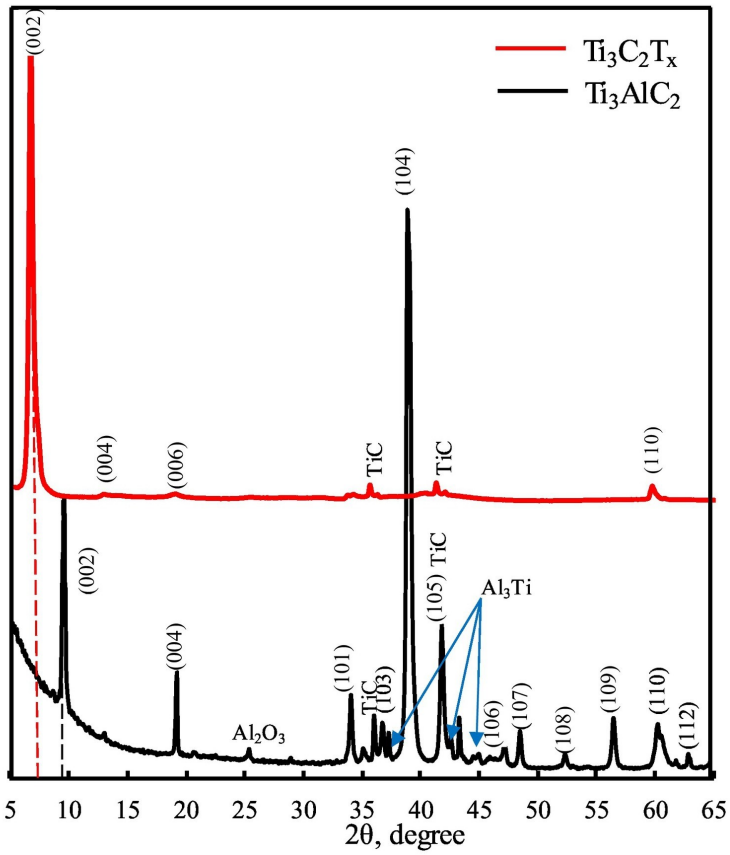

Figure 2.2.: XRD pattern of a $Ti_3C_2T_x$ MXene compared to the Ti_3AlC_2 MAX-phase precursor. The shift of the (002) diffraction peak to the left in the case of MXenes indicates an increase in the interplanar spacing between the $M_{n+1}X_n$ planes due to the removal of the A element of the MAX phase and the intercalation of terminations T_x and H_2O. In addition, the diffraction peaks of the 3D MAX phase have almost completely disappeared, confirming the 2D character of the synthesized MXenes. Used under terms of https://creativecommons.org/licenses/by-nc-nd/4.0/, from [32].

MXenes are synthesized from MAX phases by removing its A element. Consequently, for example, an M_3AX_2 MAX phase yields an $M_3X_2T_x$ MXene. By removal of the A element, M element surfaces are immediately functionalized by surface groups that originate from the etching environment. The surface groups are covalently binding to the transition metal and weakly binding via vdW interactions to surface groups of neighboring sheets [13]. Typical termination species of wet-chemically produced MXenes are T_x :, $= O$, $-OH$, $-F$ and $-Cl$. Furthermore, H_2O is introduced between the layers

in this approach due to the water based solution. The bonding of $-OH$ to the sheets gives rise to additional hydrogen bonds between the layers [34]. It should be noted at this point that the enumerated surface terminations can be influenced and modified as discussed in Chapter 2.1.3.
There are several ways to remove the A element from a MAX phase. One proven approach is chemical etching. Here, an HF solution is used at room temperature [35]. This was also the route to synthesize the first $Ti_3C_2T_x$ MXene from a Ti_3AlC_2 MAX phase [11]. Over the years, it has also been established to use $HCl + LiF$ to etch the A element. This approach is milder and safter than etching with HF. Furthermore, the flouride salt generally increases the interplanar spacing of MXenes which facilitates the subsequent delamination of MXene sheets [27]. Zhang et al. (2018) [36] report the synthesis of Mo_2C MXenes via chemical vapor deposition. In this approach, surface terminations T_x could be avoided [36]. Another possibility for the synthesis of MXenes from MAX phases is the use of Lewis acidic molten salts (LAMS) [13]. As this process is nonaqueous an occurrence of $= O$ and $-OH$ terminations can be prevented [27].
The result after the removal of the A element are stacked MXene sheets. Here, for instance, the lattice c-parameter observed for a Ti_3AlC_2 MAX phase precursor of 1.83 nm is expanded to 2.35 nm for the corresponding $Ti_3C_2T_x$ MXene, as apparent from Figure 2.2.
The stacked MXenes can be delaminated, generally by ultra sonic treatment. The sonication breaks the vdW and hydrogen bonds between the layers and, as a result, single 2D MXene sheets are obtained [14]. Another possibility for delamination is the MILD approach, which stands for minimally intensive layer delamination. Here, the MXenes are mechanically shaken or stirred, whereby larger flakes can be achieved [35]. This approach is suitable when the vdW bonds are weakend due to large interplanar spacings for example achieved when etching with HCl/LiF as described above.
After the synthesis the MXenes are usually filtered and dried [37]. For sample preparation they can be dispersed in deionized water or various organic solvents in order to be deposited on a substrate by means of spin or spray coating (see also Chapter 4.2 and 4.3).

2.1.2. Properties and applications

MXenes possess a long list of attractive properties which, in combination with the 2D character of these materials, opens up an extensive range of applications. In the following, some selected properties of MXenes are summarized and the fields of application discussed. The magnetism of MXenes is deliberately omitted and treated separately in Chapter 2.1.4. Due to the sheer amount of knowledge gained about MXenes in recent years, it is pointed out that only the proverbial tip of the iceberg can be illuminated in the following.
Looking at the structure of MXenes, the c-lattice parameter of MXenes is between 1.5 nm for Ti_2CT_x and 3 nm for $Nb_4C_3T_x$ [14]. The a-lattice parameter amounts to 0.31 nm in the case of $Ti_3C_2T_x$ [14]. In this context, MXenes show a dependence of the structural stability on the surface terminations T_x [14]. Lipatov et al. (2018) [38] have shown that the effective elastic modulus of a single $Ti_3C_2T_x$ MXene sheets is 0.33 ± 0.03 TPa. This value is higher than that

of graphene oxide and thus among the highest measured values for 2D materials [38]. The described structural and mechanical properties of MXenes open up several application areas. One possibility is to use them as reinforcing additives in polymers or coatings, with the positive side effect of improving electrical conductivity [38, 39]. Other potential applications that build on the structural advantages of MXenes lie in the domain of nanoresonators and membranes [38].
A substantial fraction of MXenes possess high electrical conductivity up to 20 000 S/cm [40]. As an example, Dillon et al. (2016) [41] have generated thin Ti_3C_2 MXene films on various substrates using an aqueous solution and spin coating demonstrating conductivities up to 6500 S/cm. Miranda et al. (2016) [42] have confirmed the metallic behavior of $Ti_3C_2T_x$ is maintained down to the monolayer level. Römer et al. (2017) [43] found a dependence between the surrounding humidity and the electrical conductivity of $Ti_3C_2T_x$ MXenes. Moreover, the conductivities could be modified in this work by exposing the samples to a O- or H-plasma [43]. According to Sang et al. (2016) [44] atomic defects have little effect on the electrical conductivity. By looking at Halim et al. (2014)'s work [45], however, one finds a measurable increase in resistivity due to defect formation. Hart et al. (2019) [18] have shown that the electrical conductivity of MXenes depends on the surface terminations. By removing $-$F and $-$Cl terminations, they observed an increase of the electrical conductivity of $Ti_3C_2T_x$ MXenes [18]. In addition Halim et al. (2014) [45] demonstrate that the resistivity in MXenes at low temperatures ($<$70 K) can be described by weak localization, a phenomenon of based on electron backscattering [46]. Contrary to the already listed, some MXenes could exhibit the properties of semiconductors. As for instance Ti_2CO_2 is theoretically predicted to be a semiconductor with a band gap of 0.88 eV [47]. In relation to the electrical conductivity MXenes also show rather high Seebeck coefficients [48].
The targeted optimization of the electrical properties of MXenes goes in two contrarious directions. On the one hand, an ever higher metallic conductivity of the MXenes is aimed at. This serves, among other purposes, the use of MXenes as electromagnetic shieldings, sensors and energy storage materials as well as in optoelectronics and for conformal/wearable electronics [49]. On the other hand, the semiconductor properties of some MXenes can be used in the field of spintronics and thermoelectrics [50].
Of particular interest for spintronics are MXenes that exhibit semi-metallicity, i.e., metallic conductivity for one spin direction, e.g. spin$^{\uparrow}$ state, and insulating behavior for the other, such as theoretically predicted for Ti_2NO_2 [15].
MXenes are also promising materials for rechargeable batteries, supercapacitors, Li-ion batteries and beyond Li-ion batteries, as they have a high storage capacity for various ions while their diffusion barrier in MXenes is low [51]. For example in the work of Zhang et al. (2019) [52], one finds high Li-ion storage capacities and Li-ion adsorption energies for $Ti_3C_2T_x$ MXenes after removal of the surface terminations $-$F and $-$OH. Moreover, in this study a comparatively low activation energy of only 0.34 eV to 0.43 eV for Li-ion diffusion in $Ti_3C_2T_x$ is found, facilitating the transport and intercalation process in these materials [52]. This is of particular interest to the battery and accumulator industry, which is looking for ever more efficient, low-cost and resource-

saving electrical storage systems. In this regard, MXenes are also particularly ideal as electrode materials in next level, beyond Li-ion batteries, and Li-ion capacitors due to their properties such as large and tunable interlayer spaces, excellent hydrophilicity, extraordinary conductivity, compositional diversity, abundant materials and tunable surface chemistries [53, 54].
MXenes are good adsorbers for heavy metal ions and organic dyes [55], radionuclides [56] and gas molecules [57]. Kim et al. (2020) [58] demonstrate increased adsorption efficiency for methylene blue and methyl orange dyes using $Ti_3C_2T_x$ MXenes. In addition, photocathalythic features for MXenes were demonstrated [59]. Such properties open a wide range of possibilities in applications as sensors and filtration materials used in air and water purification. Jin et al. (2022) [60] reveal electroactive Fe/$Mo_2TiC_2T_x$ MXenes that can be used to filter micropollutants in water. Ding et al. (2023) [61] fabricated based on $Ti_3C_2T_x$ MXenes so-called $Ti_3C_2T_x$ MXenes/polyaniline hybrid non-woven fabrics. These are used to obtain a neutral pH value of acidic water such as occurs in the form of acid rain [61]. The latter example illustrates very well the importance MXenes can have in relation to environmental and health factors. MXenes are expected to be of great relevance in this field in the coming years.

2.1.3. Tailoring the surface terminations T_x

As described above, many properties of MXenes depend on the chosen terminations T_x. This raises the question of what possibilities there are to tune the T_x. In principle, a distinction can be made between a chemical and a physical approach, both of which are discussed in the following.
Via suitable chemical reactions, surface terminations can be removed and replaced by others. Ding et al. (2023) [13] have shown that the respective terminations T_x found after synthesis can be substituted by T_x : −S, −Se, −Te, −P, −Sb, −Br, −I. An example from this work is a $Ti_3C_2Cl_2$ Mxene, where the surface termination −Cl have been removed by Ga in a first step. The introduced Ga atoms have a low electron affinity and fill the empty d orbitals of the M element. As a result, the M element reaches a lower oxidation state and the bonds with the −Cl terminations are released. The Cl atoms can then be removed together with the introduced Ga. The Ti_3C_2 MXenes without terminations were subsequently oxidized by a $CuBr_2$ compound. The Lewis base $T^- = P^{3-}$ from an ionic Cd_3P_2 compound features 3 free electron pairs. Together with the Lewis base $T^- = Br^-$ from the $CuBr_2$ compound, it can stabilize the oxidation state of the MXenes by covalent bonding to the M atoms. This finally led to a $Ti_3C_2(P_{0.4}Br_{0.6})_x$ MXene [13]. Thus, in this case, the terminations can be changed from Cl to Br and P via a termination-free intermediate state.
In addition to the described chemical approach for tailoring T_x, surface terminations can also be tuned physically via annealing processes. Here, the thermal energy breaks the bonds of the surface terminations with the M atoms of the MXenes and, as a consequence, the present surface terminations can diffuse and finally desorb from the surface [55].
Density functional theory (DFT) calculations predict for $Ti_3C_2T_2$ MXenes that −OH termina-

tions have the lowest binding energy to the MXene sheets of 5.9 eV compared to −F or = O terminations with binding energies of 7.1 eV or 9.6 eV [62]. In this context, experimental data shows that the −OH terminations in $Ti_3C_2T_x$ MXenes start to desorb from temperatures of 650 K [18]. A fraction of the −OH molecules is further strongly bound to H_2O molecules adsorbed by the MXenes [63], which indicates a removal of water together with the −OH terminations [18]. Fluorine desorbs from $Ti_3C_2T_x$ MXenes starting at about 675 K [18]. Moreover, in the work of Hart et al. (2019) [18] and Persson et al. (2017) [64], no desorption of = O terminations in $Ti_3C_2T_x$ MXenes up to temperatures of 1050 K is observed. This is justified by the high thermal stability of the Ti-O bonds [55]. The M-X bonds of MXenes have typically been found to be stable up to temperatures of about 1050 K before decaying and disrupting the MXene structure [65, 66]. This limits the physical approach to the removal of the initial surface termination −F, −Cl and −OH while = O is preserved as a termination species.
In addition to the removal of terminations in vacuum, re-intercalation of the above listed- or new terminations can be achieved by annealing the MXenes in a suitable gaseous atmosphere. An example is the heating of a $Ti_3C_2T_x$ MXene in a NH_3 atmosphere. This leads to an exchange of the −F and = O surface terminations for −N [67].

2.1.4. Towards magnetic MXenes

The magnetism of MXenes is still poorly understood. One reason for this is that no MAX phase or MXene with Fe, Co and Ni is reported to date, even though stable MXenes with the M element composed of these elements are predicted [12]. However, a modification of the surface terminations can also lead to an increase of the density of states (DOS) at the Fermi level. Analogously to the 3d metals Fe, Co and Ni, this is expected to fulfill the Stoner criterion (cf. Chapter 2.2.3), and lead to ferromagnetic MXenes [14, 15]. In the following, some selected findings on magnetic ordering in MXenes are summarized to give an overview of the current state of knowledge.
Simulations of the DOS by Xie et al. (2013) [68] for monolayer $Ti_{n+1}X_n$ MXenes reveal that, in particular without surface terminations, high DOS are obtained at the Fermi level. Moreover, the calculated DOS of $Ti_{n+1}C_n$ at the Fermi level is 1.9-3.2 times higher than that of the MAX phase precursor material $Ti_{n+1}AlC_n$ [68]. This can be observed in Figure 2.3 for a Ti_2C and a Ti_2CO_2 MXene as well as for a Ti_2AlC MAX phase.
In the presence of surface terminations T_x, the DOS of MXenes at the Fermi level generally decreases. This can be explained by the formation of p-d bonds between the surface terminations T_x and the M atoms of the MXenes [14]. Exceptions in this respect are the MXenes Cr_2C and Cr_2N where theoretical predictions point towards ferromagnetism also in the terminated state [14]. For example, in the case of Cr_2NF_2 it is theoretically predicted that the ferromagnetic order is maintained up to near room temperature (RT), while the magnetic moment ranges up to 3.23 μ_B per Cr atom [69]. Also, stable ferromagnetic ground states are expectd for Mn_2N, terminated with −F, −OH or = O as well as for Ti_2NO_2 and Cr_2NO_2 MXenes [15].

Cr_2NO_2 and Mn_2NO_2 MXenes are theoretically predicted to be intrinsic Ising ferromagnets [16]. In case of Mn_2NF_2, it is reported by Kumar et al. (2017) [15] that the calculated energy for a non-magnetic ground state is higher by 7.1 eV compared to a ferromagnetic ground state. In addition, the simulated DOS suggests a metallic conductivity for the spin$^{\uparrow}$ and insulating behavior for the spin$^{\downarrow}$ component. This is due to a theoretically predicted band gap of 1.0 eV to 2.1 eV generated by a strong magnetic exchange field which causes a shift of the minority spins across the Fermi edge [15].

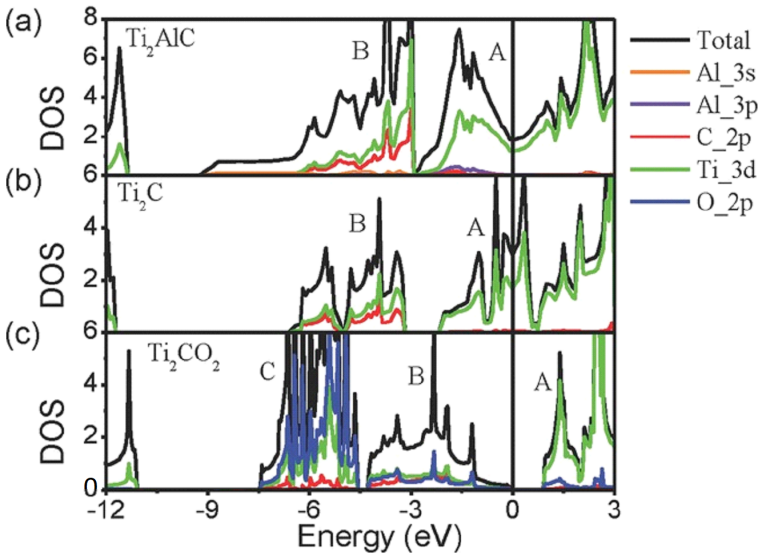

Figure 2.3.: Simulations of the DOS for a Ti_2C MXene without surface terminations as well as for the terminated state Ti_2CO_2. Furthermore, the DOS of the Ti_2AlC MAX phase precursor is shown. In this context, the total DOS as well as the DOS of Al 3s and 3p, C 2p, Ti 3d and O 2p are given. It is evident that the DOS at the Fermi edge for MXene decreases significantly in the terminated state. The unterminated Ti_2C MXene, on the other hand, has a higher DOS at the Fermi edge than the MAX phase precursor. Used and edited with permission of John Wiley and Sons - Books, from [14].

Antiferromagnetic behavior is also predicted for some MXenes like Ti_3C_2 and Ti_3N_2 [14]. In general, intra- and interlayer antiferromagnetism are the most commonly anticipated states by DFT for magnetic ordering in MXenes [15]. In addition, Kumar et al. (2017) [15] report of mixed states, e.g. ferromagnetic order between two neighboring MXene layers and antiferromagnetic order within the sheets. This is expected for Ti_2NF_2 and $Ti_2N(OH)_2$ among others [15]. The ferromagnetic and antiferromagnetic order in MXenes is predicted not to be caused by direct exchange, but by double and super exchange due to the distances between the metal ions in the MXene layers of about 0.3 nm [15].

2.2. Characteristics of magnetism

In this chapter, the basic properties of magnetism are summarized in view of the targeted ferromagnetic properties of $Ti_3C_2T_x + Fe$ MXenes. First, in Chapter 2.2.1, a general overview of the quantities connected to magnetism is given and the different types of magnetism are outlined. Subsequently, the properties of collective magnetism, which includes ferromagnetism, are

discussed in Chapter 2.2.2. Moreover, in Chapter 2.2.3 the ferromagnetic behavior of the 3d transition metal Fe is treated. Finally, the special features of magnetism in reduced dimensions are discussed in Chapter 2.2.4.

2.2.1. Basic classifications of magnetism in matter

The basic quantities used in connection with magnetism are the magnetic moment $\boldsymbol{\mu}$, the magnetization $\mathbf{M}$, the magnetic susceptibility χ, the magnetic field strength $\mathbf{H}$ and the magnetic flux density $\mathbf{B}$. Here χ appears as a proportionality factor between the magnetization and the magnetic field according to [70]:

$$\mathbf{M} = \chi \mathbf{H}. \tag{2.1}$$

This makes χ an indication of how well a material can be magnetized and is used to divided magnetism into 3 different categories: dia-, para- and collective magnetism.
For diamagnetism, $\chi_{dia}(T) = const. < 0$ which means that the magnetization vector of a diamagnetic material is always directed opposite to the field vector of an external field $\mathbf{H}$. This can be understood by the example of superconductors, which are ideal diamagnets. In these, ring currents are excited in an external field, which in turn causes a magnetic field that is directed antiparallel to its source according to Lenz's rule. Each element has a diamagnetic contribution to the magnetism.
Paramagnetism is defined by $\chi_{para} > 0$, meaning that the magnetic moments in a paramagnetic material are aligned parallel to an external field. In the absence of an external magnetic field, the magnetization in these materials disappears, as the magnetic moments average out over time.
Collective magnetism, describes a spontaneous ordering of magnetic moments below a critical temperature, which is caused by an exchange interaction and can only be explained by quantum mechanics. The susceptibility for collective magnetism is basically $\chi_{coll} \gg 0$, whereby it depends on the temperature, the field strength $\mathbf{H}$ and the magnetization history of a material [71].
Ferromagnets show a parallel orientation of the magnetic moments below the critical temperature, which is referred to as the Curie temperature T_C. In case of antiferromagnetism, the magnetic moments of equal magnitude arrange themselves antiparallel below the Néel temperature T_N, whereby they compensate each other and the total magnetization disappears.

2.2.2. Collective magnetism

Magnetic exchange interactions

Magnetic exchange interactions can be used to explain the long-range order of magnetic moments in ferro-, and antiferromagnetic materials below a critical temperature. A distinction is made between direct and indirect exchange [72].
The direct exchange interaction is based on an interplay of the Coulomb interaction and the

Pauli principle [71]. The latter states in the case of fermions that the overall wave function of a quantum system of indistinguishable particles must be antisymmetric. In the case of two neighboring electrons with spins $\boldsymbol{S_i}$ and $\boldsymbol{S_j}$, this leads to two states. A singlet state that describes an antisymmetric spin wave function and a symmetric spatial wave function and a triplet state that describes an antisymmetric spatial wave function and a symmetric spin wave function [71]. Comparing the energy of the singlet state E_S and the triplet state E_T yields the exchange integral according to [71]:

$$J = \frac{E_S - E_T}{2}. \tag{2.2}$$

A positive exchange integral results in ferromagnetic, a negative in antiferromagnetic order [72]. If the overlap of the wave functions is small, direct exchange becomes irrelevant and magnetic ordering occurs as a result of indirect exchange interactions [71]. A distinction is made between different types of indirect interactions, like super exchange, RKKY interactions or double exchange. For details, the reader is referred to respective literature [71].

Ferromagnetism

The magnetic order caused by the exchange interactions can be described in the model of Weiss as the result of an internal molecular field, in the case of a ferromagnet

$$\mathbf{B}_{mf} = \lambda \mathbf{M}, \tag{2.3}$$

where λ describes the molecular field constant [73]. Typical values of B_{mf} are in the range of a few 1000 T [71]. In this model, the relative magnetization below the Curie temperature T_C is according to [71]:

$$\frac{M}{M_S} \propto \left(1 - \frac{T}{T_C}\right)^{1/2}. \tag{2.4}$$

The magnetization at $T = T_C$ is not continuously differentiable, therefore a 2nd order phase transition occurs [71]. For temperatures $T \longrightarrow 0$, spin waves, quantized as magnons, must also be taken into account [71]. These dominate the temperature-dependent behaviour of the magnetization for $T/T_C < 1/2$ and lead to Bloch's law for $T \longrightarrow 0$ given by [74]:

$$M(T) \propto T^{3/2}. \tag{2.5}$$

The susceptibility above the Curie temperature T_C results in

$$\chi = \lim_{B \to 0} \frac{\mu_0 M}{B} = \frac{C}{T - T_C}, \tag{2.6}$$

the so-called Curie-Weiss law [73].
If there is no external magnetic field applied, the magnetization of the sample is $M = 0$ for

$T > T_C$. If an external magnetic field is present, the magnetization becomes $M \neq 0$ for $T \geq T_C$. Here, an increasing external field can stabilize the ferromagnetic phase, leading to an increase in T_C [75].

Magnetic anisotropy

The previous considerations do not take into account any energy dependence with regard to the direction of the magnetization $\mathbf{M}$. However, the materials found in practice are usually anisotropic in terms of magnetism. The most prominent anisotropies in this context are the magnetocrystalline and shape anisotropy.
The magnetocrystalline anisotropy describes preferred directions of the magnetic moments along certain crystallographic axes of the atomic lattice. This is due to the link between the atomic orbitals and the lattice structure [71]. As the spins are coupled to the atomic orbitals via spin-orbit interactions, this results in preferred directions (easy axis) for the magnetization [71].
Polycrystalline materials composed of randomly oriented grains do not exhibit magnetocrystalline anisotropy. However, as soon as the shape of a sample deviates from a sphere, so-called shape anisotropy occurs [71]. This is due to the generated stray field, which causes a demagnetization field inside the material [71]. If a material has a contribution of magnetocrystalline and shape anisotropy, the latter is always dominant [71].

Magnetic domains

In the absence of an external magnetic field, ferromagnets exhibit defined areas with different magnetization directions [76]. These areas are referred to as magnetic domains. Within a domain, all magnetic moments are arranged parallel and the magnetization corresponds to the saturation magnetization [71].
In a sample, the domains are arranged to minimize the overall magnetization. As a result the stray field energy of the sample is reduced. On the other hand, the formation of domains requires energy, as the preferred parallel arrangement of the magnetic moments in ferromagnets must be deviated from in the boundary region of two domains. This is also referred to as domain walls, in which the magnetization vector gradually changes its direction [72]. The direction of magnetization in adjacent domains can be perpendicular or antiparallel to each other [71].
The width of a domain wall is defined by two opposing energy contributions. On the one hand, the change in direction of the magnetization vector requires energy, as a result of which the domain walls tend towards an infinite width [73]. On the other hand, the magnetic anisotropies favour an alignment of the magnetization along the easy axis. In the case of high anisotropies, this leads to a minimization of the domain wall width [73]. Typical widths for domain walls are in the range of 40 nm for Fe [71].
Further additional domains can occur at the surface/interface of a sample due to symmetry breaks, which further minimize the stray field. These are also referred to as closure domains

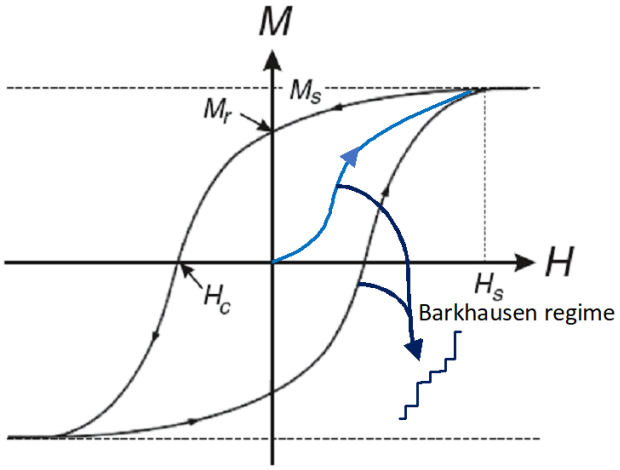

Figure 2.4: Magnetization of a ferromagnet in an external magnetic field. The initial magnetization curve of a demagnetized sample is shown in blue. Pinning of the domain walls to defects leads to Barkhausen jumps when the further increase of the external field causes a sudden displacement of the domain walls. This process is irreversible and leads to a hysteresis curve, shown in black. The hysteresis curve shows a coercive field H_C and a remanence M_r. Used and edited with permission of Springer Nature BV, from [71].

which strongly depend on the magnetic anisotropy of the sample [71].
In a small external field **H**, domains whose magnetization directions deviate by small angles from **H** grow by shifting the domain walls [71]. At higher fields, there is also a rotation of the magnetization in the direction of the external field [71]. In the case of an ideal crystal, these two processes are reversible [71].
In a real crystal, however, defects occur that lead to so-called pinning of the domain walls [73]. In this case, the displacement of the domain walls is "jerky" (Barkhausen jumps), as indicated in Figure 2.4, and irreversible [72]. After the initial magnetization of a demagnetized sample (blue curve in Figure 2.4), this leads to a magnetic hysteresis loop with a remanence $M_r(H = 0) \neq 0$ and a coercive field H_c.

2.2.3. Ferromagnetism of the 3d transition metal Fe

Fe exhibits ferromagnetic behavior at RT and above [17]. As Fe is a late 3d transition metal, the magnetic moments are delocalized. Here, the collective magnetism can be understood by observing the density of states of the spin$^{\uparrow}$ and spin$^{\downarrow}$ electrons at the Fermi level [73].
It can be seen that in the case of a strong exchange interaction and high density of states $g(E_F)$, the spontaneous splitting of the spin states, i.e. spin flips of the spin$^{\downarrow}$ electrons (minority spins) into the spin$^{\uparrow}$ band (majority spins), leads to a reduction in the total energy [76]. Consequently, a ferromagnetic behavior results. This can be expressed by the Stoner criterion [77, 78], which is given by

$$J \cdot g(E_F) \geq 1, \tag{2.7}$$

with J beeing the exchange integral [79]. Paramagnetic behavior follows for $J \cdot g(E_F) < 1$. It is noteworthy that at values of $J \cdot g(E_F)$ just below 1, an increase in the paramagnetic susceptibility

occurs, which is referred to as stoner enhancement [71].
The Curie temperature of Fe is as high as 1028 K [80]. Furthermore, Fe has 8 electrons in 4s and 3d states of which 0.95 electrons are quasi free and 7.05 electrons are located in the 3d band [71]. 4.62 of these 3d electrons are majority spins and 2.43 are minority spins, resulting in the magnetic moment of $2.2\,\mu_B$ [71]. Since Fe has holes in both the minority and majority band it is classified as a weak ferromagnet [73].

2.2.4. Ferromagnetism in reduced dimensions

Limiting a materials dimensionality leads to a changes in magnetic properties including the Curie temperature, magnetic anisotropy, coercive field and magnetic moment [71, 81]. This is due to finite size effects (size and shape, e.g. thin film, nanoparticles (NP), etc.), as well as the increasing influence of surfaces and interface effects (including symmetry breaking), influences of the electronic environment (substrate, surrounding matrix) and magnetic interactions [81].
In small clusters the number of atoms ranges from single-digit to double-digit numbers [82]. Here, significant changes in magnetism, e.g. variations in magnetic spin and orbital moments, can occur due to small changes in cluster size and structure (non-scalable regime) [71].
In NP the magnetic response is independent of small changes in the number of atoms (scalable regime) [71, 82]. However, the domain structure of a NP depends on its size. This can lead, for example, to vortex structures, which have a lasting effect on the shape of a hysteresis curve [71]. Below a critical size of the NP, only single domain particles are observed (Stoner-Wohlfarth particles) [71]. In this case, if the product of the energy density of the magnetocrystalline anisotropy with the volume of the particle is small compared to the thermal energy, flips of the magnetization direction along the easy axis of the crystal occur due to thermal excitations [71]. The time between two flips is given by the Neél relaxation time, which is much shorter than the intergation time of a magnetization measurement [83]. The measured magnetization of a large number of such NP is therefore zero (superparamagnetism).
In 2D structures, such as a ferromagnetic thin film on a substrate, hybridization of the electronic states can occur at the interface [71]. In the case of a non-magnetic substrate, this generally leads to a decrease of magnetic moments near the interface [71]. In addition, a lower Curie temperature can be observed when the thickness of the ferromagnetic film is reduced [79]. In the 2D limit, i.e. in the case of one monolayer of a material, according to the Hohenberg-Mermin-Wagner theorem, no long-range order is expected in isotropic materials for $T > 0$ due to thermal fluctuations. However, ferromagnetic order for $T_C > 0$ can be stable due to interlayer coupling, spin exchange interaction, finite size effects and high anisotropies of the crystal [4, 84]. Interlayer coupling can arise with stacked magnetic thin films. If, for example, two thin ferromagnetic layers are separated by a sufficiently thin non-magnetic layer (a few angstrom Å) an indirect RKKY exchange of the ferromagnetic layers can occur, coupling them antiferro- or ferromagnetically [71]. Roughness at the interfaces generally weakens these interactions [71].

2.3. Diffusion in solids

In this work Fe is intercalated into $Ti_3C_2T_x$ MXenes to obtain ferromagnetic properties of these 2D vdW materials. Here, the Fe intercalation is based on diffusion processes. Consequently, the basic equations and mechanisms for the macroscopic description of diffusion, based on the work of Adolf Fick, as well as the microscopic diffusion mechanisms and the temperature dependence of diffusion are discussed in Chapter 2.3.1.
In addition, the particularities of diffusion in stacked 2D vdW materials, which include the $Ti_3C_2T_x$ MXenes investigated here, are highlighted in Chapter 2.3.2.

2.3.1. The theory of diffusion

Macroscopic model of diffusion: Fick´s laws

Fick's laws can be used for the macroscopic description of a diffusion process. They were derived in 1855 by Adolf Fick on the basis of empirical observations [85]. The laws of Fick can be applied to isotropic and anisotropic media.
Fick's first law describes the relationship between the flux $\mathbf{J}$ of diffusing particles/atoms and their concentration C

$$\mathbf{J} = -D\boldsymbol{\nabla}C, \tag{2.8}$$

where $\boldsymbol{\nabla}C$ describes the concentration gradient and D is a proportionality factor, also called diffusion coefficient, with the unit $m^2\,s^{-1}$ [86]. In the case of an anisotropic medium, D is a symmetrical second-order tensor, leading to a form of Equation 2.8 given by [86]:

$$\begin{aligned} J_1 &= -D_1\frac{\partial C}{\partial x^2} \\ J_2 &= -D_2\frac{\partial C}{\partial y^2} \\ J_3 &= -D_3\frac{\partial C}{\partial z^2}. \end{aligned} \tag{2.9}$$

For an isotropic medium, the diffusion coefficient is identical, $D_1 = D_2 = D_3$, in all spatial directions.
The change in concentration in an infinitesimally small test volume results from the difference of the particles that diffuse into and out of this volume, as expressed by the continuity equation according to [87]:

$$-\boldsymbol{\nabla}\cdot\boldsymbol{J} = \frac{\partial C}{\partial t}. \tag{2.10}$$

Fick's second law then results from Equations 2.8 and 2.10

$$\frac{\partial C}{\partial t} = \boldsymbol{\nabla}\left(D\boldsymbol{\nabla}C\right), \tag{2.11}$$

which is called the diffusion equation [86]. It describes the relationship between the temporal change in concentration at a specific location and the spatial change in diffusion flux $\mathbf{J}$.
In the case of interdiffusion, diffusion is not only caused by a concentration gradient but also by a chemical potential. Hereby, the chemical composition varies along the diffusion path, resulting in different chemical potentials that are associated with different diffusion coefficients [86]. The diffusivity at a location z in a material is therefore dependent on the concentration of the diffusant at this location. Thus, for Equation 2.11 in the case of diffusion in 1D and Cartesian coordinates it follows

$$\frac{\partial C}{\partial t} = D\left(C\right)\frac{\partial^2 C}{\partial z^2} + \frac{dD(C)}{dC}\left(\frac{\partial C}{\partial z}\right)^2, \tag{2.12}$$

with the concentration-dependent diffusion coefficient $D(C)$ [86]. Equation 2.12 is a non-linear differential equation that cannot be solved analytically. However, there are two methods (Boltzmann - Matano and the Sauer and Freise method) to obtain the diffusivities experimentally from depth profiles of the concentration [86].
The situation becomes simpler if the diffusion is only caused by a concentration gradient. Then the diffusivity D in Equation 2.11 is independent of the concentration, which means that the diffusion in 1D can be simplified to

$$\frac{\partial C}{\partial t} = D\frac{\partial^2 C}{\partial z^2}. \tag{2.13}$$

Equation 2.13 is a 2nd order linear partial differential equation that can be solved by selecting suitable initial and boundary conditions. This allows various diffusion problems to be described as shown below for two examples.
The first example is the diffusion of a thin film deposited on a sample. The diffusion in the z-direction, into the sample, is to be considered here. The initial condition $C\left(z, t=0\right) = M\delta(z)$ is given by the fact that the entire diffusing material is on the surface ($z = 0$) at time $t = 0$. M describes the number of diffusing atoms per unit area and $\delta(z)$ is the Dirac delta function. Together with the boundary condition that the sample has a quasi-infinite expansion in the diffusion direction z, a solution for Equation 2.13 can be found which is according to [87]:

$$C\left(z,t\right) = \frac{M}{\sqrt{\pi D t}} \cdot exp\left(\frac{-z^2}{4Dt}\right). \tag{2.14}$$

This expression can be used to determine the concentration of the diffusant at any location z of the sample at a time t.
The setup of the second example is analogous to the first. The difference is a constant concentration of the diffusing material on the surface of the sample. This is the case, for instance, if a sufficiently thick film is deposited. Therefore, at $z = 0$ there is always a reservoir of diffusing material with a constant concentration $C_s = C_0/2$, forming a diffusion couple with the sample.

The solution of Equation 2.13 for this problem is given by the Grube-Jedele formula

$$C(z,t) = C_s \cdot \mathrm{erfc}\left(\frac{z}{2\sqrt{Dt}}\right), \tag{2.15}$$

where erfc describes the error function [86].

Microscopic model of diffusion

Fick's laws are well suited to describe a diffusion process macroscopically. For the microscopic description, it is necessary to consider various diffusion mechanisms, which are discussed below. First, the diffusion of atoms across a material's lattice is addressed. This diffusion mechanism is observed in particular in the case of interdiffusion, self-diffusion and in alloys [86]. In the simplest case, diffusion takes place by exchanging the lattice site with the nearest neighbor (direct exchange mechanism) [86]. However, this involves a large expansion of the lattice and consequently a high activation enthalpy ΔH, which describes the energy required to initiate a diffusion process [86]. Therefore, a collective movement of several atoms, for example by rotation around a lattice site, is often observed (cyclic exchange mechanism) [87].
Diffusion through jumps between neighboring lattice vacancies is energetically even more favorable [86], which is also referred to as the vacancy mechanism. This is observed in particular with self-diffusion in metals and alloys [86].
Small atoms can diffuse via interstitial sites of a crystal lattice. Interstitial diffusion occurs, for example, in connection with the diffusion of hydrogen and carbon atoms in metals [87]. The activation enthalpies for interstitial diffusion are considerably smaller than for lattice diffusion. For example, the activation enthalpy for C diffusion in Nb of 1.5 eV is well below the activation enthalpy of 4.1 eV for Nb self-diffusion [86]. This is due to the fact that no additional energy is required for the described direct or cyclic exchange mechanisms or the formation of defects. Hence, the diffusion coefficients in this case are up to several orders of magnitude higher [86].
Along grain boundaries, surfaces and dislocations in the crystal lattice, interstitial and vacancy diffusion predominantly occurs [88]. The associated low activation enthalpies lead to high diffusivities that are, in the case of metals, 4-5 orders of magnitude higher than for lattice diffusion, which also leads to the term high diffusivity path [86]. This also implies that diffusion can already start at lower temperatures. In Cu, for example, self-diffusion along grain boundaries already takes place at room temperature (RT) due to the low activation energy for this process [86].
Grain boundaries result whenever two adjacent single crystals show a different crystallographic orientation at their interface [86]. A typical example of a material that shows a large number of grain boundaries is a polycrystal, as it consists of numerous monocrystalline grains that are twisted or tilted against each other. Thereby, a grain boundary is characterized by its width δ, which is usually in the range of 0.5 nm, and its diffusivity D_{gb} [86].

Dependence of diffusion on temperature

Diffusion is generally temperature-dependent, whereby the diffusivities increase with increasing temperature. The temperature dependence of the diffusion coefficient often corresponds to an Arrhenius' law

$$D = D_0 \cdot exp\left(-\frac{E_A}{k_B T}\right), \tag{2.16}$$

where k_B describes the Boltzmann constant, T the absolute temperature, E_A the activation energy for diffusion and D_0 the so-called frequency factor [86]. E_A and D_0 are referred to as activation parameters for diffusion [86]. Typical values for the activation energy in metals and

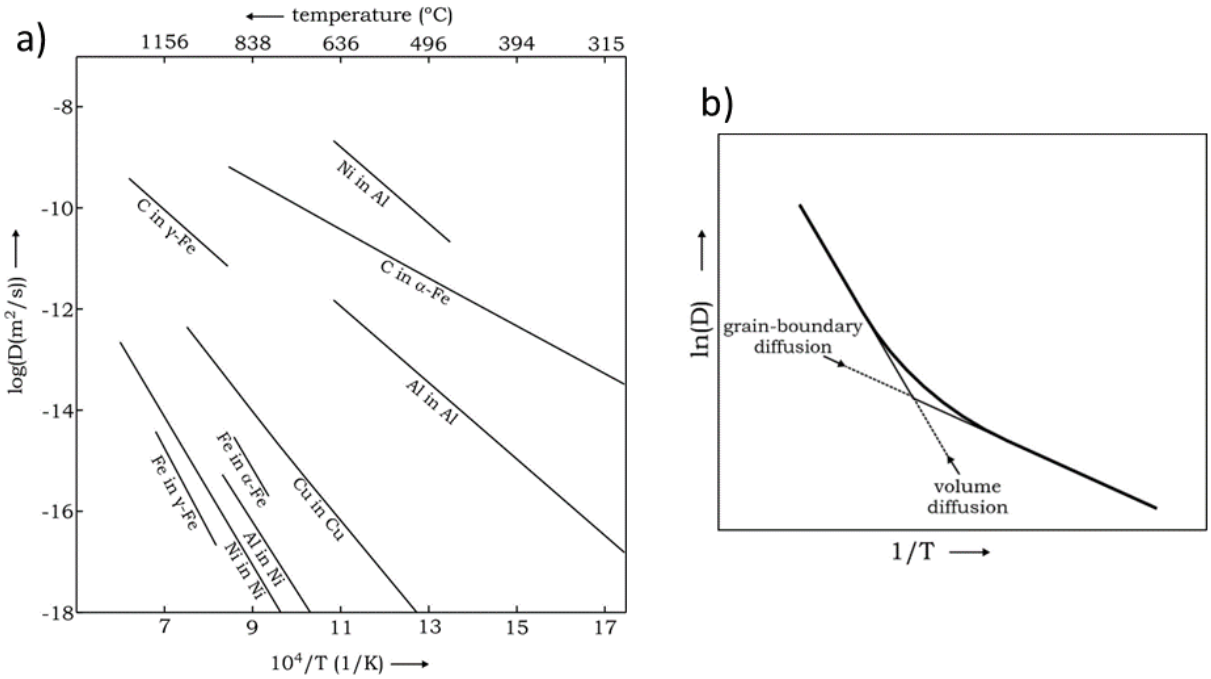

Figure 2.5.: a) Arrhenius plot for self-diffusion and diffusion of impurities in metals. The logarithm of the diffusion coefficient is plotted as a function of the inverse temperature. The activation energy E_A can be determined from the slope of the Arrhenius lines and the frequency factor D_0 from the y-intercept. b) Non-Arrhenius behavior for a polycrystalline sample. At low temperatures, diffusion occurs along grain boundaries, while at higher temperatures there is also volume diffusion associated with a higher activation energy. Accordingly, the activation energy is temperature-dependent. Used with permission of Springer Nature BV, from [88].

alloys are in the range of 1-6 eV while for D_0 values around $1 \times 10^{-5}\,\mathrm{m}^2/\mathrm{s}$ are observed [87].
If the logarithm of the diffusion coefficient D is plotted as a function of the reciprocal of the absolute temperature T, an Arrhenius plot is obtained as shown in Figure 2.5 a) for the self diffusion and diffusion of impurities in different metals. According to Equation 2.16, the Arrhenius lines in the diagram correspond to linear functions whose slope corresponds to the activation

enthalpy

$$E_A = -k_B \cdot \frac{\partial lnD}{\partial T^{-1}}, \tag{2.17}$$

and whose y-intercept corresponds to the frequency factor D_0 [86]. The frequency factor is therefore a measure of the maximum possible diffusivity at infinite temperature.
In the case of a temperature dependence of $E_A(T)$ and thus also $D_0(T)$, the diffusivities in the Arrhenius plot no longer show a linear behavior. This can occur in particular if several diffusion mechanisms are involved in a diffusion process [87]. One example is diffusion in a polycrystalline material. Here, diffusion at low temperatures takes place along grain boundaries. The associated low activation energy leads to a small slope in the Arrhenius plot. Above a certain temperature, however, there is also volume diffusion through the crystal lattice [88]. The associated higher activation energy leads to an upward curvature of the diffusivities in the Arrhenius plot, as shown in Figure 2.5 b).

2.3.2. Diffusion in 2D layered materials

Considering the intercalation of atoms in a layered 2D vdW materials, such as the $Ti_3C_2T_x$ MXenes investigated in this work, two basic mechanisms should be considered with respect to diffusion perpendicular to the surface of the 2D sheets. This is on the one hand diffusion through the 2D sheets and on the other hand diffusion around them.
Density functional theory (DFT) calculations were performed by Zhao et al. (2014) [89] for the perpendicular diffusion of Cu in stacked graphene for the cases shown in Figure 2.6. It turns out that the activation enthalpy of 0.17 eV for diffusion around the 2D sheets, corresponding to case (5) in Figure 2.6, is significantly lower than for the other cases. Cases (2) and (4), for example, result in activation energies of 30.6 eV and 5.23 eV [89]. Ahmed et al. (2022) [90] predict activation energies of 1.2 eV for the diffusion of Cu through graphene sheets with defects, which corresponds to case (3) in Figure 2.6. This leads to the conclusion that the 2D sheets act as barriers to diffusion and that diffusion occurs primarily around the sheets.
As described in Chapter 2.1, 2D materials can be composed of several atomic layers. In the case of the $Ti_3C_2T_x$ MXenes investigated here, each of the 2D sheets consists of 7 atomic layers. As a result, the energy barrier for diffusion through the sheets tends to be higher than in the case of 1 atomic layer [91]. Consequently, diffusion around the MXene sheets can be expected for medium and heavy atoms, such as Fe. For light elements such as carbon, there is also the possibility of interstitial diffusion through the sheets, as explained in Chapter 2.3.1.
Diffusion around 2D sheets, as reported by Stark et al. (2019) [91], shows a dependence of the diffusivity on the lateral expansion of the sheets. Here, the diffusivity perpendicular to the sheets increases significantly when the lateral dimension of the 2D sheets decreases [91]. The logical conclusion that follows from this is a high anisotropy of stacked 2D materials with respect to diffusion. This can be clarified best in an example: If the lateral size of the stacked 2D sheets is, for example, 10 μm and the interplanar spacing 2 nm and the diffusing atoms are randomly

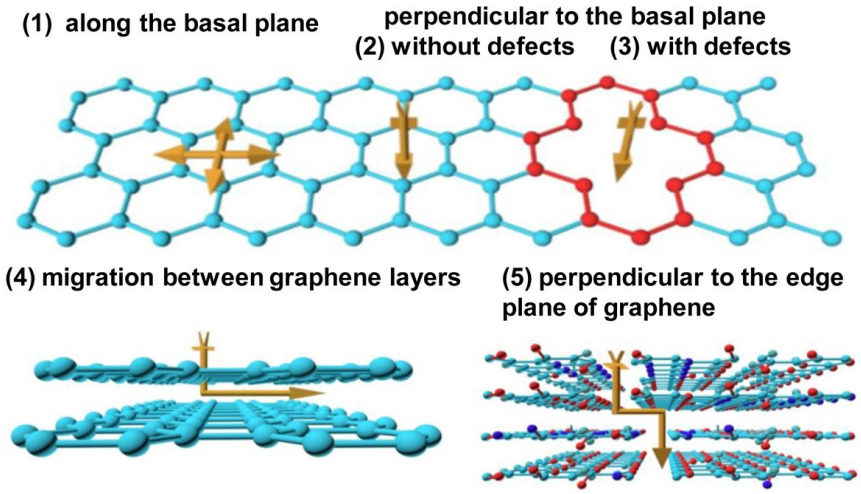

Figure 2.6.: Schematic illustration of different diffusion mechanisms in stacked 2D materials by the example of Cu diffusion in monolayer graphene. Here (1) shows the diffusion along the surface, (2) the perpendicular diffusion through a graphene sheet, (3) the diffusion through a graphene sheet with defects, (4) the permeation in bilayer graphene, (5) the diffusion around the graphene sheets. Used under terms of https://pubs.acs.org/page/policy/authorchoice_termsofuse.html, from [89].

distributed on the 2D sheets, they must travel on average 2.5 μm parallel to the sheets in order to diffuse 2 nm in the perpendicular direction.

As reported by Stark et al. (2019) [91], diffusion in stacked 2D vdW materials also depends on the interplanar spacing. Increased interplanar spacing leads to faster diffusion [91]. In MXenes, the interplanar spacing can be controlled via the surface terminations and amount of adsorbed H_2O as discussed in Chapter 2.1. Luo et al. (2017) [92], for example, show an increase in interplanar spacing for Ti_3C_2 MXenes of 177 % by intercalation of Sn^{4+}, which acts as pillars between the layers. As a result, a higher Li-ion diffusion is achieved [92].

Interlayer interactions and strain can also have an influence on the diffusion process [91]. For example, Oakes et al. (2016) [93] observed a strain dependence for Li insertion in C-MoS_2 vdW heterostructures.

2.4. Physics of the ultra high vacuum

The term vacuum comes from the Latin word *vacuus*, which means bare, free or empty. In general, a vacuum can be regarded as a reduced pressure relative to a defined ambient pressure [94]. In addition, there are also fixed pressure ranges that classify the vacuum universally, such as the rough vacuum (RV) from 1000 mbar to 1 mbar and the medium vacuum (MV) from 1 mbar to 1×10^{-3} mbar, as well as the high vacuum (HV) from 1×10^{-3} mbar to 1×10^{-7} mbar and the ultra high vacuum (UHV) from 1×10^{-7} mbar to 1×10^{-12} mbar [95].

In a vacuum chamber, the mean free path λ of the gas atoms, describing the average path between collisions, becomes larger than the dimension of the chamber below a certain pressure. This can be observed from Figure 2.7 for the different types of vacua described above. For the UHV this means that the probability of collisions between gas atoms is close to zero. Collisions with the walls of the chamber still take place. Here, even at pressures of 1×10^{-12} mbar, 4×10^{8} collisions/s with a 1 cm^2 large area are observed [94].

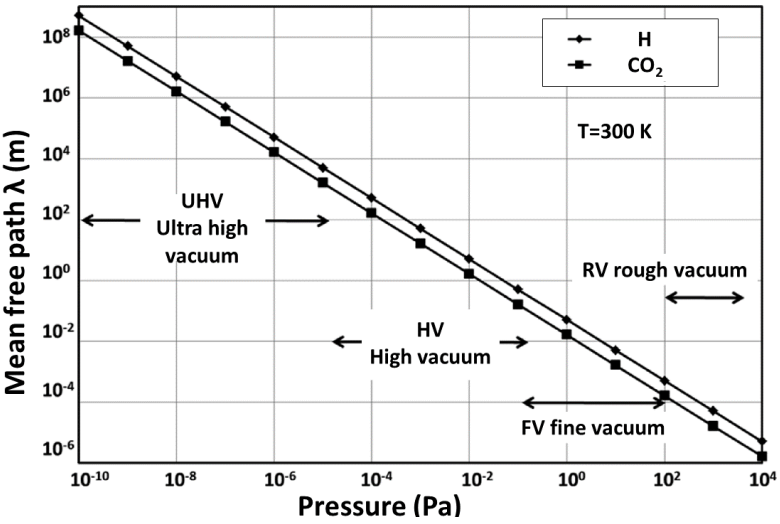

Figure 2.7.: Double logarithmic plot of the mean free path λ as a function of pressure. The mean free path in RV is in the micrometer range, while in UHV the mean free path amounts to several 10 000 km. Used and edited with permission of Springer Nature BV, from [96].

The UHV is characterized by its low residual gas quantity. This can be quantified by the monolayer formation time (MFT). The MFT indicates how long it takes for a monolayer of adsorbates to accumulate on the surface when no desorption takes place [95]. For air at a pressure of 1 mbar at RT, MFTs of around 3×10^{-6} s result, whereas these are around 36 s in HV and up to 100 h in UHV [95]. UHV chambers are therefore suitable for processes in which contamination and chemical reactions caused by residual gases must be kept at a minimum.

In regard of the present work, the small amount of residual gas in a UHV enables to monitor the removal of the surface terminations T_x of MXenes during thermal activation via mass spectrometry as outlined in Chapter 1. Furthermore, a diffusion of foreign atoms and H_2O into the MXene samples can be minimized. This ensures that the termination-free M atoms formed after thermal activation are available for the subsequnetly intercalated Fe. In this context, an oxidation of the latter can also be avoided under UHV conditions.

In the following, Chapter 2.4.1 provides an overview of the special requirements for UHV systems, while Chapter 2.4.2 discusses the steps to achieve a UHV.

2.4.1. Ultra high vacuum systems

Fundamentally, the minimum pressure achieved in a vacuum chamber is influenced by two opposing mechanisms. On the one hand, vacuum pumps lead to a reduction in pressure. On the other hand, leaks, diffusion, permeation and desorption of adsorbed and absorbed gas atoms from the walls lead to an increase in pressure [95]. As a result, an equilibrium pressure is established in

a UHV chamber after a finite time [95]. If this equilibrium pressure is sufficiently low, a UHV results. Methods for achieving such low equilibrium pressures are discussed in the following.
As the gas atoms adsorbed and absorbed by the inner walls of a vacuum chamber gradually desorb into the vacuum, the volume of a UHV chamber and thus the surfaces exposed to the vacuum are generally minimized. In this way, a lower equilibrium pressure can be achieved in a shorter period of time [94]. In addition, materials are selected for the chamber walls that contain only a small amount of gas and have low permeability for gas atoms. For example, He can permeate through glass while metals have a certain permeability for H_2 [94]. Porous solids such as plastics contain up to 1 % of their weight as gases, with H_2O molecules making up the largest proportion [94]. This leads to high desorption rates even after several month/years, which is why they are avoided in UHV [94]. Usually, UHV chambers are made of special steel or stainless steel alloys while copper sealing rings are used to join different components together [95].
When generating a UHV by initially pumping a system from ambient pressure, the flow ranges from viscous (movement of the gas atoms depending on the pressure gradient [95]) to molecular flow (statistical movement of the gas atoms, independent of the pressure gradient [94]) are passed. This is why a combination of different vacuum pumps is required. In general, it is important to ensure that the pumping cross section of the selected pumps is sufficient for the respective vacuum chamber [95]. In addition, the pumps should preferably be connected to the chamber directly or via short pipes with a large diameter in order to avoid high flow resistances [95].
In the range from 1000 mbar to about 1×10^{-3} mbar, pre-pumps are used. A distinction is made between different designs. An example are membrane pumps, which vary the volume in the pump chamber by deflecting a diaphragm and thus create a vacuum [95].
Below roughly 1×10^{-3} mbar, turbo molecular pumps (TMP) are used. This type of vacuum pump ensures efficient pumping of gases in the molecular flow range [95]. TMPs consist of 9 to 13 rotor blades arranged one behind the other with stationary stators in between. If the rotational speed of the rotor blades is of the same order of magnitude as the thermal speed of the gas atoms (1800 m/s for hydrogen and 450 m/s for oxygen) a momentum transfer accelerates them into the pump [94]. There, the stators decelerate the gas atoms again so that they can be captured by the 2nd rotor stage [94]. Once the gas atoms have reached the last stage, they must be removed by a backing pump.
Titanium sublimation pumps (TSP) are based on the principle of chemical bonding of gas atoms through chemical reactions with an Ti film evaporated on the pump walls. In this way, residual gases, with the exception of noble gases, can be effectively pumped starting from pressures of less than about 1×10^{-4} mbar [94].
The ion getter pump (IGP) ionizes the residual gas atoms and then accelerates them onto a Ti cathode. Upon impact, the gas atoms can be buried in the cathode and simultaneously sputter away Ti atoms that bind the residual gas atoms to the inner walls of the pump [94]. In contrast to TSPs, IGPs can also pump noble gases [94].
To determine the total pressure in a UHV chamber in the low pressure range from 1×10^{-3} mbar

to 1×10^{-12} mbar ionization pressure sensors are used. Their principle is based on the ionization of the residual gas atoms and measurement of the pressure dependent ion current [95]. A mass spectrometer also filters the ionized residual gas atoms according to their mass and can thus measure the partial pressure of an individual gas component [95]. Here the sum of the individual partial pressures amounts to the total pressure [97].

2.4.2. Generation of an ultra high vacuum

When a UHV system is pumped down from atmospheric pressure, the balance between adsorption and desorption of atoms on a surface is disturbed [96]. Here, mainly desorption of adsorbed and absorbed atoms occours, which is referred to as degassing [94]. This continuous degassing prevents a UHV from being reached.
In particular, water molecules are adsorbed by any surface exposed to atmospheric air, forming a thin liquid film of up to a few monolayers [94]. In addition, porous materials as well as oxidation layers of metals can absorb water molecules. This is also reflected in the fact that after the initial pump-down of a vacuum chamber, the residual gas composition consists of 90–95 % water vapor [94]. The activation energies for the desorption of water molecules from a stainless steel surface are between 0.9 eV and 1.1 eV and thus significantly higher than the typical desorption energies for physisorbed atoms (a few 100 meV) [95]. This leads to long residence times of H_2O on the inner chamber walls of several weeks [94].
In addition to the pure desorption of adsorbed atoms, the diffusion and subsequent desorption of absorbed gas atoms from the chamber walls, re-adsorption and surface diffusion of gas particles play a decisive role in the degassing process [95]. This results in the degassing time t

$$\frac{t}{t_a} = ln\left(\frac{8}{\pi^2 f}\right), \tag{2.18}$$

where t_a is the degassing time constant and f is the degree of degassing [95]. For absorbed H atoms in a 2 mm thick stainless steel sheet, for example, one observes degassing times of 170 a at a temperature of 295 K [95]. As it is not practical to wait several years for the chamber to reach a UHV, the degassing process must be accelerated.
This is achieved by heating the vacuum chamber to temperatures of around 425 K for several days, also known as bake-out. At the elevated temperatures, the residence time of adsorbed atoms, including water, is significantly reduced. In addition, the diffusion of absorbed atoms to the surface is accelerated according to Equation 2.16. In the case of the 2 mm thick stainless steel sheet addressed before, the degassing time of the absorbed H atoms is reduced to 6 d at 500 K [95]. Consequently, the time to reach a UHV can be cut to a few days with this approach.

3. Ultra high vacuum chamber for *in situ* MXene investigations

$Ti_3C_2T_x$ MXenes are treated in ultra high vacuum (UHV) to guarantee clean conditions. This includes a thermal activation to remove the surface terminations T_x and the intercalation of Fe. For both processes UHV conditions are required. In the case of thermal activation, UHV conditions prevent diffusion of residual gas atoms and H_2O into the sample and allow monitoring by mass spectrometry. Additionally, in the case of Fe deposition and intercalation, the UHV prevents an oxidation of the latter (cf. Chapter 7).
In order to generate the UHV conditions needed, a decommissioned vacuum chamber is put back into operation and modified so that it meets the above-mentioned requirements for the treatment of MXenes. In the following, the modification of the UHV chamber is described in Chapter 3.1 as well as the installed functionalities and measurement techniques in Chapter 3.2 and 3.3.

3.1. UHV chamber and load lock

Figure 3.1 a) shows the UHV chamber made of stainless steel in its decommissioned state and in b) after the modifications described in the following.
A load lock is installed to the UHV chamber to enable sample transfer. The load lock can be pumped from ambient pressure to 1×10^{-6} mbar within 30 min. A bakeout is not necessary. After about 1 h, a pressure of 1×10^{-7} mbar is reached and the valve to the UHV chamber can be opened. This is followed by a brief increase in the base pressure of the UHV chamber from 5×10^{-11} mbar to around 1×10^{-8} mbar. About 20 min after the sample transfer, the pressure in the UHV chamber drops back to 5×10^{-11} mbar. Using a transfer stick, the sample in question, which is attached to a sample plate (see Figure 3.2), can be transferred to the UHV chamber or from the UHV chamber to the load lock. In the load lock, up to 5 sample plates can be placed in a sample storage also shown in Figure 3.2.
A combination of a membrane pump and turbo molecular pump (TMP) (*Pfeiffer* HiCube-Eco) is used to pump the load lock and also serves as a pre-pump for the TMP (*Varian* TV301 Navigator) of the UHV chamber which requires an inlet pressure of at least 1×10^{-1} mbar. In addition the UHV chamber is pumped by a titanium sublimation pump (TSP) and ion getter pump (IGP). A cold cathode sensor (*Pfeiffer* IKR 070) is used to read the pressures in the UHV chamber below 1×10^{-3} mbar. The lower measuring limit of this sensor is 1×10^{-11} mbar for air (N_2) [98]. In addition, a Pirani sensor (*Pfeiffer* TPR 010) is installed to measure up to ambient

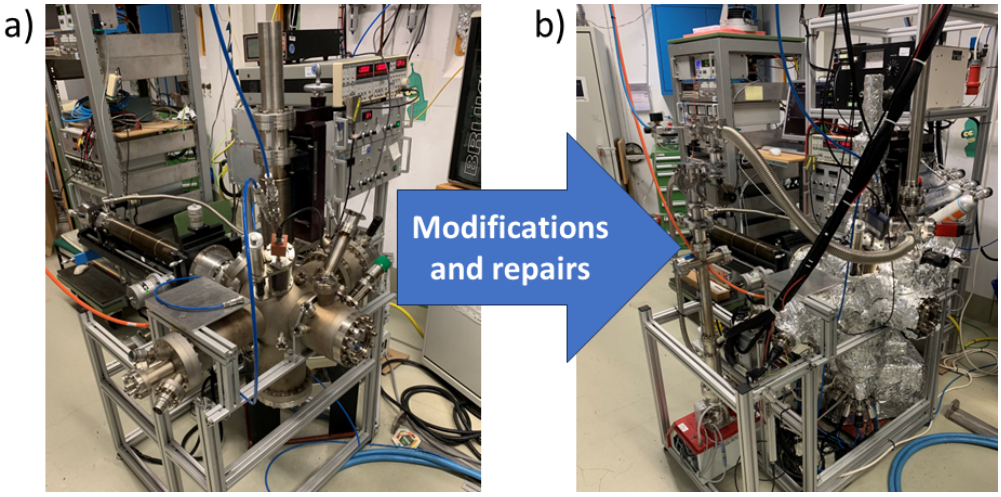

Figure 3.1.: a) Decommissioned UHV chamber prior to the modifications and repairs. Here the stainless steel body with various flanges and the manipulator in the background of the picture can be seen. b) UHV chamber after the modifications. The chamber is wrapped in aluminum foil for a more homogeneous heating of the chamber during bake-out. The two racks at the background of the pictures contain the electronics for supplying the various components of the chamber.

pressure when the chamber is vented. For the load lock, a full-range transmitter (*Pfeiffer* PKR 361) is selected, which consists of a Pirani and cold cathode sensor and can cover a pressure range from 1000 mbar to 1×10^{-9} mbar [99].

To achieve UHV conditions in the UHV chamber, a bake-out is performed. A homegeneous heating of the chamber is ensured by wrapping it with heating tapes and aluminum foil as can be seen in Figure 3.1 b). The bake-out temperature is 425 K with the excheption of the sample manipulator which is only baked at 375 K. A separate heater is also integrated into the pump body of the TSP and IGP. Bake-outs are performed for a period of 2-3 day. After cooling the chamber to room temperature (RT), a decrease in pressure of around 1.5 orders of magnitude is achieved. The minimum base pressure of the UHV chamber is 5×10^{-11} mbar.

In order to move a sample inside the UHV chamber, it consists of an x-, y-, z- and θ-manipulator, which can also be used as a liquid He flow cryostat. At its end, a custom-made electron beam (e-beam) sample heater is installed, which is capable of generating the temperature of 1000 K that can be maximally applied to MXenes before their decomposition (see Chapter 2.1.3). Further details on the sample heater are given in Chapter 3.2.1.

Three holes are milled into the DN 160 bottom flange of the UHV chamber, as shown in Figure 3.2, into which DN 40 flanges with attached pipe sections are welded. This allows up to 3 evaporators to be mounted later on. Even if 3 evaporators are not required for this work, this opens up further possibilities for future applications of the UHV chamber. The welded-in flanges all point towards the center of the chamber, as indicated in Figure 3.2. Details on the evaporators used in this work, their control and performance can be found in Chapter 3.2.2.

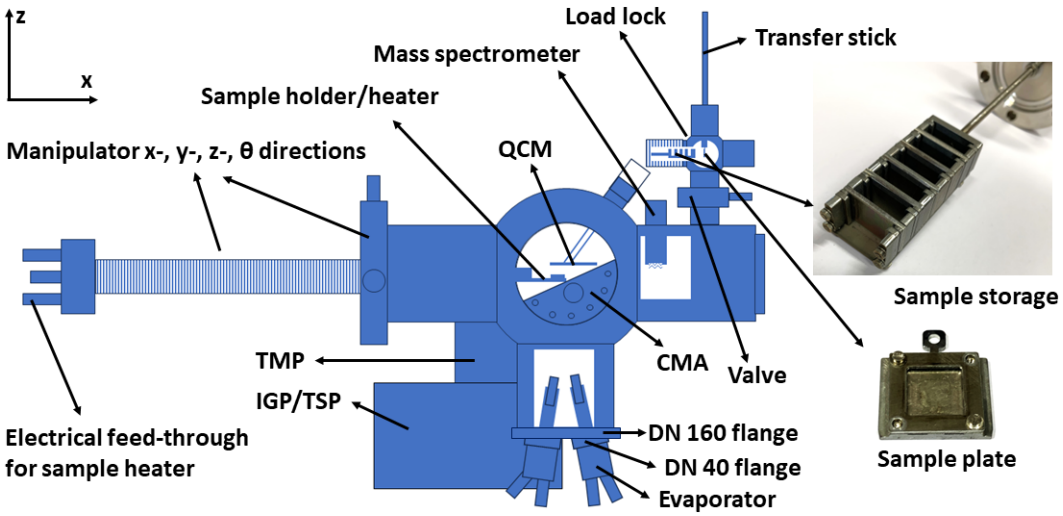

Figure 3.2.: Sketch of a side view of the UHV chamber after the modifications. Starting from the left, the manipulator is shown with the sample heater attached to its end. The TSP, IGP and TMP are indicated in the background. Shown in the bottom is the DN 160 base flange of the chamber with welded-in DN 40 flanges to mount evaporators. The inclination of the DN 40 flanges ensures that the inserted evaporators point towards the center of the chamber. The QCM can be moved into the center of the chamber from above. From the perspective shown, the CMA is mounted to the chamber in the direction of view. The mass spectrometer and the load lock are located in the right-hand part of the chamber. Using the sample transfer stick, a sample fixed on a sample plate can be removed from the sample storage in the load lock and transferred to the sample heater in the UHV chamber. The sample plates can carry substrates with a size of up to 10 mm×10 mm×1 mm.

To measure the thickness of the materials deposited with the evaporators, the UHV chamber is equipped with a quartz crystal monitor (QCM). A water cooling system reduces drifts of the measured thickness due to heat radiation from the evaporators. Also, a new thin film monitor (STM-2 from *INFICON*) with a computer interface is installed to digitally display, record and store the measured film thickness and deposition rate.
As shown in Figure 3.2, the UHV chamber is also equipped with a mass spectrometer (VGQ from *Thermo Onix*) to monitor the thermal activation of MXenes and a cylindrical mirror analyzer (CMA) (DESA 100 from *Staib Instruments*) for *in situ* AES measurements of their composition. Operational details, calibration and sensitivity of the mass spectrometer and the CMA are discussed in Chapter 3.3.1 and 3.3.2.

3.2. Functionalities

In order to achieve ferromagnetic properties by treating the MXenes in UHV as described in Chapter 1, the UHV chamber is equipped with a sample heater and an Fe evaporator. The sample heater is utilized to thermally activate the MXenes, as well as to provide the thermal

energy necessary to intercalate the Fe film deposited on the sample surface by the Fe evaporator. In addition, an evaporator for carbon is required to cover the samples with a few nanometers of C to block diffusion of H_2O into the MXenes and prevent oxidation of Fe during *ex situ* analysis. In the following, Chapter 3.2.1 presents the selected sample heater and its functionality as well as its implementation in the UHV chamber. Chapter 3.2.2 presents the evaporators used, their control and calibration.

3.2.1. Sample holder/heater

In coordination with the sample transfer stick and the sample storage in the load lock, the sample heater is selected to be compatible with the sample plates shown in Figure 3.2.
The sample plates used in this work are custom-made from molybdenum and were designed in collaboration with the *VAb Components GmbH*. Here, the sample carriers are configured in such a way that they can carry substrates with a maximum size of 10 mm×10 mm and thicknesses of up to 1 mm. The substrates are placed in a recess in the center of the sample plates and fixed with a molybdenum mask. The mask is attached with tantalum screws, which presses the substrate down at the edges on a 0.5 mm wide strip. This ensures that the contact surface of the substrate on the sample carrier is maximized, resulting in more uniform heating of the samples. Molybdenum and tantalum are chosen here as materials due to their high melting points. In addition, they are UHV compatible due to low degassing rates.
For the thermal activation of the $Ti_3C_2T_x$ MXenes, temperatures of up to 1000 K are required as discussed in Chapter 2.1.3. An e-beam heater is best suited to reach these temperatures and, if necessary, maintain them for several hours. To mount the selected e-beam sample heater to the end of the sample manipulator as shown in Figure 3.3 a) on the right, a special adapter is needed which was also designed in cooperation with the *VAb Components GmbH*. As the sample manipulator can also be used as a liquid He flow cryostat, it has to be taken into account that the adapter must ensure an optimal thermal coupling of the sample holder to the cryostat. Therefore, the sample holder and the adapter are made of gold-plated copper, which ensures good thermal coupling. As a result, the samples can be cooled down to 10 K-20 K (manufacturer's specification, not verified). Although *in situ* cooling is not used in the present study, it may be advantageous for the future use of the UHV chamber.
In addtion to the gold-plated copper body the sample heater consists of a slot for the sample plates machined into a molybdenum block at the front end, as shown in Figure 3.3 a) on the right. To thermally isolate the molybdenum block and the sample plate from the copper body at high temperatures, a sapphire disk is positioned between them. Located under the slot for the sample plates is a filament to which a maximum heating current of 5 A and a negative high voltage of 2 keV are applied. The negative high voltage accelerates the electrons emitted by the filament towards the grounded sample plate, which heats the latter and the sample attached to it. This is visualized in Figure 3.3 a) in the left-hand image for a temperature of 1300 K. To supply the filament with the heating current and the negative high voltage, a high-voltage

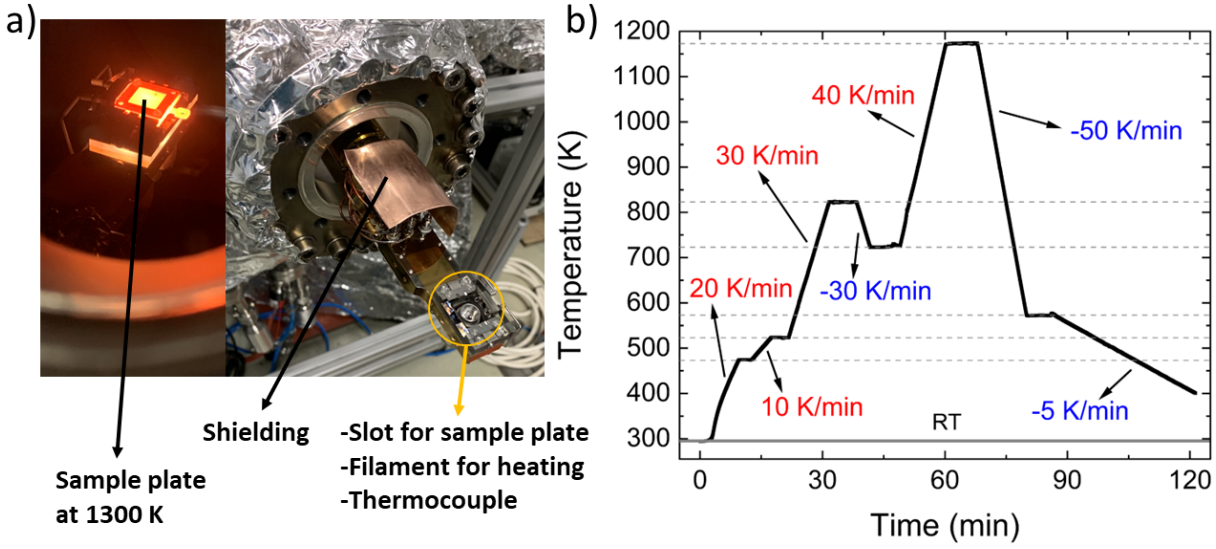

Figure 3.3.: In a), the right-hand photo shows the sample heater attached to the end of the sample manipulator. The molybdenum block with the slot for the sample plates can be seen at the front end of the gold-plated copper body of the sample heater (circled in yellow). The filament is framed in the center of the molybdenum block. The K-type thermocouple for measuring the sample temperature is located at the rear end of the insertion slot for the sample plates. In order to thermally decouple the molybdenum block and the sample plate from the copper body, a sapphire disk is inserted between them. A shield is installed to protect the high-voltage contacts of the sample heater from short circuits caused by Fe deposition on the MXene samples. The picture on the left shows the sample heater with inserted sample plate in operation at a sample temperature of 1300 K. b) Sample temperature as a function of time for heating/cooling rates from 5 K/min to 50 K/min set in the PID control program of the sample heater up to 1175 K. Here, the set temperature can be approximated by the PID control with an accuracy of 1 K to 2 K.

UHV feedthrough is installed on the manipulator as sketched in Figure 3.2. On the vacuum side, Kapton insulated cables are wired to the connectors of the sample heater. Since vapor deposition of electrically conductive materials such as Fe on the samples can lead to short circuits between the high-voltage connections of the sample heater, a shield is mounted, as shown in Figure 3.3 a).

To measure the sample temperature, the sample heater is equipped with a K-type thermocouple which presses against the string side of the sample plate. Since the heating of the sample plate is highest in the center of the plate due to the impinging electrons, the measured temperatures may deviate slightly downwards from the actual temperature at the substrate surface. The deviation here is estimated to be a maximum of 5 K. Despite the sapphire disk, the gold-plated copper body of the sample heater warms up during longer heating times. However, according to the manufacturer, it should not exceed a temperature of 475 K, as the gold coating would diffuse into the copper and the thermal coupling to the liquid He crystat would no longer be guaranteed.

A second K-type thermocouple is therefore installed to monitor the temperature of the body of the sample heater. In addition, the liquid He cryostat is purged with nitrogen gas at room temperature (RT), which ensures additional cooling of the cryostat an prevents overheating.
The sample heater is controlled by a PID control sotware (self-written with *Delphi*). The program reads the actual temperature of the sample via an analog-digital converter, compares it with the target temperature and regulates the heating current of the filament and thus the emission of electrons at the constant negative high voltage of 2 kV. The program also makes it possible to heat or cool to a set temperature with heating/cooling rates between 5 K/min to 50 K/min. The sample temperature read out with the measuring software as a function of time can be viewed for different heating/cooling rates in Figure 3.3 b). This shows that the actual sample temperature can be kept within a range of 1 K to 2 K of the set temperature by the PID control for a wide range of heating/cooling rates.

3.2.2. Electron beam evaporators for Fe and C deposition

Iron is deposited as a thin film of typically 6 nm (see Chapter 6.1) on the MXenes in the UHV chamber with an electron beam (e-beam) evaporator. The Fe film is then intercalated by annealing the samples with the sample heater. Before removing the samples from the UHV chamber for *ex situ* analysis, a thin C film is deposited by e-beam evaporation to block diffusion of H_2O into the MXenes and prevent oxidation of the deposited/intercalated Fe. As can be seen in the following chapters, a 6 to 8 nm thick C film provides an effective protection against oxidation and does not react with either the Fe or the Ti_3C_2 MXenes. Moreover, for magnetic measurements, the diamagnetic signal of the C film can simply be subtracted as a linear background from a potential ferromagnetic signal of the MXenes with intercalated Fe.
E-beam evaporators, which belong to the thermal evaporators, have the advantage over other physical vapor deposition (PVD) techniques, such as sputtering, that no increased pressures are caused by process gases required for the deposition process, thus preserving the UHV. In addition, the kinetic energy of the evaporated atoms is lower, which leads to more homogeneous films at lower roughness (cf. Figure A.1 in the Appendix).
The melting temperature of Fe is 1520 °C while C sublimates at >3600 °C [100]. To achieve a vapor pressure of 1×10^{-10} mbar for Fe and C, temperatures of 1000 K and 1758 K are required respectively [101]. Consequently, the vapor pressures necessary for the deposition of the two elements are reached below their melting points. This allows Fe and C to be evaporated directly from Fe and C rods. E-beam evaporators are best suited for this, as they only heat the tip of the respective rod with the electron beam, which is more energy-efficient than heating the entire amount of material in the evaporator as in the case of an effusion cell.
Fe is evaporated from a 4-pocket e-beam evaporator. With this evaporator, four individual elements can be evaporated simultaneously if required, whereby the evaporation rates for each material can be controlled separately. This is achieved by a power supply unit that applies a positive high voltage of 2 kV to the evaporation materials and at the same time enables individ-

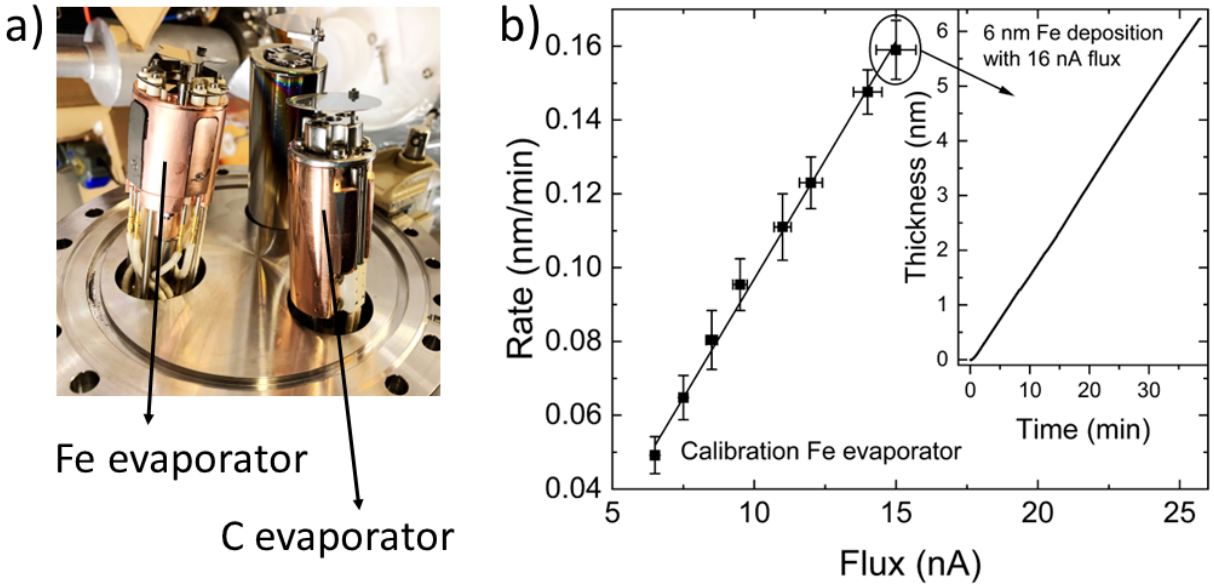

Figure 3.4.: a) Electron beam evaporators for Fe and C mounted to the DN 40 flanges welded into the DN 160 bottom flange of the UHV chamber as also schematically sketched in Figure 3.2. Here the heads of the evaporators can be seen, that will be located inside the vacuum chamber and into which the materials for evaporation are inserted. The third evaporator in the background is an effusion cell, which is not needed for this work, but can be used later together with the electron beam evaporators for the growth of MAX-phase thin films in the UHV. b) Fe deposition rates achieved with the Fe evaporator and measured with the QCM as a function of the set flux. The flux is regulated to a set value by adjusting the emission current using a PID controller in the evaporator control software. As the flux is correlated to the number of evaporated atoms, the deposition rate increases linearly with the flux. The inset shows the deposition of 6 nm Fe at a flux rate of 16 nA. Here, a linear increase in the deposited Fe thickness can be seen. It follows that the deposition rate of Fe can be kept stable at a constant value over the entire evaporation process by PID control of the flux rate.

ual control of the heating current of the filament and thus the emission current for each pocket. In this study, high-purity Fe rods (99.99 %) with a diameter of 2 mm and a length of 21 mm are installed in all 4 pockets. This allows the intervals for replacing used up Fe rods to be extended. A rod is used up when the shortest distance between the rod and the filament of the respective evaporator pocket is greater than 7 mm. In this case, the emission current at the maximum possible heating current of the filament of 5.5 A is no longer sufficient to heat the Fe rods to such an extent that the desired evaporation rate is achieved. To control of the individual evaporator pockets the flux rate is considered. The flux rate reflects the ionization of evaporated atoms by collision with the electrons that form the emission current. It is therefore directly correlated with the quantity of evaporated atoms. A PID controller integrated into the control software of the power supply unit compares the actual value of the flux rate with the entered setpoint value and adjusts the emission current and thus the Fe evaporation rate accordingly.

C is evaporated from a 4 mm thick graphite rod using a single pocket e-beam evaporator. Here, a constant positive high voltage of 2 kV is applied to the C rod while the emission current (about 130 mA) is controlled by reading the flux rate. An advantage of this e-beam evaporator is that the C rod can be moved, allowing the distance to the filament to be readjusted. In this way, the C rod does not need to be replaced during this thesis. The evaporator is operated via an analog power supply unit with an analog flux controller. To achieve digital control, the flux controller is modified and operated via a digital-to-analog converter using a software program (self-written with *Delphi*). The program features a PID controller that records the actual value of the flux and adjusts the emission current according to the set flux value.
The two evaporators are mounted to the modified flange (see Chapter 3.1) at the bottom of the UHV chamber. The flange removed from the UHV chamber with the installed evaporators is shown in Figure 3.4 a). A water cooling system is installed for both evaporators to protect the parts around the evaporator pockets from overheating.
For evaporation, the sample heater is moved to the center of the UHV chamber with the manipulator, whilst facing the side with the inserted sample plate towards the evaporators. The quartz crystal monitor (QCM) can also be moved into this position so that it is at the same height directly next to the sample heater, as sketched in Figure 3.2. In order to determine the thickness of the deposited films and to determine which flux rates are associated to which deposition rates of a material, the QCM is calibrated. Here, 3 parameters have to be taken into account. These are the density of the deposited material, the ratio of the acoustic impedance of the deposited material to the acoustic impedance of the oscillating quartz, also known as the Z-ratio, and the tooling factor T [102]. The density D and Z-ratio Z are known for most elements. However, the tooling factor depends on the geometry of the sample to the QCM and the positioning of the evaporators and must first be calibrated for the respective system. The tooling factor T is defined as

$$T = \frac{d_{actual}}{d_{QCM}} \times 100, \tag{3.1}$$

where d_{actual} describes the actual deposited film thickness and d_{QCM} the film thickness measured with the QCM [102]. To calibrate the tooling factor, 9.2 nm Fe is deposited on a $Si(100)/SiO_2$ substrate according to the QCM. The actual deposited layer thickness, which results in 15.7 ± 0.9 nm (see Figure A.1 in the Appendix), is then determined using *ex situ* ellipsometry. Inserting both values into Equation 3.1 results in a tooling factor of 170.6 ± 17.1.
After calibration, the QCM can be used to determine the deposition rates of Fe and C for different flux rates, as shown in Figure 3.4 b) for Fe and in Figure A.2 in the Appendix for C. Here, a linear correlation between the flux rate and the deposition rate can be seen. The inset in Figure 3.4 b) shows a deposition of 6 nm Fe at a target flux rate of 16 nA set in the control software of the evaporator. The linear increase in the layer thickness of the deposited Fe film measured with the QCM shows that the PID control of the control software ensures stable deposition with a constant deposition rate.

3.3. *In situ* characterization techniques

For *in situ* analysis of the chemical composition of the MXenes before and after the thermal activation as well as for the monitoring of the Fe intercalation, Auger electron spectroscopy (AES) is used. In addition, the chamber is equipped with a mass spectrometer to observe the thermal activation. This will allow to identify at which temperature the respective surface terminations T_x are removed from the MXene samples (see Chapter 5.1).
In the following Chapter 3.3.1 and 3.3.2, the principle of function, tuning and achieved performance of the mass spectrometer and AES installed in the UHV chamber are outlined. Other *ex situ* measuring techniques used in this thesis are explained in the text where needed.

3.3.1. Mass spectrometry

A mass spectrometer makes it possible to measure the partial pressures of individual gas components of a gas mixture. In addition, the total pressure can be determined from the sum of the partial pressures. Since different gas components exhibit gas atoms with different atomic masses, the ratio of mass to charge m/e can be used to separate individual gas components from a gas mixture and thus measure their partial pressure [95].
For this purpose, the utilized mass spectrometer (VGQ from *Thermo Onix*) consists of 3 essential components which are located inside the UHV chamber and are connected via a UHV feedthrough to a corresponding power supply unit. The system is operated using a software supplied by the manufacturer.
The first component is an ionizer consisting of a filament that serves as a cathode and a metal cage with an applied positive high voltage that acts as an anode. The electrons emerging from the filament are accelerated towards the cage and collide with the residual gas atoms present in the UHV chamber, ionizing them. The ionized gas atoms are then accelerated through an electrostatic focusing optic into a quadrupole mass filter. The quadrupole mass filter consists of 4 stainless steel rods arranged parallel to each other in a square cross-section. Diagonally opposite rods are electrically connected to each other. A combination of radio frequency voltage (RF) and DC voltage is applied to these electrically paired rods, whereby the signs and phases for the rod pairs are reversed [103]. As a result, the ionized gas atoms entering the mass filter are directed onto spiral trajectories. The radius described by the ions depends on the ratio of RF to DC amplitude and the ratio of m/e. For a constant RF and DC amplitude, only ions with a certain mass ratio m/e pass through the filter while all other ions collide with the stainless steel rods. If the ratio of the RF and DC amplitudes is kept constant while the amplitudes are increased or decreased, the passage range of the mass filter can be varied and thus a selected range of m/e ratios scanned [95]. The resolution of the quadrupole mass filter is defined by the ability to differentiate between different m/e values while it is set by the ratio of RF to DC amplitude [95]. As this ratio is kept constant, the resolution is also constant over the entire scanning range and therefore for all recorded mass spectra. The resolution achieved by the mass spectrometer used

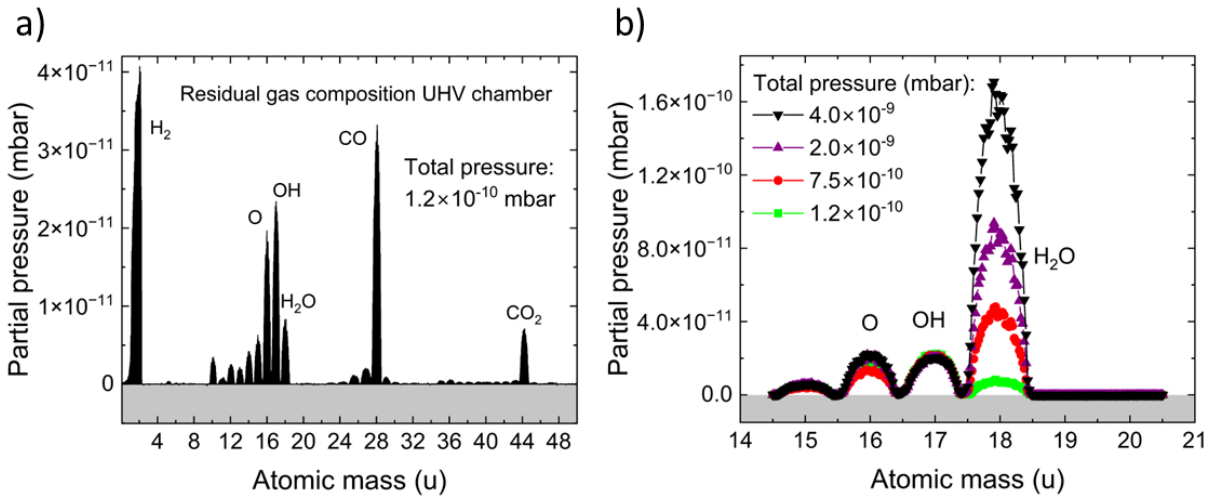

Figure 3.5.: a) Mass spectrum showing the residual gas composition in the UHV chamber after calibration of the mass spectrometer. The atomic mass in u is shown on the x-axis and the partial pressure in mbar on the y-axis. The peaks indicate that the residual gas spectrum of the UHV chamber is composed of the typical components found after bake-out: H_2, OH/H_2O, CO and CO_2. The spectrum was measured at a total pressure in the UHV chamber of 1.2×10^{-10} mbar. b) Mass scan from 14.5 u to 20.5 u. The total pressure in the UHV chamber is increased by letting in atmospheric air via a fine dosing valve. The humidity of the air leads to an increase in the partial pressure of H_2O. If the resolution of the mass spectrometer is insufficient, the increase in the partial pressure of H_2O would also lead to an increase in the partial pressures of the neighboring gas components in the mass spectrum OH (17 u) and F (19 u). Since this is not the case, a resolution better than 1 u can be concluded.

in this study is better than 1 u, as described below. Finally, the filtered ion current is converted into a measurable signal using an electron multiplier, which serves as a detector [103].

In order to determine the partial pressure of the relevant gas components from the detected ion current, the mass spectrometer needs calibration. For this, the resolution of the mass filter is reduced until all ionized gas atoms with any m/e ratio reach the detector. The detected ion current is therefore equal to the sum of all partial pressures, which corresponds to the total pressure in the UHV chamber. This pressure is known from the cold cathode pressure sensor and can be entered into the control software of the mass spectrometer. Based on this, the control software can subsequently determine the partial pressure of any gas component.

In addition to the pressure calibration, the position of the masses is corrected and the resolution is optimized. The correction of the masses ensures that when the gas component with mass X is measured, it also appears at the corresponding position in the mass spectrum. For this purpose, gases such as He (4 u), Ar (40 u), H_2 (2 u) and O_2 (32 u) are introduced into the UHV using a fine dosing valve. Since the atomic mass units for these gases are known, the masses can be corrected using the control software of the mass spectrometer. Finally, the resolution is optimized according to the manufacturer's guidelines by adjusting the ratio of RF to DC amplitude. The

successful calibration can be seen from the mass spectrum of the residual gas composition of the UHV chamber shown in Figure 3.5 a). The mass spectrum shows the typical residual gas composition of a UHV chamber after bake-out with the gas components H_2, OH/H_2O, CO and CO_2 [104].
As discussed in Chapter 2.1.3, the expected surface terminations to be removed during thermal activation of the investigated $Ti_3C_2T_x$ MXenes are given by T_x : −F, −Cl,and −OH. In addition to desorption of the surface terminations, desorption of the H_2O adsorbed by the MXenes is also expected. Looking at the atomic masses of these elements, it can be seen that O (16 u), OH (17 u), H_2O (18 u) and F (19 u) lie directly next to each other in the mass spectrum. The resolution of the mass spectrometer is therefore crucial, as an increase in one gas component would lead to an increase in the neighboring components when the resolution is insufficient. To test the resolution after calibration, atmospheric air is let into the chamber via the fine dosing valve and the mass range from 14.5 u to 20.5 u is scanned as shown in Figure 3.5 b). Due to the humidity of ambient air, there is an increase in H_2O the further the fine dosing valve is opened, indicated by the increase in the total pressure in the UHV chamber. The partial pressures of OH and F, on the other hand, remain constant. This implies a sufficiently high resolution, which is estimated to be around 0.1 u, as also specified by the manufacturer.

3.3.2. Auger electron spectroscopy

The Auger electron spectroscopy (AES) can be used in particular to determine the near-surface composition of a material under investigation. In addition, Auger spectra contain information about the chemical state and binding energies of the atoms of a sample [105]. However, obtaining this information from the spectra requires a higher effort, as compared to the more demanding X-ray photoelectron spectroscopy (XPS).
The underlying effect of the AES, the Auger effect, was discovered by Pierre Auger in 1925 [105]. Here, an electron close to the nucleus of an atom, for example in the K shell, is released by collision with a high-energy electron (3-5 keV) [106]. The resulting free space is then filled by an electron of a higher energy level, for example the L_1 shell. The energy released during this relaxation is transferred to another electron, for example from the $L_{2,3}$ shell, which then leaves the atom with the energy $E_A = E_K - E_{L_1} - E_{L_{2,3}}$ [106]. In this case, the electron leaving the atom is called KLL Auger electron. In addition to the emission of an Auger electron, X-ray quanta can be emitted, although this is less efficient, especially for light elements [105]. In the case of C the yield of KLL Auger electrons vs. X-ray quanta is around 99 % vs. 1 % [107]. For Ti the yield of KLL Auger electrons is about 70 %, while for the LMM transition it is also about 99 % [107].
The energies of the Auger electrons are characteristic for the respective element, which allows the near-surface composition of a sample to be determined [106]. In the spectrum of backscattered electrons, the Auger electrons add on top and lie in the range between 30 eV and 2000 eV [108]. In order to carry out AES measurements, the cylindrical mirror analyzer (CMA) installed in the

UHV chamber is used. The CMA consists of an inner cylinder and a surrounding outer cylinder between which an electric field is generated by applying a voltage [109]. The CMA also features an electron gun that can generate a focused electron beam with electron energies of 0-5 keV. Thereby, the CMA is electrically driven by a high-voltage power supply.
When the electron beam hits a sample, Auger and secondary electrons are generated. In addition, there is inelastic and elastic backscattering of the primary electrons [105]. Some of the Auger, secondary and backscattered electrons can subsequently enter the area between the outer and inner cylinder of the CMA, where they describe an energy-dependent trajectory caused by the electric field. As a result, depending on the applied voltage, only electrons with a certain energy can enter the detector of the CMA. The detector in this case is an electron multiplier [109]. By varying the field between the cylinders, any range of electron energies can be scanned, resulting in an Auger spectrum which shows the intensity (proportional to the number of electrons detected) as a function of the electron energy.
Due to the secondary and backscattered electrons, the spectrum recorded by the CMA contains a large background on which the intensities of the Auger peaks are small [106]. Given that the maximum slope of the background is significantly smaller than that of an Auger peak, the first derivative of the intensity with respect to the energy is used instead, i.e. obtained by the use of a lock-in amplifier. This allows the background in the differentiated spectrum to be minimized and the Auger signal to be maximized [106]. In addition, the electron yield of the utilized electron multiplier decreases nonlinearly below about 200 eV in order to further suppress the high secondary electron signal at low energies [108, 109]. For this reason, all Auger spectra recorded in this work show a nonlinear decrease in the signal at energies lower than 200 eV. As this background is instrumentally caused, it is subtracted for all spectra.
In the differentiated spectrum, an Auger peak exhibits a maximum and a minimum, which results from the maximum positive/negative slopes of an Auger peak in the non-differentiated spectrum. Since the maximum slopes of an Auger peak in the non-differentiated spectrum are correlated with its intensity, in the differentiated spectrum the difference between maximum and minimum is determined, which is also referred to as the peak-to-peak amplitude. The peak of the elastically backscattered primary electrons in differentiated form, which was measured for the calibration of the CMA at a primary electron beam energy of 1 keV, is depicted in Figure 3.6 a) as an illustration.
In this work, only Auger spectra in differentiated form are recorded. For this purpose, the voltage between the inner and outer cylinder of the CMA is modulated. From the modulation and measurement signal, a lock-in amplifier can calculate the differentiated signal which is ultimately transmitted to a computer with a *LabView* measurement software. This software is also used to enter the energy range to be scanned and the scan rate for an Auger spectrum to be recorded.
To achieve an optimal adjustment of the CMA installed in the UHV chamber, the elastic peak of the backscattered electrons is measured and the peak-to-peak amplitude maximized. A primary electron energy of 1 keV is used for this purpose. Besides the setting parameters of the lock-in

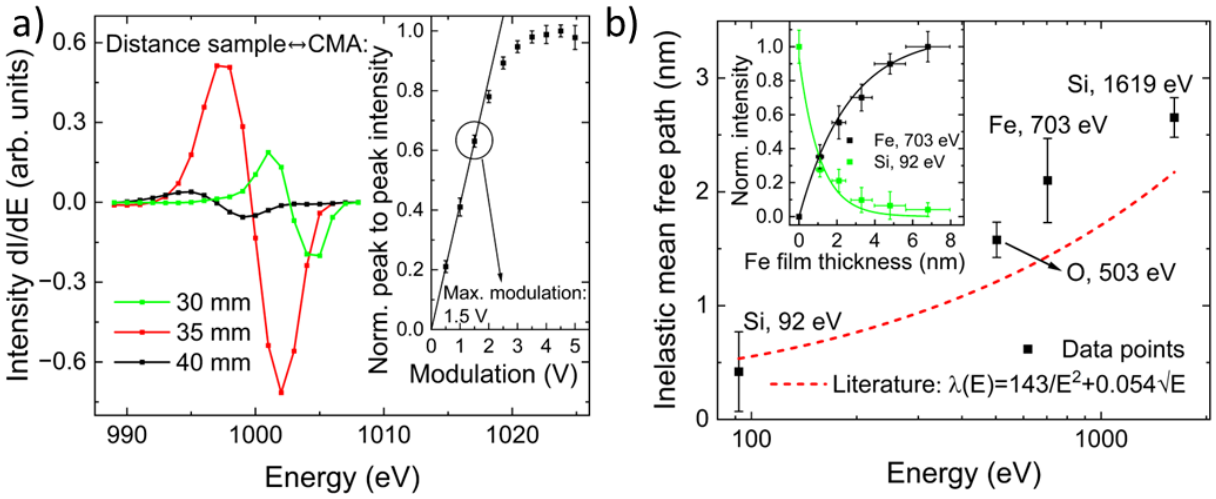

Figure 3.6.: a) Peak of the elastically backscattered primary electrons (1 keV) in differentiated form. A maximum peak-to-peak amplitude can be achieved at a distance of 35 mm from the sample to the CMA input optic, as shown in red. At larger distances (black curve) or smaller distances (green curve), the peak-to-peak amplitude decreases and the peaks shift to lower or higher energies. The inset shows the dependence of the normalized peak-to-peak intensity on the modulation amplitude of the lock-in amplifier. Above a modulation of 1.5 V, a non-linear behavior is observed due to overmodulation leading in an instrumental broadening of the peaks. b) IMFP of Auger electrons as a function of their energy for $Si_{1,2}$ (92 eV, 1619 eV), O (503 eV) and Fe (703 eV). The red dashed line shows the energy dependance of the IMPF of electrons in pure (solid) elements according to the work of Seah et al. (1979) [110]. The IMFP is a measure of the information depth of the AES for the respective electron energy. The IMFP is determined in the UHV chamber by AES measurements on a $Si(100)/SiO_2$ substrate onto which Fe is deposited. By fitting the measured peak-to-peak intensities of the Auger peaks of the substrate and the deposited Fe film as a function of the deposited Fe film thickness, the IMFP can be obtained. As an example, the inset shows the fits to the peak-to-peak intensities of the 92 eV Si peak and the 703 eV Fe peak as a function of the Fe thickness.

and the analyzer, the emission characteristics of the electron gun and the position of the sample relative to the CMA are optimized in this process. Here, the distance between the sample and the inlet opening to the CMA is particularly decisive, as can be seen in Figure 3.6 a). A maximum signal can be achieved at a distance of 35 mm, while a significant reduction in the peak-to-peak amplitude and a shift in the peak position to higher or lower energies is observed at smaller or larger distances (green or black curve in Figure 3.6 a)).

A further increase in the sensitivity of the CMA can be achieved by increasing the modulation amplitude and the primary beam current generated by the electron gun. However, it should be noted that the peak-to-peak amplitude no longer increases linearly with the modulation amplitude in the case of overmodulation, but rather an instrumental broadening of the peaks takes place [108]. The measured peak-to-peak amplitude of the elastic peak as a function of

the modulation amplitude is shown in the inset in Figure 3.6 a). Overmodulation occurs above 1.5 V, which is why this value is used for sample characterization. Considering the peak-to-peak amplitude of the elastic peak as a function of the primary beam current shown in Figure A.3, a non-linear behavior is observed above 20 μA. This results from heating and charging effects as well as damage to the sample by the electron beam [108, 111]. Therefore, a primary beam current of 20 μA is used for all further measurements. All Auger spectra recorded in this work are acquired with the optimized settings discussed and a primary electron energy of 3 keV.
For the qualitative evaluation of an Auger spectrum, the occurring peaks are compared with standard spectra, found for example in the work of Davis et al. (1976) [108]. This makes it possible to identify the elements present in the first few nanometers close to the sample surface. A quantitative analysis must be carried out to determine the atomic concentrations of elements in the sample. Under constant measurement parameters, the Auger electron yield is element-specific and depends in particular on the ionization cross section [112]. For this reason, the determined peak-to-peak amplitudes of the Auger peaks of different elements in an Auger spectrum cannot be directly set in relation to each other to determine the respective atomic concentration. Instead, Auger sensitivity factors must be used, which can be found in the literature for different primary electron energies [108]. These sensitivity factors are determined from measurements with pure elemental standards or calculated and are universally valid [112]. The sensitivity factors used in this work are taken from the work of Davis et al. (1976) [108].
Using the sensitivity factors, the atomic concentration of an element in the sample can then be determined according to [108]:

$$C_x = \frac{I_x}{S_x \cdot d_x} \cdot \left(\sum_\alpha \frac{I_\alpha}{S_\alpha \cdot d_\alpha} \right)^{-1} . \tag{3.2}$$

Here, I_x describes the peak-to-peak amplitude of the element x, S_x is the associated sensitivity factor and d_x is the scale factor which is calculated via $d_x = L_x \cdot E_{m,x} \cdot I_{p,x}$. Here L_x defines the sensitivity of the lock-in amplifier, $E_{m,x}$ the modulation amplitude and $I_{p,x}$ the primary beam current. The sum represents the ratios $\frac{I_\alpha}{S_\alpha \cdot d_\alpha}$ of all elements occurring in the sample.
There are 2 main sources of error in this method for determining the atomic concentration. The first is the sensitivity factors for Auger electron energies below 200 eV. Here, the yield of the electron multiplier decreases nonlinearly as described above, which reduces the peak-to-peak amplitudes compared to the peaks above 200 eV. Therefore, the sensitivity factors for the low energy peaks need to be adjusted [112]. Secondly, effects such as chemical bonding can lead to a distortion of the peak shapes, which is reflected in the differentiated spectrum in a changed peak-to-peak amplitude [108].
In order to determine the information depth achieved with the AES, the inelastic mean free path (IMFP) λ of the Auger electrons must be considered [110]. In general, the IMFP indicates the mean distance that an electron can travel in a solid without an inelastic collision. Here it

depends on the one hand on the energy of the traveling electron and on the other hand on the material in which the electron is traveling in [110].
To evaluate the IMFP, a Si(100)/SiO_2 substrate is inserted into the UHV chamber and Auger scans are performed of the Si peak at 92 eV and 1619 eV as well as the O peak at 503 eV. Subsequently, Fe is deposited on the substrate using the Fe evaporator and the deposited layer thickness is measured with the QCM. After deposition of some angstrom (Å) of Fe, Auger scans of the previously mentioned elements and additionally of the Fe peak at 703 eV are performed repeatedly. The peak-to-peak intensities of the Fe peak and the Si peak at 92 eV are shown as a function of the measured Fe layer thickness in the inset of Figure 3.6 b).
According to the work of Seah (1972) [113], the intensity curve of the deposited film (here Fe) can be described by the fit function

$$I = I_\infty \left(1 - exp\left(-\frac{d}{n^1}\right)\right), \quad \text{with} \quad n^1 = \left(1 - exp\left(-\frac{1}{\lambda}\right)\right)^{-1}, \tag{3.3}$$

where I is the measured peak-to-peak intensity of the Fe Auger peak, I_∞ is the peak-to-peak intensity at infinite Fe thickness, d is the measured thickness of Fe and λ is the IMFP. The intensity curve of the substrate elements is analogously described by [113]:

$$I = I_0 \cdot exp\left(-\frac{d}{n^1}\right). \tag{3.4}$$

Here, I_0 is the Auger peak-to-peak intensity of the bare substrate. By fitting Equation 3.3 and 3.4 to the data points, the IMFP can be obtained as a fit parameter. The IMFP is then plotted as a function of the corresponding Auger electron energy as shown in Figure 3.6 b). In addition, the energy dependance of the IMFP of electrons in pure (solid) elements according to the work of Seah et al. (1979) [110] is shown as a red dashed line.
The divergence of the data points from the curve expected according to literature at higher electron energies can be explained by the roughness of the deposited Fe film. This is in the range of 1.7 ± 0.7 nm as seen from ellipsometry measurements (see Figure A.1 b) in the Appendix). Therefore, the actual Fe layer thickness on the substrate can deviate downwards from the average Fe layer thickness determined with the QCM. This leads to a shift of the measured IMFP to higher values. For this reason, Equation 3.3 and 3.4 take into account that the Fe growth on the substrate does not take place layer by layer, but that new layers start to grow before one layer is completed [113]. However, the slight upward deviations of 0.5 nm of the calculated IMFPs compared to the literature values in Figure 3.6 b) for higher electron energies show that this correction is not sufficient to account for the roughness of the deposited Fe layer.

4. Synthesis of $Ti_3C_2T_x$ MXenes and sample preparation

This chapter addresses the synthesis of $Ti_3C_2T_x$ MXenes (in Chapter 4.1) along with the preparation of the samples investigated in this work. In this context, an efficient and suitable way for sample preparation is the coating of the MXenes from an aqueous suspension onto $Si(100)/SiO_2$ substrates. In this process, the MXene sheets arrange on the substrate horizontally while stacking on top of each other. Using the approaches of spin coating (Chapter 4.2) and spray coating (Chapter 4.3), different sample thicknesses, coverages and roughnesses of the MXenes on the substrates can be achieved depending on the requirements of further treatment steps and measurement methods. For electrical transport measurements and transmission electron microscopy (TEM) measurements additional preparation steps are necessary which will be discussed in Chapter 4.4 and Chapter 4.5.

4.1. Synthesis of $Ti_3C_2T_x$ MXenes

The synthesis of MXenes starts with a powder Ti_3AlC_2 MAX phase as precursor material. The powder MAX phase was produced at the RWTH Aachen in the group of Prof. Dr. Jesus Gonzales-Julian by pressureless sintering at 1450 °C in an inert atmosphere. The MAX phase precursor powder has an average grain size of 10-15 μm, which is a measure of the upper possible size range of the synthesized MXene flakes. To synthesize $Ti_3C_2T_x$ MXenes, the A element Al of the MAX phase is removed by selective chemical etching using wet chemistry. More detailed, a minimally intensive layer delamination (MILD) is used. In this process, 1 g of Ti_3AlC_2 MAX phase powder is slowly added to a mixture of 1.6 g LiF dissolved in 20 ml 9M HCl. The mixture is then stirred continuously for 24 h at 40 °C. After this step, the suspension is successively washed with demineralized water by centrifugation until a neutral pH value is reached. During washing, the reaction product (AlF_3) is washed out and an aqueous $Ti_3C_2T_x$ MXene suspension is obtained with the surface terminations $T_x := O, -OH$, as well as $-F, -Cl$ as a result of etching with LiF and HCl. The composition of the surface terminations is further investigated via Auger electron spectroscopy (AES) in the following Chapter 4.2. As a last step of the synthesis, the suspension is filtered and dried in a vacuum at 80 °C.

The successful conversion of the Ti_3AlC_2 MAX phase into $Ti_3C_2T_x$ MXenes by etching the A element Al can be observed from a structural analysis via X-ray diffraction (XRD). The XRD pattern shown in Figure 4.1 was recorded with a *Bruker* D8 diffractometer using Cu-K_α radia-

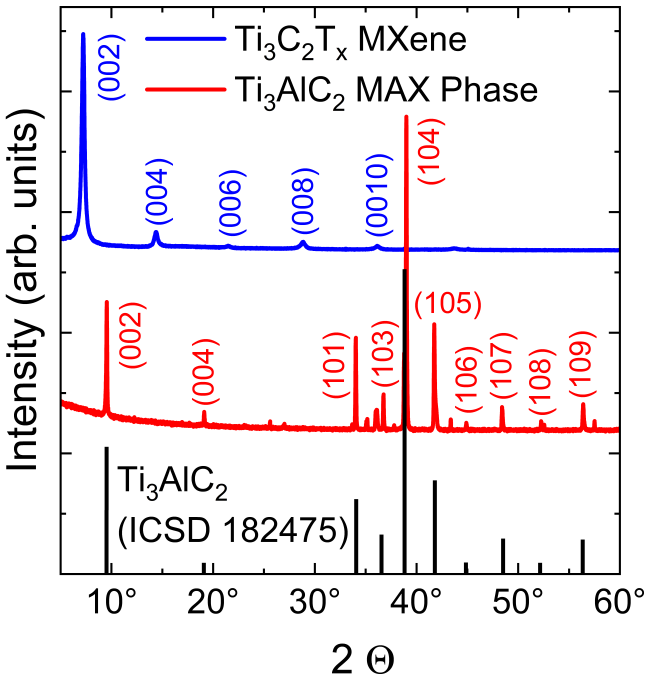

Figure 4.1: XRD pattern (Cu-K_α = 0.154 06 nm) of the Ti_3AlC_2 MAX phase precursor shown in red and the synthesized $Ti_3C_2T_x$ MXenes shown in blue. The peak assignment for the MAX phase was carried out by comparison with the corresponding data of the ICSD, shown as black columns. The blue curve no longer contains diffraction peaks associated with the 3D character of the MAX phase, indicating a successful synthesis of the 2D $Ti_3C_2T_x$ MXenes [115].

tion with an X-ray wavelength of 0.154 06 nm. The diffraction peaks of the powder MAX phase precursor (XRD pattern in red) are assigned by comparison with the data from the inorganic crystal structure database (ICSD) [114]. Here one finds the (002) diffraction peak at 9.5°, which originates from the stacked MX layers separated by the A layers. In addition, the diffraction peaks associated with the 3D character of the MAX phase can be seen at angles around 40° and higher, as also expected from the literature (see Figure 2.2).

After etching the A element, the blue diffraction pattern in Figure 4.1 is obtained, which represents the synthesized $Ti_3C_2T_x$ MXenes. Here, the (002) diffraction peak is located at 7.2° and shows almost twice the intensity compared to the MAX phase. Furthermore, the higher Bragg order (00l) peaks with only about 6 % intensity can be seen. The diffraction peaks attributed to the 3D nature of the MAX phase have disappeared, confirming the 2D character of the MXenes. The left shift of the (002) diffraction peak compared to the MAX phase shows an increase in the interplanar spacing between the stacked MX layers. This is due to the breaking of metallic bonds between the M and A element, subsequent functionalization by surface groups T_x and intercalation of H_2O molecules.

4.2. Spin coating $Ti_3C_2T_x$ MXenes on $Si(100)/SiO_2$ substrates

As already mentioned, the further processing of MXenes includes thermal activation in ultra high vacuum (UHV) and mass spectrometry to determine at which temperatures which surface terminations are removed. In order to obtain a sufficiently large signal during mass spectrometry, the samples must consist of a large number of MXene sheets. At the same time, the aim is for the MXene sheets to be arranged parallel to the substrate surface whilst stacking on top of

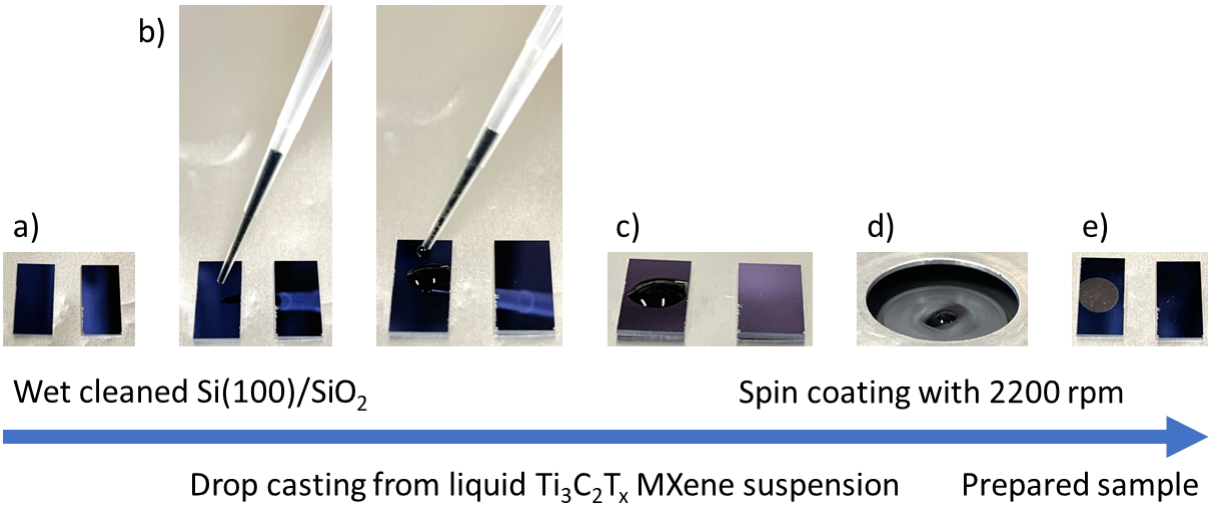

Figure 4.2.: a) Photographs of $Si(100)/SiO_2$ substrates after wet cleaning with acetone and ethanol in an ultrasonic bath. b) Instilling 5 μl aqueous $Ti_3C_2T_x$ MXene suspension onto the substrates with a fine-dose pipette. The result is a droplet of the aqueous MXene suspension on the substrate, as shown in c). d) Spin coating the droplet of the aqueous MXene suspension at a speed of 2200 rpm. Through spin coating, the MXene sheets are aligned horizontally on the substrate while stacking on top of each other. The spin coater is stopped when the MXene suspension has completely dried out (after about 30 min), as shown for the final state of the sample in e). Here, the dark gray circle on the left substrate is the spin coated MXenes.

each other. In this context, an infinite expansion of the sample in the z-direction for a thickness of the stacked MXenes of at least 60 nm can be assumed for the investigation of diffusion of a typically 6 nm thick Fe film into the MXenes. This is due to the fact that Fe, as observed in Chapter 6.1, penetrates into the MXene up to a maximum of about 50 nm. As a result, the boundary conditions for solving the diffusion equation are simplified (cf. Equation 2.11). The above requirements for the MXene samples can be met by the spin coating method as explained in the following.

In order to spin coat the synthesized $Ti_3C_2T_x$ MXenes, they must first be dispersed in Milli-Q water. For this purpose, 1 mg of the MXenes is mixed with 1 ml Milli-Q water. To completely disperse the MXenes the container with the MXene-water mixture is placed in an ultrasonic bath for 30 min. The resulting aqueous suspension can then be used for several weeks (if stored in O free atmosphere or at low temperatures $\sim 7\,^{\circ}C$) before the MXenes begin to oxidize. During oxidation, O dissolved in water reacts with the Ti atoms and forms TiO_2, while the C bonds with Ti are released in the form of graphite. The oxidation process can be observed when the MXene suspension, which is initially black, turns grey and later white as the oxidation process progresses.

Once the aqueous suspension has been prepared, it can be deposited on suitable substrates. Here, any reaction of the $Ti_3C_2T_x$ MXene sheets with the substrate must be avoided. Especially with

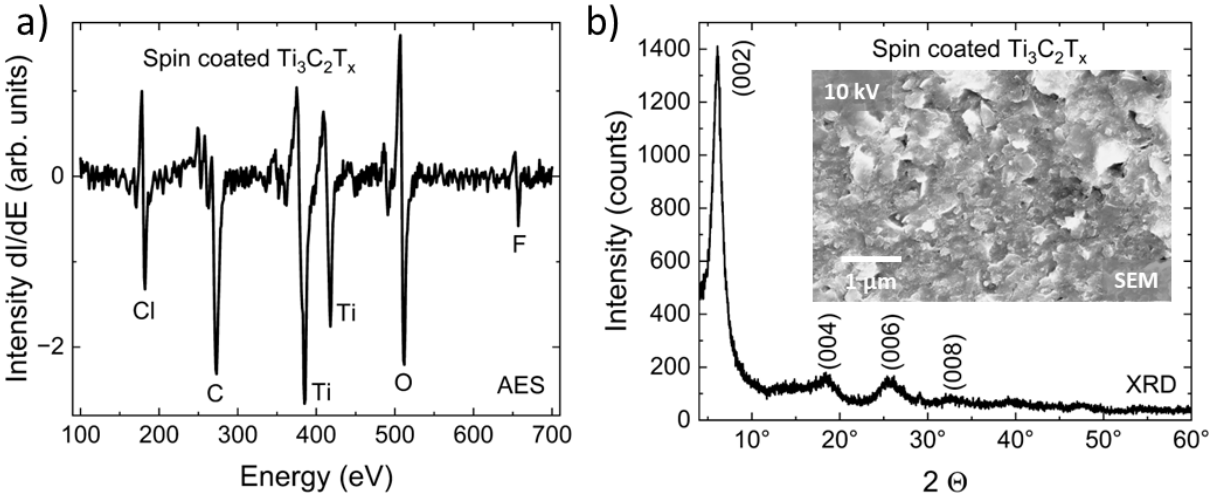

Figure 4.3.: a) Auger spectrum of a spin coated MXene sample, recorded from 100 eV to 700 eV. The Auger spectrum shows Ti and C peaks originating from the Ti_3C_2 MXene layers, as well as Cl, F and O peaks, which qualitatively indicate the chemical composition of the surface terminations T_x. Since the AES only detects elements with an atomic number > 3, $-OH$ is observed via a contribution to the O peak. b) XRD pattern (Cu-K_α =0.154 06 nm) from 0° to 60° of the spin coated $Ti_3C_2T_x$ MXenes on $Si(100)/SiO_2$ substrates. The diffraction pattern shows the expected diffraction peaks of the MXenes, as already observed in Figure 4.1. Additionally, the inset shows an SEM image of the sample surface taken at 10 kV with a magnification of 20 K. It can be seen that the MXene sheets are aligned horizontally, with the smallest or largest MXene flakes in the range of 100 nm or 1 μm.

regard to thermal activation, it is important that no interactions with the substrate occur - even at higher temperatures.

For thin Ti films (d $<$ 100 nm) on Si(100), Si(110) and Si(111) substrates, an interdiffusion process of the Ti into the Si is generally observed, which leads to a formation of $TiSi_2$ [116, 117]. This process is accelerated when the samples are annealed to temperatures above room temperature (RT). Thereby the formation of $TiSi_2$ is the lowest for Si(100) substrates [117]. For a $Si(100)/SiO_2$ substrate with a 50 nm thick oxide layer on which a 30 nm Ti film is evaporated in UHV and then annealed to 600 °C, the formation of $TiSi_2$ can be reduced to a few nanometers at the interface [116]. At the same time, a few nanometers of titanium oxide are formed while uppermost 20 nm pure Ti remains [116]. As the Ti atoms on the surface of the MXene sheets are already bound to the surface terminations, a reaction between the MXene sheets and a $Si(100)/SiO_2$ substrate can be ruled out. Nevertheless, there may be a higher amount of T_x : = O terminations in the vicinity of the interface after thermal activation.

Consequently, $Si(100)/SiO_2$ substrates with a 100 nm thick oxide layer are chosen for the MXenes to be deposited on. The thick oxide layer has the additional advantage that a tunnel effect through the substrate can be prevented when carrying out transport measurements. In addition, Si(100) has a large XRD peak at about 69° for Cu-K_α radiation [118], so that an overlap with

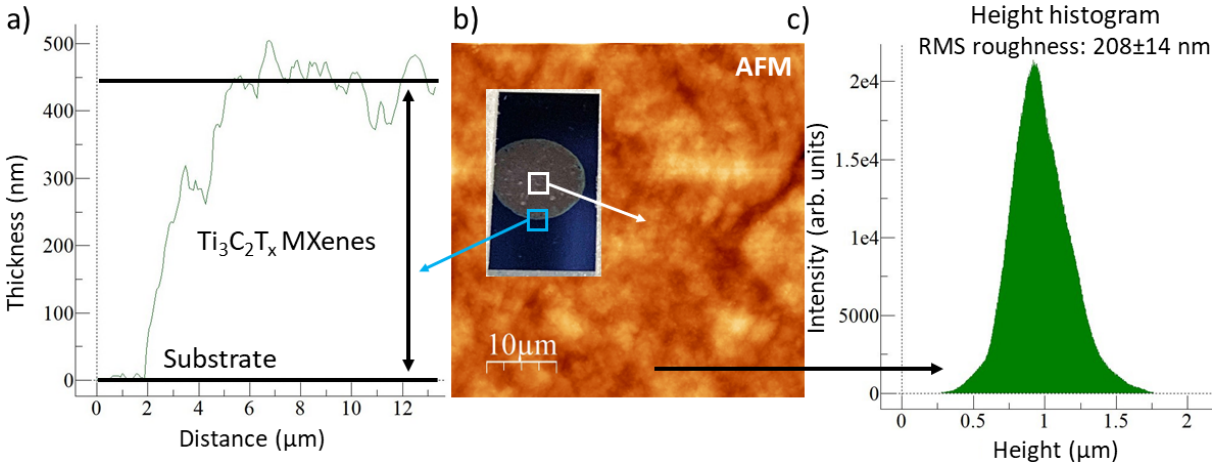

Figure 4.4.: a) MXene thickness measured by AFM across the edge of the spin coated sample, as indicated by the blue box in the adjacent photograph of the sample. It follows that the MXene sample exhibits a thickness of approximately 450 nm within the first 10 μm from the sample edge. b) AFM image of an area of 50 μm×50 μm in the center of the sample, as indicated by the white box in the inset photograph of the spin coated MXene sample. The AFM imaging provides quantitative information about the topography of the sample surface. Here it can be seen that the MXenes are not arranged homogeneously on top of each other, but that the stacked sheets form mounds, which suggests a higher surface roughness. c) Hight histogram showing the height of the sample at each pixel in relation to the lowest point of the scanned area shown in figure b). From the distribution of heights, a RMS roughness, of 208 ± 14 nm is extracted. The position of the peak of the height histogram of 0.98 μm also indicates the average sample thickness in relation to the lowest point of the observed area, giving a lower estimate of the absolute sample thickness in the center.

the diffraction peaks of the MXenes can be excluded.

First, the Si(100)/SiO_2 substrates with a size of 5 mm×10 mm and a thickness of 0.525 mm are cleaned with acetone and ethanol for 20 min each in an ultrasonic bath to remove contaminants and adhesive residues from the production and the protective film. The wet cleaned Si substrates are shown in Figure 4.2 a). After cleaning the substrates, 5 μl of the aqueous MXene suspension is applied to the center of each substrate using a fine dosing pipette as shown in Figure 4.2 b). The substrate with the deposited drop of MXene suspension (see Figure 4.2 c)) is placed on the rotating disk of a spin coater set to a rotational speed of 2200 rpm as shown in Figure 4.2 d). In this process, the set speed ensures that the centripetal forces align the MXene flakes horizontally. Here, 2200 rpm is the maximum possible rotational speed at which the MXene solution is not centrifuged off the substrate. This allows for larger sample thicknesses to be achieved with higher homogeneity. The samples are let to spin for about 30 min until the Milli-Q water has completely evaporated and a dry film remains, which can be observed in Figure 4.2 e).

In situ AES spectra of the spin coated MXenes show the qualitative composition of the samples. The Auger peaks, shown in Figure 4.3 a), are assigned using the Handbook of Auger Electron

Spectroscopy [108]. One finds the expected Ti and C peaks which originate from the Ti_3C_2 MXene sheets, as well as O, Cl and F peaks which reflect the composition of the surface terminations. Since H has no Auger transition, the $-$OH terminations can only be observed via their contribution to the O peak.
The XRD pattern for structural analysis of the spin coated samples, recorded with a *PANalytical* X'Pert PRO MPD diffractometer using Cu-K_α radiation, is shown in Figure 4.3 b). There is a good agreement of the positions of the diffraction peaks with those observed after the MXene synthesis shown in Figure 4.1. Moreover, peaks originating only from (001) planes are observed, confirming that the MXenes sheets are preferentially aligned along the c axis. From the inset scanning electron microscopy (SEM) image in Figure 4.3 b), recorded with a *Zeiss* LEO 1530 with Gemini field emission gun, it can be seen that the substrate is completely covered by MXenes. The smallest and largest MXene flakes have a diameter in the range of 100 nm and 1 μm respectively.
In order to determine the sample thickness and roughness of spin coated samples, they are analyzed using atomic force microscopy (AFM). AFM measurements are carried out using a *Park Systems* XE-70 AFM in non-contact tapping mode. As shown in Figure 4.4 a), a sample thickness of 450 nm results from AFM measurements at the sample edge. The variance of this thickness is given by the roughness of the film, which is determined by taking an AFM image in the center of the sample. As mentioned in Chapter 4.1, the maximum size of MXene sheets is up to 15 μm. To avoid measuring only on the surface of one MXene sheet, which would falsify the measured roughness, a sample area of 50 μm$\times$50 μm is considered. From the recorded AFM image, shown in Figure 4.4 b), it can be seen that the stacked MXene sheets form large mounds of several micrometers in diameter. This is expected to result in a high roughness, which is further quantified by analyzing the AFM images with the software *WSxM* [119]. The software reads the height in each pixel with respect to the lowest point in the viewed area and counts recurring heights. The resulting hight histogram is plotted in Figure 4.4 c). The extracted root mean square (RMS) roughness of the sample is 208 ± 14 nm. The position of the maximum of the height histogram of 0.98 μm shows the average sample thickness in relation to the lowest point in the observed area and is therefore a lower estimate of the absolute sample thickness. As a result, the sample thickness in the center is at least 2 times higher than at the edge of the sample.
In summary, spin coating is a fast and straightforward method for producing MXene samples, resulting in a high thickness of horizontally aligned and vertically stacked MXene sheets. A disadvantage here is that spin coating leads to inhomogeneities in the sample thickness from the center to the edge as well as to an overall high degree of roughness.

4.3. Spray coating $Ti_3C_2T_x$ MXenes on $Si(100)/SiO_2$ substrates

Fe does not penetrate deeper into the MXene than 50 nm, as will be discussed later in Chapter 6.1. In the case of spin coated MXenes, this would lead to a proportion of about 10 % and less

of MXenes with intercalated Fe, since their thickness amounts to 500 nm and more (cf. Chapter 4.2). It is therefore advisable to reduce the sample thickness of MXenes so that Fe can penetrate the majority of the sample.

The high roughness of the spin coated samples, as explained in the previous chapter, is a limiting factor when reducing the sample thickness, as below a certain thickness a closed coverage of the substrate is no longer guaranteed. This is a problem, for example, when transport measurements are to be carried out on the samples. For this reason, another technique is used for sample preparation, namely spray coating. Spray coating allows a more precise control of the amount of MXene sheets deposited on the substrate, resulting in lower thicknesses and roughness compared to spin coating, as demonstrated in the following.

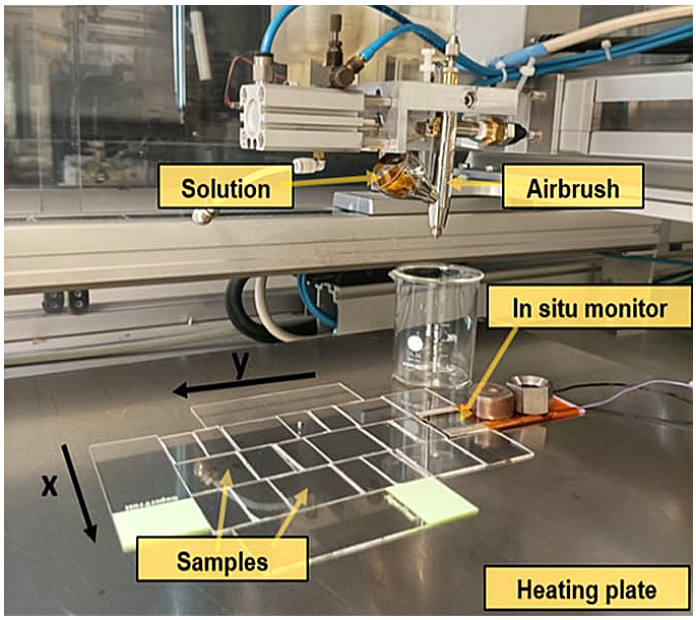

Figure 4.5.: Photograph of the spray coating setup of MXenes on $Si(100)/SiO_2$ substrates. The setup consists of a heating plate on which the substrates are placed and an *in situ* monitor to observe the coverage of the substrates by the MXenes during deposition. The airbrush with the container holding the aqueous MXenes suspension vaporizes the latter into a fine spray that coats the samples. To ensure rapid evaporation of the remaining liquid of the coated MXenes suspension, the heating plate is warmed up to 90 °C. To control the spray coater, the pressure and flow rate of the airbrush, the coating direction in the x-y-plane and the number of deposition cycles can be regulated [120].

Spray coating is carried out at the Laboratory of Materials Science and Physical Engineering (LMPG) at the University Grenoble-Alpes. For spray coating, 0.08 mg of the synthesized $Ti_3C_2T_x$ MXenes are mixed with 1 ml isopropanol. The isopropanol has a different surface tension than Milli-Q water, which leads to fast evaporation and as a consequence to more homogeneous surfaces of the films. This plays a major role for the spray coated samples, as the targeted thicknesses here are only around 10 % of the thicknesses of the spin coated samples. The MXene suspension in isopropanol is filled into an airbrush spray coater shown in Figure 4.5. The deposition is controlled by varying the direction of the generated spray jet in x-y-directions as well as its pressure, flow rate and deposition cycles. As for spin coating, the MXenes are sprayed onto $Si(100)/SiO_2$ substrates with a 100 nm oxide layer,

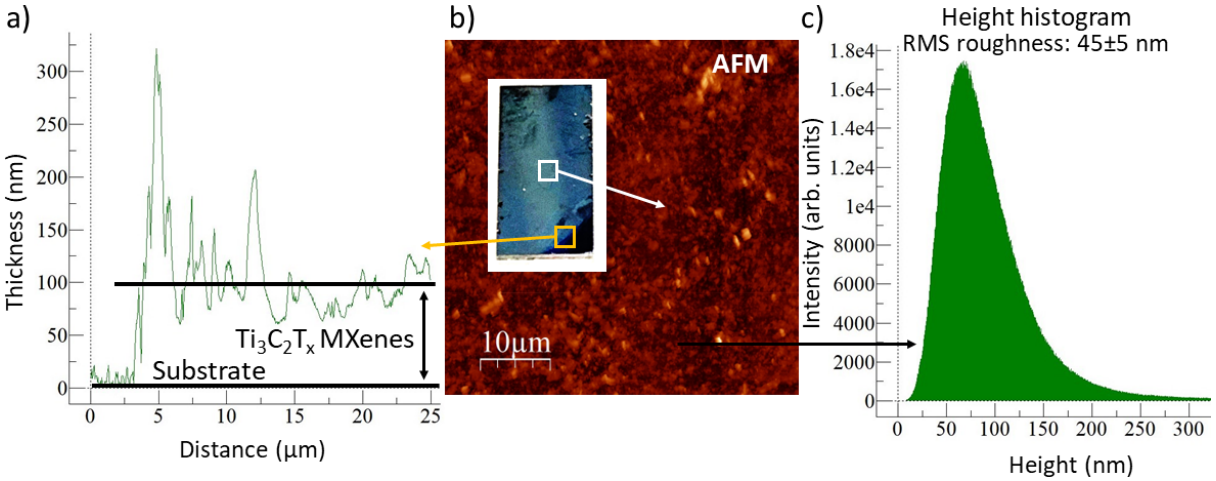

Figure 4.6.: a) Thickness of the deposited MXenes measured by AFM at an edge of the Si substrate to the spray coated MXenes, as indicated by the yellow box in the adjacent photograph of the sample. The edge is achieved by removing a piece of Kapton tape that is attached to the substrate during the spray coating process. It follows that the MXenes have a thickness of about 100 nm in the vicinity of the edge. b) AFM image of a surface of 50 μm×50 μm in the center of the sample, as indicated by the white box in the inset photo of the MXene sample. The AFM image shows a more homogeneous distribution of MXenes on the substrate compared to the spin coated sample (see Figure 4.4 b)). Hence, the stacked MXenes do not form mounds but are evenly distributed on the sample, indicating a lower roughness. c) Height histogram extracted from the AFM image from b), which provides an RMS roughness of 45 ± 5 nm.

which are placed on a hotplate (see Figure 4.5) heated to 90 °C during deposition to ensure rapid evaporation of the isopropanol. To monitor the coverage of MXenes, the resistance is measured between two insulated contacts placed on a glass substrate in the deposition plane (see Figure 4.5). A resistance can be measured here ($G\Omega$ range) as soon as the MXenes form a perculation layer. With further deposition cycles the resistance is continuously decreased. The measured resistance is therefore a good indication of when the deposition must be stopped in order to obtain the desired MXenes with minimum thickness and high degree of substrate coverage. For additional calibration of the layer thickness, AFM measurements are carried out (see below).
Looking at the XRD pattern after spray coating of $Ti_3C_2T_x$ MXenes, a diffraction pattern corresponding to that after MXene synthesis and spin coating of MXenes is revealed (see Figure 4.1 and 4.3 b)), confirming the preservation of the MXene structure with preferential orientation along the c axis. SEM images of the sample surface show MXene flakes in the size range from 200 nm to 1.5 μm. In addition, complete coverage of the substrate can be identified. The XRD pattern and a SEM image of the spray coated samples are shown in Figure A.4 in the Appendix. In contrast to the spin coated samples, the entire substrate area is covered with MXenes during spray coating. For this reason, one substrate is covered at its corner with Kapton tape during deposition, which is removed again after spray coating. This results in an edge to the substrate

which is not covered by MXenes, as can be seen in the inserted photograph of the spray coated sample in Figure 4.6 b). At this edge, the height difference from the substrate to the sample is measured via AFM (cf. Chapter 4.2), which is about $t = 100 \pm 50\,\text{nm}$ as shown in Figure 4.6 a). To obtain information about the surface roughness in the center of the sample, an AFM image of a $50\,\mu\text{m} \times 50\,\mu\text{m}$ large area is acquired (see Figure 4.6 b)). Compared to the AFM image of the spin coated sample in Figure 4.4 b), a higher homogeneity of the surface can be observed, which indicates a lower surface roughness. For further quantification, a height histogram of the recorded sample area is extracted using the software *WSxM* [119] (see Figure 4.6 c)). The resulting RMS roughness equals $45 \pm 5\,\text{nm}$. The sample heights in the histogram are measured relative to the lowest point of the observed region (reference point). Here, the peak of the height distribution is located at 93.7 nm. Due to the technical specifications of the spray coater, it can be expected that the thicknesses of the MXene film at the edge and the center of the substrate are approximately the same. Consequently, the peak position of the high histogram closely reflects the average thickness of the sample that was also observed at the edge to the substrate. This indicates that the reference point of the height histogram corresponds to the bare substrate or the substrate covered with only a couple of MXene sheets.
For the spray coated samples, it can be concluded that thicknesses of only about 10 % of the spin coated samples can be achieved, while at the same time reducing the surface roughness to less than a quarter. This is not yet the perculation limit as SEM measurements indicate a complete coverage of the substrate surface by MXenes. If necessary, the deposition cycles of the spray coater can therefore be further reduced. On the other hand, the height histogram from AFM measurements indicates, as explained above, that the substrate is sporadically not covered or only covered with a few MXene layers. If the thickness of the sample is further reduced, the probability increases that areas of the substrate are not covered by MXenes, even though the perculation limit has not yet been reached. In case of Fe deposition and intercalation this might result in Fe clusters forming in these areas, superimposing the signal of intercalated Fe in MXenes. Therefore, the sample thickness of about 100 nm presented here is a good compromise between complete coverage of the substrates and minimum thickness.

4.4. Lithography for *in situ* transport measurements

There are many ways to perform transport measurements on the MXene samples. One option chosen in this study is to press measuring pins into the samples from the surface. The advantage here is that this method can be carried out on any sample without further preparation steps. On the other hand, this is problematic for electrical transport detection of MXenes during Fe intercalation. If the sample is annealed *in situ* and the resistivity is measured at the same time using the technique described above, the pressing of the measuring pins into the sample changes the diffusion properties of the Fe in the area of the pins, which leads to a falsification of the measurement results. Also, there is a risk of losing contact to the sample. In addition, the gold

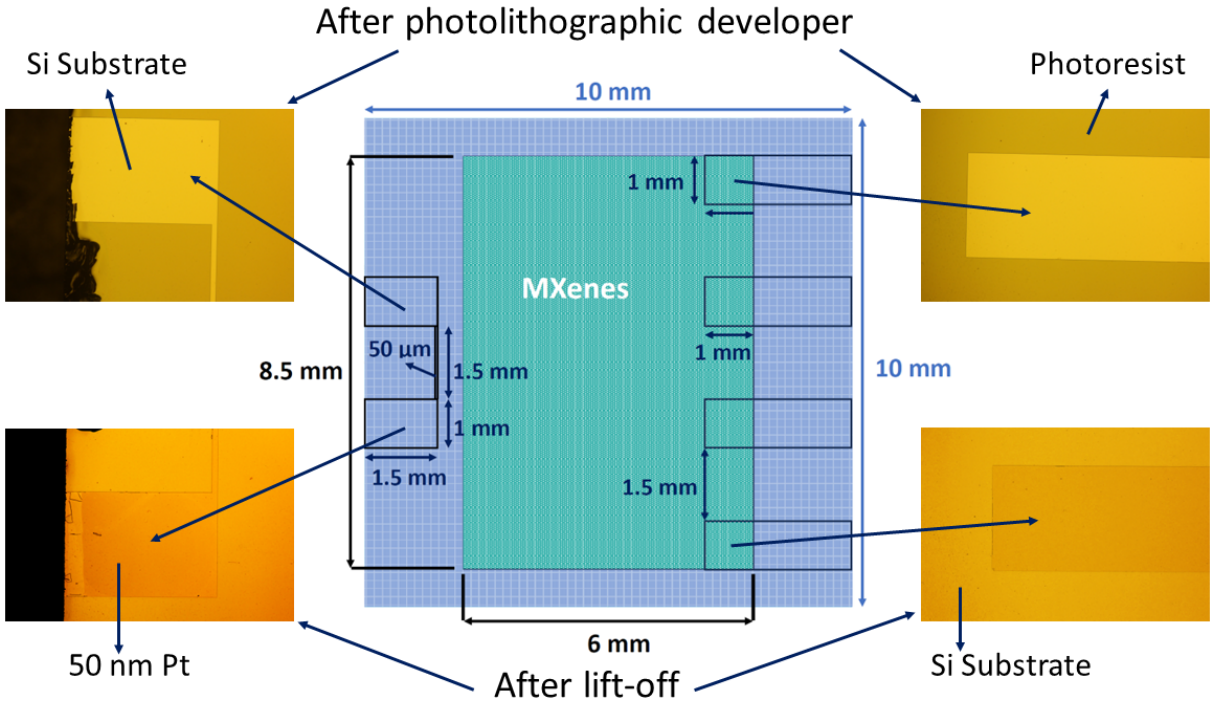

Figure 4.7.: The center image shows the lithographic design for four-probe inline transport measurements on the MXenes. Here, the light blue area depicts the 10 mm×10 mm $Si(100)/SiO_2$ substrates used, with the 4 contacts on the right side. The green area in the center indicates the MXenes, which are to be spray coated onto the lithographic structure through a suitable mask. The contacts are arranged at a distance of 1.5 mm from each other, while the width of the contacts is 1 mm. The contact area covered by the MXenes is 1 mm×1 mm. On the left side of the substrate are 2 more pins connected through a 50 μm wide Pt wire for temperature measurements. The top left and right optical microscope images show the layout written with UV light on the resist-covered substrates. Here, the resist in the areas exposed to UV light is removed by a photo developer, leaving the bare Si substrate. The lower left and right images show the lithographic structure after the deposition of 50 nm Pt and the removal of the Pt and resist from the remaining substrate areas (lift-off).

of the gold-plated measuring pins may diffuse into the MXenes at elevated temperatures. To avoid these effects, it is more suitable to use substrates with a lithographic structure made of a (thermally) stable material onto which the MXenes are coated.

For the lithography, 10 mm×10 mm $Si(100)/SiO_2$ substrates are used. In a first step, the substrates are wet cleaned with acetone and ethanol in an ultrasonic bath for 20 min each. Since these substrates are supplied with a natural oxide layer of only a few nanometers and for the reasons mentioned in Chapter 4.2, a thicker oxide layer is grown by placing the sample in a furnace heated to 800 °C at ambient pressure. Acording to the work of Deal et al. (1965) [121] the growth rate of the SiO_2 layer at 800 °C in dry oxygen (air) is about 8 nm/h. Thus the substrates are baked for 13 h to achieve the targeted thickness of the oxide layer of 100 nm. However, the thickness of the oxide layer actually achieved is only about 10 nm to 20 nm, as later revealed by

a cross-sectional analysis using transmission electron microscopy (TEM).
The lithographic structure to be written onto the substrates with Pt is shown in Figure 4.7. Here one can see the arrangement of the 4 contacts for the selected four-probe-in-line measurement geometry and the area where the MXenes are to be spray coated later. In addition, there are two further contacts on the opposite side of the contacts for electrical measurements, which are connected by a 50 μm thin wire. This loop serves as a thermometer when the sample is annealed to intercalate the Fe by measuring the temperature dependent resistance of the Pt.
The lithographic structure was written onto the substrates in the clean room of the AG Lorke at the University of Duisburg-Essen by Yasaman Jarrahi Zadeh from the Lorke group. Here, the substrates are first covered with a micrometer thick photoresist layer by spin coating them at 6000 rpm for 1 min. After coating the photoresist, the latter is further dried on a hotplate at 100 °C for 1 min. In the next step, the areas on the substrate where the contacts are to be located are illuminated with a focused UV light beam using a UV printer (Smart Print UV from *Microlight3D*), which consists of an automated x-y-table and a UV light source that can write structures down to 1.5 μm (manufacturer's specification). The substrate is then exposed to a photolithographic developer for 30 s, which removes the parts of the photoresist that were exposed to the UV light, as shown in Figure 4.7. Subsequently, 50 nm Pt is deposited on the substrates using a sputter coater (*Leica* EM ACE600). In a final step, the Pt covered substrates are exposed to acetone heated to 60 °C, isopropanol at room temperature and water in that order to wash off the resist and the Pt deposited on the resist in the remaining areas. This procedure is called lift-off. As a result, Pt only remains at the positions on the substrate where the contacts should be arranged according to the layout, as shown in Figure 4.7.

4.5. Sample preparation for transmission electron microscopy

A special preparation procedure is developed and applied to examine the $Ti_3C_2T_x$ MXenes after thermal activation and Fe intercalation in the transmission electron microscope (TEM). Here, the aim is to arrange the MXenes sheets on a TEM grid in such a way that the stacking direction of the MXenes is perpendicular to the surface normal of the TEM grid. This makes it possible to examine the cross section of the MXene samples. As a result, concentration profiles of the intercalated Fe can be measured by scanning transmision electron microscopy together with energy-dispersive X-ray spectroscopy (STEM-EDS) to determine the diffusivities of Fe in the MXenes spatially resolved (see Chapter 6.1).
To prepare the TEM samples, cylinders with a pointed tip (see Figure 4.8) are cast from epoxy resin using a custom-made mold. The cylinders have a length of 2 cm and a diameter of 5 mm. The casting of the cylinders takes place in two steps. First, only half of the cylinder is cast (as if the whole cylinder were to be halved along the cylinder axis). Then a thin film of epoxy resin is applied to the surface of the half cylinder at the tapered end which is then pressed onto the spin or spray coated MXene sample to be examined. The thin film of epoxy resin causes

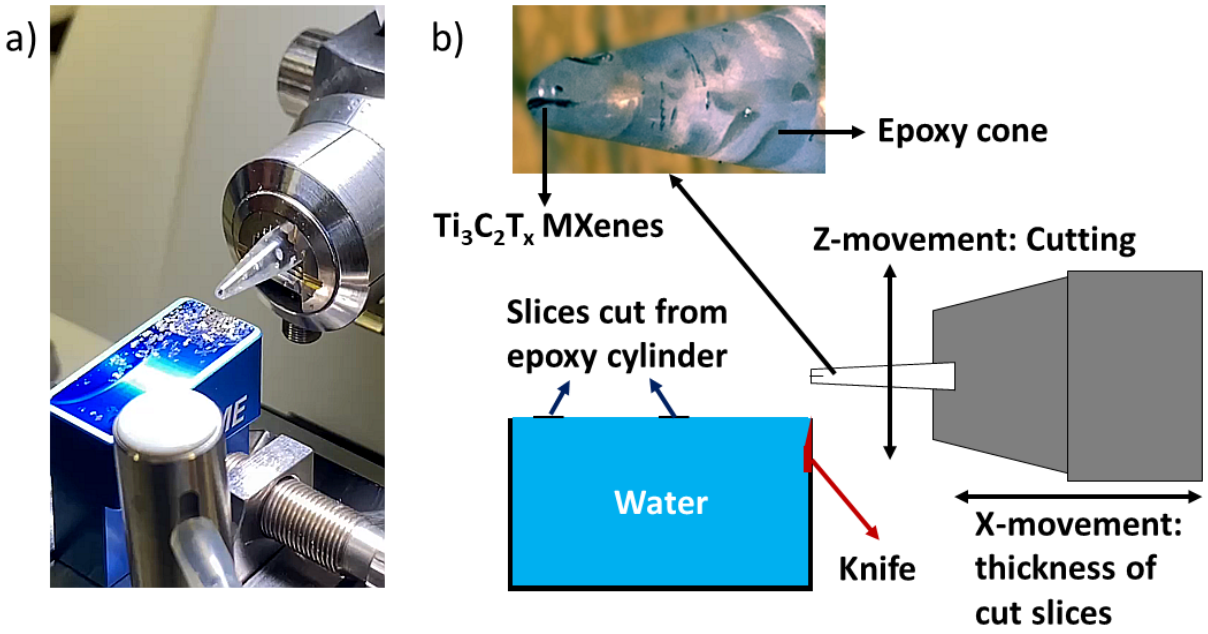

Figure 4.8.: a) Image of the ultramicrotome arm to which an epoxy cylinder with embedded MXenes is attached, and the diamond coated knife with a reservoir filled with distilled water in blue. The cut slices of the epoxy cylinder are floating on the water to be picked up and placed on a TEM grid. b) Schematic illustration of the ultramicrotome arm and the diamond covered knife. The MXenes of a spin or spray coated sample are lifted from the Si substrates and embedded in the tip of a tapered epoxy cylinder. This cylinder is then attached to the ultramicrotome arm, which performs a vertical movement to cut slices from the tip of the epoxy cylinder at a cutting speed of 20 mm/s. After each complete cutting movement, the arm is moved forward by a certain distance, which determines the thickness of the slices cut. The thickness of the cut slices here is about 100 nm. A diamond covered knife is used to perform the cuts, which is attached to a container filled with distilled water. This allows the cut slices to float on the surface of the water, making it easier to pick them up with tweezers and place them on a TEM grid.

the MXenes to be lifted from the substrate and adhere to the tip of the half cylinder. The half cylinder with the MXenes is then placed in the mold and the missing half of the cylinder is filled with epoxy resin. After curing, a complete cylinder is obtained in which the MXene film lifted from the substrate is embedded parallel to the cylinder axis in the center of the lower tapered end as shown in Figure 4.8 b).

The epoxy resin cylinders are subsequently cut with a ultramicrotome (*Leica* EM UC7/FC7) from the tapered end. This can be seen in Figure 4.8 a) and schematically in Figure 4.8 b). To cut the samples, the arm of the ultramicrotome to which the epoxy cylinder is attached performs an automated vertical movement. The cutting speed is thereby set to 20 mm/s. In addition, the arm moves forward by a set distance after each full cutting movement, which determines the thickness of the slices cut. Here, the thickness of the cut slices is set to 100 nm to achieve

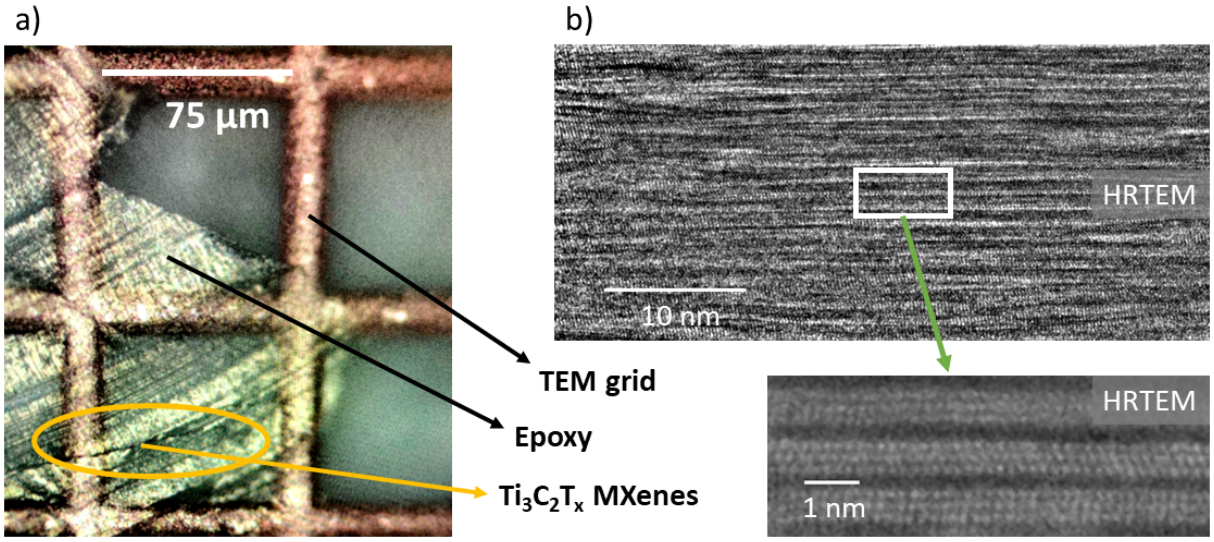

Figure 4.9.: a) Optical microscope image of a slice from an epoxy cylinder with embedded MXenes from a spin coated sample cut with the ultramicrotome and placed on a Cu-TEM grid with 200 mesh. The thickness of the slice is about 100 nm. The yellow circle highlights the embedded MXenes, which are visible as a thin black line. b) Section of a FFT filtered HRTEM image (upper image) with atomic column resolution of the sample shown in a). One can see the alignment of the MXene sheets, which are stacked on top of each other. As the MXenes stem from a spin coated sample, this proves the efficiency of aligning the MXene sheets horizontally on the substrate using this method. Nevertheless, there are some sheets that have a small angle ($\alpha < 10°$), as can be seen for example in the upper left corner and the lower right corner of the HRTEM image. In addition, an enlarged FFT filtered HRTEM image of 3 stacked MXene sheets of the same sample is shown (lower image). Here the interplanar spacing between the sheets as well as the arrangement of the Ti atomic columns in the typical zigzag pattern already sketched in Figure 2.1 can be observed.

stable epoxy slices. A diamond covered knife is mounted in front of the ultramicrotome arm to perform the cuts. In addition to the actual knife, the diamond knife consists of a basin filled with distilled water. This ensures that the slices cut from the epoxy cylinder float on the surface of the water, making it easier to pick them up with ring-shaped tweezers.
The slices collected from the water surface are then placed on Cu-TEM grids with 200 Mesh. This can be seen in Figure 4.9 a). Here, the MXenes can be identified as a thin black line in the epoxy slice. To improve the conductivity of the samples for subsequent analysis in the TEM, a 2 nm thick C film is deposited on the TEM grids with the MXene samples by flash evaporation. Since the stacking direction of the MXene sheets in the epoxy cylinder is parallel to the cutting plane, the stacking direction of the MXene sheets is perpendicular to the surface normal of the cut epoxy slices. As the epoxy slices are placed horizontally on the TEM grids, the stacking direction of the MXenes is also perpendicular to the surface normal of the TEM grids. The thickness of the slices of 100 nm is, as mentioned above, needed as a compromise to get a stable

slice of epoxy while the embedded MXenes are partly thin enough to be TEM transparent. In this way, the cross section of the stacked MXene layers can be analyzed in the TEM, as shown in Figure 4.9 b) as an example for MXenes from a spin coated sample. TEM measurements are performed in this context with a *JEOL* JEM-2200FS C_S-corrected TEM/STEM operated at 200 kV [122].

From the upper high resolution transmission electron microscopy (HRTEM) image of the sample cross section shown in Figure 4.9 b) (fast Fourier transform (FFT) filtered with *ImageJ* [123]), it can be seen that the MXene sheets are stacked on top of each other. In addition, the TEM analysis supports the observations made in Chapter 4.2 and Chapter 4.3 based on the SEM images and XRD patterns regarding the horizontal alignment of the MXene layers on the substrates. This is evident from the sample geometry of the TEM samples explained above. On the other hand, some MXene sheets deviate from the horizontal orientation by small angles ($\alpha < 10°$), as can be seen in Figure 4.9 b) at the top left and lower right of the upper HRTEM image.

In the lower HRTEM image (FFT filtered with *ImageJ*) shown in Figure 4.9 b), the atomic columns of 3 stacked MXene sheets can be observed in detail. Here the bright dots indicate Ti atomic columns. Each sheet consists of 3 Ti layers, corresponding to the M_3X_2 structure. The Ti atoms in neighboring sheets are arranged in a typical zigzag pattern as already sketched in Figure 2.1. In addition, the interplanar spacing of the Mxene sheets is visible, which will be investigated in more detail below in Chapter 5.2.

5. Thermal activation of $Ti_3C_2T_x$ MXenes

In this chapter, the results of the thermal activation of $Ti_3C_2T_x$ MXenes in ultra high vacuum (UHV) conditions are presented and discussed.
First, the efficiency of thermal activation, i.e. a heat treatment, with regard to the removal of the initial surface terminations is presented in Chapter 5.1. In this context, the composition of the MXenes before and after thermal activation is examined using *in situ* Auger electron spectroscopy (AES). Furthermore, the temperatures at which the corresponding surface terminations are removed from the MXenes are determined by *in situ* mass spectrometry measurements.
In Chapter 5.2, the structure and stacking of the $Ti_3C_2T_x$ MXenes before and after thermal activation is analyzed based on X-ray diffraction (XRD) and wide angle X-ray scattering (WAXS) measurements. The interplanar spacings between MXene sheets identified here are then compared and discussed in the context of the findings for as prepared MXenes.

5.1. Partial removal of initial surface terminations T_x

To thermally activate MXenes, they are annealed in UHV conditions at temperatures up to 1000 K, using a constant heating rate of 10 K/min (cf. Chapter 3.2.1). Once the temperature of 1000 K is reached, it is kept constant for 10 min to allow complete diffusion of the desorbed termination species before cooling to room temperature (RT) at a rate of 30 K/min. The maximum temperature of 1000 K is chosen as this is the temperature at which the structure of $Ti_3C_2T_x$ begins to degrade. This is demonstrated, for example, by Seredych et al. (2019) [66] for the annealing of $Ti_3C_2T_x$ MXenes in a He atmosphere (ambient pressure).
The thermal activation of spin coated MXenes in the UHV chamber is recorded by mass spectrometry to determine at which temperatures which surface terminations T_x are removed as gaseous components. As the mass spectrometer can only record the partial pressures of different gas components as a function of time, the abscissa is subsequently converted into a temperature. For this purpose, given that the sample heater enables a constant heating rate (see Figure 3.3 b)), here 10 K/min, this value is multiplied by the time elapsed after the start of the heating process and added to the starting temperature (295 K).
As described in Chapter 3.3.1, the mass spectrometer filters the gas atoms according to their mass to charge ratio m/e. The surface terminations of the investigated $Ti_3C_2T_x$ MXenes are composed of $T_x := O$, $-F$ and $-Cl$, as discussed in Chapter 4.2. In addition, $-OH$ terminations and H_2O adsorbed by the MXene sheets are to be expected as described in Chapter 2.1.3. For

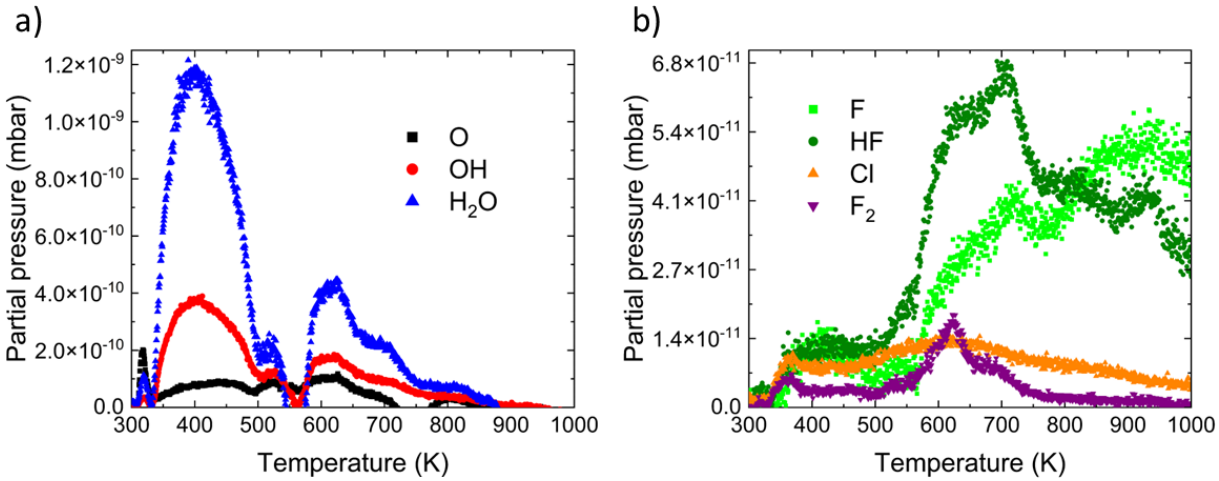

Figure 5.1.: a) Partial pressures of the terminations = O and −OH emerging from the MXenes as well as H_2O as a function of the sample temperature after background removal. A correlated course of OH and H_2O can be observed, whereby two temperatures (400 K and 625 K) indicate a removal of these components from the MXenes. In contrast, the temperature dependent curve of the partial pressure of O does not show any clear signal for the removal of this termination species. b) Partial pressures of the terminations −F and −Cl emerging from the MXenes as well as the diatomic fluorine molecule F_2 and the inorganic molecule HF as a function of the sample temperature after background removal. There is an incipient removal of −F at 575 K. An increase in the partial pressures of HF and F_2 at this temperature suggests that they are partially formed from the desorbed F atoms. A clear increase of the partial pressure of Cl cannot be observed. There is only a slight increase at around 490 K, which reaches its maximum at approximately 610 K.

this reason, the partial pressures of the atomic masses 16 u (O), 17 u (OH), 18 u (H_2O), as well as 19 u (F) and 35 u (Cl) are recorded [124].

During thermal activation, the signal of the partial pressures is always superimposed by a background caused by the residual gases in the vacuum chamber. In addition, the heating process is also accompanied by the desorption of adsorbed and absorbed atoms from the sample plate, the substrate and the body of the sample heater, as these are also heated up. In order to solely probe the signal of the MXenes, it is therefore necessary to perform the thermal activation twice with the parameters described above. The first measurement is carried out with a bare Si(100)/SiO_2 substrate. The second measurement is performed using a spin coated MXene sample (cf. Chapter 4.2). The partial pressures as a function of the sample temperature are plotted for O, OH and H_2O for the first and second measurement in Figure A.5 and for F and Cl in Figure A.6 in the Appendix.

If the partial pressures of the first measurement are subtracted from those of the second measurement for the respective atomic masses, the desorption signals of the MXene terminations are obtained. This can be viewed in Figure 5.1. Due to the overall higher partial pressures of O, OH and H_2O, these are plotted together in Figure 5.1 a). The partial pressures of F and Cl are shown

in Figure 5.1 b). For the diatomic fluorine molecule F_2 (38 u) and the inorganic compound HF (20 u), correlations are observed with the temperature dependent curve of the partial pressure of F, which is why these are also displayed in Figure 5.1 b).
Looking at Figure 5.1 a), it can be seen that starting at about 350 K H_2O and OH are desorbing to vacuum. The correlated trend of the partial pressures of H_2O and OH indicates a joint removal of these components as already observed from a thermogravimetric-mass spectrometric analysis by Hart et al. (2019) [18] for $Ti_3C_2T_x$ MXenes annealed up to 975 K in a He atmosphere (ambient pressure). Note that the resolution of the mass spectrometer in this work can easily separate 1 u (cf. Chapter 3.3.1). This further indicates a binding of $-$OH to H_2O, as previously observed by Halim et al. (2016) [63], who studied $Ti_3C_2T_x$ MXenes by X-ray photoelectron spectroscopy (XPS). The maximum of the partial pressures is reached at about 400 K, whereupon a decrease occurs. This is followed by a renewed correlated increase in the partial pressures of H_2O and OH at around 575 K, which reaches its maximum at 625 K and then slowly decreases again. From about 900 K, the background adjusted partial pressure approaches 0, which means that H_2O and OH no longer desorb from the MXenes into the vacuum. Consequently, it can be concluded that these components have been completely removed from the MXenes.
The work of Hart et al. (2019) [18] shows a removal of $-$OH terminations and H_2O from $Ti_3C_2T_x$ MXenes at about 385 K. In addition, a removal of $-$OH is observed at 625 K. Both temperatures are therefore consistent with the temperatures observed in this work. However, it is not clear from the work of Hart et al. (2019) [18], why the removal of $-$OH (and in this work also H_2O) is observed at two different temperatures. Most likely, physically adsorbed water is removed at a lower temperature from the surface of MXenes, whereas a higher temperature is required to remove the water from the interlayer space. However, to prove this, it is necessary to study the interplanar distances between MXene sheets at corresponding temperatures. By examining the interplanar spacing after thermal activation at a temperature of 425 K, it can be determined whether $-$OH and H_2O have been removed from between the sheets, as especially the water leads to an increase in the interplanar spacing [125]. If the interplanar distance does not decrease, the peak of the partial pressures of OH and H_2O at 425 K can be attributed to a removal of these components from the sample surface or inner voids of MXene stacks. If the interplanar distance decreases after thermally activating at $T > 625$ K, the second peak can be attributed to a removal of H_2O and $-$OH sitting in between the sheets. The higher temperature required to remove the $-$OH and H_2O molecules from between the sheets can be explained by a higher desorption energy, 5.9 eV in the case of $-$OH, due to hydrogen bonding between the layers (cf. Chapter 2.1.3). Another possible explanation is that intercalated H_2O forms a solvation shell around Li^+ cations that were spontaneously intercalated during the synthesis process. The analysis of the interplanar distances is addressed in the following Chapter 5.2.
Looking at the signal of the partial pressure of O in Figure 5.1 a), it can be seen that it is significantly lower than that of H_2O and OH. In addition, there is no clear increase in partial pressure, which reflects a "positive" strong binding of $=$ O terminations. This is evident from the work of

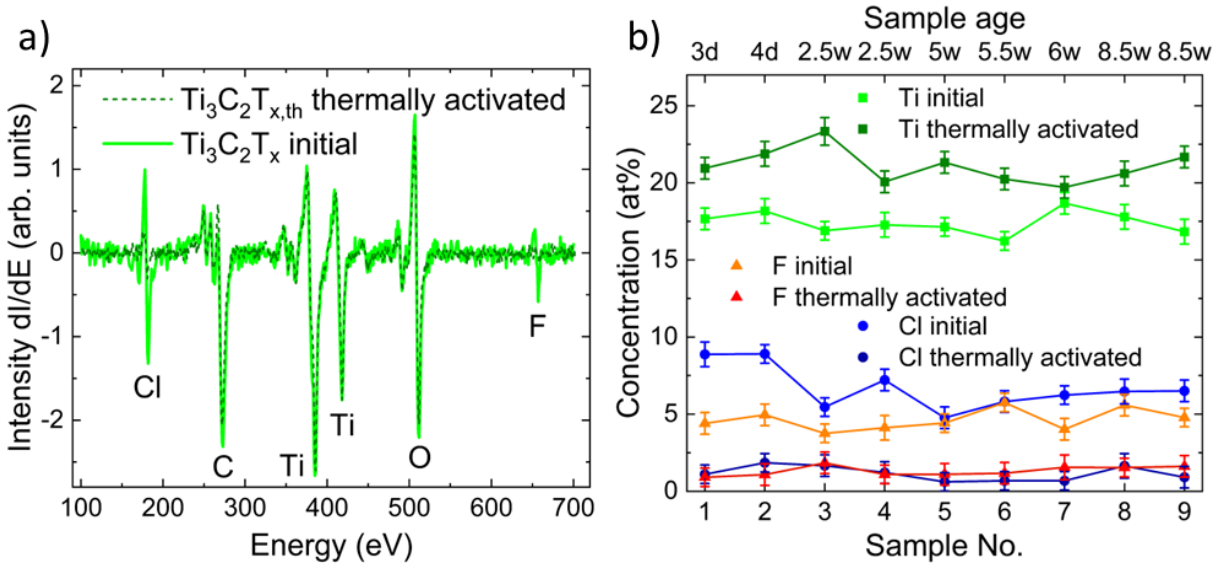

Figure 5.2.: a) Auger spectra of a spin coated MXene sample before and after thermal activation at T = 1000 K. The spectra are normalized to the Ti peak at 418 eV. It can be seen that the signals of F and Cl decrease after thermal activation and fall within the detection limit of the CMA, indicating complete removal. In addition, a slight decrease in the O signal is observed, which is attributed to the removal of −OH and H_2O, while the majority of the = O terminations remain in the MXenes. b) Atomic concentration of Ti, Cl and F in the MXene samples before and after thermal activation, determined from Auger spectra of 9 different spin coated samples from one sample batch. The age of the samples at the time of measurement is plotted in addition to the sample number. There is a decrease in the atomic concentrations of F and Cl due to thermal activation, resulting in a removal of 80 % to 90 % of the initial −F and −Cl terminations. At the same time, the Ti concentration increases from about 17.5 at% to 21 at% which is due to the removal of −Cl and −F as well as −OH and H_2O. Importantly, there is no aging effect and the atomic concentrations of the elements considered are approximately constant for all samples before or after thermal activation.

Persson et al. (2017) [64], which shows that below 1050 K no removal of = O terminations can be expected. Note that MXenes disrupt from about 1000 K.

Looking at Figure 5.1 b), an onset of removal of −F can be observed at about 575 K. The increase of HF and F_2 at the same temperature suggests that they are formed in the course of thermal activation after desorption of −F. The observed temperature of 575 K is about 100 K below the temperature expected by the work of Hart et al. (2019) [18] for the removal of −F. An error in the calibration of the sample temperature can be ruled out here, as the temperatures for removing −OH correspond exactly to the temperatures measured by Hart et al. (2019) [18]. One possible explanation is the higher sensitivity achieved with the mass spectrometer in this work due to the measurement in UHV conditions compared to the thermogravimetric-mass spectrometric analysis of Hart et al. (2019) [18] in a He atmosphere at ambient pressure. This enables

a more precise measurement of the onset of desorption at the lower partial pressures observed for F compared to those of OH or H_2O.
From the measured partial pressure of Cl, no clear temperature can be identified at which a removal of this termination species sets in (see Figure 5.1 b). Only a slight increase can be observed at 490 K which reaches its maximum at about 610 K. However, compared to the F peak, the peak of the partial pressure of Cl is only about 1/10 as large. This is despite the fact that the atomic concentration of Cl atoms in the sample is about 2 % higher than the concentration of F atoms (see Figure 5.2), as demonstrated by the AES study discussed in the following.
To quantitatively test the extent to which terminations can be removed by thermal activation, Auger spectra of the spin coated MXenes are recorded before and after thermal activation. This is shown exemplarily for one sample in Figure 5.2 a). From a qualitative observation of the Auger spectrum before thermal activation, shown in light green, it is evident that the Ti and C peaks of the Ti_3C_2 MXene layers as well as a composition of the surface terminations of T_x : $= O$, $-F$, $-Cl$ are clearly detectable by AES. From the mass spectrometry discussed above, it is also evident that additional $-OH$ terminations are present. However, H does not have an Auger transition [108], which is why OH and H_2O are observed by their contribution to the O Auger peak.
After thermal activation of the $Ti_3C_2T_x$ MXenes (dashed dark green line in Figure 5.2 a)), the F peak in the Auger spectrum has disappeared and the intensity of the Cl peak is slightly above the detection limit of the cylindrical mirror analyzer (CMA). This indicates an almost complete removal of these termination species. In addition, the intensity of the O peak has decreased slightly, which is attributed to the removal of the $-OH$ terminations and H_2O. However, the almost unchanged peak to peak amplitude of the O signal allows the conclusion that the majority of the $= O$ terminations remain in the MXenes as termination species, as also seen from mass spectrometry measurements. In this respect, the observations from the AES measurements and mass spectrometry are consistent. On the other hand, the almost unchanged O signal also indicates that most $-OH$ terminations and/or H_2O are still present in the uppermost 5 nm of the sample probed by the surface-sensitive AES (cf. Chapter 4.2). However, since mass spectrometry clearly indicates a removal of $-OH$ and H_2O, this observation must be limited to the surface of the sample. One possible cause for this could be H_2O which desorbs from the gold plated copper body of the sample heater during annealing. The latter reaches a maximum temperature around 130 °C towards the end of the annealing process (cf. Chapter 3.2.1), when the sample has already cooled back down to this temperature range. In this context, a resulting increased partial pressure of H_2O in the UHV chamber may lead to an adsorption of H_2O on the sample surface and thus to the nearly unchanged O Auger peak observed after thermal activation.
In addition to the $Ti_3C_3T_x$ MXenes synthesized for this work (see Chapter 4.1), a thermal activation and analysis of commercial $Ti_3C_2T_x$ MXenes from the startup *Nanoplexus* is performed by AES as a reference. Here, a similar behavior is found upon thermal activation (see Figure A.7 in the Appendix). However, the MXenes from *Nanoplexus* show a smaller peak to peak ampli-

tude of the O Auger peak relative to the Ti peak, indicating fewer = O and −OH terminations compared to the $Ti_3C_3T_x$ MXenes synthesized and analyzed in this work.
Since = O, −OH and H_2O contribute to the O Auger peak, a quantitative evaluation of the Auger spectra is only meaningful with regard to the calculation of the concentrations of the surface terminations −F and −Cl. In addition, the concentration of Ti in the samples, assumed being unchanged upon annealing, is determined as a reference.
To extract the atomic concentrations from the spectra, first the peak to peak amplitudes of the Auger peaks of all occurring elements are determined. These are then set in relation as described in Chapter 3.3.2 using Equation 3.2 together with the associated sensitivity factors [108]. In this way the total elemental contribution is set to 100 %. The result is shown in Figure 5.2 b) for 9 different spin coated samples of one sample batch. The age of the sample at which the measurement was performed is also plotted. The error bars result from the background noise of the CMA, which causes an error when determining the peak-to-peak amplitudes. This error is approximately the same for all elements and samples considered.
Figure 5.2 b) shows that the atomic concentration of Cl decreases by about 6 at% due to thermal activation and falls into the range of 1 at%. This corresponds to a removal of ∼90 % of the initial −Cl terminations. At the same time, the concentration of F decreases by about 4 at% down to approximately 1 at%. This equates with a removal of ∼80 % of the −F terminations by heat treatment at T = 1000 K for 10 min. Also, the concentration of Ti increases for all samples after thermal activation from approximately 17.5 at% to about 21 at%. This corresponds to the removal of −F and −Cl terminations and additionally of −OH terminations and H_2O (see Figure 5.2 a) and b)). The non-normalized peak-to-peak amplitude of the Ti Auger peak at 418 eV is approximately the same before and after thermal activation for the samples considered, indicating that the number of Ti atoms in the samples is conserved.
Importantly, Figure 5.2 b) shows a high degree of reproducibility of the thermal activation to remove −F and −Cl. In addition, the measured F, Cl and Ti concentrations are approximately constant within the error of the measurements for all samples before or after thermal activation, regardless of the age of the samples.
Summarizing, a removal of the −OH terminations located between the MXene sheets together with H_2O is expected setting in at a temperature of 575 K. However, this still needs verification (see following chapter). The removal of the −F terminations starts at about 575 K. A defined temperature for the removal of Cl cannot be identified from its partial pressure as a function of temperature. Removal of = O from the MXenes cannot be observed. Analysis of the samples before and after thermal activation by AES confirms the results of mass spectrometry with regard to = O terminations remaining in the MXenes. A quantitative analysis of the Auger spectra also shows a high efficiency and reproducibility of thermal activation for the removal of −F and −Cl terminations, with 80 % to 90 % of the terminations originally present being removed. Consequently, thermal activation of the samples is suitable to remove most −F-, −Cl- and −OH terminations as well as H_2O, while = O remains as termination species in the MXenes.

5.2. Interplanar spacing in thermally activated $Ti_3C_2T_{x,th}$ MXenes

As a result of the removal of the A element from a MAX phase precursor during MXene synthesis, the M element surfaces are immediately functionalized by surface terminations that originate from the etching environment and replace the A element for each sheet (cf. Chapter 2.1.1). Consequently, the surface terminations have a significant influence on the interplanar spacing (d-spacing of (002) peaks) of the MXene sheets [125]. In addition, water molecules that are intercalated between the layers affect the interplanar spacing [126]. In view of the removal of surface terminations and H_2O by thermal activation (see Chapter 5.1) it is important to investigate the influence of this heat treatment on the interplanar spacing. This is of great relevance for the intercalation of Fe in the further course, since the interplanar spacing is expected to have a significant influence on the diffusion of atoms in layered 2D materials, as discussed in Chapter 2.3.2. Details regarding the diffusion of Fe in $Ti_3C_2T_x$ MXenes are discussed in Chapter 6.

In the following, the interplanar spacing after thermal activation at temperatures of 1000 K and 400 K is measured and compared with the one observed for the as synthesized MXenes. From the latter it can be deduced whether the signal of OH and H_2O observed by mass spectrometry at 400 K originates from a removal of these components between the sheets or from the sample surface and inner voids of MXene stacks (cf. Chapter 5.1).

For a first overview, *ex situ* X-ray diffraction (XRD) patterns of spin coated MXene samples before and after thermal activation at 1000 K are recorded with a standard laboratory X-ray diffraction device (X'Pert PRO MPD from *PANalytical*) using Cu-K_α radiation. The interplanar spacings can then be calculated from the peak positions of the (002) diffraction peak. However, this shows that small changes (a few tenths of an angstrom (Å)) in the interplanar spacing in the first few tens of nanometers of the samples, as suspected for the intercalation of Fe (see Chapter 7.2), cannot be resolved with sufficient accuracy. The results of the XRD measurements can be found in Figure A.8 in the Appendix.

To achieve higher sensitivity, the diffraction patterns of spray coated samples are recorded using *ex situ* wide angle X-ray scattering (WAXS). The WAXS measurements are performed at the P03 microfocus and nanofocus X-ray scattering (MiNaXS) beamline of the PETRA III storage ring. Here, the X-ray beam with high intensity ($\geq 10^{11}$ photons/s) and a beam size of 10 μm×30 μm hits the sample under grazing incidence (0.1° to 1°) and is then captured by a CCD camera, which serves as a detector [127]. The grazing incidence results in a maximum information depth of around 30 nm. This setup enables a spatially resolved measurement of diffraction patterns, whith high sensitivity [127]. The interplanar spacing calculated from the peak position of the (002) diffraction peak can thus be measured with high accuracy.

For each sample, 61 scattering images of the diffracted X-ray beam from different sample areas are recorded with the CCD camera with an acquisition time of 10 s each. However, for the non-thermally activated sample, only 15 scattering images with an aquisition time of 10 s are

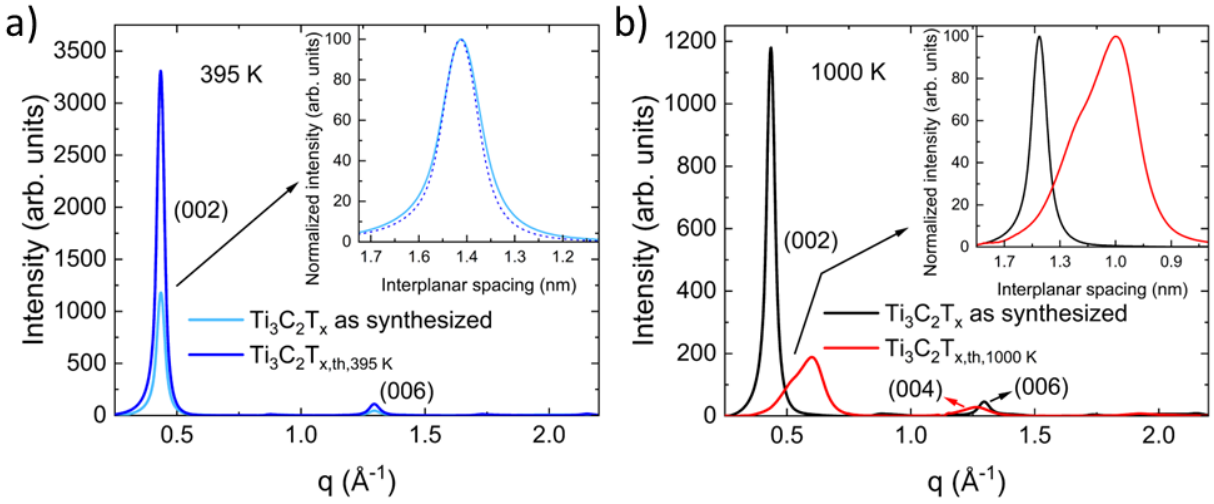

Figure 5.3.: a) Diffraction patterns obtained from WAXS measurements as a function of the scattering vector q of a thermally non-activated (light blue) and a thermally activated (395 K) spray coated sample (blue) [128]. The peaks are assigned by matching them with XRD spectra of the MXenes (see Figure 4.1). The inset shows the normalized (002) peak of both samples as a function of the interplanar spacing of the MXene sheets. Here, the maxima of both peaks are found at identical q vector, indicating no change in the interplanar spacing. For quantitative determination of the interplanar spacings, the normalized (002) peaks are fitted by a pseudo-Voigt function (see Figure A.9 a)). b) Diffraction pattern from WAXS measurements on a thermally non-activated (black) and a thermally activated (1000 K) spray coated sample (red) as a function of the scattering vector q [128]. The inset with the normalized (002) peaks of both samples as a function of the interplanar spacing shows a reduction in the interplanar distance after thermal activation. In addition, the corresponding peak (red) has a shoulder that implies a second interplanar spacing occurring in the sample. Therefore, the (002) peak after thermal activation is fitted by two Gauss functions (see Figure A.9 b)) for a quantitative analysis of the interplanar spacings.

recorded. To evaluate the acquired scattering images, the measured intensity is read out as a function of the scattering vector q (parallel to the stacking direction of MXenes). The scattering vector is calibrated using a LaB_6 reference sample. The diffraction patterns obtained for the respective sample areas investigated are then averaged and smoothed before the background is subtracted in a second step. The resulting diffraction patterns are shown in Figure 5.3 a) for the thermally non-activated sample and a sample thermally activated at 395 K. Figure 5.3 b) shows the resulting diffraction patterns of the thermally non-activated sample and a sample thermally activated at 1000 K.

Looking at Figure 5.3 a), it is evident that the diffraction peaks of the thermally non-activated sample (light blue) and the thermally activated (395 K) sample (blue) have identical d-spacing. To quantify this further, the position of the peak maximum of the (002) peak is determined for both samples by fitting with a pseudo-Voigt function, as shown in Figure A.9 a) in the Appendix.

The interplanar spacing then results from the scattering vector q according to

$$d_{inter} = \frac{2\pi * n}{q}, \tag{5.1}$$

where n describes the diffraction order [129]. In this context, the inset in Figure 5.3 a) shows the normalized intensity of the (002) diffraction peak of the two samples as a function of the interplanar spacing. The determined interplanar spacing for the thermally non-activated MXene results in 1.44 ± 0.06 nm and for the thermally activated (395 K) MXene in 1.45 ± 0.06 nm.
In the light of the the mass spectrometry results discussed in the previous chapter, it becomes obvious that the peak of the partial pressures of OH and H_2O around 400 K (see Figure 5.1 a)) cannot be due to a removal of $-$OH and H_2O molecules located between the MXene sheets. This is due to the fact that the water sitting in between the MXene sheets contributes to an increased interplanar spacing [125]. Therefore, the hypothesis that the signal observed from mass spectrometry must originate from the $-OH/H_2O$ removed from the surface and inner voids of the samples is confirmed. Consequently, thermal activation at 395 K does not lead to a reduction in the interplanar spacing.
However, if one looks at Figure 5.3 b), it is evident that the thermal activation at 1000 K leads to a significant reduction in the interplanar spacing compared to the non-thermally activated sample. Furthermore, from the inset in Figure 5.3 b) it can be seen that a shoulder is present in the (002) diffraction peak after thermal activation. For this reason, the diffraction peak is fitted by 2 Gauss functions as shown in Figure A.9 b) in the Appendix to quantitatively determine the interplanar spacings. The two occurring interplanar spacings result in 1.03 ± 0.07 nm and 1.21 ± 0.09 nm.
The work of Ma et al. (2020) [130] shows that the interplanar spacing of HF etched $Ti_3C_2T_x$ MXenes is about 1 nm. This is confirmed by the work of Hadler-Jacobsen et al. (2021) [131], where an interplanar distance of 0.95 nm is observed for $Ti_3C_2T_x$ MXenes with mixed surface terminations ($T_x := O$, $-$OH, $-$F). Moreover, if a subset or only one of the aforementioned termination species is present in the MXenes the interplanar spacing does not change. An exeption are pure $-$OH terminations where larger interplanar distances of 1.13 nm are anticipated from DFT calculations [131]. For LiF/HCl etched $Ti_3C_2T_x$ MXenes ($T_x := O$, $-$OH, $-$F, $-$Cl terminations) an interplanar spacing of 1.28 nm is reported [130, 132]. Here, the $-$Cl terminations lead to an increase of the interplanar spacing, as they cause local undulations in mixed termination layers [133]. In addition, $-$Cl terminations enable high Li ion storage capacities. Remaining Li ions from the etching process can thus form inorganic LiCl, which can also increase the interplanar spacing [134]. Apart from the etching procedure, H_2O has also a decisive influence on the interplanar spacing [135]. This leads, as described in the work of Ghidiu et al. (2014) [135] for LiF/HCl etched $Ti_3C_2T_x$ MXenes, to a "clay-like" swelling in a humid environment, as a result of the intercalation of several layers of water between the MXene sheets. This was also observed by Liu et al. (2022) [126] for $Ti_3C_2T_x$ MXenes at various temperatures in

ambient environments with different humidity. Note that for this reason, all thermally activated MXenes are covered with 8 nm C before they are removed from the UHV chamber, which blocks the diffusion of H_2O into the samples in ambient conditions.

The observed interplanar spacing of 1.44 nm of the non-thermally activated $Ti_3C_2T_x$ MXenes synthesized in this work by chemical etching with LiF/HCl (see Chapter 4.1) deviates upwards by 0.16 nm from the above mentioned value expected from the literature. This can be attributed to the presence of additional intercalated H_2O sitting in between the MXene sheets [135].

After thermal activation at 1000 K, the majority of $-$F and $-$Cl terminations are removed. In addition, $-$OH and H_2O molecules are removed while $=$ O is preserved as a termination species, as discussed in the previous Chapter 5.1. Here, the reduction of the interplanar spacing to 1.03 ± 0.07 nm and 1.21 ± 0.09 nm is attributed in particular to the removal of H_2O from between the sheets. However, the occurrence of the two observed interplanar distances cannot be explained solely by the removal of water. Further effects must be involved here, which are discussed below.

The smaller interplanar spacing of 1.03 ± 0.07 nm corresponds approximately to the interplanar spacing observed in the literature for HF etched $Ti_3C_2T_x$ MXenes [130]. From this it can be deduced that for the most part $=$ O terminations are present, possibly together with remaining $-$OH and $-$F terminations. The larger interplanar spacing of 1.21 ± 0.09 nm is 0.07 nm smaller than the interplanar spacing observed in the literature for a LiF/HCl etched $Ti_3C_2T_x$ MXene [130], but clearly above the interplanar spacing of a HF etched MXene [131]. This suggests that in addition to the $=$ O and any remaining $-$OH and $-$F terminations, there is remaining LiCl and Li^+ left in between the sheets as the latter remains even after the removal of Cl terminations. In this way, an increased interplanar spacing can be partially preserved. In both cases, it is assumed that the water has been completely removed from the samples after thermal activation at 1000 K for 10 min.

6. Fe diffusion in $Ti_3C_2T_{x,th}$ MXenes

The aim of this work is to remove the initial surface terminations T_x of the investigated $Ti_3C_2T_x$ MXenes and replace them by Fe, if possible. The removal of the surface terminations and its effect on the interplanar spacing was explained in the previous chapter. In this chapter, the diffusion characteristics of Fe in the MXenes will be discussed, starting from a continuous Fe film on top of MXenes. From thermally driven diffusion experiments, conclusions can be drawn as to what extent Fe intercalates between the MXene sheets and thus has the opportunity to bind to the termination-free Ti atoms generated by thermal activation.
In a first step, in Chapter 6.1 the diffusivity $D_\perp$ of Fe into the MXenes is determined from *in situ* Auger electron spectroscopy (AES) measurements as well as from Fe depth profiles obtained from *ex situ* X-ray photoelectron spectroscopy (XPS) measurements and scanning transmision electron microscopy together with energy-dispersive X-ray spectroscopy (STEM-EDS) cross section analysis. Furthermore, by measuring the diffusivities at different Fe annealing temperatures and plotting them in a Arrhenius plot, the activation energy E_A and the frequency factor D_0 for diffusion are derived. In Chapter 6.2, a diffusion model for the Fe diffusion in layered $Ti_3C_2T_x$ MXenes is then developed based on the findings from the previous chapter.
Finally, in Chapter 6.3, an electron transport experiment for the MXene samples is suggested to monitor diffusion. It is discussed why this provides a quick and easy way to live monitor the Fe diffusion and intercalation state of Fe in the MXenes.

6.1. Diffusivities and activation energy of diffusion

In situ analysis by Auger electron spectroscopy

The starting point of diffusion studies is an Fe film deposited on the MXenes by electron beam (e-beam) evaporation in ultra high vacuum (UHV) conditions. In the course of the diffusion experiments carried out, it was practical to set the deposited Fe film thickness to 6 nm. On the one hand, this is due to the depth sensitivity of the AES. On the other hand, this Fe amount proves to be sufficient, since even at high Fe annealing temperatures $T > 800\,K$ a residual amount of Fe remains on the sample surface. The latter was easily detected by scanning electron microscopy in conjunction with energy dispersive X-ray spectroscopy (SEM-EDS) (see Figure A.10 in the Appendix) and Auger electron scans before and after annealing (see Figure 6.1). Consequently, to increase the ratio of Fe in the MXenes with respect to surface Fe and the relative amount of Fe to Ti in MXenes, the thickness of the MXenes must be limited. This is achieved by using

spray coated MXenes as a method to produce well ordered MXene sheets on a planar substrate (cf. Chapter 4.3).

First, spin coated MXenes (see Chapter 4.2) are used for the diffusion experiments considered in this chapter. This has the advantage that the MXene samples can be considered as quasi-infinite in the z-direction, perpendicular to the MXene sheets. This simplifies the boundary conditions for solving the diffusion Equation 2.11.
As the Fe film is deposited on the entire sample surface, it can be assumed that globally there is no concentration gradient in the x-y-direction, parallel to the MXene sheets. Locally, however, this may be the case.
In the following, though, the diffusion in the z-direction of the samples is of interest. Since diffusion around the stacked MXene sheets is expected (cf. Chapter 2.3.2), a comparatively slow diffusion in the z-direction compared to the diffusion in the x-y-direction can be expected. In this context, it is important to note that the diameter of the MXene sheets is about $\sim$1 μm (see Chapter 4.2), while the distance between the sheets is only about $\sim$1 nm (see Chapter 5.2). The diffusion in the z-direction is therefore decisive for the amount of Fe initially deposited on the sample surface that can diffuse into the MXenes.
There are two ways to determine the diffusivity in z-direction. The first is to look at depth profiles of the Fe intensity. To create these profiles, however, a precise and reproducible Ar^+ sputtering process is required, which cannot be guaranteed in preparation UHV chamber. Therefore, the aforementioned Fe depth profiles are recorded *ex situ* by XPS profiling, as discussed below. However, this is a time consuming and tedious process as a sepa-

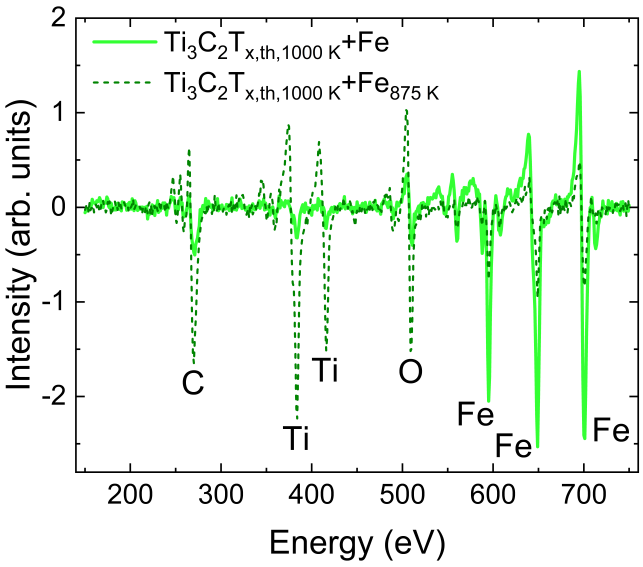

Figure 6.1.: Auger spectra (150 eV to 750 eV) of a thermally activated $Ti_3C_2T_{x,th,1000K}$ MXene sample after deposition of a 6 nm Fe film (light green), and after annealing of the Fe film at 875 K (dashed dark green). Prior to annealing, there is a pronounced Fe signal resulting from the continuous Fe film. In addition, a small signal of the MXenes is detected, which can be seen from Auger peaks of C, Ti and O. With regard to the information depth of the AES of 3λ, an incipient Fe diffusion can be observed directly by a change in the Fe concentration. After annealing, there is a significant increase in the peak-to-peak amplitudes of the Auger peaks of C, Ti and O while the peak intensity of the Fe peak decreases to 1/3. The resulting decrease in the Fe concentration at the sample surface therefore indicates a diffusion of Fe into the MXenes.

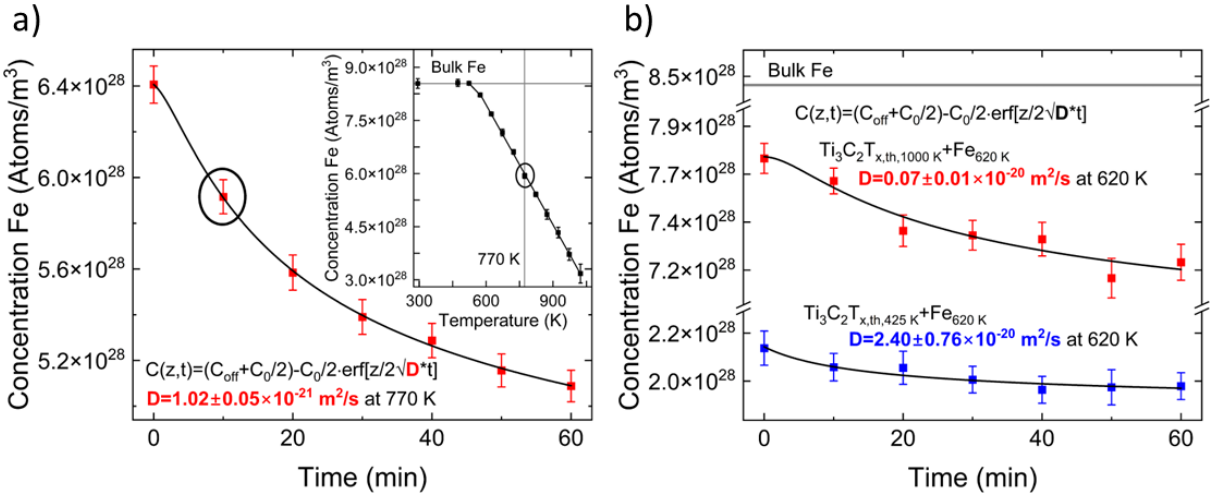

Figure 6.2.: a) Fe concentration during annealing at 770 K of an originally 6 nm thick Fe film on a spin coated MXene sample thermally activated at 1000 K, measured with AES. The decrease in Fe concentration at the sample surface is plotted as a function of annealing time and fitted by a modified form of the Grube-Jedele formula (Equation 6.1), which is a solution for 1D diffusion (Equation 2.13). From a fit the diffusivity of Fe in the MXenes at the given temperature of 770 K can be determined, which results in $D_\perp = 1.02 \pm 0.05 \times 10^{-21}\,\mathrm{m^2/s}$. The inset shows the Fe concentration on the sample surface at different annealing temperatures after an annealing time of 10 min respectively. There is a linear decrease of the Fe concentration as a function of the annealing temperature, as well as an onset of diffusion at about 525 K. b) Fe concentration as function of time determined from AES measurements of an initially 6 nm thick Fe film on the sample surface of a MXene sample thermally activated at 1000 K or 425 K during annealing at 620 K. Fitting with Equation 6.1 results in diffusivities of $D_\perp = 0.07 \pm 0.01 \times 10^{-20}\,\mathrm{m^2/s}$ or $D_\perp = 2.40 \pm 0.76 \times 10^{-20}\,\mathrm{m^2/s}$ and consequently a 35× higher diffusivity for the MXene thermally activated at lower temperature.

rate sample must be prepared for each intercalation state (different annealing temperatures and times) and capped with C as an oxidation protection.

A more efficient way to determine the diffusivities directly is to record *in situ* Auger electron spectra during the annealing of the deposited Fe film on MXenes. This allows the detection of the Fe concentration at the sample surface as a function of annealing time and temperature. Since the vapor pressures of Fe at temperatures of up to 1000 K are only in the range of up to 1.5×10^{-11} mbar [101], a decrease in the measured Fe concentration can only result from a Fe diffusion into MXenes in z-direction considering the information depth of the AES of $3\lambda \approx 5$ nm (see Figure 3.6 b)). In this context, it should be noted that, according to Beer's law, the contribution of Auger electrons to the overall Auger signal decreases exponentially with increasing escape depth. Here, 63.8 % of the detected Auger electrons originate from an escape depth of up to 1 times the inelastic mean free path (IMFP) λ, 86.5 % from up to 2λ and 95.0 % from up to 3λ [136].

Figure 6.1 shows in light green an Auger spectrum of a thermally activated $Ti_3C_2T_{x,th,1000K}$ MXene sample with a 6 nm Fe film deposited on the surface. In addition, the Auger spectrum of the sample after annealing the Fe film at 875 K is shown (dark green dashed line). It can already be seen that the Fe concentration on the sample surface decreases significantly after annealing. Also, there is a small signal of MXenes in the form of Ti, C and O Auger peaks after the deposition of 6 nm Fe. With respect to the information depth of the AES of $3\lambda \approx 5$ nm, this can be explained by the roughness of the Fe film on the MXenes, which leads to variations in the average thickness of the Fe coverage, as well as by free MXenes at sharp edges. Overall, an incipient Fe diffusion can be identified directly by a change in the measured Fe concentration.
As discussed in Chapter 2.3.1, a diffusion process is defined by the change in the concentration of the diffusing material at a certain depth of the sample z with time t. The change in Fe concentration with time is determined in the present case by recording Auger spectra of the Auger peaks of C, Ti, O and Fe after reaching the selected annealing temperature at intervals of 10 min starting at 0 min (reaching the target temperature) for 1 h. The aquisition time per spectrum is 2 min. As described in Chapter 3.3.2 the atomic Fe concentration in the sample can then be determined for each time point of diffusion according to Equation 3.2. The determined atomic Fe concentration before annealing the deposited Fe film is normalized to the concentration of bulk Fe (8.49×10^{28} Atoms/m^3 [137]).
In order to first gain an overview of the temperature at which the diffusion of Fe into the MXenes sets in, the Fe concentration at the sample surface determined after 10 min of annealing at each temperature point is plotted as a function of the annealing temperature, as seen in the inset of Figure 6.2 a). It is evident that the Fe diffusion starts at about 525 K and the Fe concentration decreases linearly with temperature as it progresses. Moreover, Figure 6.2 a) shows the time progression of the Fe concentration, exemplarily for an annealing temperature of 770 K.
As described above, due to the measurement geometry, a decrease in the Fe concentration at the sample surface can only result from a diffusion of the Fe into MXenes in z-direction. For the sake of simplicity, it is also initially assumed that no complicated interdiffusion process takes place. To fit the measured Fe concentrations as a function of the annealing time, a suitable solution of the 1D diffusion Equation 2.13 must therefore be found. Since a residual amount of Fe always remains on the surface of the samples as a reservoir, the solution of Equation 2.13 is given by the Grube-Jedele formula (Equation 2.15), which has already been discussed in Chapter 2.3.1.
The sample depth z, at which the concentration change is measured in the present case, is given by the region between the interface of the Fe film and the MXenes up to the maximum information depth of the AES of $3\lambda \approx 5$ nm. However, the collected AES signal and thus the resulting Fe concentration reflects the sum of Auger electrons up to 3λ. This also includes the surface Fe that acts as a reservoir for diffusion. To take this into account, an additional constant offset factor C_{off} is introduced. The Grube-Jedele formula then takes the modified form

$$C(z,t) = C_{off} + C_0/2 \cdot \mathrm{erfc}\left(\frac{z}{2\sqrt{Dt}}\right). \tag{6.1}$$

A fit to the data shows that Equation 6.1 can adequately describe the measured Fe diffusion as shown in Figure 6.2 a). Here, the correction factor C_{off}, the constant Fe concentration at the surface C_0 and the diffusivity are the fit parameters. For the example of an annealing temperature of 770 K shown in Figure 6.2 a), the diffusivity of Fe perpendicular to the MXene sheets, $D_\perp$, results in $1.02 \pm 0.05 \times 10^{-21}\,\mathrm{m^2/s}$.

Figure 6.2 b) shows the change of the Fe concentration over time at an annealing temperature of 620 K in the case of an MXene sample thermally activated at 1000 K (red) or at 425 K (blue). The resulting diffusivities $D_\perp$ are $0.07 \pm 0.01 \times 10^{-20}\,\mathrm{m^2/s}$ and $2.40 \pm 0.76 \times 10^{-20}\,\mathrm{m^2/s}$. In addition to the diffusivity $D_\perp$, which is a measure of the mobility of the diffusing Fe atoms in the MXenes, the activation energy and the frequency factor are key parameters in the diffusion process. In order to determine these for the Fe diffusion in thermally activated MXenes at 1000 K, the diffusivities $D_\perp$ at different Fe annealing temperatures are determined from fitting the change in Fe concentration over time by Equation 6.1 as demonstrated in Figure 6.2 a) for an annealing temperature of 770 K. The logarithm of the determined diffusivities is then plotted as a function of the inverse annealing temperature (Arrhenius plot). This can be seen in Figure 6.3. In addition, the inset in Figure 6.3 shows $D_\perp$ as a function of the annealing temperature. It can be seen that the data points for annealing temperatures up to 770 K show a linear behavior and are accordingly described by the Arrhenius law (Equation 2.16). A linear fit to the corresponding data points (black) then results in an activation energy of $0.10 \pm 0.01\,\mathrm{eV}$ and a frequency factor of $4.96 \pm 0.54 \times 10^{-21}\,\mathrm{m^2/s}$. At temperatures above 770 K, the data points (orange) in Figure 6.3 deviate from the linear behavior, which indicates a change in the diffusion mechanisms involved (cf. Chapter 2.3.1). Reasons for this are discussed in detail in Chapter 6.2.

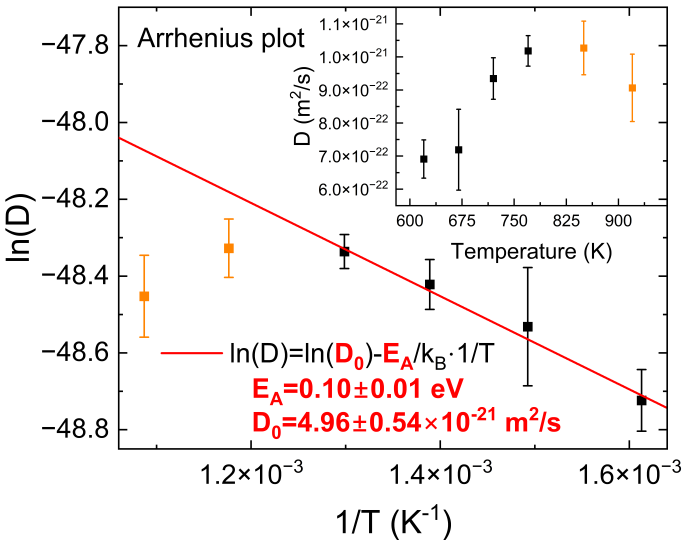

Figure 6.3.: The Arrhenius plot shows the logarithm of the diffusivities determined at different annealing temperatures for the diffusion of Fe in $Ti_3C_2T_{x,th,1000K}$ MXenes as a function of the inverse annealing temperature. The inset shows the respective diffusivities directly as a function of the annealing temperature. The data points in the Arrhenius plot show a linear behavior up to a temperature of 770 K, and accordingly fulfill the Arrhenius law (Equation 2.16). From a linear fit to the data points (black), the activation energy $E_A = 0.10 \pm 0.01\,\mathrm{eV}$ and the frequency factor $D_0 = 4.96 \pm 0.54 \times 10^{-21}\,\mathrm{m^2/s}$ can be determined. For higher temperatures, the data points (orange) show a non-linear behavior which indicates a changing diffusion mechanism.

To conclude, sources of error in the determination of the diffusion parameters by AES measurements of the Fe concentration at the sample surface during its intercalation are discussed.
The lateral resolution of the AES amounts to a few tens of microns [138]. Since the Fe concentration at the sample surface is measured, the diffusion of Fe in the x-y-direction into the area under consideration must be equal to the diffusion out of this area. Only in this case a change in the Fe concentration corresponds to a diffusion in z-direction. Statistically, this is the case if there is no concentration gradient in x-y-direction. This is ensured by the above-mentioned sample geometry and the distance to the evaporation source, which leads to a homogeneous thickness of the deposited Fe layer over the entire sample surface (see Figure A.1 a) in the Appendix). However, concentration gradients in the x-y-direction can occur locally due to the roughness of the sample surface. Considering the size of the MXene sheets of a few μm observed in the SEM (see Figure 4.3 b)) and the topographies of the samples determined from atomic force microscopy (AFM) measurements (see Figure 4.4), it is reasonable to expect, in conjunction with the low lateral resolution of the cylindrical mirror analyzer (CMA) in this context, that these effects balance each other on average.
An apparently decreasing Fe concentration that is not related to diffusion in z-direction of the sample can also occur if the Fe forms clusters on the sample surface upon annealing. In this case the Fe film thickness increases in one sample spot and decreases in the neighbouring sample areas. Here, the resulting decrease of the Auger signal coming from the MXenes in the areas where the clusters form is smaller than the increase in the areas where the Fe layer thickness decreases. This is based on the fact that, according to Beer's law, the contribution of Auger electrons to the overall Auger signal decreases exponentially with the escape depth as described above. Note that for sample areas with Fe thicknesses greater than 3λ, no decrease in Fe concentration can be measured, even if diffusion occurs in the z-direction.
The initial average Fe layer thickness of 6 nm on the MXenes is only slightly above the information depth of the AES of about $3\lambda \approx 5$ nm. Apart from this, the roughness of the Fe film on the MXenes leads to variations in the thickness of the Fe coverage. Therefore, the interface from Fe to the MXenes can be expected at the lower limit of the information depth of the AES (3λ). However, the contribution of Auger electrons from this depth to the overall Auger signal is small, so that the measured change in Fe concentration is also small. As diffusion progresses, the thickness of the Fe film remaining on the surface decreases. Therefore, changes in the measured Fe concentration also stem from smaller escape depths. Since the contribution of the Auger electrons to the overall Auger signal increases exponentially with decreasing escape depth, the measured change in Fe concentration increases in relative terms as the diffusion progresses. This results in an instrumentally caused distortion of the measured change in the Fe concentration as a function of the annealing time.
The discussed effects are a consequence of the exponential decrease of the contribution of Auger electrons to the total Auger signal with increasing escape depth according to Beer's law. The measured Fe concentration curves in Figure 6.2, however, show a change in concentration with

time, described by the Grube-Jedele formula as a solution to Fick's second law of diffusion. Therefore, the influence of both effects on the measured concentration can be classified as small compared to the concentration change caused by the diffusion of Fe in the z-direction of the samples. Errors due to variations in the surface composition as a result of adsorption and absorption of residual gases can also be excluded due to the long monolayer formation times (MFT) of several hours at pressures of 5×10^{-10} mbar in the UHV chamber during the measurements (see Chapter 2.4).

XPS depth profiling

The standard technique to determine the diffusivity of a diffusant in a solid is depth profiling. Here, the sample surface is removed step by step by sputtering, while the element specific concentration is measured at different sample depths, which demands a surface sensitive measuring technique. X-ray photoelectron spectroscopy (XPS) as a measuring tool, using X-rays to generate photoelectrons with energies characteristic of the elements present, makes this possible, as the generated photoelectrons are subject to the inelastic mean free path (IMFP) λ (see Figure 3.6). According to Beer's law, the information depth of XPS is then given by 3λ (typically a few nanometers) [136], while the lateral resolution is in the range of a few micrometers depending on the X-ray beam focus [138].
In this context, the diffusivity of Fe in the MXenes is additionally extracted from XPS depth profiles of the Fe intensity in the samples. This enables a direct comparison of the diffusion parameters derived from AES and XPS. Besides, the depth profiles allow to determine the penetration depth of Fe in the MXenes. Against the background of the observations from the AES analysis, it is then of particular interest to compare the penetration depth of Fe in MXenes that were thermally activated at low or high temperatures of 425 K or 1000 K.
For the *ex situ* recording of depth profiles, first, spin coated MXenes are treated in the UHV chamber (thermal activation, deposition of 6 nm Fe, annealing to intercalate the Fe and capping with C for oxidation protection). The Fe depth profile of a MXene sample, thermally activated at 1000 K and serving as a backup sample at a beam time of another project, is then recorded by XPS measurements at the VUV-photoemission beamline of the Elletra synchrotron light facility using an excitation energy of 830 eV. Since MXene samples thermally activated at a low temperature of 425 K were examined at a later time, the Fe depth profiles for these samples are recorded by a *ULVAC-PHI* 5000 Versaprobe II laboratory XPS using an excitation energy of 1486.6 eV (Al-K_α). In both cases, the measurements are conducted in a UHV chamber in which the sample surface is successively removed by Ar^+ sputtering, while Fe 2p XPS spectra are collected after different sputter times. The Fe intensity after a specific sputter time is then determined from the area under the two spin-orbit split Fe 2p peaks (Fe $2p_{1/2}$ and Fe $2p_{3/2}$). Finally, the sputter time is converted into the sample depth using the sputter rate. The determination of the sputter rates is described in Appendix A.10.
Figure 6.4 shows the measured Fe depth profiles in a) for a $Ti_3C_2T_{x,th,1000K} + Fe_{1000K}$ and in

b) for a $Ti_3C_2T_{x,th,425K}$ + Fe MXene with Fe intercalated at 620 K (700 K) in blue (light blue). In order to obtain the diffusivity of Fe in the MXenes from the respective Fe depth profile, the argument of the error function of the Grube-Jedele formula (Equation 2.15) is plotted as a function of the sample depth, analogous to the work of Stelter et al. (1987) [139] and Sharma et al. (1990) [140]. This can be seen in the insets of Figures 6.4 a) and b). Here, a linear increase of the argument of the error function vs. sample depth can be observed, confirming the ability of the Grube-Jedele formula to describe the diffusion problem at hand. From a linear fit to the data points, the diffusivity D can then be determined from the calculated slope via

$$D = \frac{1}{4 \cdot m^2 \cdot t}, \tag{6.2}$$

where m describes the slope of the linear fit and t the annealing time at the selected Fe annealing temperature. Since the depth profiles reflect the change of the Fe intensity along the z-direction of the samples, the determined diffusivities correspond to $D_\perp$ (diffusion perpendicular to the MXene sheets). Accordingly, a direct comparison with the diffusivities determined from AES can be made. First, however, the penetration depth of Fe into the MXenes for the three considered Fe intercalation states will be discussed.

The $Ti_3C_2T_{x,th,1000K}$ + Fe_{1000K} MXenes in Figure 6.4 a), show a significantly higher Fe intensity up to a sample depth of around 5 nm. This indicates remaining Fe on the sample surface (see Figure A.10 in the Appendix). Once the surface Fe is removed, the intensity decreases with increasing sample depth, as expected for the diffusion of Fe atoms into the MXenes. From a sample depth of 25 nm, the Fe intensity reaches low levels close to the detection limit. It can therefore be deduced that the Fe atoms predominantly diffuse into stacked MXenes up to a sample depth of about 30 nm. However, the first 5 nm of sample depth must be omitted in the analysis, as these are attributed to the Fe remaining on the surface. Thus, a penetration depth of Fe into the MXenes of about 25 nm follows. The "bulbous" shape of the depth profile further suggests that a large part of the Fe diffusing into the MXene stays within the first 7 nm below the sample surface.

Looking next at the depth profiles of Fe in the MXenes thermally activated at temperatures of 425 K in Figure 6.4 b), an initial increase in Fe intensity can be seen here, which reaches its maximum around 8 nm and subsequently decreases with increasing sample depth. The increase in Fe intensity up to 8 nm is attributed to the 8 nm thick C film, which is deposited on the sample for oxidation protection. For the lower Fe intercalation temperature of 620 K (shown in blue), a plateau appears after reaching the sample depth of 8 nm, which indicates remaining Fe at the sample surface. After this Fe has been removed, roughly after reaching a sample depth of 12 nm, the intensity of Fe decreases down to a sample depth of about 40 nm, indicating the Fe intercalation depth into the MXenes. If the first 12 nm of sample depth are omitted from from further analysis, a penetration depth of Fe into the MXenes of about 28 nm results. Note that despite the significantly lower Fe intercalation temperature, this penetration depth is 12 % larger

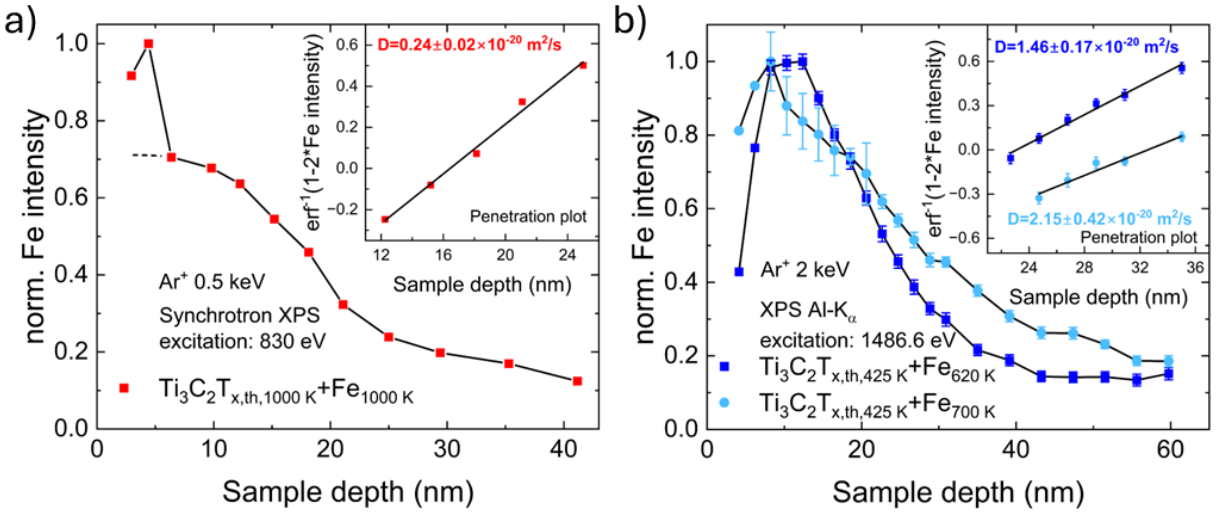

Figure 6.4.: a) Fe depth profile for a $Ti_3C_2T_{x,th,1000K} + Fe_{1000K}$ MXene sample [141]. The decreasing Fe intensity from a sample depth of about 5 nm reflects the Fe intercalated into the MXene with a penetration depth of about 25 nm. Moreover, the "bulbous" shape of the depth profile indicates that a large part of the intercalated Fe stays within the first 7 nm below the sample surface. The inset shows the argument of the error function of the Grube-Jedele formula as a function of sample depth. From a linear fit to the data points, the diffusivity of Fe in the MXenes can be determined via Equation 6.2, which results in $D_\perp = 0.24 \pm 0.02 \times 10^{-20}\,m^2/s$. b) Normalized Fe intensity as a function of sample depth for a $Ti_3C_2T_{x,th,425K} + Fe$ MXene with Fe intercalated at temperatures of 620 K (blue) and 700 K (light blue) [142]. The decreasing Fe concentration starting between 8 nm and 12 nm reflects the Fe intercalated into the MXenes with penetration depths of 28 nm or 47 nm in case of the $Ti_3C_2T_{x,th,425K} + Fe_{620K}$ or $Ti_3C_2T_{x,th,425K} + Fe_{700K}$ MXene sample. The inset shows the argument of the error function of the Grube-Jedele formula as a function of sample depth for the two samples. A linear fit to the data points leads to diffusivities of $D_\perp = 1.46 \pm 0.17 \times 10^{-20}\,m^2/s$ and $D_\perp = 2.15 \pm 0.42 \times 10^{-20}\,m^2/s$, respectively.

than for MXenes thermally activated at 1000 K. For the higher Fe intercalation temperature of 700 K (shown in light blue), no remaining Fe can be identified on the sample surface. In addition, a decrease in Fe intensity can be observed here up to a sample depth of about 55 nm. Omitting the first 8 nm of sample depth attributed to the C film on the sample surface results in a penetration depth of Fe into the MXenes of about 47 nm. This corresponds to almost twice the penetration depth observed for the $Ti_3C_2T_{x,th,1000K} + Fe_{1000K}$ MXenes. Here, neither the blue nor the light blue depth profile shows the "bulge" observed for the depth profile in Figure 6.4 a), which indicates that larger amounts of Fe also diffuse deep in the sample.

Finally, the calculated diffusivities show that, as observed in the AES study, a significantly higher diffusivity of Fe in the MXenes thermally activated at 425 K is evident (see insets in Figure 6.4). A comparison of the absolute values of the diffusivities shows that for the MXenes thermally activated at 1000 K the diffusivity determined from the depth profile is about 2 times

higher than the diffusivities observed from AES measurements for Fe intercalation temperatures between 900 K and 1000 K. In the case of the $Ti_3C_2T_{x,th,425K} + Fe_{620K}$ MXenes, Fe shows a diffusivity of $D_\perp = 1.46 \pm 0.17 \times 10^{-20}\,m^2/s$ according to the depth profile, while from the AES study a diffusivity of $D_\perp = 2.40 \pm 0.76 \times 10^{-20}\,m^2/s$ emerges. The latter is thus around 60 % larger. However, the standard deviations given for the diffusivities do not take into account the additional sources of error discussed in connection with the AES study and the error introduced from the calculated sputter rate (see Appendix A). Here, the error of the sputter rate has a direct effect on the resulting diffusivity when it is determined from Equation 6.2. Against the background of the these errors, the established depth profile analysis and and the newly introduced AES analysis show a high and convincing agreement of the measured diffusivities. Also note that with both methods a significantly higher diffusivity is observed for the samples thermally activated at 425 K compared to those thermally activated at 1000 K.
It can therefore be concluded, that the *in situ* determination of diffusivities from the measured change in Fe concentration at the sample surface using AES is a suitable, faster and more flexible alternative to the established method of determining diffusivities from depth profiles.

STEM-EDS cross section analysis

In addition to AES and XPS, it is also possible to investigate the diffusion of Fe in the MXenes using scanning transmision electron microscopy together with energy-dispersive X-ray spectroscopy (STEM-EDS). As mentioned above, AES and XPS measure the Fe intensity at the sample surface with a lateral resolution of micrometers. Fe depth profiles can be recorded here by alternately ablating the surface (sputtering) and recording the Fe intensity. Both methods therefore represent integral measurement techniques. In TEM, on the other hand, the sample cross sections deliver local information of the Fe distribution after intercalation. By means of STEM-EDS, the distribution of Fe in the MXenes can be determined directly along the sample cross section. Here, the investigation of small areas of a few square nanometers is possible. This allows a local analysis of the diffusion behavior and diffusivities of Fe in the MXenes. STEM-EDS measurements are performed in this context using a *JEOL* JEM-2200FS C_s-corrected STEM device operated at 200 kV. In conjunction with an *Oxford Instruments* EDS detector (X-MaxN 80 TLE), the possible resolution lies in the sub-nanometer range (manufacturer's specification).
Figure 6.5 shows STEM-EDS images at different positions of the sample cross section of a $Ti_3C_2T_{x,th,1000K} + Fe_{700K}$ MXene. For all sample positions shown, the stacking of the MXene sheets can be recognized. The STEM-EDS maps also illustrates the distribution of the Fe with respect to the Ti of the MXene sheets. This reveals, for example, the Fe film deposited on the sample surface as well as the concentration gradient of the Fe that diffused into the MXenes. For a quantitative analysis, the concentration in atomic percent of Fe and Ti is extracted from a selected area of the STEM-EDS maps using the software *AZtec* (Oxford Instruments). From this, the diffusivities of Fe can be determined analogously to the previous section by means of a penetration plot. As the atomic Fe concentration is significantly lower than the atomic Ti

concentration for some sample areas, both are normalized to 1 for a better comparison.
The first sample site examined (Figure 6.5 a)) shows an abrupt drop in Fe intensity along a sharp line. This is confirmed by looking at the concentration profiles of Fe and Ti in Figure 6.5 b), extracted from the white framed area in Figure 6.5 a). It can be seen here that the 6 nm Fe film is still present at the sample surface and Fe diffusion has only taken place up to a sample depth of about 13 nm at tiny amounts. Beyond this depth, the Fe concentration is zero. The penetration depth of Fe into the MXene, when omitting the thickness of the Fe film on the surface is therefore about 7 nm at this sample position. If the normalized Fe concentration is plotted in a penetration plot, analogous to the previous section, a linear behavior follows (see inset in Figure 6.5 b)), which also locally confirms the validity of the Grube-Jedele formula for describing diffusion. From the slope of a linear fit to the data points in the penetration plot, a diffusivity of Fe in MXenes of $D_\perp = 7.42 \pm 1.38 \times 10^{-22}\,\mathrm{m}^2/\mathrm{s}$ results using Equation 6.2.
In contrast to the area shown in Figure 6.5 a), no abrupt drop in the Fe concentration can be observed for the second sample spot considered, shown in Figure 6.5 c). Looking at the corresponding concentration profile of Fe and Ti in Figure 6.5 d), a normalized Ti concentration different from 0 is visible at a sample depth of 0 nm. Together with the high-angle annular dark-field (HAADF)-STEM imaging in Figure 6.5 c), it can be identified that the sample region from which the Fe and Ti concentration is extracted (white framed area) is adjacent to the remaining Fe film on the sample surface at the upper left corner. However, as the sample is slightly tilted with respect to the area investigated with EDS, there is a small distortion of the extracted Fe and Ti concentration as a function of sample depth, which is observed as a non-zero Ti concentration at 0 nm. With respect of the tilting angle it can be derived that the penetration depth of Fe into the MXene is about 2 nm smaller than the point where the Fe concentration drops to zero. Consequently, a penetration depth of about 13 nm can be established here. This corresponds to almost twice the penetration depth of Fe with respect to the sample site examined in Figure 6.5 a). The slope of the linear fit to the data points in the penetration plot in Figure 6.5 d) is not significantly influenced by the effects described before, which is why it is also reasonable to determine the diffusivity at this sample position. This results in $D_\perp = 9.89 \pm 2.36 \times 10^{-22}\,\mathrm{m}^2/\mathrm{s}$ and is about 30 % higher than the diffusivity identified for the sample site in Figure 6.5 a).
The third sample position considered is shown in Figure 6.5 e). Here, the Fe can diffuse into the MXenes along an approximately 10 nm wide passage. In the area to the right of this passage, the diffusion stops at a sharp line, analogous to the case shown in Figure 6.5 a), where Fe remains mainly on the sample surface. Looking at the Fe and Ti concentration profile along the passage in Figure 6.5 f), it is noticeable that the normalized Ti concentration here as well is non-zero at a sample depth of 0 nm. However, since the Ti concentration at 0 nm is only about 12 %, it can be deduced that the area from which the Fe and Ti concentrations is extracted (white framed area) is just below the sample surface. The penetration depth of the Fe into the MXenes is therefore at least 30 nm. The diffusivity at this sample position amounts to $D_\perp = 2.83 \pm 0.43 \times 10^{-21}\,\mathrm{m}^2/\mathrm{s}$ and is thus 4 times higher than at the sample position from Figure 6.5 a).

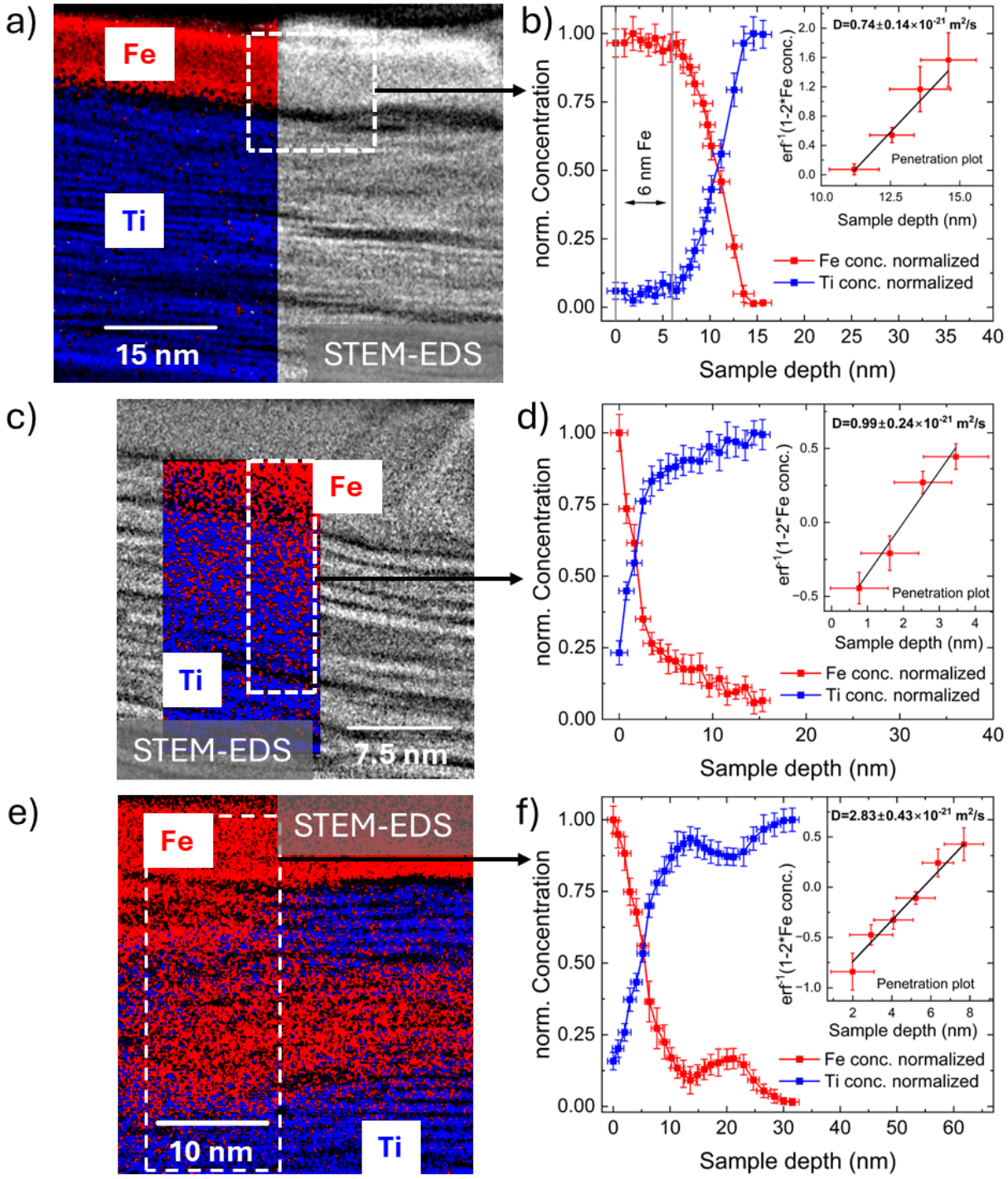

Figure 6.5.: a),c),e) STEM-EDS images of the sample cross section of a $Ti_3C_2T_{x,th,1000K} + Fe_{700K}$ MXene at different sample spots. The layered structure of the MXene sheets can be seen from the HAADF-STEM imaging, as well as the Ti and Fe distribution along the cross section from the STEM-EDS maps. b),d),f) Normalized atomic concentration of Fe and Ti, extracted from the white framed areas of the corresponding STEM-EDS maps, as a function of sample depth. The insets show the penetration plots from which the diffusivity in the corresponding sample region is determined analogously to the previous section.

Summarizing the observations from a single sample, there are areas in which the penetration depth of Fe and its diffusivity in the MXenes is significantly lower than in others. Together with the STEM-EDS images, it apparent that the MXene sheets act as barriers to the diffusing Fe atoms, so that diffusion through the layers can be excluded. Thus, diffusion in z-direction can only take place at the perimeter/rim of MXene sheets, as discussed in Chapter 2.3.2. For the position in Figure 6.5 a), one can then assume a continuous MXene sheet, which prevents diffusion into the specimen. For the case shown in Figure 6.5 c), multiple rims of adjoining MXene sheets are considered allowing a diffusion around the sheets into the sample. In the case of Figure 6.5 e), it is likely that two stacks of MXene sheets are adjoining and thus several edges of MXene sheets are located directly below each other, opening up a high diffusivity path for Fe in z-direction. The high diffusivity path ends when the edges of the MXene sheets are no longer positioned underneath each other. Then the diffusion of Fe is stopped at a continuous MXene sheet or a slower diffusion occurs around sheets, as described for the sample site in Figure 6.5 c). This causes the Fe to spread mainly in x-y-directions.
The mean value of the diffusivities $D_\perp$ determined for the three sample positions results in $D_\perp = 1.52 \pm 0.27 \times 10^{-21}\,\mathrm{m^2/s}$. The latter is shown together with the diffusivities of Fe in the spin coated MXene samples obtained from the XPS and AES study in Table 6.1. Although the

Table 6.1.: Collected diffusivities of Fe in spin coated $Ti_3C_2T_x$ MXene samples, for different thermal activation temperatures of 425 K and 1000 K and various Fe intercalation temperatures. The diffusivities are assigned to the respective measurement method (AES, XPS or STEM-EDS) used to determine them.

	Diffusivity $\left(\mathrm{m^2/s}\right)$		
Sample	AES	XPS	STEM-EDS
$Ti_3C_2T_{x,425K}$+Fe_{620K}	$2.40 \pm 0.76 \times 10^{-20}$	$1.46 \pm 0.17 \times 10^{-20}$	---
$Ti_3C_2T_{x,425K}$+Fe_{700K}	---	$2.15 \pm 0.42 \times 10^{-20}$	---
$Ti_3C_2T_{x,1000K}$+Fe_{700K}	$0.09 \pm 0.01 \times 10^{-20}$	---	$0.15 \pm 0.03 \times 10^{-20}$
$Ti_3C_2T_{x,1000K}$+Fe_{850K}	$0.10 \pm 0.01 \times 10^{-20}$	---	---
$Ti_3C_2T_{x,1000K}$+Fe_{1000K}	---	$0.24 \pm 0.02 \times 10^{-20}$	---

diffusivities were not determined for all thermal activation and Fe intercalation temperatures with each of the three measurement methods, for MXenes thermally activated at 1000 K the values acquired are sufficient for a comparison. Since there is no significant increase in diffusivities above Fe intercalation temperatures of 700 K anymore (see Figure 6.3), the diffusivities at temperatures from 700 K to 1000 K are best suited to be compared. Here, one finds that the average diffusivity determined by STEM-EDS is larger by 50 % than the diffusivity obtained from the AES study and about 40 % smaller than the diffusivity observed from XPS depth profiles. This demonstrates that the local measurements of the diffusivities at 3 different positions using STEM-EDS reflect the scenarios not accessible with the integral measurement techniques. Table 6.1 also clearly illustrates that the diffusivities of Fe in the MXenes thermally activated at 425 K are many times higher than those observed for MXenes thermally activated at 1000 K.

For the STEM-EDS analysis, it should be noted that the thickness of the sample cross section of the MXene samples is 100 nm (see Chapter 4.5). Here, the EDS measurements result in the accumulated Fe or Ti concentration for the entire thickness of the sample cross section. At the same time, however, the HAADF-STEM imaging does not allow any conclusion to be drawn as to the depth (from 0 nm to 100 nm in the transmission direction of the electron beam of the STEM) at which the observed MXene layers are located. Accordingly, for the case shown in Figure 6.5 e), for example, no precise statement can be made as to whether the Fe diffuses into/between the MXenes or forms a cluster in a void. This is addressed in more detail in the following Chapter 6.2 by developing a qualitative diffusion model based on the findings on Fe diffusion in MXenes from AES, XPS and STEM-EDS measurements.

6.2. Formulation of a diffusion model

Based on the findings from Chapter 6.1, a qualitative diffusion model is drafted to describe the diffusion and distribution of Fe in the $Ti_3C_2T_x$ MXenes.
Starting with the diffusivities, frequency factors and activation energies for the diffusion of Fe in MXenes, it can be seen that these are small compared to values typically observed for the diffusion in metals and alloys. As outlined in Chapter 2.3.1, the activation energies here are in the range of 1 eV to 6 eV while frequency factors of around $1 \times 10^{-5}\,m^2/s$ are observed. Moreover, as shown in Figure 2.5 a), diffusivities in the order of $5 \times 10^{-6}\,m^2/s$ have been reported for self-diffusion and diffusion of impurities in metals. Thus, the experimentally determined frequency factor and diffusivities for Fe in MXenes are about 14-15 orders of magnitude smaller. At the same time, the activation energy of 0.10 ± 0.01 eV is one order of magnitude smaller and lies, e.g., in the range of the activation energy of 0.17 eV, which is observed for the diffusion of Cu around graphene sheets [89]. This emphasizes a behavior as discussed in Chapter 2.3.2 for the diffusion of atoms around 2D sheets. In this model, the Fe must cover a distance parallel to the sheets which, with a diameter of the MXene sheets of roughly 1 μm (cf. Chapter 4.2), is about 3 orders of magnitude greater than it can diffuse at the rims of a sheet in the z-direction (about 1 nm, cf. Chapter 5.2). The result is a much slower diffusion perpendicular to the sheets with small activation energies for diffusion at the same time. Note that for the same width between adjacent and stacked MXene sheets, the same activation energy for diffusion in the x-y-z-directions is expected.
At this point, it is important to reconsider the arrangement of MXene sheets on $Si(100)/SiO_2$ substrates. As described in Chapter 4.2 and 4.3, MXenes are applied to the substrates as an aqueous suspension or as MXenes dispersed in isopropanol. In both cases MXenes are present as single sheets as well as stacks of MXene sheets due to the vdW forces and hydrogen bond interactions [143]. If the MXene suspension is applied to the substrates by spin or spray coating, it can be expected that the stacks of MXene sheets arrange themselves like building blocks on top of each other on the substrate. In addition, a stacking of single sheets occurs on the substrates.

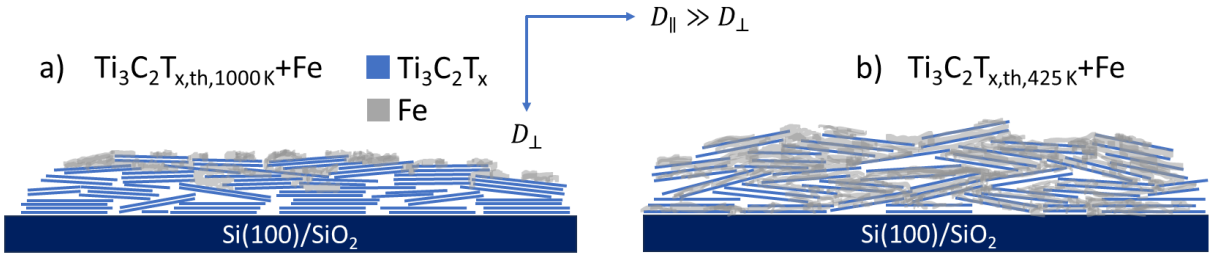

Figure 6.6.: a) Schematic arrangement of stacks of several MXene sheets (blue) on a Si(100)/SiO_2 substrate (dark blue) after thermal activation of the MXenes in UHV at 1000 K. The stacks of MXene sheets lie on top of each other like bricks, which results in gaps between them as well as some tilting of individual stacks. The interplanar distances between the individual sheets of a stack are reduced here due to thermal activation (see Chapter 5.2). For this reason, diffusion of Fe (gray) is expected in the near-surface voids between the stacks of MXene sheets, but not in between the MXene sheets. b) Schematic arrangement of stacks of MXene sheets on a Si(100)/SiO_2 substrate in the case of MXenes thermally activated at 425 K. Here, the interplanar distances between the individual MXene sheets are larger compared to the case from a) (see Chapter 5.2). This results in greater stacking heights for the same number of MXene sheets per stack. Following this, larger gaps between stacks of MXene sheets and an increased tilting of individual stacks from the horizontal are expected. Consequently, the Fe is presumed to penetrate deeper into the samples and, as a result of the larger interplanar spacing, to diffuse in between the MXene sheets.

The stacks of MXene sheets can also be identified from the atomic force microscopy (AFM) and scanning electron microscopy (SEM) images in Figure 4.6 b) and A.4. As the lateral expansion of the MXene layers is in the range of a few micrometers (see Chapter 4.2), the stacking heights of the MXenes are expected to be 2-3 orders of magnitude smaller. This leads to the largely observed horizontal alignment of the MXenes on the substrates. In addition, it is reasonable to assume that voids form between the stacks of MXene sheets. In Figure 6.6 a), a possible arrangement of the stacks of MXene sheets on a substrate is schematically shown.

It is not clear from the collected data whether the Fe diffuses around individual MXene sheets or around the stacks of several MXene sheets. However, it is likely that the spaces between the stacks of MXene sheets offer significantly more space for the diffusing Fe atoms than the spaces between the individual MXene layers. Therefore, diffusion around the stacks of MXene sheets is preferred as a low activation energy for diffusion is experimentally determined. Note that this is not in conflict with the observed slow diffusion perpendicular to the MXene sheets, since the lateral expansion of the MXene sheets is expected to be still 2-3 orders of magnitude higher compared to the stacking heights.

In the following, two cases are distinguished: MXenes thermally activated at high temperatures of 1000 K and MXenes thermally activated at low temperatures of 425 K. In Chapter 5.2 it was discussed that thermal activation at 1000 K leads to an up to 30 % smaller interplanar distance compared to thermal activation at 425 K. Consequently, a similar number of MXene layers

stacked on top of each other results in lower stack heights. This leads to smaller voids between the stacks and less misorientation of MXenes from the horizontal alignment. In other words, the stacks of MXene sheets are more tightly packed. The opposite is the case for the thermal activation MXenes at 425 K. The schematic arrangement of the stacks of MXene sheets on the substrate according to this model in the case of a MXene thermally activated at 1000 K and a MXene thermally activated at 425 K can be compared in Figure 6.6.

First Fe diffusion in the case of MXenes thermally activated at 1000 K is considered. Diffusion of the Fe into voids between stacks of MXene sheets is initially expected here due to the lower activation energy required for this process. A possible onset of diffusion between individual MXene layers should then be characterized by a second higher activation energy. According to Equation 2.17, a larger activation energy results from a larger slope of the logarithm of the diffusivity ($ln(D)$) vs. the inverse temperature ($1/T$) in the Arrhenius plot. In the present case, this would be attributed to the fact that an additional diffusion between the individual MXene sheets increases the mobility of the Fe atoms, which by definition leads to higher diffusivities and thus to a non linear upward curvature of $ln(D)$ in the Arrhenius diagram towards higher temperatures. One can understand this in analogy to the Arrhenius plot for a polycrystalline sample in Figure 2.5 b), where volume diffusion is observed in addition to grain boundary diffusion at elevated temperatures. Looking at the Arrhenius plot with the experimentally determined diffusivities of Fe in $Ti_3C_2T_{x,th,1000K}$ MXenes in Figure 6.3, initially a linear behavior of $ln(D)$ vs. $1/T$ up to 800 K is found. The resulting slope from a linear fit to the data leads to an activation energy of 0.10 ± 0.01 eV which, for the reasons discussed, is assigned to the diffusion of Fe into voids between stacks of MXene sheets. Above this temperature, however, the slope of the course of $ln(D)$ vs. $1/T$ decreases. Consequently, no second higher activation energy describing diffusion between individual MXene sheets can be identified. Instead, the diffusivities decrease with increasing temperature. This indicates that Fe is "blocked" from diffusing further into the MXenes from a certain depth, as also observed from the STEM-EDS images (see Figure 6.5 a)).

The observations therefore support the hypothesis that the Fe only diffuses into the voids between the MXene stacks, but not between the individual MXene layers. Furthermore, the described blocking of diffusion indicates that the Fe can only diffuse into the surface near voids. This is confirmed by looking at the Fe depth profile in Figure 6.4 a), which has a bulbous shape indicating that most of Fe stays within the first 7 nm below the sample surface after intercalation. The hypothesis of Fe diffusing into the surface near voids but not in between the MXene sheets is also supported when looking at the STEM-EDS images from Figure 6.5 a) and e). For the case in a), a stack of MXene sheets in a region far from the edges of the sheets is investigated. Here, a diffusion of Fe atoms into the sample is blocked by the continuous MXene layers, causing the sharp interface between Fe and Ti. If the Fe would diffuse around/between individual MXene sheets, a diffusion of Fe atoms into the observed sample region from the left and right should be found. In this case, no sharp drop of the Fe intensity would be observed. The sample position shown in Figure 6.5 e) allows the conclusion that a location is imaged where the Fe diffuses from

between two stacks of MXene sheets into an underlying void. This can be explained in particular by the fact that the Fe after it diffused in z-direction primarily spreads to the right, but not to the left. For the MXenes thermally activated at 1000 K, it can be summarized that the Fe largely diffuses into surface near voids between the stacks of MXene sheets and forms clusters there. This is also shown schematically in Figure 6.6 a). The remaining Fe forms clusters on the surface as can be seen from Figure A.10 in the Appendix.
Compared to MXenes thermally activated at 1000 K, up to 35 times higher diffusivities and 2 times larger penetration depths of Fe into MXenes were observed for the MXenes thermally activated at 425 K (see Figure 6.2 b) and 6.4). As mentioned earlier, the 30 % larger interplanar distance here leads to 30 % larger stack heights of MXene stacks compared to those in a MXene thermally activated at 1000 K (for the same number of MXene sheets per stack). In the arrangement of several stacks of MXene sheets on a substrate as sketched in Figure 6.6, this leads to larger voids between the stacks and greater misorientations of the stacks from the horizontal alignment. The deviations from the horizontal orientation cause the effective distance that the Fe atoms must travel in the horizontal direction to diffuse at the edge of a sheet/stack in the z-direction to become smaller, and at the same time enable diffusion in the z-direction when moving parallel to the surface of the MXene sheets. As a result, the diffusivity in z-direction can be significantly increased [144]. Together with the larger voids between the MXene stacks, this can explain the observed higher diffusivities in the z-direction compared to the MXenes thermally activated at 1000 K.
However, it is not clear whether a diffusion of Fe in between the MXene sheets occurs for the MXenes thermally activated at 425 K. Looking at the STEM-EDS image in Figure 6.5 c), the concentration gradient of Fe suggests a diffusion of Fe atoms around the MXene sheets as discussed in Chapter 6.1. Thus, diffusion of Fe between the MXene sheets can occur even in MXenes thermally activated at 1000 K, although diffusion into the near-surface voids dominates. However, this implies an increased probability for the occurrence of Fe diffusion in between MXene sheets for MXenes thermally activated at 425 K. This is due to the larger interplanar spacing which results in a lower activation energy for a diffusion between sheets (cf. Chapter 2.3). The surface terminations that largely remain after thermal activation at 425 K may also have an influence on the diffusion behavior of Fe between the sheets, as discussed in Chapter 7.1. Overall, a diffusion of Fe into voids between the MXene stacks as well as between individual MXene sheets is therefore considered likely for the MXenes thermally activated at low temperatures (425 K), as also sketched in Figure 6.6 b).
For further analysis of the location and chemical state of the intercalated Fe atoms in the MXene samples, polarized X-ray absorption near edge structure (XANES) spectra are recorded at the Ti and Fe K-edge. The X-ray linear dichroism (XLD) measured in this context provides informations about the local structural environment of intercalated Fe atoms. Results and details of these measurements are discussed in Chapter 7.1.

6.3. Correlation of electrical resistivity and Fe diffusion

With the previously discussed methods applied to measure the diffusion of Fe in $Ti_3C_2T_x$ MXenes, the diffusion parameters and, based on these, a diffusion model has been developed. The latter can be used to achieve a desired Fe intercalation state by selecting the appropriate annealing times and temperatures. However, monitoring the actual intercalation state *in situ* is not possible. Therefore, a further measurement technique is needed that fulfills this task.
Electrical transport measurements on the MXenes during Fe intercalation are particularly useful here. In this context, the underlying hypothesis is that the diffusion of Fe into MXenes increases the conductivity between the MXene sheets or stacks of MXene sheets. Furthermore, the resistivity of the MXene samples depends significantly on the surface terminations as also investigated by Hart et al. (2019) [18]. This is a great advantage because, in addition to the change in resistivity due to Fe intercalation, changes in the composition of the existing surface terminations T_x can be observed. Another important aspect is that this measurement technique does not lead to any electrical alteration/destruction of the sample.
As explained in the previous chapter, especially for MXene samples thermally activated at low temperatures of 425 K, a diffusion of Fe between MXene sheets is expected. In this case, however, the initial surface terminations and intercalated water between the layers, as seen in Chapter 5.1, are still present. The Fe diffusion starts at about 525 K as seen in Figure 6.2 a). The surface terminations and water are removed starting from about 625 K as discussed in Chapter 5.1. This allows the conclusion that Fe diffuses between the MXene sheets when most of the terminations and water are still present, as these provide the necessary larger interplanar distance not present in the samples thermally activated at 1000 K (cf. Chapter 5.2). However, temperatures between 525 K and 625 K are not yet sufficient to accomplish binding of Fe, located between the MXene layers, to termination-free Ti atoms of MXene sheets, as this can only be enabled by removing the surface terminations at temperatures above 625 K. On the other hand, this means that a thermal activation at 1000 K is not desirable and that it is more favorable to achieve a binding of Fe to Ti atoms of the MXene sheets by removing the surface terminations and water during Fe intercalation. To test this hypothesis, the transport measurements on the samples during Fe intercalation offer a good opportunity, as changes in resistivity are expected due to Fe diffusing into the MXenes, and a removal of surface terminations at higher temperatures.
Electrical transport measurements on MXenes during the intercalation of Fe are carried out in a high vacuum (HV) chamber with a base pressure of 1×10^{-7} mbar, as for technical reasons no electrical transport measurements can be carried out with the sample heater in the ultra high vacuum (UHV) chamber yet. Spray coated MXenes on $Si(100)/SiO_2$ substrates with a lithographic structure are used for the transport measurements (see Chapter 4.4). In the UHV chamber, a 6 nm Fe film is then deposited on the MXenes after thermally activating them at different temperatures. Subsequently the samples are covered with a 7 nm C film for the transfer to the HV chamber. A mask ensures that the Fe and C film is only applied to the area of spray coated

MXenes marked in green in Figure 4.7. The thickness of MXenes on the substrates is approximately 100 ± 30 nm as determined via atomic force microscopy (AFM) measurements analog to Chapter 4.3. A closed, maximally thin coverage of MXenes is crucial here, as this allows a higher ratio of Fe to MXenes to be achieved. This is then expected to lead to a stronger influence of Fe on the resistivity. The sample holder installed in the HV chamber is specially designed for the requirements at hand and can be seen in Figure A.12 a) in the Appendix. A heating element ensures that the samples can be heated up to temperatures of 800 K. For technical reasons, the temperature is not measured via the lithographic structure as described in Chapter 4.4, but by means of a K-type thermocouple placed between the heating element and the sample. Parallel to heating, the contact pins of the sample holder enable electrical transport measurements. The arrangement of the measuring pins of the sample holder is selected so that they press on the 4 Pt contact pads of the lithographic structure on the substrates (cf. Figure 4.7).
For the electrical transport measurements, a current of 1 mA is applied to the two outer contacts while the voltage between the two inner contacts is measured. The electrical resistivity ρ can then be determined according to [145]:

$$\rho = G \cdot \frac{U}{I} \cdot t. \tag{6.3}$$

Here, U describes the measured voltage, I the applied current, t the thickness of the sample and G the geometric correction factor. The geometric correction factor for the lithographic structure's four probe in line measurement geometry (see Figure 4.7) results in

$$G = \frac{1}{2} \cdot \frac{\pi}{ln(2)} \cdot R\left(\frac{a}{b}, \frac{b}{s}\right), \tag{6.4}$$

where a and b are the edge lengths of the rectangular area of the spray coated MXenes and s is the distance between the contacts [145]. R results according to the work of Topsoe (1968) [145] in the present case with $a = 8.5$ mm, $b = 6$ mm and $s = 1.5$ mm (see Figure 4.7) in 0.69 and thus G in 1.56.
As discussed in Chapter 2.1.2, MXenes can exhibit metallic or semiconducting properties. Looking at the works of Hart et al. (2019) [18] and Halim et al. (2014) [45], $Ti_3C_2T_x$ MXenes show metallic behavior in the temperature range from 100 K to 1000 K. This can be observed in the presence of surface terminations and intercalated water as well as after their removal. However, with ongoing removal of the terminations and water, the overall resistivity decreases. The counter-effect was investigated by Römer et al. (2017) [43] for $Ti_3C_2T_x$ MXenes, where a 26-fold higher resistance was observed when the samples were removed from high vacuum and exposed to a relative humidity of 80 % at ambient pressure.
Figure A.12 b) in the Appendix illustrates that the $Ti_3C_2T_x$ MXenes used in this work show the expected metallic behavior. At low temperatures of a few 10 K, however, an increase in resistivity can be observed. This can be explained by weak localization, as also described in the work of

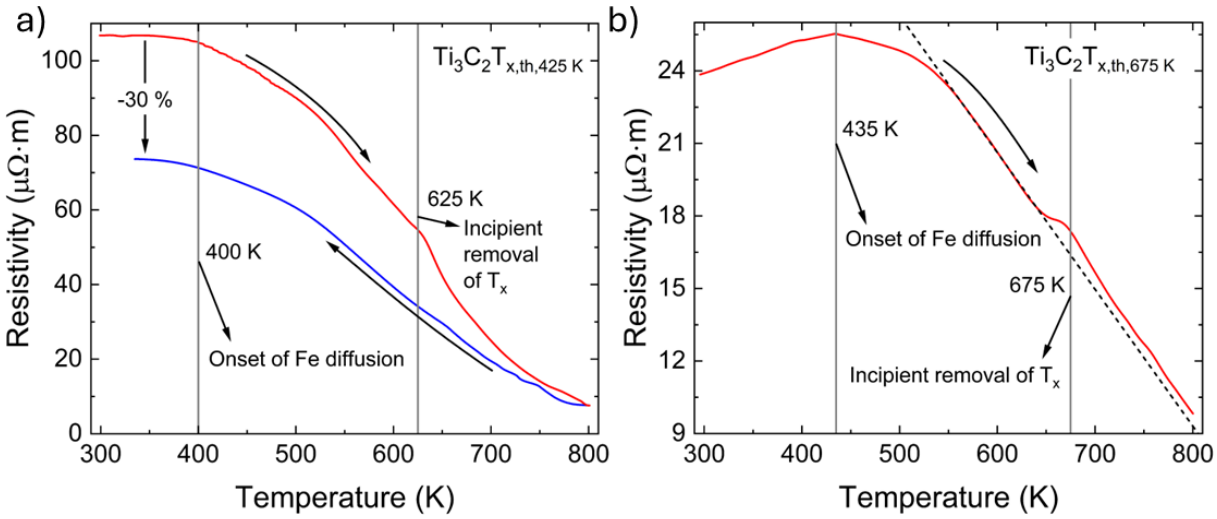

Figure 6.7.: a) Resistivity as a function of temperature of $Ti_3C_2T_x$ MXenes thermally activated at 425 K. Initially there is a 6 nm thick Fe film deposited on the MXenes which is covered by 7 nm C. Annealing of the sample leads to a diffusion of Fe into the MXenes starting at about 400 K as indicated by the decreasing resistivity. At temperatures of 625 K, an additional removal of surface terminations and intercalated water sets in, as evident from the larger negative slope of the resistivity. Cooling the sample down from 800 K to RT results in an increasing resistivity. This is attributed to thermally activated electron range hopping across the intercalated Fe atoms, which decreases as the thermal energy decreases when cooling the sample. Also a 30 % lower resistivity is observed after cooling back down to RT, which is attributed to the intercalation of Fe and the removal of surface terminations and intercalated water. b) Resistivity as a function of annealing temperature analogous to a) for a MXene thermally activated at 675 K. Until the onset of Fe diffusion at 425 K, the metallic behavior expected for $Ti_3C_2T_x$ MXenes is observed. The onset of Fe diffusion then leads to a decrease in resistivity with increasing temperature. At 675 K the remaing surface terminations and water are removed as evident from the slope change of the resistivity (compared to black dotted line). This seems reasonable in view of the thermal activation of the sample at 675 K.

Halim et al. (2014) [45]. When intercalating Fe into the sample, the described metallic behavior is maintained while the overall resistivity decreases (see Figure A.12 b) in the Appendix).
Comparing the resistivities presented in Figure 6.7 a) and b) for MXenes thermally activated at 425 K and 675 K, respectively, a 4 times higher resistivity is observed at room temperature (RT) for the lower thermal activation of 425 K. From Figure 5.1, it evident that in the case of MXenes thermally activated at 675 K, part of the surface terminations and water have already been removed, unlike for MXenes thermally activated at 425 K. This is consistent with the observation by Hart et al. (2019) [18] of reduced resistivity with the removal of surface terminations. Looking at the temperature dependance of the resistivity during heating from 300 K to 800 K in Figure 6.7, a decrease in resistivity with increasing temperature can be seen. This behavior was also observed in the work of Hart et al. (2019) [18] and was attributed to the removal of

the surface terminations and water. As seen in Chapter 5.1, however, a removal of the surface terminations is only expected from about 625 K. Yet, for the cases shown in Figure 6.7 a) or b), the resistivity starts to decrease at 400 K or 425 K respectively. This is explained by the onset of Fe diffusion into the samples. However, these temperatures deviate by about 100 K downwards from the observed temperature of 525 K for the onset of Fe diffusion in $Ti_3C_2T_{x,th,1000K}$ MXenes thermally activated at 1000 K (see Figure 6.2 a)). This is explained by larger voids between stacks of MXene sheets and larger interplanar distances between the sheets observed for lower thermal activation (cf. Chapter 5.2 and 6.2). In this context, a smaller activation energy and consequently a lower temperature for the onset of Fe diffusion is likely (cf. Chapter 2.3.1).
For the MXene thermally activated at 425 K shown in Figure 6.7 a), the negative slope of the resistivity increases with increasing temperature starting from 625 K. This corresponds exactly to the expected temperature for the removal of the surface terminations. For the MXenes thermally activated at 675 K, this change appears at a temperature of 675 K (see Figure 6.7 b)). This seems reasonable, as removal of the surface terminations up to this temperature already took place in the UHV chamber. The removal of the surface terminations is therefore continued where it was stopped. The change in slope is significantly smaller than for the MXene in Figure 6.7 a), which indicates that a certain amount of the surface terminations and intercalated water from between the sheets were already removed in the UHV chamber.
Cooling the samples back down to 300 K after reaching 800 K leads to an increase in resistivity with decreasing temperature as seen in Figure 6.7 a). It should be noted at this point that the resistivity upon cooling to RT for the MXene from Figure 6.7 b) could not be recorded for technical reasons. When 300 K is reached again, the resistivity is about 30 % lower than before the annealing of the samples (see Figure 6.7 a). This is attributed to both the intercalation of Fe, as also evident from Figure A.12 b) in the Appendix, and the removal of the surface terminations and water. The increase in resistivity with decreasing temperature can be understood in the context of thermally activated electron range hopping. By Halim et al. (2018) [146] it was found that this is the operative conduction mechanism between individual MXene layers in free-standing thin films of Mo_2CT_x MXenes. This is also confirmed by Zheng et al. (2022) [147], who investigated $Nb_4C_3T_x$ and $Ti_3C_2T_x$ MXenes by a combination of terahertz and static electrical transport measurements and found that the charge transport within flakes is due to band-like transport, while the transport between the flakes is due to thermally activated hopping. In the present case, the intercalated Fe atoms, whose number increases with increasing annealing temperature, are likely to act as a "bridge" that shortens the charge transfer distance and leads to increased electron range hopping between the individual layers and stacks of MXene sheets. Upon cooling to 300 K, the thermal energy decreases and causes a decrease in electron range hopping, which leads to the observed increase in resistivity.
In summary, measuring the resistivity during the intercalation of Fe is a quick and easy way to simultaneously monitor the diffusion of Fe into the MXene and the removal of the surface terminations. In addition, changes in electrical properties of the sample can be observed.

7. Structural and chemical state of Fe in $Ti_3C_2T_{x,th}$+Fe MXenes

As explained in Chapter 6, it is hypothesized that it depends on the thermal activation temperature experienced by MXenes prior to Fe intercalation whether there is a clustering of diffusing Fe atoms in the MXene samples or rather a diffusion of Fe in between MXene sheets. Thus, for MXenes thermally activated at 1000 K, a clustering of Fe is expected in voids between stacks of MXene sheets, while for MXenes thermally activated at 425 K, also a diffusion of Fe atoms in between the sheets is postulated.
To verify this, X-ray absorption spectroscopy (XAS) measurements are carried out on the samples. This allows the X-ray linear dichroism (XLD) at the Fe K-edge to be determined which provides information about the local structural environment of intercalated Fe. It is therefore expected that this technique will be able to distinguish between Fe atoms arranged in the form of clusters and Fe atoms intercalated between the hexagonal MXene layers. In addition, XAS measurements provide information about any chemical bonds of Fe, e.g. with the MXene sheets. The results of these measurements are discussed in Chapter 7.1.
Moreover, Chapter 7.2 discusses the interplanar spacing after intercalation of Fe in MXenes. From this it can be deduced whether Fe intercalation leads to a change in the interplanar distance of MXene layers, thus providing indirect evidence for a possible diffusion of Fe in between the sheets.

7.1. Local environment of Fe in $Ti_3C_2T_{x,th}$+Fe MXenes

To identify the local structural environment of Fe in the MXenes, XAS measurements are carried out. XAS investigates the excitation of core level states by X-rays. If the energy of the X-rays is equal to the energy difference for a transition from an occupied core level state to the lowest unoccupied state, a so-called absorption edge is observed. The energy at which an absorption edge is considered is thereby element-specific [148]. The investigation of the X-ray absorption near this absorption edge is also referred to as X-ray absorption near-edge structure (XANES). The XANES provides information on the local electronic structure of the respective element under consideration via the shape of the absorption spectrum and the energy of the absorption edge [148].
It should be noted that the lattice structure can lead to a small anisotropy of the spatial distribution of the local density of unoccupied states [149]. As a result, linear polarized light in

different orientations is absorbed to different degrees at the absorption edge under consideration. The difference between the absorption spectra recorded for the different polarization directions is referred to as XLD. The XLD signal therefore provides information about the local structural environment in which the element under consideration is situated.
XANES spectra were recorded at the Fe and Ti K-edge of the MXene samples at the ID12 beamline of ESRF using linearly polarized light with different polarization directions hitting the samples under grazing incidence [150]. The linearly polarized X-rays are generated by a quarter wave plate (diamond (111)). The polarization direction can be rotated by 90° so that XANES spectra are recorded for a horizontal and vertical polarization direction with respect to the sample. The X-ray absorption is then detected using the total fluorescence yield. This is an indirect measurement method that detects the photons emitted during the refilling of the empty core level states and thus enables bulk sensitivity [149].
To support the analysis of the data and their interpretation, density functional theory (DFT) calculations are performed. This is done in two steps. First, local geometry optimizations of the compound are carried out using the *CASTEP* code according to the work of Clark et al. (2005) [151]. In this context, the electronic exchange-correlation energy is chosen based on the generalized gradient approximation of the Perdew-Burke-Ernzerhof scheme [152]. To optimize the unit cell geometry, the first Brillouin zone is sampled following the Monkhorst–Pack scheme with a k-point separation less than $0.04\,\text{Å}^{-1}$. Here, the geometry optimization is continued until the forces acting on the atoms are below $0.01\,\text{eV/Å}$. All calculations are subject to periodic boundary conditions and use on-the-fly generated pseudopotentials, conducted with *CASTEP* version 23.1. Furthermore, an orbital resolved population analysis utilizes the Mulliken scheme. In a second step, the optimized atomic coordinates and unit cell parameters together with the atomic orbital population serve as input for calculations performed within the *FDMNES* package [153], using multiple scattering theory. Here, a cluster radius about twice as large as the minimum lattice parameter is chosen while using a non-self-consistent method for the excited atom. This takes into account the core hole and an additional electron at the first available valence level. Furthermore, the calculations include spin-orbit interactions while only considering the dipolar transition electric component. The final states and the Fermi energy are then determined after the first iteration step with the isotropic atomic displacement factor being $0.03\,\text{Å}^2$. Lastly, to convolute the absorption spectra at the K-edge of Ti and Fe atoms, a Seah-Dench broadening with $A = 0.5$ and $\Gamma_m = 5\,\text{eV}$ is applied.

For each sample, a set of XANES spectra are recorded at the Fe K-edge at 300 K for both polarization directions at grazing angles of 15° and, if necessary, at a further angle of 12°. The measurements at different incidence angles make it easier to remove any diffraction peaks eventually occuring. At the Ti K-edge, 2 spectra are recorded for each polarization direction at an incidence angle of 7°. Since a large number of Ti atoms are present in the samples compared to the Fe concentration, two spectra are sufficient to achieve a satisfactory signal-to-noise ratio.

To evaluate the recorded XANES spectra, a constant background is first subtracted at the pre- and post-edge using the analysis tool *PyMca* (Python multichannel analyzer) [154], before normalizing the spectra. Any diffraction peaks are then removed and all 6 (2) spectra for Fe (Ti) of one polarization direction are averaged using the analysis software *Origin* (OriginLab). The data is subsequently smoothed with a moving average and normalized again. Then the spectra obtained for both polarization directions are subtracted from each other to obtain the XLD signal. The averaged XANES spectrum of both polarization directions as well as the corresponding XLD signal at the Ti K-edge can be viewed for a $Ti_3C_2T_x$, a $Ti_3C_2T_{x,th,425K} + Fe_{620K}$ and a $Ti_3C_2T_{x,th,1000K} + Fe_{650K}$ MXene in Figure 7.1 a). For the Fe K-edge the respective spectra can be found for a 6 nm Fe reference on a $Si(100)/SiO_2$ substrate annealed at 750 K and a $Ti_3C_2T_{x,th,1000K} + Fe_{650K}$ MXene in Figure 7.2, while for a $Ti_3C_2T_{x,th,425K} + Fe_{700K}$ and a $Ti_3C_2T_{x,th,675K} + Fe_{800K}$ MXene they are depicted in Figure 7.3.
It should be noted that all MXene samples analyzed here are spray coated MXenes (see Chapter 4.3). The thermal activation, deposition of 6 nm Fe and intercalation of Fe takes place in the ultra high vacuum (UHV) chamber (cf. Chapter 3). For transfer to the ESRF, the samples are covered with 6 nm C as an oxidation protection before being removed from the UHV. A slightly different preparation is used for the $Ti_3C_2T_{x,th,675K} + Fe_{800K}$ MXene, whose XANES spectrum and XLD signal are shown in Figure 7.3. Here, 6 nm Fe are first deposited on the MXenes in the UHV chamber and then, without its intercalation, covered with 7 nm C. The intercalation of Fe is then performed at 800 K in a high vacuum (HV) chamber at the ID12 beamline of ESRF while simultaneously performing electrical transport measurements as described in Chapter 6.3. After completion of the Fe intercalation and transport measurements, the sample is transferred via a load-lock into an adjacent HV chamber for measurements of XANES spectra.
Looking first at the XANES spectra at the Ti K-edge in Figure 7.1 a), it is obvious that the spectra after thermal activation and Fe intercalation do not show significant differences compared to the untreated $Ti_3C_2T_x$ state, shown in dark green. There is also no difference between the MXene thermally activated at 1000 K, shown in red, and the MXene thermally activated at a lower temperature of 425 K, shown in light green. A comparison with the literature shows a good agreement between the XANES spectra measured by Magnuson et al. (2020) [159], who studied the chemical bonding within $Ti_3C_2T_x$ MXenes during thermal annealing in an N_2 atmosphere up to 1000 K using XANES, and the spectra presented here. The XANES spectrum from DFT calculations of a $Ti_3C_2O_2$ MXene, in which oxygen atoms are located on A and B adsorption sites (see Figure 7.1 b)), as also discussed in the work of Persson et al. (2017) [64], is shown in black dashed lines in Figure 7.1 a). The very simplified approach of a MXene completely terminated by oxygen already gives good qualitative agreement with the measured XANES spectra, where all features observed in the experimental data are included/recognizable.
Considering the XLD signal in Figure 7.1 a) in a next step, no fundamental difference can be determined between the respective MXenes states here either. In addition the DFT simulated XLD signal of a $Ti_3C_2O_2$ MXene can adequately describe the measured XLD signal up to 5 keV.

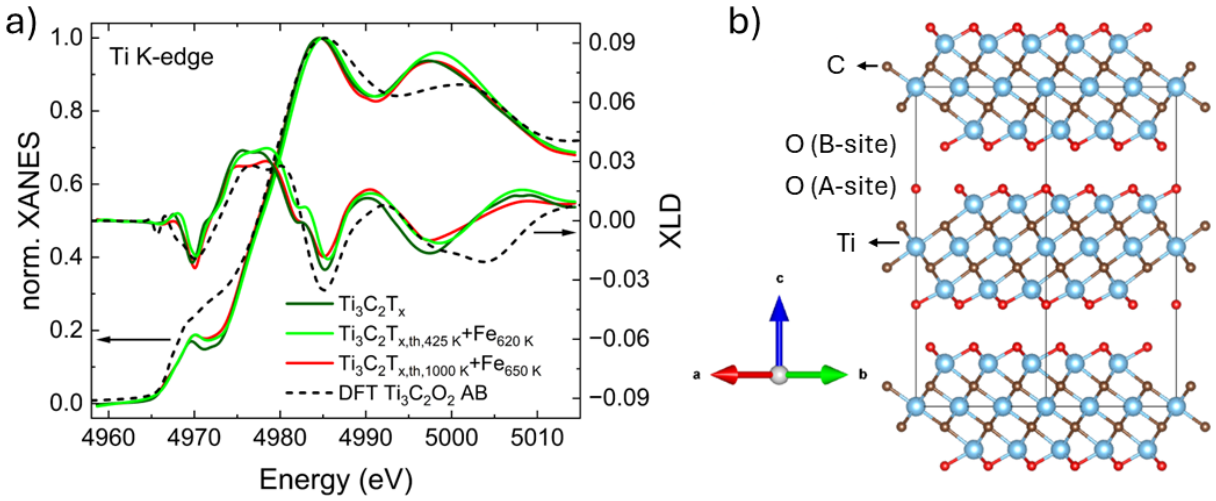

Figure 7.1.: a) XANES spectra [155, 156], showing the normalized XANES signal as a function of energy at the Ti K-edge for a $Ti_3C_2T_x$, a $Ti_3C_2T_{x,th,425K} + Fe_{620K}$, and a $Ti_3C_2T_{x,th,1000K} + Fe_{650K}$ MXene in dark green, light green and red, respectively. A XANES spectrum from DFT calculations of a $Ti_3C_2O_2$ MXene with O terminations located on A and B adsorption sites (see figure b)) is shown as a black dashed line. In addition to XANES spectra, corresponding XLD signals of the respective samples and the DFT simulated MXene are depicted (same color code). It can be seen that thermal activation and Fe intercalation do not cause any significant changes in the XANES spectra or XLD signals. Furthermore, the experimental XANES spectra and XLD signals can be qualitatively well described by the DFT spectrum. However, slight deviations occur towards higher energies, which are related to the simplified approach of a complete termination by oxygen of the DFT simulated MXene. b) Schematic structure of the DFT simulated $Ti_3C_2O_2$ MXenes along the lattice c-axis visualized with *VESTA* [157, 158]. Ti atoms are shown in blue and C atoms in brown. The oxygen atoms in red are located in equal numbers on A (fcc) adsorption sites (on top of Ti atoms) and B (hcp) adsorption sites (on top of C atoms).

Above 5 keV, however, there is a difference due to slightly different atomic configurations and electronic structures as a result of the many possibilities for the composition and atomic positions of surface terminations that were not taken into account in the DFT calculations.

It can be summarized that there are no major changes in the XANES and XLD spectra at the Ti K-edge due to the removal of the surface terminations T_x and the intercalation of Fe. The measured XANES spectra and XLD signals can be qualitatively described by DFT simulation of a $Ti_3C_2O_2$ MXene, despite complete termination of the non-thermally activated MXenes by $T_x := O, -OH, -F$ and $-Cl$. This leads to the conclusion that, on the one hand, the structure of the Ti_3C_2 MXene layers remains unchanged by the intercalation of Fe. According to initial DFT calculations carried out in this context, but not presented here in detail, the incorporation of Fe into the sheets would lead to a strong change in the XLD signal. On the other hand, removing the surface terminations T_x by thermal activation has little effect on the XLD signal. In analogy, it is therefore assumed that a possible diffusion of Fe in between the MXene

layers likewise causes only small changes in the XLD/XANES signal at the Ti K-edge. Therefore, the XANES spectra and XLD signals of Fe at the Fe K-edge are considered in the next step.

Here, the state of the intercalated Fe in MXenes thermally activated at a high temperature of 1000 K will be discussed first. Figure 7.2 shows the XANES spectrum of a $Ti_3C_2T_{x,th,1000K} + Fe_{650K}$ MXene in red, and the spectrum of a 6 nm Fe reference on a $Si(100)/SiO_2$ substrate annealed at 750 K in blue. A comparison of the two signals reveals identical spectroscopic features at the absorption, as well as pre- and post-absorption edge. A comparison with literature data shows that the observed XANES spectra of both states correspond to that of bcc Fe [160]. This is further confirmed by DFT calculation of an XANES spectrum of bcc Fe, shown as black dashed lines. Looking at the corresponding XLD signal, it is approximately zero for the Fe reference on the $Si(100)/SiO_2$ substrate as well as for Fe intercalated in MXenes. This confirms the bcc character of Fe, as no XLD signal is observed for cubic structures [161], also indicated by the black dashed zero line of the simulated XLD signal.

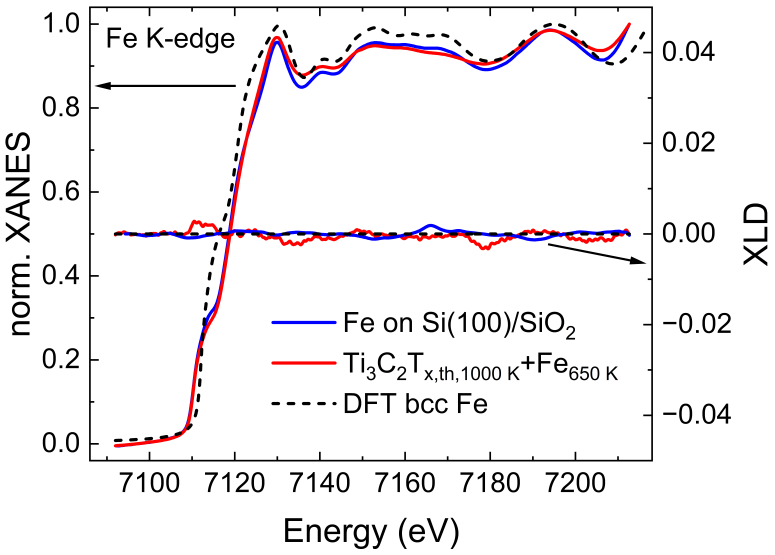

Figure 7.2.: XANES spectrum, showing the normalized XANES signal as a function of energy, and corresponding XLD signal at the Fe K-edge for a 6 nm Fe film on a $Si(100)/SiO_2$ substrate annealed at 750 K in blue, and a $Ti_3C_2T_{x,th,1000K} + Fe_{650K}$ MXene in red. The normalized XANES spectrum and XLD signal from DFT calculations of bcc Fe are shown as black dashed lines [156]. Here, the simulated and experimental spectra show good qualitative agreement. As expected for the cubic bcc structure, the XLD signal is zero. This confirms the hypothesis that Fe forms clusters with a bcc structure in the MXenes thermally activated at high temperatures of 1000 K, as already suspected from the findings of the diffusion study (see Chapter 6).

To summarize, in the case of Fe diffusion in between the MXene sheets, a large number of Fe atoms would be located in the local structural environment of the hexagonal MXene layers. Consequently, the measured XANES spectrum would differ from bcc Fe and a non-zero XLD signal would be expected. Since this is not the case, the observations confirm the case previously discussed in Chapter 6.2, a clustering of Fe in voids between stacks of MXene sheets when the MXenes are thermally activated at high temperatures of 1000 K. Note that also no oxidation of

Fe occurs, which confirms the efficiency of the 6 nm C layer as an oxidation protection.
Besides the previous statements, however, there is the possibility that Fe diffuses between the MXene layers and forms a bcc structure if a sufficient number of Fe monolayers (ML) can accumulate between the sheets. This is attributed to the effect described in the work of Hsieh et al. (2021) [162], where a relaxation of a strained Fe fcc structure on a Ir substrate into a Fe bcc structure is observed above a certain number of Fe ML on the substrate. However, a significant increase in the MXene interplanar distance after the Fe intercalation would be expected in this case. In addition, as explained in Chapter 6.1, no diffusion between the layers is evident from the diffusion parameters. On the other hand, when considering a stack of MXene sheets, it is likely that some sheets at the edge of this stack will extend further beyond a certain point than others, e.g. due to a larger diameter. This can be illustrated by means of an example: 2 MXene sheets with a large diameter and one MXene sheet with a smaller diameter located between them is considered. In this setup of a stack of 3 MXene sheets, there is an area around the edge of the stack where the interplanar distance between the two outer sheets is twice as large as in the center of the stack, as the space between them is no longer filled by the 3rd MXene sheet. Consequently, a larger amount of Fe can diffuse between the two outer layers in this region and may form a bcc structure there. In this case, it is also conceivable that a continuous accumulation of bcc Fe increases the interplanar distance between the two outer sheets, resulting in an increase in the interplanar distance within the entire stack. To verify this, the interplanar spacing of the MXene sheets in the samples thermally activated at 1000 K before and after the Fe intercalation is analyzed in Chapter 7.2.
In the following, the local structural environment of Fe intercalated in MXenes thermally activated at low temperatures (< 675 K) will be discussed. Comparing the XANES spectrum of the $Ti_3C_2T_{x,th,425K} + Fe_{700K}$ MXene shown in green in Figure 7.3 with the spectrum of the $Ti_3C_2T_{x,th,1000K} + Fe_{650K}$ MXene in Figure 7.2, it is obvious that the two spectra are fundamentally different. On the other hand, the XANES spectrum of the $Ti_3C_2T_{x,th,425K} + Fe_{700K}$ MXene is qualitatively similar to that of the $Ti_3C_2T_{x,th,675K} + Fe_{800K}$ MXene, shown in orange in Figure 7.3. Detailed comparison to literature data shows a match between the XANES spectra from Figure 7.3 and the XANES spectrum of Fe_3C [163]. This is supported by the XANES spectrum obtained from DFT calculations for Fe_3C (black dashed) in Figure 7.3, which reflects all spectroscopic features of the experimental XANES spectra.
The next step is to look at the corresponding XLD spectra of the two states under consideration, which reveal a pronounced XLD signal (see Figure 7.3). In view of the larger interplanar distances for MXenes that are thermally activated at low temperature (see Chapter 5.2) and the higher diffusivities of Fe in the MXenes in this case (see Chapter 6), this initially indicates that the XLD signal is caused by a diffusion of Fe in between the MXene sheets. This can be explained by the large number of Fe atoms that would be found in the local environment of the hexagonal MXene layers. However, as explained above, the corresponding XANES spectra are similar to those of Fe_3C.

Comparing the XLD signal of Fe_3C (black dashed) obtained from DFT calculations with the measured signals, it is evident that all spectroscopic features suggested by DFT are found in the experiments at, however, slightly different spectral weight. The observations therefore strongly suggest that the intercalated Fe forms Fe_3C in the MXenes thermally activated at low temperatures. Note that Fe does not oxidize here, although the water intercalated between the MXene layers is still present when the diffusion of Fe into the MXenes sets in (see Chapter 5.1 and 6.3). In the following, possible reasons are discussed as to why the Fe intercalated into the MXenes is present in an Fe_3C structure, and whether Fe_3C also sits in between the MXene sheets.

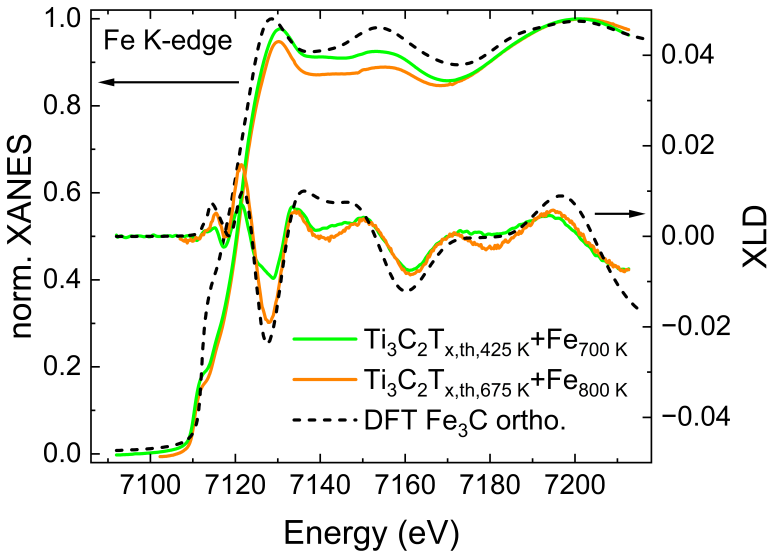

Figure 7.3.: XANES spectra, showing the normalized XANES signal as a function of energy, and corresponding XLD signal at the Fe K-edge for a $Ti_3C_2T_{x,th,425K} + Fe_{700K}$ and a $Ti_3C_2T_{x,th,675K} + Fe_{800K}$ MXene in green and orange, respectively. The normalized XANES spectrum and XLD signal from DFT calculations of Fe_3C are shown as black dashed lines [156]. The spectra suggest that Fe is located within a Fe_3C structure in MXenes thermally activated at low temperatures $< 675\,K$.

In general, the question arises here as to why Fe forms Fe_3C in the MXenes thermally activated at low temperatures $< 675\,K$, while it is present in a bcc structure in the MXenes thermally activated at 1000 K. To answer this question, the $Ti_3C_2T_{x,th,1000K} + Fe_{650K}$ and the $Ti_3C_2T_{x,th,425K} + Fe_{700K}$ MXene sample from Figure 7.2 and 7.3 are compared. Both samples are spray coated MXenes from the same sample batch. Both samples are thermally activated in the UHV chamber before depositing 6 nm Fe, which is then intercalated *in situ* before the samples are covered with 6 nm C as described above. Note: the only difference between the two samples is that the MXene thermally activated at 425 K still possesses all surface terminations, while in the other sample O is the largely remaining surface termination (see Chapter 5.1).

The 50 K higher Fe intercalation temperature of 700 K for the above mentioned MXene sample thermally activated at 425 K compared to the sample thermally activated at 1000 K can be excluded as a cause for Fe_3C formation. This is due to the fact that for all investigated samples and Fe intercalation temperatures from 600 K to 800 K Fe is always found as bcc Fe in the MXenes thermally activated at 1000 K, while in MXenes thermally activated at temperatures $< 675\,K$ it occurs in the form of Fe_3C. In this context, Fe_3C is metastable over the entire temperature range

while its decomposition rate generally increases with increasing temperature [164, 165]. Here, according to the phase diagram of Fe-C, a metastable phase of α-Fe (bcc) + Fe_3C occurs below 1000 K [166]. In the work of Al-Joubori et al. (2018) [164], Fe_3C was prepared by ball milling pure Fe powder with 6.7 wt% C powder for 30 h at room temperature. The Fe_3C powder was then sintered at 600 °C and 70 MPa to consolidate it in bulk form. In addition, the sintered samples were annealed in a vacuum sealed quartz tube at 900 °C. It was found that solely the Fe_3C phase can be observed for the ball-milled powder and the sintered samples, while the samples vacuum annealed at 900 K exhibit a Fe and Fe_3C phase [164]. Consequently, up to a temperature of 600 K no significant decomposition of Fe_3C takes place, while at 900 K an increased decomposition occurs. It can be deduced that mechanical techniques such as ball milling favor the synthesis of Fe_3C, since the necessary mixing of Fe and C can take place at low temperatures close to room temperature. In the present work, however, elevated temperatures are required to enable the diffusion of C into Fe, necessary for the formation of Fe_3C. For the MXenes that are thermally activated at 1000 K, it is therefore assumed that due to a low diffusivity of C in Fe at the applied Fe intercalation temperatures, no Fe_3C phase can be formed. As a result, only bcc Fe is observed here. For the MXenes, thermally activated at temperatures below 675 K, an additional factor is postulated that enables higher diffusion of C into the Fe already at a lower temperatures, thus leading to the formation of Fe_3C. As discussed earlier, this can only be caused by one or more termination species, which, in contrast to the MXenes thermally activated at 1000 K, are still largely present in these samples.

In this context, the Cl terminations are suspected to be responsible for an enhanced diffusion of C into Fe. As explained in the work of Lara et al. (1997) [167], Cl or C adsorb on a Fe surface by accepting d-electrons of Fe. When Cl and C are co-adsorbed, they compete for these electrons. This causes a decrease in the heat of adsorption for C as the number of Cl atoms increases, resulting in a decrease in the activation energy for the diffusion of C into the Fe [167]. Consequently, even at lower temperatures, higher diffusivities are expected for C in Fe in the presence of Cl atoms. This is supported by the observations of Kinoshita et al. (2022) [168], who investigated the growth of carbon nanotubes starting from a ferrocene catalyst at 760 °C under the influence of Cl_2 at concentrations from 0 ppm to 450 ppm. It was found that the addition of Cl_2 increases the diffusion rate of C in the Fe containing catalysts, which enables increased growth rates of carbon nanotubes [168].

Next, sources of carbon required for the formation of Fe_3C are discussed. Looking at the work of Näslund et al. (2022) [169], where $Ti_3C_2T_x$ MXenes were investigated by X-ray photoelectron spectroscopy (XPS), it is obvious that MXenes always contain a fraction of graphite-like carbon. In addition, residues of alcohol, for example isopropanol used in this work for spray coating MXenes on $Si(100)/SiO_2$ (see Chapter 4.3), can act as a carbon source [169]. Additionally, there is the possibility that carbon is introduced when Fe is intercalated while being covered by C, as in the case of the $Ti_3C_2T_{x,th,675K} + Fe_{800K}$ MXenes from Figure 7.3. The more pronounced XLD signal here compared to the $Ti_3C_2T_{x,th,425K} + Fe_{700K}$ MXene indicates that an increased

amount of C is available, which generally favors the formation of Fe_3C [166]. In addition to the aforementioned C sources in MXenes, also the carbon of the Ti_3C_2 MXene sheets needs to be considered. Since no changes in the XANES and XLD spectra at the Ti K-edge are observed after the Fe intercalation (see Figure 7.1 a)), it follows that the C atoms incorporated in the Ti_3C_2 layers remain in their original locations. However, Fe may bind to the MXene sheets as a termination species, partially mimicking the electronic structure of Fe_3C. In this context, it should be noted that a possible termination of the MXenes by Fe is very diverse and that the XANES and XLD signal at the Ti K-edge as a result of Fe as termination species remain almost unchanged. This can be seen from first DFT calculations carried out in this context, but not presented here in detail. Consequently, this is not in conflict with the almost unchanged experimentally observed XANES and XLD signals at the Ti K-edge in Figure 7.1 a).
It remains to be clarified whether Fe_3C sits between the MXene sheets or forms clusters in voids. First of all, it should be noted that, as observed in Chapter 6.3, Fe diffusion sets in before the removal of the surface terminations, including $-$Cl, at higher temperatures. It is therefore reasonable to expect that the Fe distributes in the MXene samples before a formation of Fe_3C occurs. There are two possible pathways/scenarios. One is an arrangement of Fe between the MXene sheets, which is made possible by the large interplanar distance, the other is a clustering of Fe in voids regardless of the large interplanar spacing. In the first case, when the $-$Cl terminations are removed, it can be argued that the Cl atoms support the formation of Fe_3C from the mixture of Fe and C atoms available between the sheets. Alternatively, Fe may bind to the MXene sheets as a termination upon removal of the initial T_x thus mimicking the electronic structure of Fe_3C as explained above. In the second case, there is the possibility that the removed Cl terminations, when diffusing from the region between the MXene layers into the voids, enable the formation of Fe_3C clusters there. However, if there is only adsorption of Cl on the surface of the Fe clusters, it can be assumed that the diffusivity of C in Fe is merely increased in the vicinity of the surface. Consequently, for larger Fe clusters that have accumulated in voids between MXene stacks, only part of the Fe may be able to form a Fe_3C structure. Generally, it is expected that both cases discussed occur in the samples and that Fe_3C is present between the MXene sheets as well as in the voids between the stacks of MXene sheets. In this context, it should also be noted that against the background of the metastability of Fe_3C, part of the Fe is likely to be present in the form of an α-Fe (bcc) phase. All in all, the arguments discussed here demonstrate that an arrangement of Fe_3C and/or Fe in a local environment similar to that of Fe_3C in between the MXene sheets is likely.
In order to consolidate the findings of this chapter and to confirm/refute a diffusion of Fe in between the MXene sheets, in the following Chapter 7.2 results from X-ray diffraction (XRD) and wide angle X-ray scattering (WAXS) measurements on MXenes thermally activated at 1000 K or temperatures < 675 K are considered. Here, the aim is to check the extent to which the interplanar spacing of the MXene sheets changes after the intercalation of Fe. This can serve as an indirect evidence of a potential diffusion and arrangement of Fe in between the MXene sheets.

7.2. Influence of intercalated Fe on interplanar spacing in MXenes

In this chapter, it is investigated whether and to what extent the interplanar distance between MXene layers changes due to the intercalation of Fe. In this way, differences between the obtained bcc Fe and Fe_3C MXene samples may show up and allow a better understanding of the position and morphology of the intercalated Fe species.
The interplanar distances are determined by WAXS measurements, analogous to Chapter 5.2, on spray coated MXenes thermally activated at 1000 K with Fe intercalated at different temperatures. The extracted diffraction patterns as a function of scattering vector q for a $Ti_3C_2T_{x,th,1000K}$, a $Ti_3C_2T_{x,th,1000K} + Fe_{700K}$ and a $Ti_3C_2T_{x,th,1000K} + Fe_{800K}$ MXene in green, black and red accordingly, are displayed in Figure 7.4 a). In addition, a diffraction pattern for a spray coated $Ti_3C_2T_{x,th,425K} + Fe_{620K}$ MXene is recorded using XRD. This can be found in Figure 7.4 b). The XRD measurements were performed in Bragg-Bretano geometry with an Empyrian diffractometer from *Malvern Panalytical* using Cu-K_α radiation. XRD measurements were carried out on this sample, as no WAXS measurements were possible at the P03 beamline of the PETRA III storage ring at the given time. However, it has been shown that XRD measurements also allow an adequate determination of occurring changes in the interplanar distance (see also Figure A.8 in the Appendix), since the (002) diffraction peak of the MXenes is rather pronounced. The insets in Figures 7.4 a) and b) show the normalized (002) diffraction peaks of the measured samples as a function of interplanar spacing, calculated from the scattering vector q according to Equation 5.1 or for the XRD measurements from Bragg's law.
First, the case of MXenes thermally activated at a high temperature of 1000 K will be discussed. Looking at the normalized (002) peaks in the inset in Figure 7.4 a), the shoulder previously observed in Chapter 5.2 can also be found after the Fe intercalation. From a qualitative analysis, it is not apparent that there is a shift in the position of the shoulder or the position of the peak maximum due to the intercalation of Fe. Furthermore, no additional shoulder appears indicating a third interplanar spacing after Fe intercalation. To quantify this, the normalized (002) diffraction peaks of the three samples considered are fitted each by two Gauss functions (see Figure A.9 b)). The interplanar spacings resulting from the positions of the maxima of the Gauss fits (Peak 1 and Peak 2) are then plotted as a function of the respective sample in Figure 7.5. The fitting yields a slight increase of 0.014 nm and 0.004 nm after the Fe intercalation for the larger interplanar distance (Peak 1) and the smaller interplanar distance (Peak 2), respectively.
The observed increase in interplanar spacing between the sheets is small compared to the distribution of spacings, which is reflected by the error bar in Figure 7.5 corresponding to the full width at half maximum (FWHM) of the Gauss fits. Nevertheless, an upward trend of the interplanar spacing is identified with increasing Fe intercalation temperature. Since especially the larger interplanar distance (Peak 1) increases, a diffusion of single Fe atoms between the sheets as also observed in Figure 6.5 c) is suggested. As the Fe is not in a bcc environment here, this must be a very small fraction, as otherwise an XLD signal would be expected (cf. Figure 7.2).

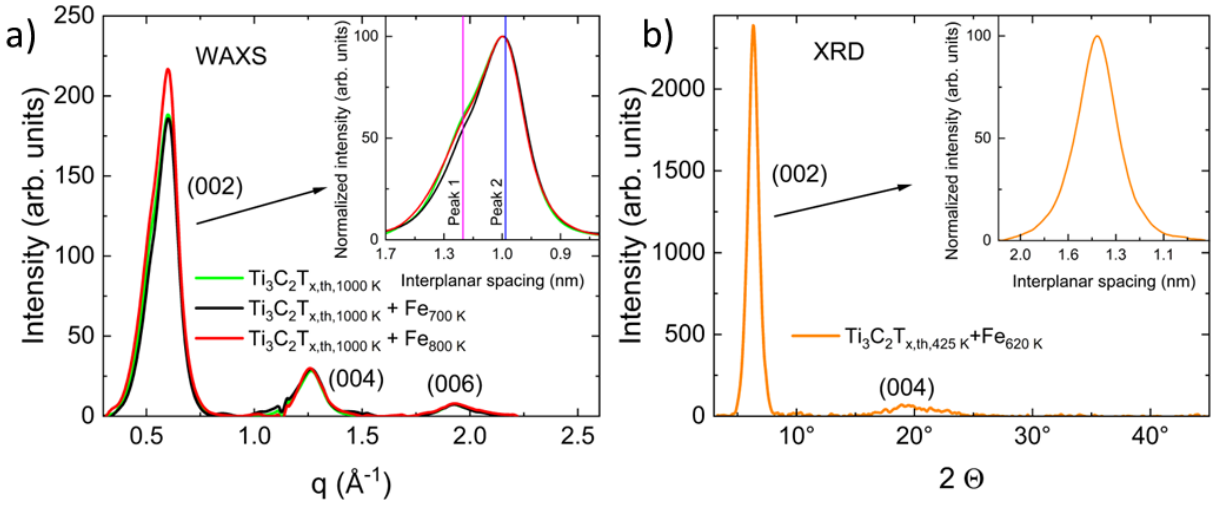

Figure 7.4.: a) Diffraction pattern from WAXS measurements on spray coated MXene samples as a function of the scattering vector q [128]. Shown are the diffractograms of a $Ti_3C_2T_{x,th,1000K}$ (green), a $Ti_3C_2T_{x,th,1000K} + Fe_{700K}$ (black) and a $Ti_3C_2T_{x,th,1000K} + Fe_{800K}$ (red) MXene. The inset shows the normalized (002) diffraction peaks of the specified samples as a function of the interplanar spacing. The (002) diffraction peaks show a shoulder at higher interplanar distances. The (002) peaks are fitted by 2 Gauss functions, whereby two interplanar distances follow from the positions of the peak maxima. The position of the maximum of the first Gauss fit is labeled Peak 1 (magenta), that of the second Peak 2 (blue). b) XRD pattern (Cu-K_α = 0.154 06 nm) of a spray coated $Ti_3C_2T_{x,th,425K} + Fe_{620K}$ MXene. The diffraction peaks are assigned by matching with the XRD spectrum from Figure 4.1. Inserted here is the normalized (002) diffraction peak as a function of the interplanar distance, which is determined from the diffraction angle using Bragg's law. To quantitatively determine the interplanar spacing, the normalized (002) peak is fitted by a pseudo-Voigt function (see Figure A.9 a)).

An arrangement of bcc Fe between the layers can be excluded with high certainty, as significantly larger interplanar distances between the MXene layers would be expected in this case (cf. Chapter 7.1). In addition, an accumulation of larger quantities of bcc Fe between the layers would be detectable with WAXS as additional spots in the scattering images, which, however, are not observed. A possible arrangement of bcc Fe between the MXene sheets in the region of the edge of a MXene stack, as discussed in Chapter 7.1, is also not recognizable here from a distinct increase in the interplanar spacing. Accordingly, an accumulation of bcc Fe in voids of MXene samples thermally activated at 1000 K remains most likely.

Second, the case of MXenes thermally activated at temperatures < 675 K is addressed. Taking a look at the normalized (002) peak of the $Ti_3C_2T_{x,th,425K} + Fe_{620K}$ MXene sample in the inset of Figure 7.4 b), it is noticeable that no additional shoulder is observed here. In addition, it can be seen that the interplanar distance is significantly larger than for the previously considered case of MXenes thermally activated at 1000 K. In order to quantify this further, the normalized (002) diffraction peak is fitted by a pseudo Voigt function (see Figure A.9 a)). From

the so obtained peak position, the interplanar spacing is determined using Bragg's law, which results in 1.39 ± 0.11 nm and is also added in Figure 7.5. The error bar reflects the FWHM. The orange dashed lines in Figure 7.5 illustrate the jump of the significantly larger interplaner spacing found here compared to the two interplanar spacings occurring in MXenes thermally activated at 1000 K. In the following, it is discussed whether the interplanar distance of 1.39 ± 0.11 nm is the result of an arrangement of Fe between the MXene layers.

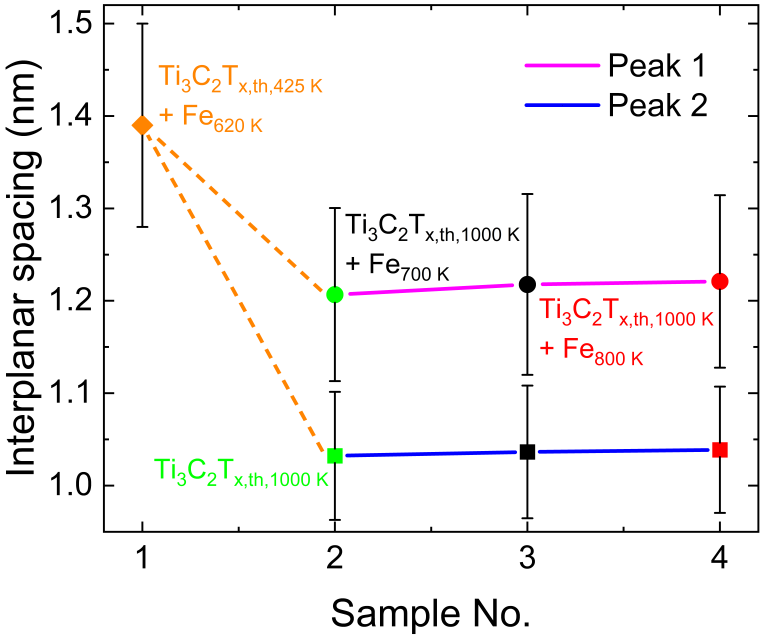

Figure 7.5.: Interplanar spacings of samples after different thermal treatments. The error bar corresponds to the FWHM of the Gauss/pseudo-Voigt fits. For MXenes thermally activated at 1000 K, the two occurring interplanar distances from the position of the shoulder (Peak 1) and the main peak (Peak 2) are plotted (cf. Figure 7.4 a)). After Fe intercalation at 800 K, there is a slight increase of 0.014 nm (Peak 1) and 0.004 nm (Peak 2), compared to the $Ti_3C_2T_{x,th,1000K}$ MXene without intercalated Fe. For the MXenes thermally activated at 425 K with Fe intercalated at 620 K, there is only a single, significantly larger interplanar spacing of 1.39 ± 0.11 nm found in the samples. Here, the orange dashed lines highlight the difference to the two interplanar spacings of the MXenes thermally activated at 1000 K. Since a removal of the majority of the water from between the MXene sheets is expected at a temperature of 620 K (see Figure 5.1 a)), the interplanar distance is systematically larger than those observed after removal of adsorbed/intercalated water without intercalated Fe (see Chapter 5.2).

First of all, it should be noted that the maximum temperature experienced by the sample is 620 K. Based on the findings from Chapter 5.1, the onset of the removal of surface terminations (also $-Cl$) can be expected around this temperature. In addition, Chapter 6.3 shows that at 620 K a comparatively large portion of Fe is already intercalated into the MXenes. Following the discussion in Chapter 7.1, a formation of Fe_3C at an Fe intercalation temperature of 620 K can also be considered possible. This is supported by Figure A.13 a) in the Appendix, which shows the XANES and XLD signal at the Fe K-edge of the $Ti_3C_2T_{x,th,425K} + Fe_{620K}$ MXene compared to those of the $Ti_3C_2T_{x,th,425K} + Fe_{700K}$ MXene from Figure 7.3. The same spectroscopic features are found here with a slightly lower spectral weight.

As the sample is held for 30 min at a temperature of 620 K, it can be deduced that water and −OH have been removed from between the sheets to large extents (cf. Figure 5.1 a)). Yet, water is primarily responsible for large interplanar distances, as discussed in Chapter 5.2. This is also apparent from the up to 0.41 nm smaller interplanar spacing of 1.03 ± 0.07 nm after thermally activating MXenes at 1000 K, where a complete removal of water is expected (cf. Chapter 5.2). In the literature, typical interplanar distances of about 1.28 nm are reported for LiF/HCl etched $Ti_3C_2T_x$ MXenes (see Chapter 5.2). Consequently, the interplanar spacing of 1.39 nm found after Fe intercalation shows a systematic upward deviation from these values. This points to Fe and/or Fe_3C being located between the MXene layers, resulting in the large interplanar spacing. However, Fe_3C has a large unit cell with the unit cell parameters $a = 0.45$ nm, $b = 0.51$ nm and $c = 0.67$ nm [170]. This may indicate that Fe, as discussed in the previous Chapter 7.1, binds to the MXene sheets as a termination species, partially mimicking the electronic structure of Fe_3C. Additionally, there is the possibility that Fe_3C forms preferentially at defects in the Ti_3C_2 MXene layers.

It should be noted that the XLD signal for the $Ti_3C_2T_{x,th,425K} + Fe_{620K}$ MXene considered here is qualitatively the same but slightly smaller than the signal of the $Ti_3C_2T_{x,th,425K} + Fe_{700K}$ MXene (cf. Figure A.13 a)). This is why with increasing Fe intercalation temperature, it is expected that further Fe will diffuse in between the MXene sheets leading to a further increase in the interplanar spacing. At the same time, however, the higher temperatures also lead to the removal of additional surface terminations (see Chapter 5.1). Assuming that both effects are approximately in balance, the interplanar distance is postulated to be within the range of 1.39 nm also for higher Fe intercalation temperatures.

In summary, the analysis of the interplanar distances in the MXenes after Fe intercalation further indicates a formation of Fe_3C and/or Fe in a local environment similar to that of Fe_3C in between the MXene layers for the MXenes thermally activated at temperatures < 675 K, which supports the previously proposed hypothesis from Chapter 7.1.

8. Magnetism of $Ti_3C_2T_{x,th}$+Fe MXenes

As the title of this chapter suggests, the magnetic properties of $Ti_3C_2T_{x,th}$ + Fe MXenes will be presented to complete this work. In this context, it is of particular interest to check whether ferromagnetism occurs in the samples above room temperature (RT). Based on the results of the above chapters, it is reasonable to focus on two cases. The case of MXenes thermally activated at 1000 K, in which intercalated Fe is expected as near-surface bcc Fe clusters in voids of the samples, and the case of MXenes thermally activated at temperatures < 675 K, where a formation of Fe_3C and/or Fe in a local environment similar to that of Fe_3C, e.g. upon binding to the MXene sheets as a termination species, is considered likely between MXene sheets.
For the second case, it is useful to check whether a Curie temperature similar to that of Fe_3C can be observed, which undergoes a ferromagnetic to paramagnetic phase transition at 485 K [171]. To determine the Curie temperature, the magnetization is recorded as a function of temperature, usually in a small field. In addition, magnetic hysteresis loops are measured at different temperatures for both cases described above. In this way, the saturation magnetizations and coercive fields of the samples can be determined and potential changes occurring after intercalation of Fe into MXenes identified. A comparison of the coercive fields also provides information on whether the intercalation of Fe leads to a harder or softer magnetic behavior. The collected temperature and field dependent magnetization data is analyzed and discussed in Chapter 8.1.
To investigate the local electronic structure of the intercalated Fe element specifically under magnetic ordering, X-ray magnetic circular dichroism (XMCD) spectra at the Fe K-edge are studied. These measurements promise to provide a "magnetic fingerprint" of intercalated Fe in MXenes. The results of the XMCD study are analyzed in Chapter 8.2.

8.1. Magnetic response of $Ti_3C_2T_{x,th}$+Fe MXenes

As outlined above, the Curie temperature is to be determined from temperature-dependent magnetization curves and the coercive fields and saturation magnetizations from magnetic hysteresis loops. Consequently, the magnetization of the samples is to be recorded as a function of temperature or external field. To this end, a vibrating sample magnetometer (VSM) is used.
The basic working principle of a VSM is the oscillation (vibration) of a sample in an external magnetic field within a pair of so-called pick-up coils, as described in the fundamental work of Foner (1959) [172]. Based on Farady's law of induction, the oscillating magnetized sample causes a voltage in the pick-up coils from which the magnetic moment of the specimen can be

determined [173]. Thus, VSM is a technique that allows the direct measurement of the total magnetic moment of a sample. By varying the external magnetic field and the temperature, the magnetic moment can be determined as a function of these parameters.
A PPMS DynaCool from *Quantum Design* is used for the VSM measurements in this study. Here, the external magnetic field is generated by a superconducting solenoid, which can generate fields up to 9 T, whereas in this work fields of up to 1.5 T are sufficient to achieve the saturation magnetization of the samples. In addition, the PPMS can also be used to perform temperature-dependent measurements over a wide temperature window, which in this work ranges from 5 K to 400 K and from 400 K to 900 K using two different sample holders. In this context, a high signal-to-noise ratio enables the detection of magnetic moments $< 6 \times 10^{-9}$ Am^2 at 300 K (manufacturer's specification).
As the VSM is used to measure the total magnetic moment, a normalization with the volume of the measured specimen is required to obtain the magnetization, i.e. to compare different samples. In the present case, it is of particular interest how the magnetization of Fe initially deposited on the MXenes changes due to its intercalation. Given that the MXenes themselves do not show collective magnetism, as described in Chapter 2.1.4, the underlying volume of the sample is calculated from the thickness of the Fe film originally deposited on MXenes and the lateral expansion of the sample under consideration. To determine the latter, the sample is placed on graph paper, a photo is taken and used to calculate the area of the substrate with the image processing program *ImageJ* [123]. This approach is subject to relatively large errors, which is why the saturation magnetizations determined from hysteresis loops in Chapter 8.1.2 also exhibit rather significant errors of up to ± 150 kA/m.
Any diamagnetic contributions, e.g. from the sample holder or the adhesive tape used to attach the samples, are observed as a negative linear background in the recorded hysteresis loops. This can be removed by subtracting a negative linear slope determined by fitting the hysteresis curves in the region of the saturation magnetization. This also shows that the diamagnetic contributions dominate over the paramagnetic contributions of e.g. $Ti_3C_2T_x$ MXenes or Fe atoms intercalated deep in the sample, which would give rise to a positive background.

8.1.1. Curie temperature of $Ti_3C_2T_{x,th}$+Fe MXenes

It is reasonable to first check whether the Curie temperature for the case mentioned earlier, where intercalated Fe in MXenes is expected in the form of Fe_3C and/or in a local environment similar to that of Fe_3C, is in the range of the Curie temperature of this material. Consequently, a temperature dependent magnetization curve of spray coated $Ti_3C_2T_{x,th,675K} + Fe_{800K}$ MXenes, whose X-ray absorption near-edge structure (XANES) and X-ray linear dichroism (XLD) spectra are depicted in Figure 7.3, is recorded. This is shown in Figure 8.1 a). Here, the measurement was carried out in the sample plane from low to high temperatures at 300 mT. This is sufficient to overcome any hysteretic effects. The shape of the curve in Figure 8.1 a) resembles the shape of a ferromagnetic phase transition in the presence of an external magnetic field.

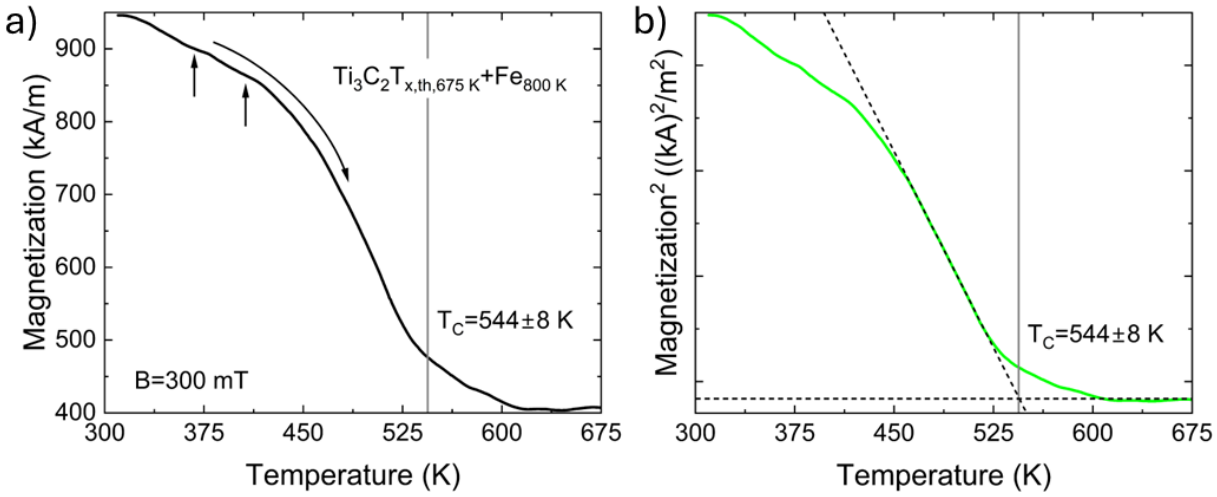

Figure 8.1.: a) Magnetization vs. temperature from 310 K to 675 K of a $Ti_3C_2T_{x,th,675K}$ + Fe_{800K} MXene sample. The measurement is performed from low to high temperature in the sample plane at 300 mT. The observed temperature-dependent magnetization corresponds to that of a ferromagnetic phase transition whose Curie temperature results in 544 ± 8 K according to the fitting in b). This value is about 60 K above the Curie temperature of Fe_3C. In addition to the main phase, there are potential extra phases around 370 K and 405 K, indicated by the arrows. b) Determination of the Curie temperature of the ferromagnetic phase transition from a) by plotting the square of the magnetization vs. temperature. According to the molecular field model (Equation 2.4), the Curie temperature can be derived from the intersection of a linear fit to the data points, shown in black dashed, with the x-axis. Since a residual magnetization of 400 kA/m remains after the phase transition, which indicates another ferromagnetic phase with a higher Curie temperature, the intersection of the linear fit with the black dashed horizontal line at $(400\,\mathrm{kA/m})^2$ is determined here. This results in $T_C = 544 \pm 8\,\mathrm{K}$.

To determine the Curie temperature, the square of the magnetization is plotted against the temperature, as described in the work of Bayreuther et al. (1996) [174]. The intersection point with the x-axis ($M = 0$) is then determined via a linear fit to the data, as illustrated in Figure 8.1 b). Consequently, this approach treats the phase transition as described by Equation 2.4 according to the molecular field model, with the order parameter $\beta = 1/2$ (see Chapter 2.2.2). It should be noted that the magnetization after this phase transition is still 400 kA/m, which is due to the occurrence of another ferromagnetic phase with a higher Curie temperature. This is explained by remaining bcc Fe in the samples ($T_C = 1028\,\mathrm{K}$). Accordingly, the intersection point of the linear fit with the horizontal black dashed line at $(400\,\mathrm{kA/m})^2$ shown in Figure 8.1 b) is determined rather than the intersection point with the x-axis. The resulting Curie temperature is found to be $544 \pm 8\,\mathrm{K}$, as also displayed in Figure 8.1. Figure 8.1 a) also indicates two additional phases, which are marked by the two arrows at around 370 K and 405 K. Nevertheless, the strong decrease from 950 kA/m to 400 kA/m indicates the transition of the main phase with $T_C = 544\,\mathrm{K}$, which will be the focus of the following discussion.

If the measured Curie temperature is compared with the Curie temperature of Fe_3C ($T_C = 485\,K$), an upward deviation of almost 60 K can be seen. This seems surprising when considering an arrangement of Fe_3C in between MXene layers, since a reduction of Curie temperature with decreasing particle size or layer thickness is generally expected due to finite size and interface effects (cf. Chapter 2.2.4) [81]. However, if Fe_3C would merely form clusters in voids of MXenes, the observed upward deviation cannot be explained either.
A possible reason could be alternative configurations of Fe, e.g. a binding to MXene layers as terminating atoms, partially mimicking the electronic structure of Fe_3C, as discussed in Chapter 7.1. In addition, in this case, as for a formation of Fe_3C between MXene layers, there may be mixing of electronic states at the interface to termination-free Ti atoms of MXenes (cf. Chapter 2.2.4). This could then, as was the original idea of this work (see Chapter 1), lead to an increase in the density of states (DOS) at the Fermi level of MXenes. As a possible consequence, the Stoner criterion may be fulfilled, resulting in ferromagnetic behavior of MXenes. If this is the case and magnetic coupling of the ferromagnetic layers occurs, this can stabilize the ferromagnetic phase and lead to a higher Curie temperature, as also theoretically calculated by Feng et al. (2022) [175] for 2D MnSn multilayers when increasing their thickness from 1 to 3 monolayers. Such a magnetic coupling should be evident from changes in the exchange splitting of spin$^{\downarrow}$ and spin$^{\uparrow}$ states of intercalated Fe (cf. Chapter 2.2.3), which is probed in the XMCD measurements in Chapter 8.2.
As discussed in Chapter 7.1 a metastable phase of α-Fe + Fe_3C occours below 1000 K. However, as reported by Schneider et al. (2001) [176] there is also a possibility of a three phase equilibrium of α-Fe/Fe_3C/Fe_5C_2. Here the Curie temperature of the carbon richer compound Fe_5C_2 is reported to be 538 K [177]. Considering the work of Zhao et al. (2021) [178], it is obvious that the XANES spectrum of Fe_5C_2 is not significantly different from that of Fe_3C. However, it should be noted that for mixed Fe_3C/Fe_5C_2 phases, Fe_3C is observed as the majority phase [177]. In addition, the question arises as to the carbon sources for the formation of the carbon-richer Fe_5C_2 phase in MXenes (cf. Chapter 7.1). This leads to the conclusion that an additional Fe_5C_2 phase cannot be (solely) responsible for the observed upward deviation of the Curie temperature.

8.1.2. Saturation magnetization and coercive field of $Ti_3C_2T_{x,th}$+Fe MXenes

In the following, magnetic hysteresis loops for the two cases of MXenes with intercalated Fe described above are considered. Here, the external field is applied in the sample plane. Applying an out-of-plane magnetic field to the samples causes their magnetization to increase linearly with the field and drop back to zero in the same way when the field is removed, identifying this as the hard direction of magnetization.
The in-plane hysteresis curves are shown for a $Ti_3C_2T_{x,th,1000K} + Fe_{700K}$ MXene at temperatures of 10 K in black, 100 K in green and 300 K in red in Figure 8.2 a). For $Ti_3C_2T_{x,th,675K} + Fe_{800K}$ MXenes from the previous chapter, the hysteresis curves are recorded at 5 K (blue), 100 K (black), 200 K (green) and 300 K (red), as depicted in Figure 8.2 b).

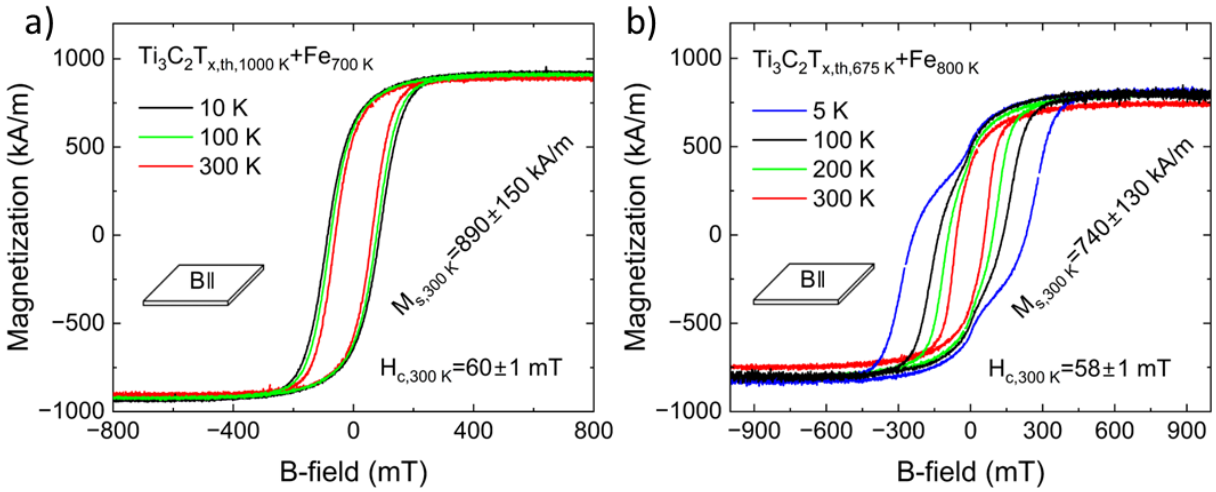

Figure 8.2.: a) Magnetic hysteresis curves of a $Ti_3C_2T_{x,th,1000K} + Fe_{700K}$ MXene in in-plane geometry at temperatures of 300 K (red), 100 K (green) and 10 K (black). At 300 K, a saturation magnetization of 890 ± 150 kA/m and a coercive field of 60 ± 1 mT are found. The saturation magnetization amounts to 60 % of the value for an Fe film initially deposited on the samples (see Figure A.13 b)) while the coercive field is 8 times higher. As the temperature decreases, both the coercive field and the magnetization increase slightly. The latter can be explained by Bloch's law (Equation 2.5). The increase of the coercive field with decreasing temperature is attributed to pinning of domain walls due to reduced thermal energy. b) Magnetic hysteresis curves of a $Ti_3C_2T_{x,th,675K} + Fe_{800K}$ MXene taken in in-plane geometry at temperatures of 300 K (red), 200 K (green), 100 K (black) and 5 K (blue). The saturation magnetization at 300 K results in 740 ± 130 kA/m and the coercive field in 58 ± 1 mT. Below about 100 K, the hysteresis curves show a broadening that leads to a significant increase in coercive field. Also, at 5 K there is a small shift of the hysteresis loop along the field axis of -3.5 mT. These observations indicate an exchange coupling of a ferromagnetically soft and hard material in the sample.

Considering first the case of $Ti_3C_2T_{x,th,1000K} + Fe_{700K}$ MXenes, where intercalated Fe is expected as near-surface bcc Fe clusters in voids of the samples (see previous chapters), a coercive field of 60 ± 1 mT and a saturation magnetization of 890 ± 150 kA/m are found at $T = 300$ K. Comparing these with the corresponding values of a hysteresis curve of Fe initially deposited on MXenes as a 6 nm film, shown in Figure A.13 b) in the Appendix, an 8-fold higher coercive field is observed after Fe intercalation. On the other hand, the saturation magnetization drops to around 60 % as a result of Fe intercaltion. Since the X-ray absorption spectroscopy (XAS) data from Chapter 7.1 clearly indicate bcc Fe, oxidation of Fe and formation of other compounds can be excluded as a cause for the reduced saturation magnetization. Instead, the decrease in saturation magnetization and increase in coercive field is attributed to formation of small Fe clusters in MXene samples. Here, it is expected that finite size and interface effects lead to changes in the saturation magnetization and coercive field (cf. Chapter 2.2.4) [81], while the majority of Fe sees its standard bcc environment.

A look at the hysteresis curves at different temperatures in Figure 8.2 a) shows a slight increase in coercive field to 87 ± 1 mT at 10 K, as typical for ferromagnetic materials [179]. The reason for this lies in the energy required to unpin a domain wall (see Chapter 2.2.2). The input of thermal energy reduces this energy and helps to overcome the potential of the pinned state, causing the coercive field to decrease with increasing temperature. In addition, a slight increase in saturation magnetization can be identified with decreasing temperature, which can be explained by Bloch's law according to Equation 2.5.

Next, the case of $Ti_3C_2T_{x,th,675K} + Fe_{800K}$ MXenes shown in Figure 8.2 b) is examined. Here, the coercive field at 300 K amounts to 58 ± 1 mT and the saturation magnetization to 740 ± 130 kA/m. The coercive field is thus comparable to that of $Ti_3C_2T_{x,th,1000K} + Fe_{700K}$ MXenes. However, the saturation magnetization is only about 80 % as high. Considering the saturation magnetization of Fe_3C (1131 kA/m) [180] and of Fe (1715 kA/m) [181], only 65 % of the saturation magnetization would be expected if Fe were present in this sample exclusively in the form of Fe_3C. However, these considerations should be treated with caution in view of the large errors due to volume determination. The overall lower saturation magnetization and larger coercive field compared to the corresponding values of the Fe film originally deposited on MXenes (see Figure A.13 b)) are explained by finite size and interface effects, as in the case discussed above. It is worth noting that the two cases considered behave similarly at 300 K, with the exception of the slightly lower saturation magnetization, which is attributed to formation of Fe_3C and/or Fe in a local environment similar to that of Fe_3C.

Looking at the hysteresis loops of $Ti_3C_2T_{x,th,675K} + Fe_{800K}$ MXenes at low temperatures, a significant increase in coercive field with decreasing temperature can be observed. At 100 K the coercive field already amounts to 133 ± 1 mT and at 5 K is as high as 239 ± 1 mT. In addition, the hysteresis loops at 5 K (blue) and 100 K (black) in Figure 8.2 b) show that the change in magnetization when the external field is reversed displays a discontinuity at around 0 mT, which broadens the hysteresis curves. This indicates that the pinning of domain walls can only be overcome at significantly higher B-fields. Moreover, a small shift of -3.5 mT along the field axis is observed at 5 K (blue curve in Figure 8.2 b)). Both observations indicate an exchange coupling of a ferromagnetically soft with a ferromagnetically hard material, as also investigated by Polisetty et al. (2008) [182], who studied an exchange-coupled bilayer of ferromagnetically hard CoPtCrB and ferromagnetically soft CoCr. Here, the magnetically hard material with high coercivity leads to a pinning of the magnetically soft material with high saturation magnetization [183], while interlayer exchange shifts the hysteresis loop of the soft material along the field axis [182]. This is also referred to as exchange spring magnet [183].

The state of intercalated Fe in MXenes can be considered diverse, as outlined in the previous chapters. Consequently, various causes for the occurrence of exchange coupling can be assumed here. For example, as discussed in Chapter 7.1, Fe_3C is metastable, so that there is always a mixed phase of α-Fe and Fe_3C. This is supported by the temperature-dependent magnetization curves (see Figure 8.1 a)) where a residual magnetization of 400 kA/m is observed after the

phase transition at 544 K, which is attributed to remaining bcc Fe (see Chapter 8.1.1). Also, there is the possibility of a small part of Fe in a Fe_5C_2 phase (cf. Chapter 8.1.1). Additionally, other configurations of Fe must be considered, e.g. binding to MXene layers as a termination species, partially mimicking the electronic structure of Fe_3C (cf. Chapter 7.1). In this context, it is expected that Fe in the aforementioned configurations is also located in between the MXene sheets (cf. Chapter 7). It is therefore postulated that there are some preferred atomic configurations of intercalated Fe in MXenes that exhibit hard or soft ferromagnetic behavior and that are magnetically exchange-coupled. To what extent an intrinsically ferromagnetic behavior of the Ti_3C_2 MXene layers occurs as a potential result of hybridization of electronic states of Fe and Ti atoms, leading to exchange coupling as hypothesized in Chapter 8.1.1, cannot be deduced from the present data. However, the exchange coupling proposed by hysteresis loops is consistent with the hypothesis put forward in the previous chapter that the increased Curie temperature compared to the Curie temperature of Fe_3C is a consequence of magnetic exchange coupling. To further decipher the magnetic behavior of the samples, the magnetism of intercalated Fe in MXenes is investigated element-specifically by XMCD measurements at the Fe K-edge in the next chapter.

8.2. Magnetic fingerprint of Fe in $Ti_3C_2T_{x,th}$+Fe MXenes

The electronic structure of intercalated Fe in MXenes is investigated by XMCD measurements for the two cases discussed above. From the analysis of hysteresis curves and the increased Curie temperature, a magnetic exchange coupling was deduced in Chapter 8.1 for $Ti_3C_2T_{x,th,675K} + Fe_{800K}$ MXenes. For this case, which represents MXenes thermally activated at low temperatures < 675 K with intercalated Fe, it is of particular interest to investigate whether an exchange coupling can be identified here as well.

The XMCD is based on the transfer of angular momentum from circularly polarized X-rays to excited photoelectrons when the former are absorbed at an absorption edge (cf. Chapter 7.1). If left and right cicularly polarized X-rays are used and the density of states for $spin^{\downarrow}$ and $spin^{\uparrow}$ states is exchange-split, there is a higher absorption for one helicity than for the other. The XMCD signal then results from the difference between the XANES spectra for left and right circularly polarized light. In contrast to XMCD at the L-edge, which also provides information on the spin moment, K-edge XMCD only probes the orbital magnetic moment [149]. This is because the s-state is not spin-orbit split here [149]. Note that the 4p state of Fe might be slightly populated due to hybridization with 3d states, so they get polarized by spin-orbit coupling.

The XMCD measurements are performed at beamline ID12 of ESRF. Here, 16 XANES spectra are recorded at 300 K for each sample at the Fe K-edge with left and right circularly polarized X-rays, which hit the sample under 15° grazing incidence in $B = \pm 1$ T parallel to X-ray. Thus, a total of 64 XANES spectra and 16 XMCD signals per B-field direction are obtained. For evaluation, first the 64 XANES spectra and the 16 XMCD signals of each field direction are av-

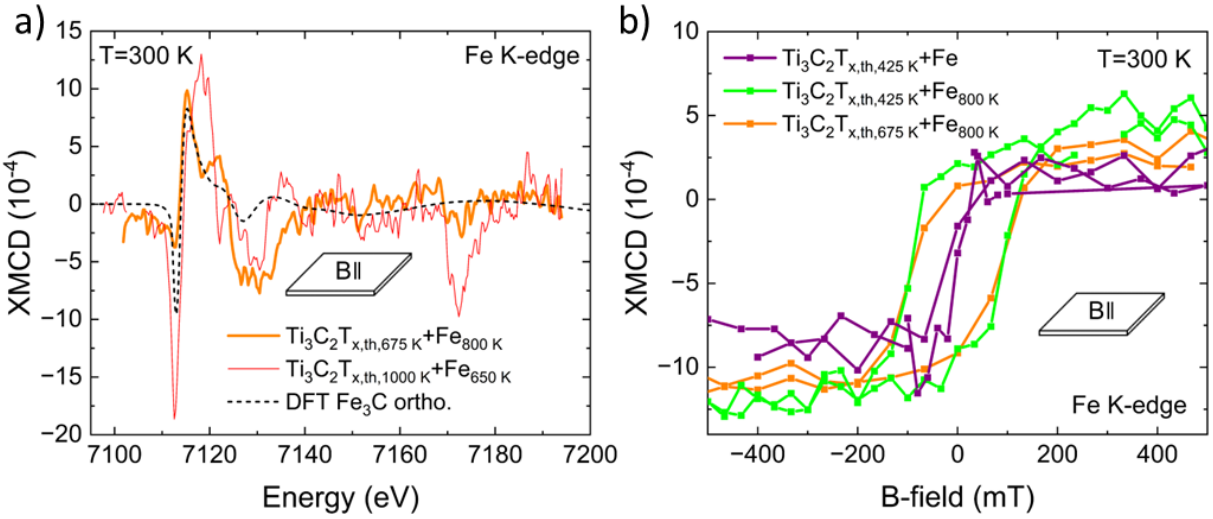

Figure 8.3.: a) XMCD spectra at the Fe K-edge at 300 K of a $Ti_3C_2T_{x,th,675K} + Fe_{800K}$ MXene in orange and a $Ti_3C_2T_{x,th,1000K} + Fe_{650K}$ MXene in red relative to the normalized XANES intensity (see Figure 7.2 and 7.3) [155]. In addition, the XMCD spectrum from DFT simulations of Fe_3C is shown as a black dashed line [156]. A comparison with the literature shows an agreement of the red spectrum with that of Fe, while the orange spectrum shows spectroscopic features observed for Fe_3C. However, as the comparison with the DFT simulated XMCD signal shows, the orange spectrum also exhibits features not observed for Fe_3C. b) XMCD signal recorded at the maximum (7116 eV) of XMCD spectra at the Fe K-edge as a function of external field in in-plane geometry at 300 K. This is plotted for a $Ti_3C_2T_{x,th,425K} + Fe$ MXene with a 6 nm Fe film on the surface in violet, for the same sample after Fe intercalation at 800 K in green, and for $Ti_3C_2T_{x,th,675K} + Fe_{800K}$ MXenes in orange. The resulting hysteresis curves prove the ferromagnetic behavior of intercalated Fe element-specifically. Furthermore, in analogy to the magnetometry measurements, an increase in coercivity is observed after Fe intercalation.

eraged. The resulting 2 XMCD spectra (one for each field direction) are also averaged, whereby the signal obtained is divided by 2 and added to or subtracted from the averaged XANES signal. In this way, the subtraction of the two resulting XANES spectra would again yield the XMCD spectrum. However, the two XANES signals are first normalized and then subtracted from each other, resulting in the XMCD signals shown in Figure 8.3 a) for a $Ti_3C_2T_{x,th,675K} + Fe_{800K}$ MXene in orange and a $Ti_3C_2T_{x,th,1000K} + Fe_{650K}$ MXene in red. As the corresponding XANES spectra of both samples have already been shown in Figure 7.3 and 7.2, also in orange and red, respectively, they are not displayed here.

Comparing the XMCD spectra shown in Figure 8.3 a) with the work of Duman et al. (2005) [184], who investigated Fe_3C by XMCD measurements at the Fe K-edge at room temperature and pressures up to 20 GPa, spectroscopic features can be found for the orange-colored spectrum that are also observed in the XMCD spectrum of Fe_3C. Looking additionally at the DFT simulated (cf. Chapter 7.1) XMCD spectrum of Fe_3C, which is shown as a black dashed line,

a similarity can also be seen here. However, there are three distinctive features in the recorded spectrum (orange) that are not observed in the DFT simulated signal and also not present in the XMCD spectrum of Fe_3C measured by Duman et al. (2005) [184]. These are, on the one hand, the peak that occurs at the shoulder at 7121 eV and on the other hand the dips around 7130 eV and 7173 eV. The spectroscopic features of the red spectrum in Figure 8.3 a) are similar to those found in XMCD spectra of Fe [184]. This is consistent with the observations from Chapter 7, according to which an accumulation of bcc Fe in voids of the samples is expected for $Ti_3C_2T_{x,th,1000K} + Fe_{650K}$ MXenes.
The dip at 7173 eV in the orange spectrum indicates that some Fe is still present in the samples that is not in the form of Fe_3C and/or Fe in a local environment similar to that of Fe_3C. This is supported by the non-vanishing magnetization after the phase transition at 544 K (see Figure 8.1 a)), which indicates remaining bcc Fe in the samples. The peak at 7121 eV and the dip around 7130 eV are interpreted as a consequence of the discussed diversity of possible atomic configurations of intercalated Fe in MXenes thermally activated at $T < 675$ K, which is also considered to be the reason for the observed magnetic exchange coupling (see discussion in Chapter 8.1.2). In order to gain further insights into preferred atomic configurations of intercalated Fe in MXenes and the resulting magnetic properties of the samples, further DFT calculations are necessary, which take into account a termination of MXenes by Fe at different adsorption sites, as well as an arrangement of Fe_3C/Fe in between MXene sheets. As these are considerably more complex than the simulation of Fe_3C or bcc Fe, they are not performed within the scope of this work. Additional experimental approaches to further resolve the magnetic behavior of MXenes with intercalated Fe are discussed in Chapter 10.
Finally, Figure 8.3 b) is considered. Here, the XMCD signal at the maximum (7116 eV) of XMCD spectra at the Fe K-edge is shown under variation of the B-field in in-plane geometry at $T = 300$ K. This is presented for a $Ti_3C_2T_{x,th,425K}$ + Fe MXene with a 6 nm Fe film on the surface in violet, for the same sample after intercalation of Fe at 800 K in green, and for $Ti_3C_2T_{x,th,675K} + Fe_{800K}$ MXenes in orange. Hysteresis curves are visible here, confirming the ferromagnetic behavior of intercalated Fe element-specifically. In addition, an increase in coercive field is observed after Fe intercalation. Here, intercalated Fe in $Ti_3C_2T_{x,th,675K} + Fe_{800K}$ MXenes shows a coercive field of 85 ± 10 mT when measured at half saturation magnetization, i.e. at an XMCD intensity of -4×10^{-4}. The coercive field shows a slight upward deviation compared to the value obtained from magnetometry measurements for this sample of 58 ± 1 mT (see Chapter 8.1.2). However, this is attributed to the limited number of measuring points of the hysteresis loop from XMCD measurements, which leads to a relatively large error that also prevents an evaluation of the coercive field for $Ti_3C_2T_{x,th,425K}$ + Fe MXenes with 6 nm Fe on the surface (violet curve).

9. Summary

The aim of this work was to investigate the interaction of MXenes with Fe to form a new magnetic 2D material. For this, the strategy chosen was to partly remove the initial surface terminations $T_x := O$, $-OH$, $-F$ and $-Cl$ of $Ti_3C_2T_x$ MXenes and replace them by Fe. Here, the motivation was to enrich the list of exceptional properties of the 2D van der Waals (vdW) materials MXenes by adding ferromagnetism, which had not yet been included. This promises potential future applications in the fields of spintronics, magnonics, quantum computing and magnetic sensing.
A decommissioned ultra high vacuum (UHV) chamber was successfully put back into operation, undergoing extensive modifications to meet the requirements for *in situ* treatment and analysis of $Ti_3C_2T_x$ MXene samples. This includes measurements of the composition by Auger electron spectroscopy (AES), annealing of MXenes at temperatures up to 1000 K to remove the surface terminations and intercalated water while monitoring the process by mass spectrometry, as well as the deposition of Fe on the samples, its thermally driven intercalation and parallel recording of the Fe diffusion process by AES.
In the following, the questions raised in Chapter 1 in connection with the objectives of this work are summarized and discussed.

First to question 1 raised in Chapter 1:

1. To what extent can the surface terminations $T_x := O$, $-OH$, $-F$ and $-Cl$ of $Ti_3C_2T_x$ MXenes be removed by annealing in UHV? What temperatures are necessary to remove which T_x species and how does the interplanar spacing between the stacked MXene sheets change?

Using *in situ* mass spectrometry, it was found that T_x : $-OH$, $-F$ and $-Cl$ as well as H_2O intercalated between MXene sheets are removed from MXenes by thermal annealing in UHV conditions starting from temperatures of around 575 K. In this context, it was shown by *in situ* AES measurements that thermal activation at 1000 K for 10 min leads to a removal of more than 80 % of the original $-Cl$ and $-F$ terminations. Furthermore the mass spectrometry measurements suggest a complete removal of the adsorbed/intercalated H_2O molecules together with $-OH$ terminations when annealing to 1000 K. This is also reflected by the interplanar spacings extracted from *ex situ* wide angle X-ray scattering (WAXS) and X-ray diffraction (XRD) measurements. Here it was established that especially intercalated water and Li^+, which remains from the synthesis of MXenes by etching the A element of a Ti_3AlC_2 MAX precursor with a mixture of HCl and LiF, have a significant influence on the interplanar distance. The removal of

intercalated water as a result of thermal activation at 1000 K leads to a decreasing interplanar spacing of up to 30 %. However, = O terminations and Li^+ can only be removed at temperatures above 1000 K, where the Ti-C bonds of the MXenes begin to degrade. This results in two interplanar distances found in the samples after annealing at 1000 K: $d = 1.03 \pm 0.07$ nm in regions mainly terminated by = O, or $d = 1.21 \pm 0.09$ nm in regions where = O and residual Li^+ remain between the layers.

Now to question 2 raised in Chapter 1:

2. Is it possible to intercalate a film of Fe deposited on a MXene sample in between the MXene sheets in UHV, and how does the diffusion process take place? What is the chemical state of the intercalated Fe? Is there an interaction between the intercalated Fe and the MXene layers? How does the intercalation of Fe change the interplanar spacing?

The diffusion parameters for Fe diffusion in $Ti_3C_2T_x$ MXenes were determined by *in situ* AES measurements, *ex situ* X-ray photoelectron spectroscopy (XPS) depth profiling and scanning transmission electron microscopy together with energy-dispersive X-ray spectroscopy (STEM-EDS) cross section analysis. It was shown that measuring the concentration of the Fe film initially deposited on the sample surface during its intercalation using *in situ* AES is a faster and more flexible alternative to the established determination of diffusivities from XPS depth profiles. In addition, the STEM-EDS cross section analysis enables local information on the diffusivities and penetration depth of Fe. The diffusion of Fe in MXenes is characterized by low diffusivities perpendicular to the sheets in the order of $D_\perp \sim 10^{-21}\,m^2\,s^{-1}$ to $\sim 10^{-20}\,m^2\,s^{-1}$ and a low activation energy of $E_A = 0.10 \pm 0.01$ eV, reflecting a diffusion around 2D MXene sheets or stacks of MXene sheets. There is a 35-fold higher diffusivity of Fe in MXenes and a 2 times greater penetration depth when MXenes are thermally activated at low temperatures (425 K) rather than at 1000 K, owing to the larger interplanar distances resulting from remaining surface terminations and intercalated water. In this context, it was shown that *in situ* electrical transport measurements during Fe intercalation allow simultaneous monitoring of Fe diffusion and removal of surface terminations/intercalated water at higher temperatures.
X-ray absorption near-edge structure (XANES) and X-ray linear dichroism (XLD) spectra at the Ti K-edge show no significant changes upon removal of the surface terminations or Fe intercalation. It is remarkable, however, that intercalated Fe is present in two different configurations depending on the thermal activation temperature of MXenes. Here, the XANES and XLD spectra at the Fe K-edge resemble the spectroscopic features of bcc Fe and Fe_3C for intercalated Fe in MXenes thermally activated at 1000 K and temperatures < 675 K, respectively. Thereby, intercalated Fe in MXenes thermally activated at 1000 K forms near-surface bcc clusters in voids of the samples. For MXenes thermally activated at temperatures < 675 K, a diffusion of Fe in between MXene layers is supported by a systematic upward deviation of the interplanar spacing ($d = 1.39 \pm 0.11$ nm) after Fe intercalation, as shown by XRD measurements. However, it

remains open if there is a formation of Fe_3C in between MXene sheets. Another question that arises in this context is whether alternative atomic configurations of Fe occur, e.g. binding to the MXene layers as a temination species partially mimicking the electronic structure of Fe_3C. Approaches to answer these questions are discussed in Chapter 10.

Finally, to question 3 raised in Chapter 1:

3. Do the $Ti_3C_2T_x$ MXenes show ferromagnetic behavior after the removal of the surface terminations and Fe intercalation? What is the Curie temperature and what is the saturation magnetization? And to what extent does the intercalated Fe contribute to the magnetism of the MXene samples?

Magnetic hysteresis loops from vibrating sample magnetometry (VSM) measurements at 300 K in in-plane geometry were observed for $Ti_3C_2T_x$ MXenes thermally activated at 1000 K or temperatures < 675 K with intercalated Fe, thus demonstrating a ferromagnetic response at ambient temperature.
For MXenes thermally activated at 1000 K with intercalated Fe, coercive fields of 60 ± 1 mT and saturation magnetizations of 890 ± 150 kA/m were identified at 300 K. These correspond to 8 times the coercive field and 60 % of the saturation magnetization observed for a 6 nm Fe film initially depsoited on the MXene sample surface. X-ray magnetic circular dichroism (XMCD) spectra measured at 300 K at the Fe K-edge of these samples show the spectroscopic features of Fe. Here, the magnetic characterization is consistent with the accumulation of bcc Fe in near-surface voids of the MXene samples thermally activated at 1000 K.
For MXenes thermally activated at low temperatures < 675 K with intercaletd Fe, coercive fields of 58 ± 1 mT and saturation magnetizations of 740 ± 130 kA/m were observed at 300 K. Below 100 K, the temperature-dependent hysteresis loops show an increasing coercive field with coupled magnetization of several layers. This results in a coercive field of 239 ± 1 mT at 5 K. The Curie temperature is 544 ± 8 K and thus 60 K higher than the Curie temperature of Fe_3C. XMCD spectra measured at the Fe K-edge at 300 K show spectroscopic features of Fe_3C but also additional features not expected for Fe_3C. Here, it remains open whether these observations reflect the diversity of possible atomic configurations of intercalated Fe in MXenes thermally activated at temperatures of < 675 K, including Fe_3C, bcc Fe as well as alternative configurations, e.g. Fe as a termination species of MXenes. Possible steps to verify this are discussed in Chapter 10.

10. Outlook

For the MXenes analyzed in this work, $=O$ terminations are always present, as the annealing temperatures required for their removal also lead to the degradation of Ti_3C_2 MXenes. For further analysis, it is therefore recommended to use a synthesis technique that prevents a termination by $=O$. One approach is the Lewis acidic molten salt (LAMS) method. This allows MXenes to be synthesized with only one termination species, for example $-Cl$ [13]. Based on the findings of this work, it can be expected that at annealing temperatures of around 700 K to 800 K, which also correspond to the typically applied Fe intercalation temperatures, $-Cl$ terminations can be completely removed leaving only Ti_3C_2 layers and intercalated Fe. In this case, a potential termination of MXenes by Fe is less complex and easier to characterize experimentally and theoretically, since no additional surface terminations need to be considered. Furthermore, there is the possibility that a state corresponding to a MAX phase may be achieved with Fe as an A element. The work of Zha et al. (2021) [185], which theoretically investigated the structural and electronic properties of a Ti_3FeC_2 MAX phase, predicts its metastability in this context.
Obtaining termination-free Ti_3C_2 MXenes with intercalated Fe is also expected to further enhance the ferromagnetic response of the samples. In the present study, it is likely that the remaining $=O$ terminations reduce the density of states (DOS) of MXenes at the Fermi level [14, 68] and also partially prevent a potential hybridization of the electronic states of Fe atoms located in between MXene layers and Ti atoms of MXenes. Here, the LAMS synthesis method opens up future opportunities to investigate the magnetism of MXenes that may be terminated exclusively by Fe. Additionally, layered structures of Fe separated by MXenes may be achieved. In this case, an investigation of Fe intercalation between thinner Ti_2C MXenes is particularly interesting. The lower thickness of only 3 monolayers in a termination-free state could enable an indirect RKKY exchange coupling between the Fe layers mediated by the electrically conductive MXene sheets. This was also investigated theoretically by Power et al. (2013) [186] for magnetically doped graphene. Such investigations might be the basis for the future use of MXenes in spintronic devices. In this context, it would also be interesting to study the interlayer RKKY exchange for MXenes consisting of other elements, as these show different DOS and sheet thicknesses (lattice c-parameters) [14].
It was demonstrated that electrical transport measurements are a suitable method to live monitor diffusion of Fe into $Ti_3C_2T_x$ MXenes as well as the removal of surface terminations T_x. Therefore, a modification of the sample heater in the ultra high vacuum (UHV) chamber allowing additional *in situ* transport measurements is suggested. In this way, the degree of Fe interca-

lation and the extent to which surface terminations have been removed can be live monitored directly in the UHV preparation chamber and controlled by regulating the annealing temperature and time. Here, the electrical contacting of the samples must be designed in such a way that sample transfers from the load lock via the transfer stick are still feasible. It is also important that the contacts are shielded during the deposition of Fe.

The low diffusivity of Fe perpendicular to layered $Ti_3C_2T_x$ MXenes and a low activation energy for diffusion were found as a result of Fe atoms diffusing around 2D MXene sheets. This resulted in part of Fe remaining on the sample surface and low ratios of Fe to Ti in the MXenes. Here, the surface Fe always superimposes the signal of Fe intercalated in MXenes. In this context, it can be expected that the diffusion of Fe into MXenes is improved by a vertical alignment of MXene sheets on the substrates [144]. This would also allow to determine the diffusivities parallel to the sheets, and to quantify the difference between vertical and parallel diffusion. In addition, it could be investigated whether the same activation energy for diffusion is observed as for horizontally aligned MXenes. One approach to achieve vertical alignment of MXenes is to apply an alternating electric field. In the work of Lee et al. (2022) [187] this was successfully demonstrated for $Ti_3C_2T_x$ MXene sheets in an aqueous suspension on a glass substrate.

From X-ray absorption near-edge structure (XANES) and X-ray linear dichroism (XLD) spectra at the K-edge of Ti and Fe, it could not be finally resolved whether intercalated Fe in MXenes thermally activated at $< 675\,\mathrm{K}$ forms Fe_3C or is in a local environment similar to that of Fe_3C, e.g. when binding to MXene sheets as a termination species. Therefore, further density functional theory (DFT) calculations of XANES and XLD spectra of MXenes terminated at different adsorption sites by Fe or of MXenes where Fe_3C is located e.g. at defects between the sheets are planned. Moreover, additional investigation of the samples, e.g. by recording the extended X-ray absorption fine structure (EXAFS) [188] at the Fe and Ti K-edge, Raman spectroscopy [188] and ultraviolet photoelectron spectroscopy (UPS) [189], is proposed to further resolve the local environment of Fe.

To further investigate the magnetism of $Ti_3C_2T_x$ MXenes thermally activated at temperatures $< 675\,\mathrm{K}$ with intercalated Fe, studied in this work by magnetometry and X-ray magnetic circular dichroism (XMCD), ferromagnetic resonance (FMR) measurements are proposed to analyze occurring magnetic anisotropies. Here, FMR measurements are also suitable for gaining further insights with regard to the magnetic coupling identified for these samples. As an example, FMR measurements were performed by Richardson et al. (2019) [190] to characterize the exchange coupling of magnetically hard FePt with magnetically soft FeCo films. Some first FMR measurements at $300\,\mathrm{K}$ performed on $Ti_3C_2T_{x,\mathrm{th},675\mathrm{K}} + Fe_{800\mathrm{K}}$ MXenes show that at a microwave frequency of $9.4\,\mathrm{GHz}$ B-fields above $1.5\,\mathrm{T}$ are necessary to observe resonance lines when the samples are rotated from an in-plane to an out-of-plane orientation with respect to the field. As it was not possible to achieve sufficiently high fields with the equipment used, further measurements with a different FMR setup will be necessary in the future. In addition, the magnetoresistance should be analyzed to further decipher the magnetic properties of the samples.

A. Appendix

A.1. Thickness, homogenity and roughness of deposited Fe films

To calibrate the quartz crystal monitor (QCM), a Fe film is deposited on a Si(100)/SiO_2 substrate in the ultra high vacuum (UHV) chamber by electron beam (e-beam) evaporation, as also described in Chapter 3.2.2. By means of *ex situ* ellipsometry measurements using a *Horiba* Uvisel 2 ellipsometer, the Fe layer thickness is determined in the corners and in the center of the substrate, as shown in Figure A.1 a). Inserting the average Fe film thickness of 15.7 ± 0.9 nm

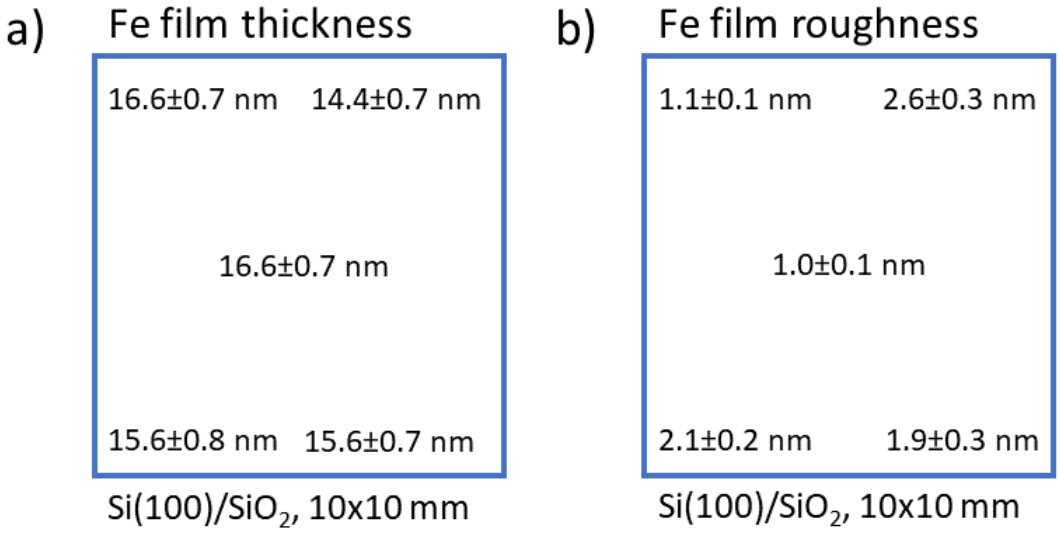

Figure A.1.: a) Thickness of a Fe film deposited on a Si(100)/SiO_2 substrate by e-beam evaporation in the UHV chamber. The layer thickness is determined both at the corners of the substrate and in the center via *ex situ* ellipsometry [191]. Here, the deposited Fe layer shows a high homogeneity over the entire substrate area with small deviations of the layer thickness from the center to the edges around 1 nm. The average Fe layer thickness amounts to 15.7 ± 0.9 nm. b) Roughness of the deposited Fe film in the corners and center of the substrate obtained from ellipsometry measurements. The average roughness of the Fe film is 1.7 ± 0.7 nm.

obtained from ellipsometry measurements and the film thickness of 9.2 nm read with the QCM into Equation 3.1 results in a tooling factor of 170.6 ± 17.1.

Figure A.1 a) shows that the Fe film is homogeneous over the entire area of the 10 mm×10 mm large substrates. Here, only slight deviations in the layer thickness of about 1 nm from the center to the corners of the substrate can be observed due to a large distance between the evaporator

and the substrate (about 30 cm). Considering the roughness of the Fe film in the different substrate areas in Figure A.1 b), it is on average 1.7 ± 0.7 nm. In view of the roughness of the spray coated MXene samples of about 45 nm (see Figure 4.6) and the roughness of the spin coated MXenes of about 200 nm (see Figure 4.4), the roughness of the deposited Fe film is negligible.

A.2. Calibration of the electron beam evaporator for C deposition

The deposition rate for electron beam (e-beam) evaporation of C in the ultra high vacuum (UHV) chamber is controlled by PID regulation of the flux rate (cf. Chapter 3.2.2). Therefore, the deposition rates at given flux rates are determined using the quartz crystal monitor (QCM). The resulting plot of the deposition vs. flux rate is shown in Figure A.2. Since the flux rate correlates with the number of evaporated atoms, a linear dependence can be seen in Figure A.2.

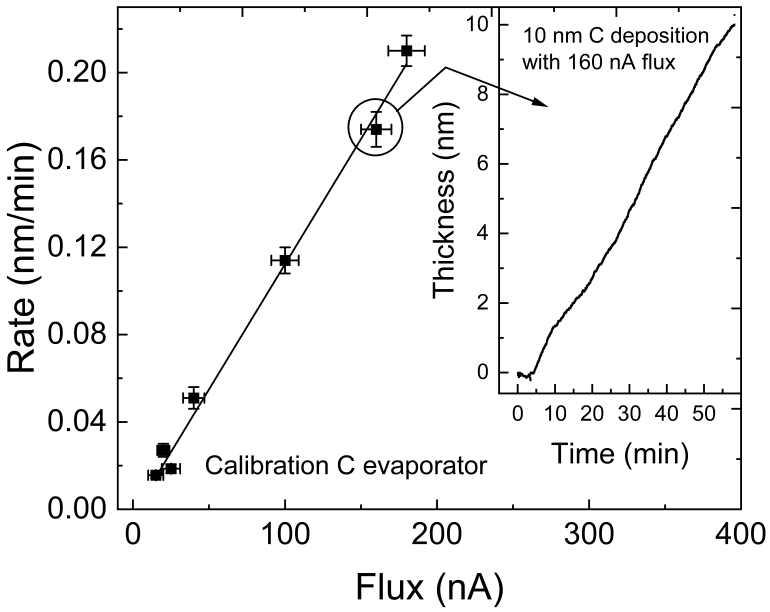

Figure A.2.: Deposition rates of C by e-beam evaporation in the UHV chamber as a function of the flux rate. The deposition rate is measured using the QCM. The flux rate is correlated with the number of evaporated atoms, which is reflected by the linear increase of the deposition vs. flux rate. The inset shows the deposition of 10 nm C at a flux rate of 160 nA. Here, an approximately linear increase in layer thickness over time can be observed. Slight deviations from the linear behavior are attributed to heat radiation of the evaporator, which brings the QCM out of its thermal equilibrium.

The deposition of 10 nm C at a set flux rate of 160 nA is shown in the inset in Figure A.2. Here, an approximately linear increase in the thickness of the deposited C film over time can be observed. Nevertheless, slight deviations from a linear slope are recognizable. This is explained by the heat radiation of the C evaporator, which is operated at temperatures of about 1800 K and more (see Chapter 3.2.2). As the PID control varies the emission current over time in order to maintain the specified flux rate, the heat radiated by the evaporator changes. This leads to fluctuations in the thickness measured by the QCM as it is brought out of its thermal equilibrium. This effect is significantly stronger for C evaporation compared to the evaporation of Fe where temperatures of around 1000 K are sufficient to generate the necessary vapor pressures (see Chapter 3.2.2).

A.3. Calibration of the cylindrical mirror analyzer for Auger electron spectroscopy

To find the settings for the optimal resolution of the cylindrical mirror analyzer (CMA) installed in the ultra high vacuum (UHV) chamber for Auger electron spectroscopy (AES) measurements, the peak-to-peak amplitude of the elatic peak of the backscattered primary electrons (1 keV) is maximized (cf. Chapter 3.3.2). One way to achieve this is by increasing the primary electron beam current. As can be seen in Figure A.3, the peak-to-peak amplitude of the elastic peak increases linearly with primary electron beam currents below 20 μA. For larger values, however, a nonlinear behavior is observed. This is due to the fact that, as explained in Chapter 3.3.2, heating and charging effects of the sample as well as its destruction by the electron beam lead to a change in the Auger peak shapes and thus to a change in the peak-to-peak amplitude in the differentiated spectrum. These effects are intensified if the primary electron beam current is increased further, which leads to the observed saturation behavior of the peak-to-peak intensity. In this context, a maximum beam current of 20 μA is used in this study.

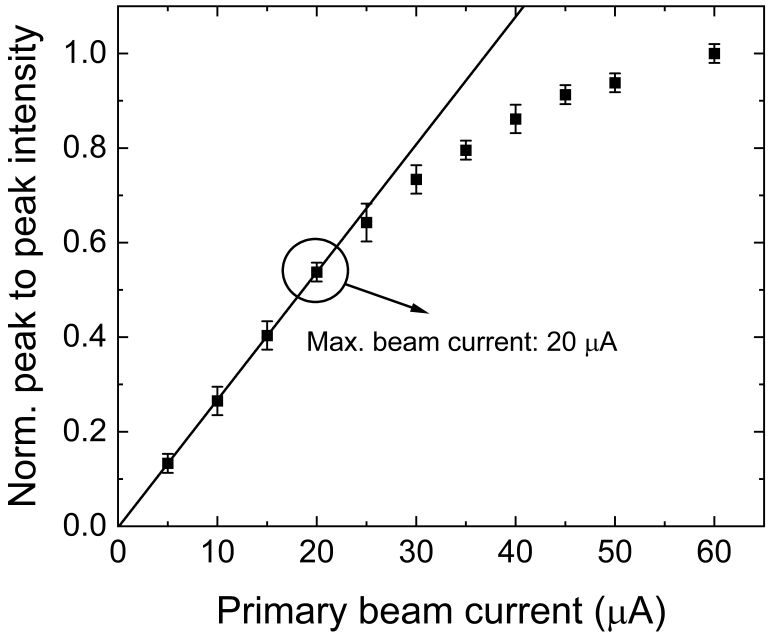

Figure A.3.: Normalized peak-to-peak intensity of the elastic peak of backscattered primary electrons as a function of the primary electron beam current. Above values of 20 μA, the peak-to-peak amplitude no longer increases linearly and begins to saturate. This is due to heating and charging effects as well as the destruction of the sample by the electron beam, which affects the Auger peak shapes and thus the peak-to-peak intensity in the differentiated spectrum.

A.4. X-ray diffraction and scanning electron microscopy on spray coated MXenes

In order to check the structure of the $Ti_3C_2T_x$ MXenes after spray coating as well as their orientation and the degree of coverage on the substrates, the spray coated samples are analyzed by X-ray diffraction (XRD) and scanning electron microscopy (SEM) analogously to the spin

coated samples (cf. Chapter 4.2). An XRD pattern and an SEM image taken after spray coating MXenes onto $Si(100)/SiO_2$ substrates are shown in Figure A.4.

The positions and relative intensity of the diffraction peaks of the XRD pattern agree well with those found after MXenes synthesis (see Figure 4.1). In addition, as for the spin coated MXenes, only diffraction peaks in the (00l) plane are observed, indicating the preferential alignment along the *c*-axis. However, the (002) diffraction peak shows only about 70 % of the intensity of the (002) peak observed for the spin coated samples (see Figure 4.3 b)). Moreover, only one (00l) peak of higher Bragg order is observed here, compared to 3 for the spin coated samples. These findings are attributed to the thin coverage of the substrates and thus to the low quantity of MXenes in the case of spray coating (cf. Chapter 4.3).

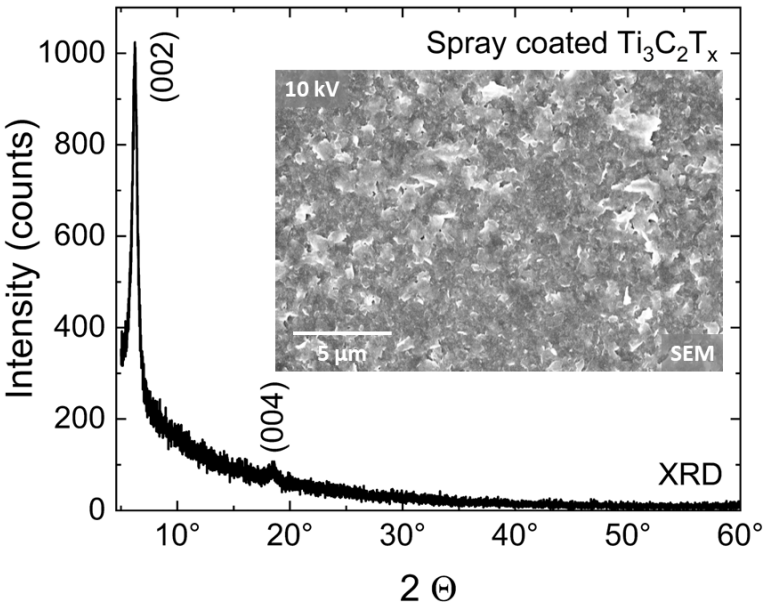

Figure A.4.: XRD pattern (Cu-K_α = 0.154 06 nm) of the spray coated $Ti_3C_2T_x$ MXenes on $Si(100)/SiO_2$ substrates recorded from 0 to 60°. The diffraction pattern shows the (00l) diffraction peaks also observed after the synthesis and spin coating of MXenes. In addition, the figure shows an SEM image of the sample surface taken at 10 kV. Here, a complete coverage of the substrate by MXenes in the observed sample area is evident as well as a horizontal alignment of the MXene sheets on the substrate. The smallest MXene flakes have a diameter of about 200 nm while the largest flakes are in the range of 1.5 μm [192].

The SEM image in Figure A.4 shows that the MXenes are arranged horizontally on the substrate, with the diameters of the flakes ranging from a maximum of 1.5 μm to a minimum of 200 nm. Furthermore, a complete coverage of the substrate by MXenes can be deduced from the section of the sample surface observed. This is supported by the atomic force microscopy (AFM) analysis discussed in Chapter 4.3.

A.5. Mass spectrometry reference measurements

The partial pressures of the termination species T_x desorbing from the MXenes into the vacuum during thermal activation are superimposed by a background caused by residual gases in the

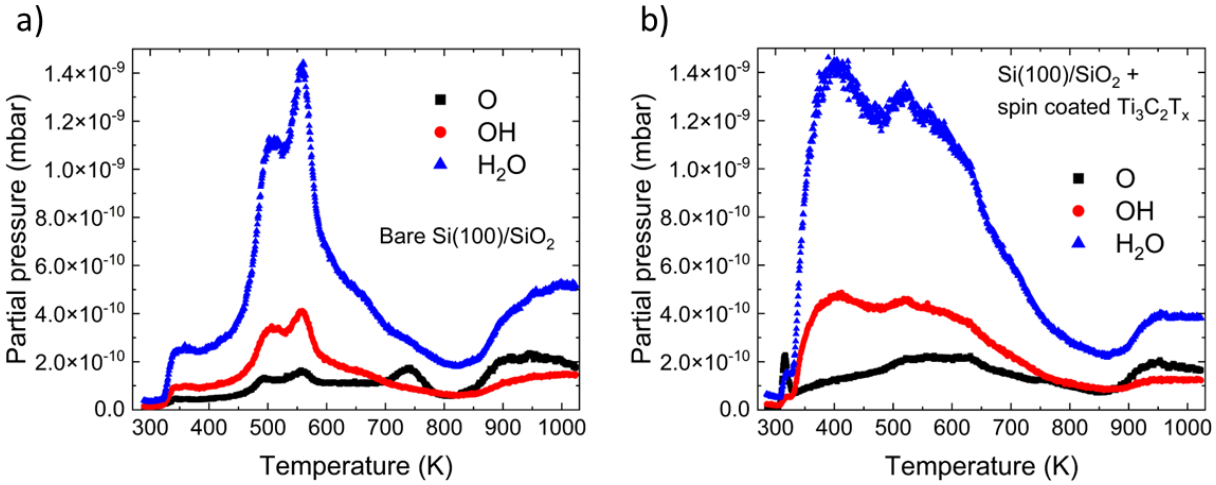

Figure A.5.: a) Partial pressures of O, OH and H_2O as a function of the sample temperature in the case of a bare $Si(100)/SiO_2$ substrate. b) Partial pressures of O, OH and H_2O as a function of the sample temperature in the case of a spin coated MXene sample.

ultra high vacuum (UHV) chamber. This background signal must be subtracted as described in Chapter 5.1. Accordingly, the thermal activation by annealing the samples to 1000 K at a heating rate of 10 K/min is recorded via mass spectrometry once for a bare $Si(100)/SiO_2$ substrate without MXenes (1st measurement) and a second time for a spin-coated MXene sample (2nd measurement). If the relevant partial pressures of the 1st measurement are subtracted from those

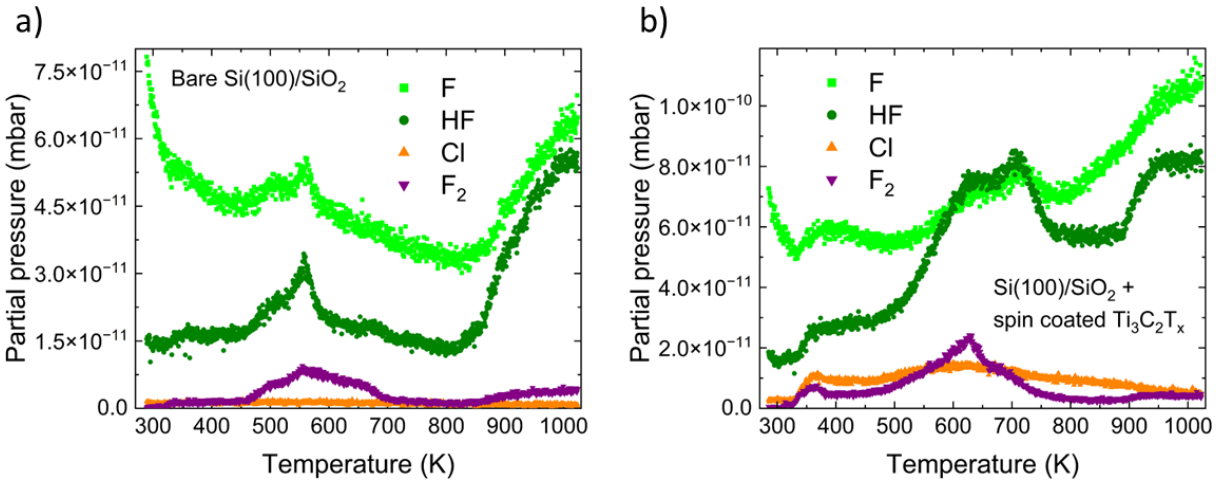

Figure A.6.: a) Partial pressures of F, Cl, HF and F_2 as a function of the sample temperature in the case of a bare $Si(100)/SiO_2$ substrate. b) Partial pressures of F, Cl, HF and F_2 as a function of the sample temperature in the case of a spin coated MXene sample.

of the 2nd measurement, the resulting signal solely reflects the partial pressures of the surface terminations that are removed as gaseous components during thermal activation.

Figure A.5 shows the partial pressures of O, OH and H_2O as a function of the sample temperature for the 1st measurement in a) and for the 2nd measurement in b). Figure A.6 shows the partial

pressures as a function of the sample temperature of F and Cl as well as of HF and F_2 for the 1st measurement in a) and for the 2nd measurement in b). The resulting partial pressures after background substraction are shown in Figure 5.1.

A.6. Thermal activation of commercial $Ti_3C_2T_x$ MXenes from *Nanoplexus*

The company *Nanoplexus* is a startup from Manchester dealing with the production and application of 2D materials, in particular MXenes and graphene [193]. In this context, *Nanoplexus* produces and distributes $Ti_3C_2T_x$ MXenes, amongst others. Here it is interesting to compare to what extent the commercial $Ti_3C_2T_x$ MXenes from *Nanoplexus* differ from the $Ti_3C_2T_x$ MXenes synthesized in this work (cf. Chapter 4.1). This allows to deduce whether the synthesis approaches deviate (composition of T_x) and how the commercial MXenes behave upon thermal activation. For this purpose, the MXenes from *Nanoplexus* are spin coated onto $Si(100)/SiO_2$ substrates and analyzed by Auger electron spectroscopy (AES). In addition, the samples are thermally activated at 1000 K for 10 min followed by recording a second Auger spectrum. The measured spectra are shown exemplarily for one sample in Figure A.7.

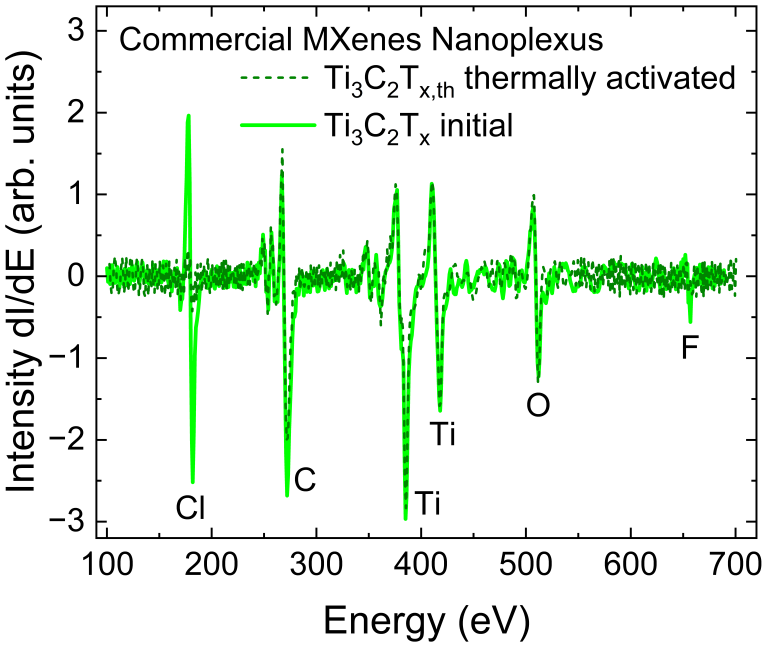

Figure A.7.: Auger spectra of $Ti_3C_2T_x$ MXenes from *Nanoplexus* before (light green) and after (dark green dashed) thermal activation at 1000 K. The two spectra are normalized to the Ti peak at 418 eV. Before thermal activation, the Ti and C signal of the Ti_3C_2 MXenes is observed, as well as signals of Cl, O/OH and F which indicate the composition of the T_x. After thermal activation, the signals of the terminations −F and −Cl fall within the detection limit of the CMA, suggesting efficient removal. On the other hand, the O peak remains almost unchanged, which indicates the preservation of = O as a termination species.

Prior to the thermal activation, the Auger spektrum of MXenes from *Nanoplexus* ($MXene_1$) shows the same composition of surface terminations (T_x : = O, −OH, −F, −Cl) as identified for the MXenes used in this work ($MXene_2$) (see Figure 5.2 a)). However, $MXene_1$ shows more

$-$Cl and less $=$ O/$-$OH/H_2O relative to the Ti peak at 418 eV than $MXene_2$. This may be due to a higher amount of HCl and less LiF when etching the A element of the MAX phase precursor. Nevertheless, analogous to $MXene_2$, the signals of $-$Cl and $-$F of $MXene_1$ fall below the detection limit of the cylindrical mirror analyzer (CMA) as a result of thermal activation. This underlines the efficiency of thermal activation to remove these components. As for $MXene_2$, the O signal of $MXene_1$ remains almost unchanged after thermal activation, which indicates that $=$ O remains as a termination species (also see discussion in Chapter 5.1).

A.7. Interplanar spacing of MXenes by X-ray diffraction analysis

To obtain an initial overview of changes in interplanar spacing between MXene sheets due to thermal activation, X-ray diffraction (XRD) measurements are performed on thermally non-activated and thermally activated (1000 K) spin coated MXenes with a *PANalytical* X'Pert PRO MPD diffractometer using Cu-K_α radiation. Subsequently, more sensitive wide-angle X-ray scattering (WAXS) measurements are performed on spray coated MXenes as discussed in Chapter 5.2.

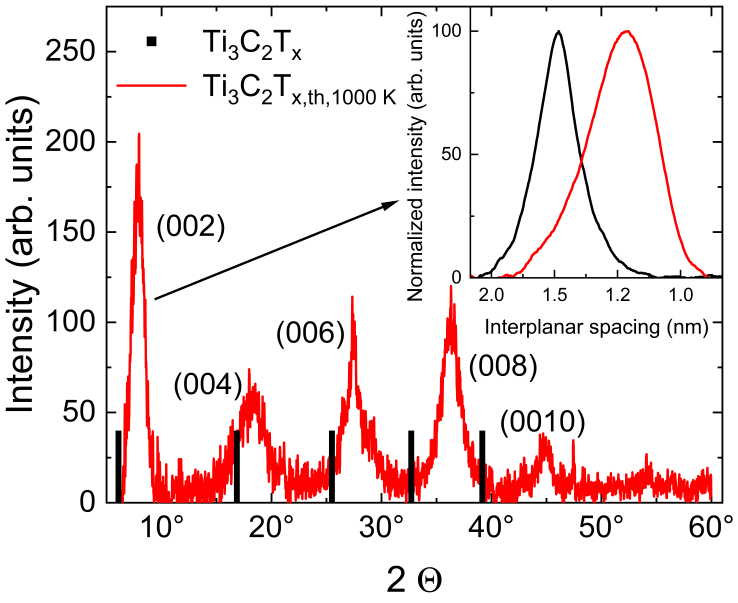

Figure A.8.: XRD pattern (Cu-$K_\alpha = 0.154\,06$ nm) of a spin coated MXene sample thermally activated at 1000 K (red). The peak positions of the diffraction peaks, determined from the XRD pattern of a thermally non-activated, spin coated sample, are marked by black columns. The inset shows the normalized and smoothed (002) diffraction peak of both samples as a function of the interplanar spacing. Here, a significant reduction of the interplanar distance and an asymmetry of the (002) diffraction peak (red) can be seen after thermal activation.

The recorded XRD pattern for a MXene thermally activated at 1000 K for 10 min is shown in red in Figure A.8. The peak positions of the diffraction peaks from measurements on a thermally non-activated MXene sample are marked as black columns. The inset also shows the normalized and smoothed (002) diffraction peak of both samples as a function of the interplanar spacing, derived from Bragg's law.

Looking at the peak positions of the (002) diffraction peaks in Figure A.8 a decrease in the interplanar distance after thermal activation can be seen. By fitting the (002) diffraction peak of the thermally non-activated sample

(black) with a pseudo-Voigt function (see Figure A.9 a)), an interplanar spacing of 1.45 ± 0.12 nm follows. This corresponds exactly to the interplanar distance observed later from WAXS measurements (see Chapter 5.2). Considering the (002) diffraction peak after thermal activation (red) an asymmetry is evident. This becomes even clearer with a shoulder in the (002) peak observed from WAXS measurements (see Figure 5.3 b)). For this reason, the diffraction peak is fitted by two Gauss functions (cf. Figure A.9 b)). From the two peak positions obtained in this way, interplanar spacings of 1.12 ± 0.10 nm and 1.26 ± 0.16 nm result. Comparing these with the interplanar distances observed in Chapter 5.2 from WAXS measurements (1.03 ± 0.07 nm and 1.21 ± 0.09 nm), there is a slight upward deviation. This could be explained by a longer time needed for the surface terminations to diffuse out of the thicker spin coated samples examined here. As a result, a larger number of surface terminations and H_2O may remain in the MXenes, which leads to larger interplanar spacings (cf. Chapter 5.2).

A.8. Fitting of the normalized (002) diffraction peak

To determine the position of the peak maximum of the (002) diffraction peaks, they are fitted before and after thermal activation as explained in Chapter 5.2. The interplanar spacing of the

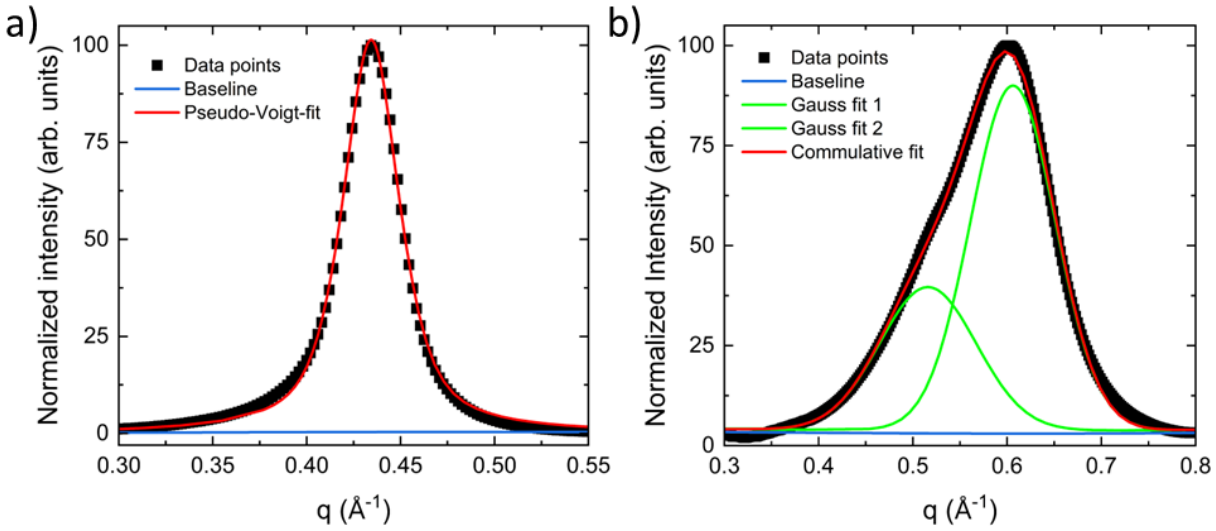

Figure A.9.: a) Pseudo-Voigt fit (red) of the (002) diffraction peak from WAXS measurements on a spray coated MXene sample thermally activated at 395 K. To perform the fit, a baseline (blue) is subtracted in a first step. The peak position and the FWHM can then be determined from the fit parameters. Here, the FWHM indicates the error of the resulting interplanar distance. b) Subtraction of a baseline (blue) and subsequent fitting by two Gauss functions (green) of the (002) diffraction peak obtained from WAXS measurements on a spray coated sample thermally activated at 1000 K. The commulative fit (red) shows good agreement with the data. The two Gauss fits lead to two peak positions, resulting in two different interplanar distances occurring in the sample.

MXenes can then be calculated from the respective peak position according to Equation 5.1 for wide-angle X-ray scattering (WAXS) measurements or for X-ray diffraction (XRD) measurements according to Bragg's law. The error of the interplanar distance obtained in this way is given by the full width at half maximum (FWHM) of the fit. Before thermal activation and after thermal activation at 395 K, a pseudo-Voigt function can be selected to fit the measured (002) diffraction peaks [194]. This is shown in Figure A.9 a), as an example, for the (002) diffraction peak obtained from WAXS measurements on a spray coated sample thermally activated at 395 K. After a thermal activation at 1000 K, the (002) diffraction peak shows an additional shoulder and an asymmetry, which is why two Gauss functions are fitted here. This is shown as an example in Figure A.9 b) for the (002) diffraction peak of a thermally activated (1000 K) spray coated sample obtained from WAXS measurements. The two peak positions found here result in two interplanar distances that occur in the sample.

A.9. Sample surface of $Ti_3C_2T_{x,th}$+Fe MXenes after Fe intercalation

In order to achieve a binding of Fe to termination-free Ti atoms of thermally activated $Ti_3C_2T_x$ MXenes, a typically 6 nm Fe film is deposited on the MXenes under ultra-high vacuum (UHV) conditions and intercalated by thermally driven diffusion as described in Chapter 6.1. In this

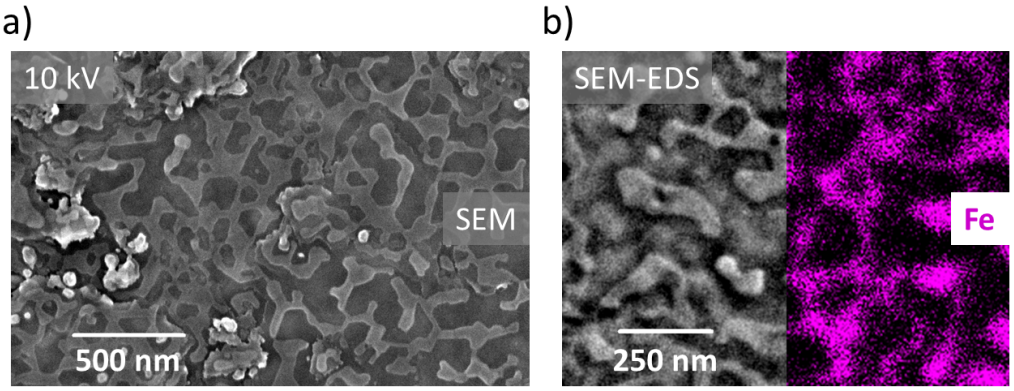

Figure A.10.: a) SEM image taken of the surface of a $Ti_3C_2T_{x,th,1000K} + Fe_{1000K}$ MXene after intercaltion of an initially 6 nm thick Fe film on the MXenes at 1000 K. A "camouflage pattern" is visible here, where the bright gray areas are attributed to remaining Fe on the sample surface as confirmed by the SEM-EDS measurements in b). It follows that after Fe intercalation about 50 % of the sample surface remain covered by Fe. b) SEM-EDS image of the sample from a). Here, the magenta colored areas indicate regions containing Fe which demonstrates that the light gray areas in a) show Fe that remains on the sample surface.

context, the area of the sample surface that remains covered by Fe after intercalation is an indication of whether a Fe reservoir is present on the surface throughout the diffusion process. This information is crucial for determining the boundary conditions when solving the diffusion equa-

tion (Equation 2.11) to describe Fe diffusion in MXenes. Therefore, the surface of a spin coated $Ti_3C_2T_{x,th,1000K}$ MXene sample thermally activated at a temperature of 1000 K is examined by scanning electron microscopy (SEM) after intercalating an initially 6 nm thick Fe film on the MXenes at a temperature of 1000 K. The SEM images are collected using a *Zeiss* LEO 1530 with Gemini field emission gun.
A SEM image taken of the MXene sample surface after Fe intercaltion is depicted in Figure A.10 a). Here, a "camouflage pattern" is visible which indicates remaining Fe on the surface. To verify this, and to check whether the light or dark gray areas of the pattern describe Fe, the sample is analyzed using scanning electron microscopy in conjunction with energy-dispersive X-ray spectroscopy (SEM-EDS). For these measurements the above mentioned SEM device is equipped with a *Oxford Instruments* X-Max EDS detector. From the SEM-EDS measurements shown in Figure A.10 b) it is apparent, that the light gray areas in the SEM image in Figure A.10 a) represent regions of Fe remaining on the sample surface. Consequently, even after the intercalation of Fe at the maximum annealing temperature of 1000 K, before the MXene structure decomposes (see Chapter 2.1.3), some of the Fe remains on the sample surface and forms clusters there. In this way, about 50 % of the sample surface remains covered by Fe (see Figure A.10 a)). Consequently, a diffusion process of Fe into the MXenes occurs, where a reservoir of Fe is always present on the sample surface. The diffusion problem at hand can therefore be described by the Grube-Jedele formula (Equation 2.15).

A.10. Calculation of the sputter rate for XPS depth profiling

For X-ray photoelectron spectroscopy (XPS) depth profiling, the sputtering rate, i.e. the sample thickness z removed per time t, must be determined, as explained in the corresponding Chapter 6.1. In this way, the measured intensity of the Fe intercalated in the MXenes can be plotted as a function of the sample depth (see Figure 6.4), which is necessary to derive the diffusivity of Fe in the MXenes and to determine its penetration depth (cf. Chapter 6.1). The sputter rate for the measurements carried out in ultra high vacuum (UHV) at the VUV-photoemission beamline of the Elletra synchrotron light facility is calculated according to [195]:

$$\frac{z}{t} = \frac{M}{\rho \cdot N_A \cdot e} \cdot Y \cdot I. \tag{A.1}$$

Here, M describes the molar weight and ρ the density of the sputtered material, N_A the Avogadro constant, e the elementary charge, Y the sputtering yield and I the primary ion current density. Sputtering is performed with Ar^+ at an energy of 0.5 keV. The sputter yield for these parameters is then calculated using the software *SRIM* (Stopping and Range of Ions in Matter by J. F. Ziegler). Together with experimental values for the molar weight and density of the MXenes and a primary ion current density of 1.85 μA, a sputter rate of 0.098 nm/min is obtained.
For the measurements carried out in a UHV chamber using a *ULVAC-PHI* 5000 Versaprobe

II laboratory XPS, the sputter rate is determined experimentally. For this purpose, a spray coated $Ti_3C_2T_{x,th,1000K}$ + Fe MXene sample with a 6 nm Fe film deposited on the surface that is covered by 6 nm C for oxidation protection is sputtered while repeatedly recording XPS spectra of Fe 2p, Ti 2p and C 1s with ongoing sputter time. The sputtering is carried out with the same parameters as for the samples discussed in Chapter 6.1 (Ar^+ at 2 keV, see Figure 6.4 b)). The resulting intensity of Fe, Ti and C, determined from the area under the XPS spectra of Fe 2p, Ti 2p and C 1s, is shown as a function of the sputter time in Figure A.11. As the thickness of the Fe and C film is known, the sputter rate can be determined. Due to the roughness of the MXenes and the Fe film, an overlap of the signals of Fe/C and Fe/Ti is observed. For this reason, the full width at half maximum (FWHM) of the Fe signal is determined which is expected to reflect the actual deposited Fe thickness of 6 nm. The FWHM results in 5.83 min. Dividing the thickness of the Fe film by 5.83 min then yields a sputter rate of 1.03 nm/min. Comparing the point at which the C intensity in Figure A.11 reaches low levels close to the detection limit with the upper abscissa, which represents the sample depth determined from the calculated sputter rate, one finds a sample depth of around 6 nm. As this corresponds exactly to the thickness of the deposited C layer, the determined sputter rate is considered fairly accurate.

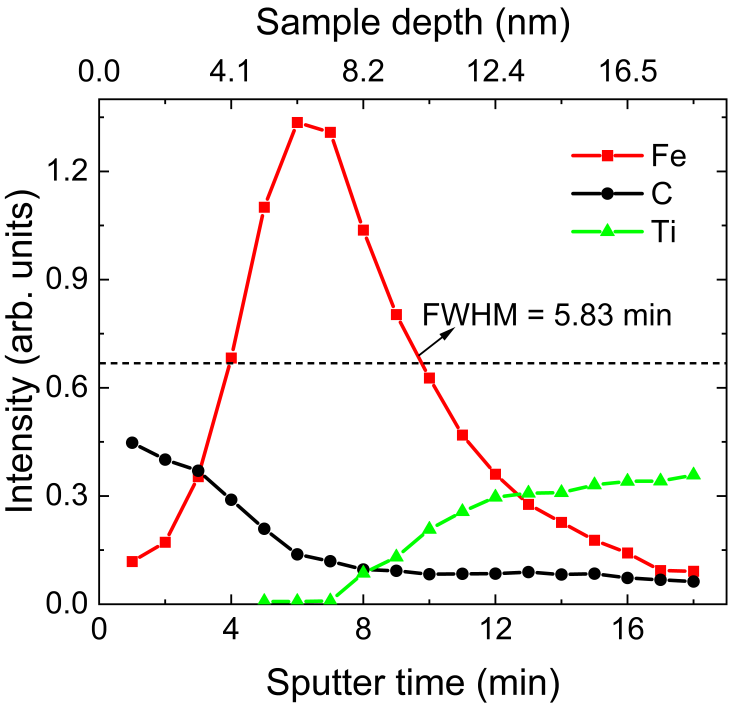

Figure A.11.: Intensity of Fe, Ti and C vs. sputtering time for a $Ti_3C_2T_{x,th,1000K}$ + Fe MXene sample with a 6 nm Fe film on the surface covered by 6 nm C [142]. Since the thickness of the Fe and C film is known, the sputter rate can be determined. As no sharp interface between Fe/C and Fe/Ti is observed, the FWHM of the Fe signal is determined. The resulting FWHM of 5.83 min together with the thickness of the Fe layer of 6 nm then leads to a sputtering rate of 1.03 nm/min. The upper abscissa shows the sample depth according to this sputter rate.

Nevertheless, for both sputter rates calculated here, an error of around 5 % to 10 % is predicted. Consequently, the specified sample depth in Figures 6.4 a) and b) are also subject to this error, which also affects the diffusivities of Fe in the MXenes determined by Equation 6.2 from the slopes in the penetration plots as discussed in Chapter 6.1.

A.11. Electrical transport measurements on $Ti_3C_2T_{x,th}$ MXenes

A specially designed sample holder is used for the electrical transport measurements on $Ti_3C_2T_x$ MXenes spray coated on $Si(100)/SiO_2$ substrates with a lithographic structure (cf. Chapter 6.3). This sample holder allows heating of the samples up to 800 K simultaneously to electrical transport measurements via 4 measuring pins that press on the contact pads of the lithographic structure on the substrates (cf. Chapter 4.4). For electrical transport measurements a current

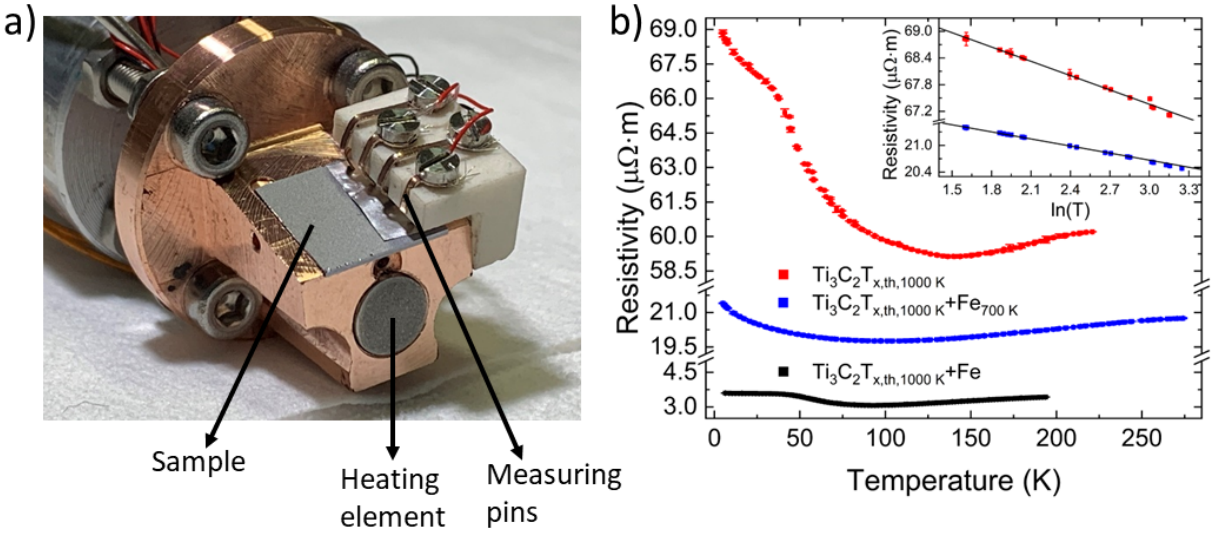

Figure A.12.: a) Sample holder for heating $Ti_3C_2T_x$ MXen samples up to 800 K and simultaneous electrical transport measurements. Heating is carried out by means of a resistive heating element. For transport measurements, substrates with a lithographic structure are used. Here, the 4 measuring pins of the sample holder press on the contact pads of the lithographic structure when the samples are placed in the corresponding recess of the sample holder. The temperature is measured using a K-type thermocouple, which is placed between the heating element and the sample. b) Resistivity as a function of temperature after the thermal activation of a $Ti_3C_2T_x$ MXene at 1000 K (red), after the deposition of 6 nm Fe on the sample surface (black) and after the intercalation of Fe into the sample at 700 K (blue). All three cases show metallic behavior. However, the red and blue curves show a strong increase in resistivity at low temperatures of a few 10 K. This is due to weak localization, as can be seen from the linear behaviour of the resistivity as a function of the logarithm of the temperature shown in the inset.

of 1 mA is applied to the two outer contacts using a *Keithley* 6221 DC and AC current source. At the same time, the voltage between the two inner pins is measured with a *Keithley* 2182A nanovoltmeter in delta mode. Heating is achieved in this context using a resistive heating element. The temperature is determined by a K-type thermocouple which is positioned between the heating element and the sample. A *LakeShore* 336 temperature controller records the actual temperature and adjusts the heating power of the heating element to the set temperature using PID control. The respective sample holder is shown in Figure A.12 a).

In addition to electrical transport measurements at temperatures $> 300\,\mathrm{K}$ with the sample holder shown in Figure A.12 a), transport measurements are also carried out on spray coated MXenes at low temperatures $< 300\,\mathrm{K}$ as shown in Figure A.12 b). However, these measurements are conducted in a PPMS DynaCool from *Quantum Design*. Here, no lithographic structure is used to contact the samples, but measurement pins are pressed into the sample from the surface as described in Chapter 4.4. A four probe in line measurement geometry is selected, whereby a current of 0.1 mA is applied to the outer two pins while the voltage between the inner pins is measured. With the distance of the measuring pins arranged in the center of the substrate of 2.26 mm, as well as the length and width of the sample of 10 mm and 5 mm, a correction factor G of 2.13 is found according to the work of Topsoe (1968) [145]. This can be used to determine the resistivity using Equation 6.3. Here, the sample thickness t is approximately $100 \pm 30\,\mathrm{nm}$ as determined from atomic force microscopy measurements (AFM) measurements analog to Chapter 4.3.
Figure A.12 b) shows the resistivities as a function of temperature for a $Ti_3C_2T_x$ MXene sample thermally activated at 1000 K (red), after the deposition of 6 nm Fe (black) and after its intercalation at 700 K (blue). Metallic behavior can be observed for all three cases. For the thermally activated MXene and the MXene with intercalated Fe, however, there is a strong increase in resistivity below temperatures of a few 10 K. If the resistivity is plotted as a function of the logarithm of the temperature in this range, a linear behavior is observed as shown in the inset in Figure A.12 b). This corresponds to weak localization as also observed by Halim et al. (2014) [45] and Halim et al. (2019) [196] for $Ti_3C_2T_x$ MXenes. Overall, it can be seen that the intercalation of Fe into the MXenes leads to an approximately 3 times smaller resistivity compared to the thermally activated MXenes. Thereby, the metallic behaviour typical for $Ti_3C_2T_x$ MXenes and the occurrence of weak localization at low temperatures are retained. The MXene with the Fe film on the sample surface shows the lowest resistivity and no occurrence of weak localization at low temperatures. This indicates that in this case mainly the Fe film on top of the surface contributes to the measured resistivity, which is reasonable considering the measurement setup.

A.12. XAS measurements on $Ti_3C_2T_{x,th}$+Fe MXenes

The X-ray absorption near-edge structure (XANES) and X-ray linear dichroism (XLD) spectrum at the Fe K-edge of a $Ti_3C_2T_{x,th,425K} + Fe_{620K}$ MXene, shown in pink in Figure A.13 a), resemble the spectra from DFT calculations of Fe_3C (see Figure 7.3), as explained in Chapter 7.2. Figure A.13 a) also shows the XANES and XLD signal at the Fe K-edge of the $Ti_3C_2T_{x,th,425K} + Fe_{700K}$ MXene from Figure 7.3 in green. Here the comparison of the spectra of both samples shows the same spectroscopic features. However, it is noticeable that the XLD signal is slightly more pronounced for $Ti_3C_2T_{x,th,425K} + Fe_{700K}$ MXenes. This indicates that a higher Fe intercalation temperature leads to a larger fraction of Fe in the form of Fe_3C and/or Fe in a local environment similar to that of Fe_3C (cf. Chapter 7).

A.13. Magnetic hysteresis loop of Fe deposited on $Ti_3C_2T_{x,th}$ MXenes

In Chapter 8.1.2 the saturation magnetizations and coercive fields of MXenes thermally activated at 1000 K and temperatures < 675 K with intercalated Fe are investigated. In the following, the saturation magnetization and coercive field of a MXene sample with Fe deposited on the sample surface are discussed, as these values serve as a reference to the results from Chapter 8.1.2. In this context, a hysteresis loop is recorded in in-plane geometry at 300 K for $Ti_3C_2T_{x,th,1000K}$ + Fe MXenes with a 6 nm Fe film on top. This is shown in Figure A.13 b). The hysteresis loop displays a saturation magnetization of 1490 ± 230 kA/m and a coercive field of 7.2 ± 1 mT. The saturation magnetization of bulk Fe is 1715 kA/m [181]. Here, a deviation of 225 kA/m arises between the measured saturation magnetization and the saturation magnetization of bulk Fe. However, the measured saturation magnetization is subject to large errors due to volume determination (see Chapter 8.1), which is considered to be the cause for the observed deviation.

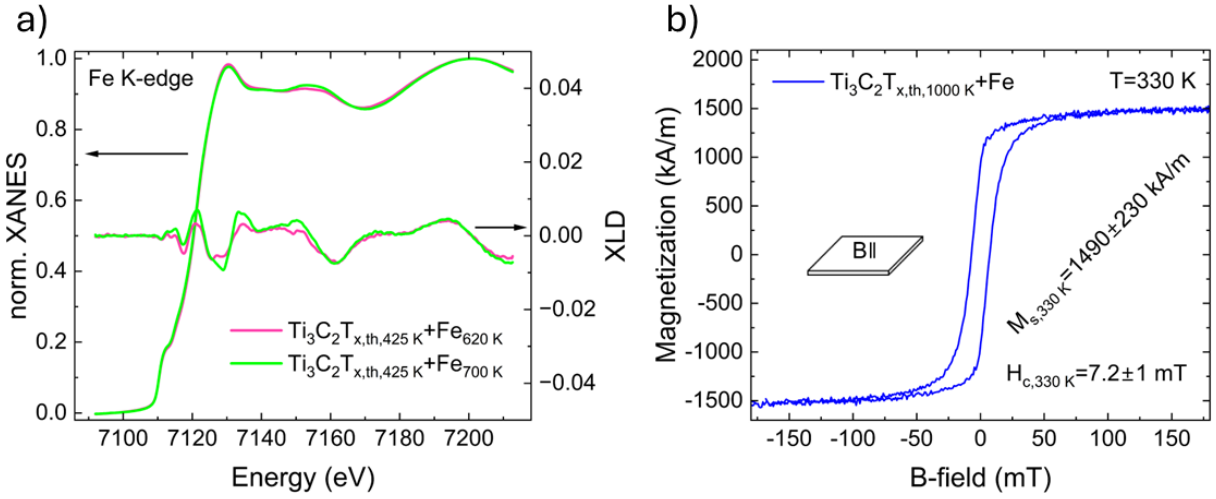

Figure A.13.: a) Comparison of the XANES and XLD spectra at the Fe K-edge of a $Ti_3C_2T_{x,th,425K}$ + Fe_{620K} MXene in pink and the $Ti_3C_2T_{x,th,425K}$ + Fe_{700K} MXene from Figure 7.3 in green [155]. The XANES spectra and XLD signals show comparable spectroscopic features with slightly different spectral weights, indicating Fe is present in an Fe_3C structure in both samples. Here, the spectroscopic features of the XLD signal are more pronounced when intercalating Fe at 700 K. b) Magnetic hysteresis loop of a $Ti_3C_2T_{x,th,1000K}$ + Fe MXene with a 6 nm Fe film on the sample surface, measured in in-plane geometry at 300 K. The hysteresis loop shows a saturation magnetization of 1490 ± 230 kA/m and a coercive field of 7.2 ± 1 mT. Here, the saturation magnetization is about 225 kA/m below the saturation magnetization of bulk Fe of 1715 kA/m. This deviation is attributed in particular to the relatively large error in volume determination.

Bibliography

[1] Thomas, S. An industry view on two-dimensional materials in electronics. In: *Nature Electronics* **4** (2021), 856–857.

[2] Lin, H., Zhang, Z., Zhang, H., Lin, K.-T., Wen, X., Liang, Y., Fu, Y., Lau, A. K. T., Ma, T., Qiu, C.-W., and Jia, B. Engineering van der Waals Materials for Advanced Metaphotonics. In: *Chemical Reviews* **122** (2022), 15204–15355.

[3] Choi, S. H., Yun, S. J., Won, Y. S., Oh, C. S., Kim, S. M., Kim, K. K., and Lee, Y. H. Large-scale synthesis of graphene and other 2D materials towards industrialization. In: *Nature Communications* **13** (2022), 1484.

[4] Huang, P., Zhang, P., Xu, S., Wang, H., Zhang, X., and Zhang, H. Recent advances in two-dimensional ferromagnetism: materials synthesis, physical properties and device applications. In: *Nanoscale* **12** (2020), 2309–2327.

[5] Palle, G. and Sunko, D. K. Physical limitations of the Hohenberg–Mermin–Wagner theorem. In: *Journal of Physics A: Mathematical and Theoretical* **54** (2021), 315001.

[6] Gibertini, M., Koperski, M., Morpurgo, A. F., and Novoselov, K. S. Magnetic 2D materials and heterostructures. In: *Nature Nanotechnology* **14** (2019), 408–419.

[7] Fei, Z., Huang, B., Malinowski, P., Wang, W., Song, T., Sanchez, J., Yao, W., Xiao, D., Zhu, X., May, A. F., Wu, W., Cobden, D. H., Chu, J.-H., and Xu, X. Two-dimensional itinerant ferromagnetism in atomically thin Fe_3GeTe_2. In: *Nature Materials* **17** (2018), 778–782.

[8] Wu, H., Zhang, W., Yang, L., Wang, J., Li, J., Li, L., Gao, Y., Zhang, L., Du, J., Shu, H., and Chang, H. Strong intrinsic room-temperature ferromagnetism in freestanding non-van der Waals ultrathin 2D crystals. In: *Nature Communications* **12** (2021), 5688.

[9] Wang, Q. H., Bedoya-Pinto, A., Blei, M., Dismukes, A. H., Hamo, A., Jenkins, S., Koperski, M., Liu, Y., Sun, Q.-C., Telford, E. J., Kim, H. H., Augustin, M., Vool, U., Yin, J.-X., Li, L. H., Falin, A., Dean, C. R., Casanova, F., Evans, R. F. L., Chshiev, M., Mishchenko, A., Petrovic, C., He, R., Zhao, L., Tsen, A. W., Gerardot, B. D., Brotons-Gisbert, M., Guguchia, Z., Roy, X., Tongay, S., Wang, Z., Hasan, M. Z., Wrachtrup, J., Yacoby, A., Fert, A., Parkin, S., Novoselov, K. S., Dai, P., Balicas, L., and Santos, E. J. G. The magnetic genome of two-dimensional van der Waals materials. In: *ACS Nano* **16** (2022), 6960–7079.

[10] Björk, J. and Rosen, J. Functionalizing MXenes by tailoring surface terminations in different chemical environments. In: *Chemistry of Materials* **33** (2021), 9108–9118.

[11] Naguib, M., Kurtoglu, M., Presser, V., Lu, J., Niu, J., Heon, M., Hultman, L., Gogotsi, Y., and Barsoum, M. W. Two-Dimensional Nanocrystals Produced by Exfoliation of Ti_3AlC_2. In: *Advanced Materials* **23** (2011), 4248–4253.

[12] Hu, Y., Liu, X. Y., Shen, Z. H., Luo, Z. F., Chen, Z. G., and Fan, X. L. High Curie temperature and carrier mobility of novel Fe, Co and Ni carbide MXenes. In: *Nanoscale* **12** (2020), 11627–11637.

[13] Ding, H., Li, Y., Li, M., Chen, K., Liang, K., Chen, G., Lu, J., Palisaitis, J., Persson, P. O. Å., Eklund, P., Hultman, L., Du, S., Chai, Z., Gogotsi, Y., and Huang, Q. Chemical scissor–mediated structural editing of layered transition metal carbides. In: *Science* **379** (2023), 1130–1135.

[14] Naguib, M., Mochalin, V. N., Barsoum, M. W., and Gogotsi, Y. 25th Anniversary Article: MXenes: A New Family of Two-Dimensional Materials. In: *Advanced Materials* **26** (2013), 992–1005.

[15] Kumar, H., Frey, N. C., Dong, L., Anasori, B., Gogotsi, Y., and Shenoy, V. B. Tunable magnetism and transport properties in nitride MXenes. In: *ACS Nano* **11** (2017), 7648–7655.

[16] Frey, N. C., Kumar, H., Anasori, B., Gogotsi, Y., and Shenoy, V. B. Tuning noncollinear spin structure and anisotropy in ferromagnetic nitride MXenes. In: *ACS Nano* **12** (2018), 6319–6325.

[17] Ma'Mari, F. A., Moorsom, T., Teobaldi, G., Deacon, W., Prokscha, T., Luetkens, H., Lee, S., Sterbinsky, G. E., Arena, D. A., MacLaren, D. A., Flokstra, M., Ali, M., Wheeler, M. C., Burnell, G., Hickey, B. J., and Cespedes, O. Beating the Stoner criterion using molecular interfaces. In: *Nature* **524** (2015), 69–73.

[18] Hart, J. L., Hantanasirisakul, K., Lang, A. C., Anasori, B., Pinto, D., Pivak, Y., Omme, J. T. van, May, S. J., Gogotsi, Y., and Taheri, M. L. Control of MXenes' electronic properties through termination and intercalation. In: *Nature Communications* **10** (2019), 522.

[19] Xu, X., Guo, T., Kim, H., Hota, M. K., Alsaadi, R. S., Lanza, M., Zhang, X., and Alshareef, H. N. Growth of 2D Materials at the Wafer Scale. In: *Advanced Materials* **34** (2022), 2108258.

[20] Liu, K. and Wu, J. Mechanical properties of two-dimensional materials and heterostructures. In: *Journal of Materials Research* **31** (2015), 832–844.

[21] Gogotsi, Y. and Anasori, B. The rise of MXenes. In: *ACS Nano* **13** (2019), 8491–8494.

[22] Raghavan, P., Ahn, J.-H., and Shelke, M. The role of 2D material families in energy harvesting: An editorial overview. In: *Journal of Materials Research* **37** (2022), 3857–3864.

[23] Mas-Ballesté, R., Gómez-Navarro, C., Gómez-Herrero, J., and Zamora, F. 2D materials: to graphene and beyond. In: *Nanoscale* **3** (2011), 20–30.

[24] Mashtalir, O., Naguib, M., Mochalin, V. N., Dall'Agnese, Y., Heon, M., Barsoum, M. W., and Gogotsi, Y. Intercalation and delamination of layered carbides and carbonitrides. In: *Nature Communications* **4** (2013), 1716.

[25] Lim, K. R. G., Shekhirev, M., Wyatt, B. C., Anasori, B., Gogotsi, Y., and Seh, Z. W. Fundamentals of MXene synthesis. In: *Nature Synthesis* **1** (2022), 601–614.

[26] Deysher, G., Shuck, C. E., Hantanasirisakul, K., Frey, N. C., Foucher, A. C., Maleski, K., Sarycheva, A., Shenoy, V. B., Stach, E. A., Anasori, B., and Gogotsi, Y. Synthesis of Mo_4VAlC_4 MAX Phase and Two-Dimensional Mo_4VC_4 MXene with Five Atomic Layers of Transition Metals. In: *ACS Nano* **14** (2019), 204–217.

[27] Wei, Y., Zhang, P., Soomro, R. A., Zhu, Q., and Xu, B. Advances in the Synthesis of 2D MXenes. In: *Advanced Materials* **33** (2021), 2103148.

[28] Persson, P. and Rosen, J. Current state of the art on tailoring the MXene composition, structure, and surface chemistry. In: *Current Opinion in Solid State and Materials Science* **23** (2019), 100774.

[29] Schultz, T., Frey, N. C., Hantanasirisakul, K., Park, S., May, S. J., Shenoy, V. B., Gogotsi, Y., and Koch, N. Surface Termination Dependent Work Function and Electronic Properties of $Ti_3C_2T_x$ MXene. In: *Chemistry of Materials* **31** (2019), 6590–6597.

[30] Kubitza, N., Büchner, C., Sinclair, J., Snyder, R. M., and Birkel, C. S. Extending the Chemistry of Layered Solids and Nanosheets: Chemistry and Structure of MAX Phases, MAB Phases and MXenes. In: *ChemPlusChem* **88** (2023), e202300214.

[31] Habib, T., Zhao, X., Shah, S. A., Chen, Y., Sun, W., An, H., Lutkenhaus, J. L., Radovic, M., and Green, M. J. Oxidation stability of $Ti_3C_2T_x$ MXene nanosheets in solvents and composite films. In: *npj 2D Materials and Applications* **3** (2019), 8.

[32] Pazniak, A., Bazhin, P., Shplis, N., Kolesnikov, E., Shchetinin, I., Komissarov, A., Polcak, J., Stolin, A., and Kuznetsov, D. $Ti_3C_2T_x$ MXene characterization produced from SHS-ground Ti_3AlC_2. In: *Materials and Design* **183** (2019), 108143.

[33] Barsoum, M. W. The $M_{N+1}AX_N$ phases: A new class of solids. In: *Progress in Solid State Chemistry* **28** (2000), 201–281.

[34] Xiong, D., Li, X., Bai, Z., and Lu, S. Recent Advances in Layered $Ti_3C_2T_x$ MXene for Electrochemical Energy Storage. In: *Small* **14** (2018), 1703419.

[35] Alhabeb, M., Maleski, K., Anasori, B., Lelyukh, P., Clark, L., Sin, S., and Gogotsi, Y. Guidelines for Synthesis and Processing of Two-Dimensional Titanium Carbide ($Ti_3C_2T_x$ MXene). In: *Chemistry of Materials* **29** (2017), 7633–7644.

[36] Zhang, Y., Wang, L., Zhang, N., and Zhou, Z. Adsorptive environmental applications of MXene nanomaterials: a review. In: *RSC Advances* **8** (2018), 19895–19905.

[37] Karlsson, L. H., Birch, J., Halim, J., Barsoum, M. W., and Persson, P. O. Å. Atomically Resolved Structural and Chemical Investigation of Single MXene Sheets. In: *Nano Letters* **15** (2015), 4955–4960.

[38] Lipatov, A., Lu, H., Alhabeb, M., Anasori, B., Gruverman, A., Gogotsi, Y., and Sinitskii, A. Elastic properties of 2D $Ti_3C_2T_x$ MXene monolayers and bilayers. In: *Science Advances* **4** (2018), eaat0491.

[39] Cai, M., Yan, H., Song, S., He, D., Lin, Q., Li, W., Fan, X., and Zhu, M. State-of-the-art progresses for $Ti_3C_2T_x$ MXene reinforced polymer composites in corrosion and tribology aspects. In: *Advances in Colloid and Interface Science* **309** (2022), 102790.

[40] Naguib, M., Barsoum, M. W., and Gogotsi, Y. Ten Years of Progress in the Synthesis and Development of MXenes. In: *Advanced Materials* **33** (2021), 2103393.

[41] Dillon, A. D., Ghidiu, M. J., Krick, A. L., Griggs, J., May, S. J., Gogotsi, Y., Barsoum, M. W., and Fafarman, A. T. Highly conductive optical quality solution-processed films of 2D titanium carbide. In: *Advanced Functional Materials* **26** (2016), 4162–4168.

[42] Miranda, A., Halim, J., Barsoum, M. W., and Lorke, A. Electronic properties of free-standing $Ti_3C_2T_x$ MXene monolayers. In: *Applied Physics Letters* **108** (2016), 033102.

[43] Römer, F. M., Wiedwald, U., Strusch, T., Halim, J., Mayerberger, E., Barsoum, M. W., and Farle, M. Controlling the conductivity of Ti_3C_2 MXenes by inductively coupled oxygen and hydrogen plasma treatment and humidity. In: *RSC Advances* **7** (2017), 13097–13103.

[44] Sang, X., Xie, Y., Lin, M.-W., Alhabeb, M., Aken, K. L. V., Gogotsi, Y., Kent, P. R. C., Xiao, K., and Unocic, R. R. Atomic Defects in Monolayer Titanium Carbide ($Ti_3C_2T_x$) MXene. In: *ACS Nano* **10** (2016), 9193–9200.

[45] Halim, J., Lukatskaya, M. R., Cook, K. M., Lu, J., Smith, C. R., Näslund, L.-Å., May, S. J., Hultman, L., Gogotsi, Y., Eklund, P., and Barsoum, M. W. Transparent conductive two-dimensional titanium carbide epitaxial thin films. In: *Chemistry of Materials* **26** (2014), 2374–2381.

[46] Bergmann, G. Quantitative analysis of weak localization in thin Mg films by magnetoresistance measurements. In: *Physical Review B* **25** (1982), 2937–2939.

[47] Xie, Y., Naguib, M., Mochalin, V. N., Barsoum, M. W., Gogotsi, Y., Yu, X., Nam, K.-W., Yang, X.-Q., Kolesnikov, A. I., and Kent, P. R. C. Role of surface structure on Li-ion energy storage capacity of two-dimensional transition-metal carbides. In: *Journal of the American Chemical Society* **136** (2014), 6385–6394.

[48] Kim, H., Anasori, B., Gogotsi, Y., and Alshareef, H. N. Thermoelectric properties of two-dimensional molybdenum-based MXenes. In: *Chemistry of Materials* **29** (2017), 6472–6479.

[49] Shahzad, F., Iqbal, A., Kim, H., and Koo, C. M. 2D Transition Metal Carbides (MXenes): Applications as an Electrically Conducting Material. In: *Advanced Materials* **32** (2020), 2002159.

[50] Gandi, A. N., Alshareef, H. N., and Schwingenschlögl, U. Thermoelectric Performance of the MXenes M_2CO_2 (M = Ti, Zr, or Hf). In: *Chemistry of Materials* **28** (2016), 1647–1652.

[51] Anasori, B., Lukatskaya, M. R., and Gogotsi, Y. 2D metal carbides and nitrides (MXenes) for energy storage. In: *Nature Reviews Materials* **2** (2017), 16098.

[52] Zhang, H., Xin, X., Liu, H., Huang, H., Chen, N., Xie, Y., Deng, W., Guo, C., and Yang, W. Enhancing Lithium Adsorption and Diffusion toward Extraordinary Lithium Storage Capability of Freestanding $Ti_3C_2T_x$ MXene. In: *The Journal of Physical Chemistry C* **123** (2019), 2792–2800.

[53] Ming, F., Liang, H., Huang, G., Bayhan, Z., and Alshareef, H. N. MXenes for rechargeable batteries beyond the lithium-ion. In: *Advanced Materials* **33** (2020), 2004039.

[54] Zhang, X., Wang, L., Liu, W., Li, C., Wang, K., and Ma, Y. Recent advances in MXenes for lithium-ion capacitors. In: *ACS Omega* **5** (2019), 75–82.

[55] Su, T., Ma, X., Tong, J., Ji, H., Qin, Z., and Wu, Z. Surface engineering of MXenes for energy and environmental applications. In: *Journal of Materials Chemistry A* **10** (2022), 10265–10296.

[56] Hwang, S. K., Kang, S.-M., Rethinasabapathy, M., Roh, C., and Huh, Y. S. MXene: An emerging two-dimensional layered material for removal of radioactive pollutants. In: *Chemical Engineering Journal* **397** (2020), 125428.

[57] Dixit, F., Zimmermann, K., Alamoudi, M., Abkar, L., Barbeau, B., Mohseni, M., Kandasubramanian, B., and Smith, K. Application of MXenes for air purification, gas separation and storage: A review. In: *Renewable and Sustainable Energy Reviews* **164** (2022), 112527.

[58] Kim, S., Yu, M., and Yoon, Y. Fouling and Retention Mechanisms of Selected Cationic and Anionic Dyes in a $Ti_3C_2T_x$ MXene-Ultrafiltration Hybrid System. In: *ACS Applied Materials and Interfaces* **12** (2020), 16557–16565.

[59] Mashtalir, O., Cook, K. M., Mochalin, V. N., Crowe, M., Barsoum, M. W., and Gogotsi, Y. Dye adsorption and decomposition on two-dimensional titanium carbide in aqueous media. In: *J. Mater. Chem. A* **2** (2014), 14334–14338.

[60] Jin, L., You, S., Ren, N., Ding, B., and Liu, Y. Mo vacancy-mediated activation of peroxymonosulfate for ultrafast micropollutant removal using an electrified MXene filter functionalized with Fe single atoms. In: *Environmental Science and Technology* **56** (2022), 11750–11759.

[61] Ding, R., Xiong, J., Yan, Q., Chen, Z., Liu, Z., Zhao, X., Peng, Q., and He, X. Achieving fast interfacial solar vapor generation and aqueous acid purification using $Ti_3C_2T_x$ MXene/PANI non-woven fabrics. In: *Materials Horizons* **10** (2023), 2262–2270.

[62] Hu, T., Li, Z., Hu, M., Wang, J., Hu, Q., Li, Q., and Wang, X. Chemical Origin of Termination-Functionalized MXenes: $Ti_3C_2T_2$ as a Case Study. In: *The Journal of Physical Chemistry C* **121** (2017), 19254–19261.

[63] Halim, J., Cook, K. M., Naguib, M., Eklund, P., Gogotsi, Y., Rosen, J., and Barsoum, M. W. X-ray photoelectron spectroscopy of select multi-layered transition metal carbides (MXenes). In: *Applied Surface Science* **362** (2016), 406–417.

[64] Persson, I., Näslund, L.-Å., Halim, J., Barsoum, M. W., Darakchieva, V., Palisaitis, J., Rosen, J., and Persson, P. O. Å. On the organization and thermal behavior of functional groups on Ti_3C_2 MXene surfaces in vacuum. In: *2D Materials* **5** (2017), 015002.

[65] Zhang, K., Di, M., Fu, L., Deng, Y., Du, Y., and Tang, N. Enhancing the magnetism of 2D carbide MXene $Ti_3C_2T_x$ by H_2 annealing. In: *Carbon* **157** (2020), 90–96.

[66] Seredych, M., Shuck, C. E., Pinto, D., Alhabeb, M., Precetti, E., Deysher, G., Anasori, B., Kurra, N., and Gogotsi, Y. High-Temperature Behavior and Surface Chemistry of Carbide MXenes Studied by Thermal Analysis. In: *Chemistry of Materials* **31** (2019), 3324–3332.

[67] Eom, W., Shin, H., Jeong, W., Ambade, R. B., Lee, H., and Han, T. H. Surface nitrided MXene sheets with outstanding electroconductivity and oxidation stability. In: *Materials Horizons* **10** (2023), 4892–4902.

[68] Xie, Y. and Kent, P. R. C. Hybrid density functional study of structural and electronic properties of functionalized $Ti_{n+1}X_n$ (X=C, N) monolayers. In: *Physical Review B* **87** (2013), 235441.

[69] Khazaei, M., Arai, M., Sasaki, T., Chung, C.-Y., Venkataramanan, N. S., Estili, M., Sakka, Y., and Kawazoe, Y. Novel electronic and magnetic properties of two-dimensional transition metal carbides and nitrides. In: *Advanced Functional Materials* **23** (2012), 2185–2192.

[70] Stefanita, C.-G. Magnetism. Basics and applications. 1st ed. Springer, Berlin/Heidelberg, 2012.

[71] Getzlaff, M. Fundamentals of Magnetism. 1st ed. Springer, Berlin/Heidelberg, 2008.

[72] Crangle, J. Solid · State Magnetism. 1st ed. Springer, New York, NY, 1991.

[73] Buschow, K. H. J. and Boer, F. R. Physics of Magnetism and Magnetic Materials. 1st ed. Springer, New York, NY, 2003.

[74] Bloch, F. Zur Theorie des Ferromagnetismus. In: *Zeitschrift für Physik* **61** (1930), 206–219.

[75] Laughlin, D. E. Magnetic Transformations and Phase Diagrams. In: *Metallurgical and Materials Transactions A* **50** (2019), 2555–2569.

[76] Stoner, E. C. Ferromagnetism. In: *Reports on Progress in Physics* **11** (1947), 43–112.

[77] Stoner, E. C. Collective electron ferromagnetism. In: *Proceedings of the Royal Society of London. Series A. Mathematical and Physical Sciences* **165** (1938), 372–414.

[78] Stoner, E. C. Collective electron ferromagnetism II. Energy and specific heat. In: *Proceedings of the Royal Society of London. Series A. Mathematical and Physical Sciences* **169** (1939), 339–371.

[79] Himpsel, F. J., Ortega, J. E., Mankey, G. J., and Willis, R. F. Magnetic nanostructures. In: *Advances in Physics* **47** (1998), 511–597.

[80] Chatterjee, B. Oxidation of iron, cobalt and nickel at the Curie temperature. In: *Solid State Communications* **27** (1978), 1455–1458.

[81] Wesselinowa, J. M. and Apostolova, I. Size, anisotropy and doping effects on the coercive field of ferromagnetic nanoparticles. In: *Journal of Physics: Condensed Matter* **19** (2007), 406235.

[82] Mangler, T. Metallcluster als mögliche Bausteine neuer Nanomaterialien. PhD thesis. Universität Konstanz, Fachbereich Physik, 2010.

[83] Enriquez-Navas, P. M. and Garcia-Martin, M. L. Application of Inorganic Nanoparticles for Diagnosis Based on MRI. In: *Frontiers of Nanoscience*. Ed. by Fuente, J. M. de la and Grazu, V. Vol. 4. Elsevier, 2012. Chap. 9, pp. 233–245.

[84] Jenkins, S., Rózsa, L., Atxitia, U., Evans, R. F. L., Novoselov, K. S., and Santos, E. J. G. Breaking through the Mermin-Wagner limit in 2D van der Waals magnets. In: *Nature Communications* **13** (2022), 6917.

[85] Fick, A. V. On liquid diffusion. In: *The London, Edinburgh, and Dublin Philosophical Magazine and Journal of Science* **10** (1855), 30–39.

[86] Mehrer, H. Diffusion in Solids. Fundamentals, Methods, Materials, Diffusion-Controlled Processes. 1st ed. Springer, Berlin/Heidelberg, 2007.

[87] Bocquet, J. L. and Brebec, G. and Limoge, Y. Diffusion in metals and alloys. In: *Physical Metallurgy*. Ed. by Cahn, R. W. and Haasen, P. 4th ed. Vol. 1. North-Holland, 1996. Chap. 7, pp. 535–668.

[88] Mittemeijer, E. J. Diffusion. In: *Fundamentals of Materials Science. The Microstructure-Property Relationship Using Metals As Model Systems.* 2nd ed. Springer International Publishing, 2022. Chap. 8, pp. 401–465.

[89] Zhao, Y., Liu, Z., Sun, T., Zhang, L., Jie, W., Wang, X., Xie, Y., Tsang, Y. H., Long, H., and Chai, Y. Mass Transport Mechanism of Cu Species at the Metal/Dielectric Interfaces with a Graphene Barrier. In: *ACS Nano* **8** (2014), 12601–12611.

[90] Ahmed, M., Li, Y., Chen, W., and Li, E.-P. First-principles investigation of copper diffusion barrier performance in defective 2D layered materials. In: *Nanotechnology* **33** (2022), 165201.

[91] Stark, M. S., Kuntz, K. L., Martens, S. J., and Warren, S. C. Intercalation of Layered Materials from Bulk to 2D. In: *Advanced Materials* **31** (2019), 1808213.

[92] Luo, J., Zhang, W., Yuan, H., Jin, C., Zhang, L., Huang, H., Liang, C., Xia, Y., Zhang, J., Gan, Y., and Tao, X. Pillared Structure Design of MXene with Ultralarge Interlayer Spacing for High-Performance Lithium-Ion Capacitors. In: *ACS Nano* **11** (2017), 2459–2469.

[93] Oakes, L., Carter, R., Hanken, T., Cohn, A. P., Share, K., Schmidt, B., and Pint, C. L. Interface strain in vertically stacked two-dimensional heterostructured carbon - MoS_2 nanosheets controls electrochemical reactivity. In: *Nature Communications* **7** (2016), 11796.

[94] Hablanian, M. H. High-vacuum technology. A practical guide. 2nd ed. Taylor and Francis Group LLC (Books) US, 1997.

[95] Jousten, K., ed. Handbuch Vakuumtechnik. 12th ed. Springer Fachmedien Wiesbaden, 2018.

[96] Wiegleb, G. Physikalische Eigenschaften von Gasen. In: *Gasmesstechnik in Theorie und Praxis. Messgeräte, Sensoren, Anwendungen.* 1st ed. Springer Fachmedien Wiesbaden, 2016. Chap. 2, pp. 7–118.

[97] Jablonka, K. M. Grundlagen der Thermodynamik für Studierende der Chemie. Die wichtigsten Themen der physikalischen Chemie. 1st ed. Springer Spektrum Wiesbaden, 2017.

[98] Pfeiffer Vacuum GmbH. IKR 070 Operating Instructions. 2013.

[99] Pfeiffer Vacuum GmbH. PKR 36X/IKR 36X Operating Instructions. 2016.

[100] Circular of the Bureau of Standards no. 35 2nd edition: melting points of chemical elements and other standard temperatures. 1915.

[101] Vapor Pressure Calculator [IAP/TU Wien]. Jan. 2024. URL: `https://www2.iap.tuwien.ac.at/www/surface/vapor_pressure` (visited on 03/29/2024).

[102] Wajid, A. Improving the accuracy of a quartz crystal microbalance with automatic determination of acoustic impedance ratio. In: *Review of Scientific Instruments* **62** (1991), 2026–2033.

[103] Thermo Onix. VGQ Operations Manual. 1998.

[104] Klopfer, A., Garbe, S., and Schmidt, W. Residual gases in vacuum systems. In: *Vacuum* **10** (1960), 7–12.

[105] Chang, C. C. Auger electron spectroscopy. In: *Surface Science* **25** (1971), 53–79.

[106] Rivière, J. C. Auger electron spectroscopy. In: *Contemporary Physics* **14** (1973), 513–539.

[107] Kotani, A. and Shin, S. Resonant inelastic x-ray scattering spectra for electrons in solids. In: *Reviews of Modern Physics* **73** (2001), 203–246.

[108] Davis, L. E., MacDonald, N. C., Palmberg, P. W., Riach, G. E., and Weber, R. E. Handbook of Auger Electron Spectroscopy. A Reference Book of Standard Data for Identification and Interpretation of Auger Electron Spectroscopy Data. 2nd ed. Eden Prairie, MN: Physical Electronics Division, Perkin Elmer Corporation, 1976.

[109] Staib Instrumente GmbH. Instruction Manual Elektron Spectrometer Model DESA 100. 2002.

[110] Seah, M. P. and Dench, W. A. Quantitative electron spectroscopy of surfaces: A standard data base for electron inelastic mean free paths in solids. In: *Surface and Interface Analysis* **1** (1979), 2–11.

[111] Pantano, C. G. and Madey, T. E. Electron beam damage in Auger electron spectroscopy. In: *Applications of Surface Science* **7** (1981), 115–141.

[112] Mroczkowski, S. and Lichtman, D. Calculated Auger yields and sensitivity factors for KLL – NOO transitions with 1–10 kV primary beams. In: *Journal of Vacuum Science and Technology A: Vacuum, Surfaces, and Films* **3** (1985), 1860–1865.

[113] Seah, M. P. Quantitative Auger electron spectroscopy and electron ranges. In: *Surface Science* **32** (1972), 703–728.

[114] NIST ICSD Web Site. n.d. URL: `https://icsd.nist.gov/` (visited on 03/30/2024).

[115] Synthesis of $Ti_3C_2T_x$ MXenes and XRD measurements by Dr. Hanna Pazniak.

[116] Iida, S. and Abe, S. Ti thin-film reaction on SiO_2/Si. In: *Applied Surface Science* **78** (1994), 141–146.

[117] Jeon, H., Sukow, C. A., Honeycutt, J. W., Rozgonyi, G. A., and Nemanich, R. J. Morphology and phase stability of $TiSi_2$ on Si. In: *Journal of Applied Physics* **71** (1992), 4269–4276.

[118] Kumar, N., Azad, S., and Chand, S. Fabrication and electrical characterization of solution processed Ni/MgO/*p*-Si/Al MIS diodes. In: *Applied Physics A* **128** (2022), 226.

[119] Horcas, I., Fernández, R., Gómez-Rodríguez, J. M., Colchero, J., Gómez-Herrero, J., and Baro, A. M. WSXM: A software for scanning probe microscopy and a tool for nanotechnology. In: *Review of Scientific Instruments* **78** (2007), 013705.

[120] Spray coating of $Ti_3C_2T_x$ MXenes on Si/SiO_2 substrates by Dr. Hanna Pazniak.

[121] Deal, B. E. and Grove, A. S. General Relationship for the Thermal Oxidation of Silicon. In: *Journal of Applied Physics* **36** (1965), 3770–3778.

[122] TEM operator: Prof. Dr. Ulf Wiedwald.

[123] Schneider, C. A., Rasband, W. S., and Eliceiri, K. W. NIH Image to ImageJ: 25 years of image analysis. In: *Nature Methods* **9** (2012), 671–675.

[124] Kurzweil, P. and Scheipers, P. Periodensystem der Elemente (PSE). In: *Chemie*. 9th ed. Vieweg+Teubner Verlag Wiesbaden, 2012. Chap. 3, pp. 31–43.

[125] Wang, C., Chen, S., and Song, L. Tuning 2D MXenes by Surface Controlling and Interlayer Engineering: Methods, Properties, and Synchrotron Radiation Characterizations. In: *Advanced Functional Materials* **30** (2020), 2000869.

[126] Liu, Y., Sheng, Z., Huang, J., Liu, W., Ding, H., Peng, J., Zhong, B., Sun, Y., Ouyang, X., Cheng, H., and Wang, X. Moisture-resistant MXene-sodium alginate sponges with sustained superhydrophobicity for monitoring human activities. In: *Chemical Engineering Journal* **432** (2022), 134370.

[127] Buffet, A., Rothkirch, A., Döhrmann, R., Körstgens, V., Kashem, M. M. A., Perlich, J., Herzog, G., Schwartzkopf, M., Gehrke, R., Müller-Buschbaum, P., and Roth, S. V. P03, the microfocus and nanofocus X-ray scattering (MiNaXS) beamline of the PETRA III storage ring: the microfocus endstation. In: *Journal of Synchrotron Radiation* **19** (2012), 647–653.

[128] WAXS measurements at beamline P03 (MiNaXS) of PETRA III storage ring and data processing by Dr. Hanna Pazniak, Andrei Chumakov, Aditya Sharma and Prof. Dr. Ulf Wiedwald.

[129] Braun, A. R. and Sachs, J. N. Extracting Experimental Measurables from Molecular Dynamics Simulations of Membranes. In: *Annual Reports in Computational Chemistry*. Ed. by Wheeler, R. A. Vol. 7. Elsevier Science and Technology Books, 2011. Chap. 6, pp. 125–150.

[130] Ma, J., Cheng, Y., Wang, L., Dai, X., and Yu, F. Free-standing $Ti_3C_2T_x$ MXene film as binder-free electrode in capacitive deionization with an ultrahigh desalination capacity. In: *Chemical Engineering Journal* **384** (2020), 123329.

[131] Hadler-Jacobsen, J., Fagerli, F. H., Kaland, H., and Schnell, S. K. Stacking Sequence, Interlayer Bonding, Termination Group Stability and Li/Na/Mg Diffusion in MXenes. In: *ACS Materials Letters* **3** (2021), 1369–1376.

[132] Zhang, T., Pan, L., Tang, H., Du, F., Guo, Y., Qiu, T., and Yang, J. Synthesis of two-dimensional $Ti_3C_2T_x$ MXene using HCl+LiF etchant: Enhanced exfoliation and delamination. In: *Journal of Alloys and Compounds* **695** (2017), 818–826.

[133] Lu, J., Persson, I., Lind, H., Palisaitis, J., Li, M., Li, Y., Chen, K., Zhou, J., Du, S., Chai, Z., Huang, Z., Hultman, L., Eklund, P., Rosen, J., Huang, Q., and Persson, P. O. Å. $Ti_{n+1}C_n$ MXenes with fully saturated and thermally stable Cl terminations. In: *Nanoscale Advances* **1** (2019), 3680–3685.

[134] Zhang, T., Chang, L., Zhang, X., Wan, H., Liu, N., Zhou, L., and Xiao, X. Simultaneously tuning interlayer spacing and termination of MXenes by Lewis-basic halides. In: *Nature Communications* **13** (2022), 6731.

[135] Ghidiu, M., Lukatskaya, M. R., Zhao, M.-Q., Gogotsi, Y., and Barsoum, M. W. Conductive two-dimensional titanium carbide 'clay' with high volumetric capacitance. In: *Nature* **516** (2014), 78–81.

[136] Brundle, C. R. and Crist, B. V. X-ray photoelectron spectroscopy: A perspective on quantitation accuracy for composition analysis of homogeneous materials. In: *Journal of Vacuum Science and Technology A: Vacuum, Surfaces, and Films* **38** (2020), 041001.

[137] Cameron, A. E. and Wichers, E. Report of the International Commission on Atomic Weights. In: *Journal of the American Chemical Society* **84** (1962), 4175–4197.

[138] Reniers, F. and Tewell, C. New improvements in energy and spatial (x, y, z) resolution in AES and XPS applications. In: *Journal of Electron Spectroscopy and Related Phenomena* **142** (2005), 1–25.

[139] Stelter, E. C. and Lazarus, D. Diffusion and thermal stability of amorphous copper zirconium. In: *Physical Review B* **36** (1987), 9545–9558.

[140] Sharma, S. and Mukhopadhyay, P. Diffusion studies in the metallic glass $Zr_{61}Ni_{39}$ by Auger electron spectroscopy. In: *Acta Metallurgica et Materialia* **38** (1990), 129–133.

[141] XPS measurements at the VUV-photoemission beamline of Elletra synchrotron light facility and data processing by Dr. Hanna Pazniak, Aditya Sharma and Paolo Moras.

[142] XPS measurements and data processing by Prof. Dr. Ulf Wiedwald.

[143] Li, X., Ran, F., Yang, F., Long, J., and Shao, L. Advances in MXene Films: Synthesis, Assembly, and Applications. In: *Transactions of Tianjin University* **27** (2021), 217–247.

[144] Lu, M., Han, W., Li, H., Li, H., Zhang, B., Zhang, W., and Zheng, W. Magazine-Bending-Inspired Architecting Anti-T of MXene Flakes with Vertical Ion Transport for High-Performance Supercapacitors. In: *Advanced Materials Interfaces* **6** (2019), 1900160.

[145] Topsoe, H. Geometric factors in four point resistivity measurement. Bulletin, No. 472-13. Haldor Topsoe - Semiconductor Division. Vedbaek, 1968.

[146] Halim, J., Moon, E. J., Eklund, P., Rosen, J., Barsoum, M. W., and Ouisse, T. Variable range hopping and thermally activated transport in molybdenum-based MXenes. In: *Physical Review B* **98** (2018), 104202.

[147] Zheng, W., Sun, B., Li, D., Gali, S. M., Zhang, H., Fu, S., Di Virgilio, L., Li, Z., Yang, S., Zhou, S., Beljonne, D., Yu, M., Feng, X., Wang, H. I., and Bonn, M. Band transport by large Fröhlich polarons in MXenes. In: *Nature Physics* **18** (2022), 544–550.

[148] Henderson, G. S., Groot, F. M. d., and Moulton, B. J. X-ray Absorption Near-Edge Structure (XANES) Spectroscopy. In: *Reviews in Mineralogy and Geochemistry*. Ed. by Henderson, G., Neuville, D., Downs, R., and Rosso, J. J. Vol. 78. De Gruyter, 2014. Chap. 3, pp. 75–138.

[149] Kammermeier, T. Structural and magnetic investigation of dilute magnetic semiconductors based on GaN and ZnO. PhD thesis. Universität Duisburg-Essen, Fachbereich Physik, 2010.

[150] Wilhelm, F., Garbarino, G., Jacobs, J., Vitoux, H., Steinmann, R., Guillou, F., Snigirev, A., Snigireva, I., Voisin, P., Braithwaite, D., Aoki, D., Brison, J.-P., Kantor, I., Lyatun, I., and Rogalev, A. High pressure XANES and XMCD in the tender X-ray energy range. In: *High Pressure Research* **36** (2016), 445–457.

[151] Clark, S. J., Segall, M. D., Pickard, C. J., Hasnip, P. J., Probert, M. I. J., Refson, K., and Payne, M. C. First principles methods using CASTEP. In: *Zeitschrift für Kristallographie - Crystalline Materials* **220** (2005), 567–570.

[152] Perdew, J. P., Burke, K., and Ernzerhof, M. Generalized Gradient Approximation Made Simple. In: *Physical Review Letters* **77** (1996), 3865–3868.

[153] Bunău, O and Joly, Y. Self-consistent aspects of x-ray absorption calculations. In: *Journal of Physics: Condensed Matter* **21** (2009), 345501.

[154] Solé, V., Papillon, E., Cotte, M., Walter, P., and Susini, J. A multiplatform code for the analysis of energy-dispersive X-ray fluorescence spectra. In: *Spectrochimica Acta Part B: Atomic Spectroscopy* **62** (2007), 63–68.

[155] Beamtime MA-5883 at beamline ID12 of ESRF: Prof. Dr. Ulf Wiedwald, Prof. Dr. Thierry Ouisse, Dr. Hanna Pazniak, Dr. Fabrice Wilhelm, Dr. Ivan Tarasov, Tim Salzmann.

[156] DFT calculations performed by Dr. Ivan Tarasov.

[157] Momma, K. and Izumi, F. VESTA: a three-dimensional visualization system for electronic and structural analysis. In: *Journal of Applied Crystallography* **41** (2008), 653–658.

[158] Structural model of $Ti_3C_2O_2$ MXenes by Dr. Ivan Tarasov.

[159] Magnuson, M. and Näslund, L.-Å. Local chemical bonding and structural properties in Ti_3AlC_2 MAX phase and $Ti_3C_2T_x$ MXene probed by Ti 1s x-ray absorption spectroscopy. In: *Physical Review Research* **2** (2020), 033516.

[160] Guo, Z., Henry, L. L., Palshin, V., and Podlaha, E. J. Synthesis of poly (methyl methacrylate) stabilized colloidal zero-valence metallic nanoparticles. In: *J. Mater. Chem.* **16** (2006), 1772–1777.

[161] Ney, V., Henne, B., Souza, M. de, Jantsch, W., Johansen, K. M., Wilhelm, F., Rogalev, A., and Ney, A. Valence state, lattice incorporation, and resulting magnetic properties of Ni in Zn/Co-based magnetic oxides. In: *Journal of Applied Physics* **133** (2023), 033904.

[162] Hsieh, C.-Y., Jiang, P.-C., Chen, W.-H., and Tsay, J.-S. Strain driven phase transition and mechanism for Fe/Ir(111) films. In: *Scientific Reports* **11** (2021), 21909.

[163] Mangarella, M. C., Ewbank, J. L., Dutzer, M. R., Alamgir, F. M., and Walton, K. S. Synthesis of embedded iron nanoparticles in Fe_3C-derived carbons. In: *Carbon* **79** (2014), 74–84.

[164] Al-Joubori, A. A. and Suryanarayana, C. Synthesis and thermal stability of homogeneous nanostructured Fe_3C (cementite). In: *Journal of Materials Science* **53** (2018), 7877–7890.

[165] Longbottom, R. J., Ostrovski, O., Zhang, J., and Young, D. Stability of Cementite Formed from Hematite and Titanomagnetite Ore. In: *Metallurgical and Materials Transactions B* **38** (2007), 175–184.

[166] Chipman, J. Thermodynamics and phase diagram of the Fe-C system. In: *Metallurgical Transactions* **3** (1972), 55–64.

[167] Lara, J., Kotvis, P., and Tysoe, W. The surface chemistry of chlorinated hydrocarbonextreme - pressure lubricant additives. In: *Tribology Letters* **3** (1997), 303–309.

[168] Kinoshita, T., Karita, M., Chikyu, N., Nakano, T., and Inoue, Y. Enhancement of catalytic activity by addition of chlorine in chemical vapor deposition growth of carbon nanotube forests. In: *Carbon* **196** (2022), 391–400.

[169] Näslund, L.-Å. and Persson, I. XPS spectra curve fittings of $Ti_3C_2T_x$ based on first principles thinking. In: *Applied Surface Science* **593** (2022), 153442.

[170] Häglund, J., Grimvall, G., and Jarlborg, T. Electronic structure, x-ray photoemission spectra, and transport properties of Fe_3C (cementite). In: *Physical Review B* **44** (1991), 2914–2919.

[171] Duman, E., Acet, M., Hülser, T., Wassermann, E. F., Rellinghaus, B., Itié, J. P., and Munsch, P. Large spontaneous magnetostrictive softening below the Curie temperature of Fe_3C Invar particles. In: *Journal of Applied Physics* **96** (2004), 5668–5672.

[172] Foner, S. Versatile and Sensitive Vibrating-Sample Magnetometer. In: *Review of Scientific Instruments* **30** (1959), 548–557.

[173] Thomson, T. Magnetic properties of metallic thin films. In: *Metallic Films for Electronic, Optical and Magnetic Applications. Structure, Processing and Properties*. Ed. by Barmak, K. and Coffey, K. Woodhead Publishing Limited, 2014. Chap. 10, pp. 454–546.

[174] Bayreuther, G., Bensch, F., and Kottler, V. Quantum oscillations of properties in magnetic multilayers. In: *Journal of Applied Physics* **79** (1996), 4509–4514.

[175] Feng, P., Zhang, X., Zhang, S., Liu, D., Gao, M., Ma, F., Yan, X.-W., and Xie, Z.-Y. Interlayer Coupling Induced Sharp Increase of the Curie Temperature in a Two-Dimensional MnSn Multilayer. In: *ACS Omega* **7** (2022), 43316–43320.

[176] Schneider, A. and Inden, G. Thermodynamics of Hägg carbide (Fe_5C_2) formation. In: *Steel Research* **72** (2001), 503–507.

[177] Abel, F. M., Pourmiri, S., Basina, G., Tzitzios, V., Devlin, E., and Hadjipanayis, G. C. Iron carbide nanoplatelets: colloidal synthesis and characterization. In: *Nanoscale Advances* **1** (2019), 4476–4480.

[178] Zhao, H., Liu, J.-X., Yang, C., Yao, S., Su, H.-Y., Gao, Z., Dong, M., Wang, J., Rykov, A. I., Wang, J., Hou, Y., Li, W.-X., and Ma, D. Synthesis of Iron-Carbide Nanoparticles: Identification of the Active Phase and Mechanism of Fe-Based Fischer–Tropsch Synthesis. In: *CCS Chemistry* **3** (2021), 2712–2724.

[179] Guzmán, J., Álvarez, N., Salva, H., Vásquez Mansilla, M., Gómez, J., and Butera, A. Abnormal temperature dependence of the coercive field in FePt thin films. In: *Journal of Magnetism and Magnetic Materials* **347** (2013), 61–67.

[180] Hofer, L. J. E. and Cohn, E. M. Saturation Magnetizations of Iron Carbides[1]. In: *Journal of the American Chemical Society* **81** (1959), 1576–1582.

[181] Dunlop, D. and Özdemir, Ö. Magnetizations in Rocks and Minerals. In: *Treatise on Geophysics*. Ed. by Schubert, G. 2nd ed. Vol. 5. Elsevier, 2015. Chap. 8, pp. 255–308.

[182] Polisetty, S., Sahoo, S., Berger, A., and Binek, C. Temperature dependence of the training effect in exchange coupled ferromagnetic bilayers. In: *Physical Review B* **78** (2008), 184426.

[183] Han, J. K., Baker, A. A., Lee, J. R. I., and McCall, S. K. Probing strongly exchange coupled magnetic behaviors in soft/hard Ni/$CoFe_2O_4$ core/shell nanoparticles. In: *Nanoscale* **15** (2023), 14782–14789.

[184] Duman, E., Acet, M., Wassermann, E. F., Itié, J. P., Baudelet, F., Mathon, O., and Pascarelli, S. Magnetic Instabilities in Fe_3C Cementite Particles Observed with Fe-Edge X-Ray Circular Dichroism under Pressure. In: *Physical Review Letters* **94** (2005), 075502.

[185] Zha, X.-H., Ma, X., Du, S., Zhang, R.-Q., Tao, R., Luo, J.-T., and Fu, C. Role of the A-Element in the Structural, Mechanical, and Electronic Properties of Ti_3AC_2 MAX Phases. In: *Inorganic Chemistry* **61** (2021), 2129–2140.

[186] Power, S. and Ferreira, M. Indirect Exchange and Ruderman–Kittel–Kasuya–Yosida (RKKY) Interactions in Magnetically-Doped Graphene. In: *Crystals* **3** (2013), 49–78.

[187] Lee, C., Park, S. M., Kim, S., Choi, Y.-S., Park, G., Kang, Y. C., Koo, C. M., Kim, S. J., and Yoon, D. K. Field-induced orientational switching produces vertically aligned $Ti_3C_2T_x$ MXene nanosheets. In: *Nature Communications* **13** (2022), 5615.

[188] Bauch, J. and Rosenkranz, R. Physikalische Werkstoffdiagnostik. Ein Kompendium wichtiger Analytikmethoden für Ingenieure und Physiker. 1st ed. Springer Vieweg, 2017.

[189] Whitten, J. E. Ultraviolet photoelectron spectroscopy: Practical aspects and best practices. In: *Applied Surface Science Advances* **13** (2023), 100384.

[190] Richardson, D., Srinivasan, K., Kalitsov, A., Ajan, A., Jain, S., Katz, S., and Wu, M. Interlayer Exchange Coupling in Magnetic Hard-Soft Bilayered Structures. In: *Physical Review Applied* **11** (2019), 044016.

[191] Ellipsometry measurements and data evaluation by Dr. Ivan Tarasov.

[192] XRD and SEM measurements on spray coated $Ti_3C_2T_x$ MXenes by Dr. Hanna Pazniak.

[193] Nanoplexus Limited. Home-Nanoplexus. Apr. 2021. URL: `https://nanoplexus.co.uk/` (visited on 03/29/2024).

[194] Jensen, H., Pedersen, J. H., Jörgensen, J. E., Pedersen, J. S., Joensen, K. D., Iversen, S. B., and Sögaard, E. G. Determination of size distributions in nanosized powders by TEM, XRD, and SAXS. In: *Journal of Experimental Nanoscience* **1** (2006), 355–373.

[195] Smentkowski, V. S. Trends in sputtering. In: *Progress in Surface Science* **64** (2000), 1–58.

[196] Halim, J., Persson, I., Moon, E. J., Kühne, P., Darakchieva, V., Persson, P. O. Å., Eklund, P., Rosen, J., and Barsoum, M. W. Electronic and optical characterization of 2D Ti_2C and Nb_2C (MXene) thin films. In: *Journal of Physics: Condensed Matter* **31** (2019), 165301.

Acknowledgements

Finally, I would like to thank everyone who has contributed to the success of this work.

Prof. Dr. Ulf Wiedwald is thanked for:

The ongoing support of my PhD project.

Valuable discussions, constructive criticism and suggestions.

Support in carrying out TEM, XPS, WAXS, magnetometry and transport measurements and processing/interpreting the data.

Prof. Dr. Thierry Ouisse is thanked for:

Agreeing to be my second reviewer.

Support in the design of the measurement geometry for *in situ* transport measurements on MXenes during Fe intercalation carried out at the ID12 beamline at ESRF.

Prof. Dr. Michael Farle is thanked for:

The opportunity to take a doctorate in AG Farle.

The opportunities for personal development within the framework of the doctoral project.

Dr. Hanna Pazniak is thanked for:

Synthesis of $Ti_3C_2T_x$ MXenes and providing details of the chemical synthesis process.

Spray coating of the MXenes onto the substrates.

Carrying out synchrotron XPS measurements together with sputtering on MXenes with intercalated Fe to extract Fe depth profiles and calibration of the related sputter rate.

Dr. Ivan Tarasov is thanked for:

DFT calculations of the XANES/XLD/XMCD spectra for Fe_3C, bcc Fe and $Ti_3C_2O_2$ MXenes at the Fe and Ti K-edge.

Ellipsometry measurements and their analysis.

Assistance in carrying out SEM, XRD and magnetometry measurements.

Stimulating scientific discussions.

Dr. Detlef Spoddig is thanked for:

Help with the execution and evaluation of AFM measurements and providing any technical support

General support, helpful advice and nice conversations.

Nicolas Josten is thanked for:

Support in finding a suitable solution to Fick's second law of diffusion to describe the Fe diffusion in MXenes.

Dr. Markus Heidelmann is thanked for:

Tips and tricks for finding the optimum measurement parameters when carrying out TEM measurements on MXenes.

Dr. Fabrice Wilhelm is thanked for:

Support in the preparation, execution and analysis of XAS and *in situ* transport measurements at the beamline ID12 of ESRF.

Yasaman Jarrahi Zadeh is thanked for:

Help with lithographic design and writing the lithographic structure on $Si(100)/SiO_2$ substrates

Dr. Tatiana Smoliarova is thanked for:

Help with TEM sample preparation

Dr. Ralf Meckenstock is thanked for:

Help with carrying out first FMR measurements on the MXenes with intercalated Fe.

Prof. Dr. Rolf Möller and Prof. Dr. Frank Meyer zu Heringdorf are thanked for:

Support in the selection of a suitable sample heater in combination with the design of the load lock system (sample storage and sample grabber) for sample transfer into the UHV chamber.

Dipl.-Ing. Ulrich von Hörsten is thanked for:

The high-voltage power supply unit for the sample heater and its wiring and connection.

Support in writing a PID control program for the sample heater and the C evaporator.

Dipl. Phys.-Ing. Michael Vennemann und Dipl. Phys. Marcus Thielen are thanked for:

Repair and modification of the well-aged high-voltage power supply unit used to operate the electron beam evaporator for C deposition in the UHV chamber.

Philipp Kükenbrink is thanked for:

The construction of the sample storage installed in the load lock of the UHV chamber.

For help with mechanical repairs/work on the UHV chamber.

Construction of the heatable sample holder for the *in situ* transport measurements on MXenes during Fe intercaltion.

Sabina Grubba and Helga Mundt are thanked for:

Always reliable, competent and fast help and support with all non-physical topics that one faces in the course of a doctorate.

Their friendly manner ensures that you (almost) always leave the secretariat in a better mood than when you entered.

All members of the AG Farle Group are thanked for:

The good working atmosphere, constant help and support with questions and nice conversations, also outside the subject areas of physics.

Acknowledgements as an associated member of the CRC/TRR 270 HoMMage for:

Personal development and positive experiences within the integrated research training program 'Junior HoMMage'.

Support by the Deutsche Forschungsgemeinschaft (DFG) within CRC/TRR 270, project B02.

Finally, I would like to thank my family for always supporting me and giving me the space I needed to write this dissertation.

DOI: 10.17185/duepublico/82171
URN: urn:nbn:de:hbz:465-20240813-075152-1